João Pedro Piroto Pereira Duarte

Estudo do comportamento do hidrogénio em semicondutores do tipo ftalocianina por técnicas de muões

Study of hydrogen in phthalocyanine semiconductors using μSR techniques

Dissertação de Doutoramento em Física - Especialidade de Física Experimental
submetida à Universidade de Coimbra

Coimbra - 2006

Este trabalho foi parcialmente financiado pelos seguintes programas:

This work was partially supported by the following programmes:

Ministério da Educação do Estado Português / Fundo Social Europeu (FSE)
Programa PRODEP III
Acção 5.3 - Formação Avançada de Docentes do Ensino Superior

Portuguese Ministry of Education / European Social Fund (ESF)
Programme PRODEP III
Action 5.3 - Advanced Formation for High Education Teaching Staff

European Commission - 6th Framework Programme
Key Action: Strengthening the European Research Area, Research Infrastructures
Contract No. RII3-CT-2004-505925

À Carina, por ser quem é

Aos meus pais, por ser quem sou

À Maria Eduarda, por quem será

Resumo

Este trabalho apresenta um estudo experimental dos semicondutores orgânicos Ftalocianina (H_2Pc), Ftalocianina de Zinco (ZnPc) e Ftalocianina de Cobre (CuPc) por técnicas de μSR, tendo-se obtido informação detalhada sobre a estrutura electrónica dos estados de carga formados pelo muão positivo nos três compostos, e sobre as interacções dinâmicas a que esses estados se encontram sujeitos.

Os resultados do estudo indicam que nas ftalocianias com carácter não magnéticas H_2Pc e ZnPc se dá a formação de três radicais muónicos paramagnéticos distintos. A estrutura hiperfina destes radicais, referidos como estados I, II e III, foi caracterizada através da medida dos parâmetros de acoplamento hiperfino em conjunto com a parameterização da sua dependência com a temperatura. Uma quarta componente paramagnética do sinal μSR foi também identificada, mas sobre a qual não foi possível retirar conclusões definitivas quanto à sua origem. Verificou-se que os parâmetros de acoplamento hiperfino isotrópicos dos três estados identificados se encontram numa região de valores entre os 100 e os 150 MHz para os estados I e II, enquanto que para o estado III esta quantidade toma valores em torno de 10 MHz. A estrutura electrónica de todos os estados possui simetria axial, caracterizada por parâmetros dipolares de cerca de 15 MHz para os estados I and II, e 20 MHz para o estado III. A origem dos estados I e II foi determinada como sendo devida à adição de muónio a uma das ligações duplas existentes nos anéis benzénicos da periferia das moléculas de ftalocianina recorrendo a cálculos de estrutura electrónica, tendo-se verificado a existência de um acoplamento entre a interacção hiperfina desses estados e modos vibracionais desses anéis. A problemática da localização do estado III também foi abordada, tomando-se como hipótese mais provável uma posição intersticial entre duas moléculas de ftalocianina.

O estudo das interacções dinâmicas de spin destes três estados revelou que o estado III está sujeito a um fenómeno de *spin exchange*, originado pela colisão com portadores de carga presentes no material. A taxa de *spin-flip* relativa a esta interacção foi deduzida a partir de medidas μSR em geometria de campo longitudinal, tendo sida determinada a barreira energética existente para a difusão de portadores de carga entre moléculas de ftalocianina localizadas dentro da mesma estrutura colunar tanto na H_2Pc, como na ZnPc.

Por fim, o sinal μSR da ftalocianina com carácter magnético CuPc foi também caracterizado. Foram identificadas duas componentes de carácter aparentemente diamagnético com taxas de relaxação separadas por cerca de duas ordens de grandeza, atribuídas a duas configurações distintas para o emparelhamento entre o electrão do radical muónico, e o electrão com spin desemparelhado localizado no átomo de cobre. Os dois emparelhamentos diferentes geram um ambiente puramente diamagnético para o muão, o que origina a componente de relaxação lenta, e uma configuração na qual existe uma densidade de spin flutuante na posição do muão, responsável pela componente de relaxação elevada.

Abstract

This work presents an experimental μSR study of the organic semiconductors Metal-free Phthalocyanine (H_2Pc), Zinc-phthalocyanine (ZnPc) and Copper-Phthalocyanine (CuPc). It produced detailed information about the electronic structure of the muon states formed in the three compounds, and about the dynamical spin interactions those states experience.

It was established that in the non-magnetic phthalocyanines H_2Pc and ZnPc, three distinct muoniated radical states bearing paramagnetic character are formed. The hyperfine structure of these radicals, labelled I, II and III, was characterised by measuring the hyperfine couplings and parameterising their temperature dependence. In addition, a fourth paramagnetic component of the μSR signal was also identified, but no definite conclusions about its origin were drawn. The isotropic hyperfine couplings of the three states were found to be of the order of 100-150 MHz for states I and II, and about 10 MHz for state III. All states were seen to possess axial symmetry, with dipolar hyperfine couplings of around 15 MHz for states I and II, and about 20 MHz for state III. States I and II were found to arise from muonium addition at the double bonds populating the outer benzene rings of the molecule using ancillary electronic structure calculations, and their hyperfine interactions were seen to couple with vibrational modes of those rings. State III was assigned to an intersticial site in-between two molecules.

The investigation of the spin dynamics of these three states revealed that state III experiences spin exchange phenomena arising from scattering with diffusing charge carriers present in the host material. The muon spin-flip rate regarding this interaction was extracted from measurements in longitudinal field, and the energy barrier for carrier jumps between phthalocyanine molecules belonging to the same columnar stack was determined in $H_2Pc$and ZnPc.

The μSR signal of the magnetic phthalocyanine CuPc was also characterised. Two diamagnetic-like components with relaxation rates differing in about two orders of magnitude were identified in this compound, which were argued to arise from different pairing configurations of the muonium's electron to the unpaired electron sitting at the copper atom. The two pairings create one purely diamagnetic environment for the muon, giving rise to the slow relaxing component, and one configuration of quickly fluctuating unpaired spin density at the muon, responsible for the fast relaxing component.

Acknowledgments

The path one must thrive to accomplish the formidable task which is living often delivers difficulties which one can only surpass with the generous help of the other, whom we then on pass to call *Friend*. Getting through a full PhD work and thesis has been a considerable part of that path for me in the last years, but for which I feel fortunate for it allowed me to sincerely pronounce the word Friend as many times I felt need to. I hereby offer my dearest thank you to:

Professor João Gil, my PhD supervisor, who has been the main support of all my work at all times. Many were the occasions in which a father would have punished, but instead I always found priceless words of encouragement and advice. I have learned much with him, not only of how to become a scientist, but also of how to become a better Man;

Professor Nuno Ayres de Campos, whom I consider to be a mentor both in Science as in Life. I am pleased to be able to express how much I look up to him, and how I find him to be an inspiring person at all levels;

Dr. Helena Alberto, member of the Nuclear Condensed Matter Physics group at the Physics Department of the University of Coimbra, who has in all occasions been a tireless friend instead of a work colleague. It was very reassuring for me knowing I could count on her for anything;

Dr. Francisco Gil, member of the Nuclear Condensed Matter Physics group, who lead me with uncomparable availability along the painstaking task of setting up all the electronic structure calculations needed for this work, and many times walked with me through the corridors of the Chemistry Department in search of answers I was not able to unravel on my own;

Dr. Benilde Costa, also member of the Nuclear Condensed Matter Physics group, to whom I have to thank all the diligent help she provided with most of the experimental work performed at Coimbra, and the great concern she always took with the degree of priority that work

sometimes had to be accomplished;

Rui Vilão, member of the Nuclear Condensed Matter Physics group, but above all a great friend and, in spite his early age, already a role model for life. He has been a wonderful companion at all times, and in fact a good part of this work is directly due to him. I hope we keep walking together in Science and life for many years to come, now that we both cross at the same time to another stage;

Professor Alois Weidinger, one of the finest and brightest scientists I have ever met. His tenacity in seeking answers to difficult questions, and still keeping the best sense of pragmatism, has been one of the most important lessons I carry from my PhD work. For the hard work, he was always the colleague when he could by his own right remain the Professor. That too, was a lesson, and I am proud to have had his help;

Professor Steve Cox, with whom I have learned more about μSR than with anyone else. I thank him for all the dedication he has vouched me with in the wonderful task that is learning μSR; often, one word was enough to make everything clear;

All the μSR instrument scientists and support staff at the Paul Scherrer Institut, namely Dr. Alex Amato, Dr. Robert Scheuermann, Dr. Chris Baines and Dr. Dierk Herlach. This work also belongs to them, and I thank them for their tireless atitude during my stays at PSI;

All the μSR instrument and scientific staff at the Rutherford-Appleton Laboratory, namely Dr. Steve Cottrell, Dr. James Lord and Dr. Adam Hilger. I likewise owe this work to them, and thank them for their full availability while I was at RAL.

Dr. Kosta Fostirupoulos, at the Hanh-Meitner Institut Berlin, not only for his direct aid with the preparation of samples, but also for his commitment at helping the Nuclear Condensed Matter Physics group to become independent in what regards that same subject. I am also indebted to Bernd Mertessacker and Hans Kubiac, who were fundamental for the accomplishment of that endeavour.

Dr. Abílio Sobral, at the Chemistry Department of the University of Coimbra, for his availability and readiness to help in all matters related with the chemistry of phthalocyanines,

both theoretical and experimental, and to Ana Maria Mendonça, for her true patience in conducting someone with so little experience through a fast course in basic Chemistry procedures;

Eng. Pinhão and all the staff at LIP's workshop in Coimbra, for their dedicated work, which in so many times was essential for the experimental accomplishments of this work;

Dr. Ana Matos Beja and all the members of the Solid State group at the Physics Department of the University of Coimbra, for their valuable help with X-ray characterisation of samples;

Pedro, my father, Ana, my mother, and Gonçalo, my brother, for all the support, love and stability they granted my out-of-the-job life, and without which I would never have gotten where I am today;

Carina, my beloved and dearest soul mate. You knew when to be a wife, a friend and also sometimes a mother. There is no day that passes in which I don't feel proud of having you by my side. This work is also your doing.

Communications arising from this work

(September 2006)

Articles in peer-reviewed international scientific journals

J. Piroto Duarte, R.C. Vilão, J.M. Gil, H.V. Alberto, N. Ayres de Campos, A. Weidinger
Muoniated radicals in the organic semiconductor zinc-phthalocyanine
Physica B: Condensed Matter **326** (2003) 94-96

J. Piroto Duarte, R.C. Vilão, H.V.Alberto, J.M. Gil, Francisco P.S.C. Gil, A. Weidinger, N. Ayres de Campos
Dynamics of muoniated radical states in phthalocyanines
Physica B: Condensed Matter **374-375** (2006) 426-429

J. Piroto Duarte, R. C. Vilão, H. V.Alberto, J. M. Gil, Francisco P. S. C. Gil, A. Weidinger, N. Ayres de Campos, K. Fostiropoulos
Muoniated radical states in the organic semiconductor phthalocyanine
Physical Review B **73** (2006) 075209

Poster communications in conferences

J. Piroto Duarte, R. C. Vilão, J. M. Gil, H. V. Alberto, N. Ayres de Campos, A. Weidinger
Muonium in the organic semiconductor zinc-phtalocyanine
9th Int. Conf. on Muon Spin Rotation/Relaxation/Resonance (MuSR 2002), Williamsburg, Virginia, USA, 3-7 June, 2002

J. Piroto Duarte, R.C. Vilão, H.V.Alberto, J.M. Gil, Francisco P.S.C. Gil, A. Weidinger, N. Ayres de Campos

Dynamics of muoniated radical states in phthalocyanines
10th Int. Conf. on Muon Spin Rotation / Relaxation / Resonance (MuSR 2005), Oxford, UK, 8-12 August 2005.

J. Piroto Duarte, R. C. Vilão, H. V.Alberto, J. M. Gil, Francisco P. S. C. Gil, A. Weidinger, N. Ayres de Campos
Probing local environment in organic semiconductors with muonium, an exotic experimental analogue of hydrogen
21st Int. Conf. on Amorphous and Nanocrystalline Semiconductor - ICANS 21, Lisbon, Portugal, 5-9 September 2005.

Contents

List of Figures

List of Tables

Chapter 1

Introduction

1.1 The study of organic semiconductors

1.1.1 Scientific context

Research on organic semiconductors in Science Materials has experienced a steep increase in recent years (Figure 1.1), producing large quantities of information regarding several aspects of their structural and transport properties under a growing interest which was partially triggered by the awarding of the 2000 Nobel prize in Chemistry to Alan J. Heeger, Alan G. MacDiarmid and Hideki Shirakawa for *"the discovery and development of conductive polymers"* [80].

Yet, much remains still to be learned about the relation between morphological, optical and electrical properties in this class of compounds [49]. Their electronic behaviour at a fundamental degree, in particular, is poorly known, especially due to the difficulty of obtaining experimental results at that level [28, 136]. For example, it becomes a fact that the picture about charge conduction mechanisms has not still reached a mature level, considering that most conduction parameters, such as the density of states in transport levels or activation energies for the conductivity, are still unknown for many organic semiconductors [28]. In addition, most of the information available has been obtained with macroscopic techniques like resistivity, Hall effect or Seebeck measurements [50, 92, 51], which are strongly influenced by grain-boundary and surface effects in a type of compounds seldom obtained in single-crystal form, and are therefore not truly sensitive to microscopic phenomena.

There is therefore a strong interest in performing experimental studies which may provide a microscopic view about organic semiconductors. Such interest involves also their behaviour

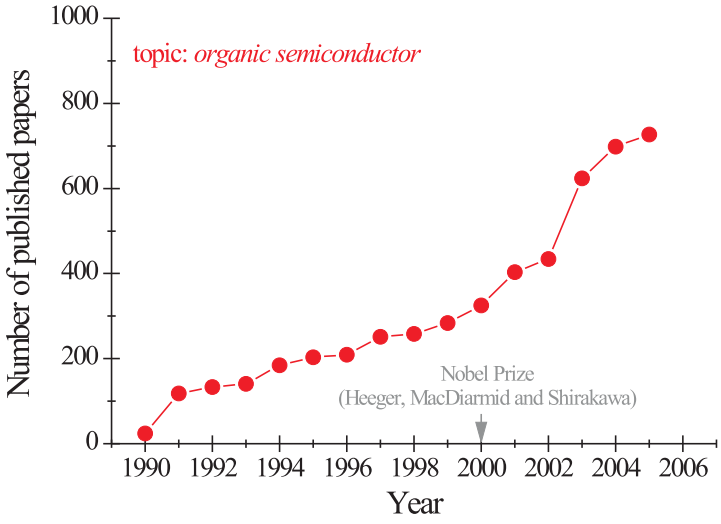

Figure 1.1: Number of published papers since 1990 matching the topic 'organic semiconductor', as obtained from a query conducted on the *Science Citation Index Expanded (SCI-EXPANDED)* database of the ISI Web of Science search tool (the ISI Web of Science is a tool belonging to The Thomson Corporation).

towards doping, since the lack of fundamental information about how the electronic properties of the material are affected is even more pronounced in that case [28, 40]. The intentional doping of a semiconductor with a small quantity of known impurities is a widely used method to control its electrical properties, which only works if the effect of the dopant on those properties is fully understood. For instance, research activity on doping is accelerating [86, 40, 81, 17, 30, 26], but with the notable exception of a very reduced number of cases in which a fair insight of how the doping mechanism operates has been obtained so far (see *e.g.* [70, 107], or [25, 26]), no real experimental understanding exists yet.

1.1.2 Technological context

Organic semiconductors are considered to be at present top candidates as alternative materials to the traditional inorganic semiconductors [60, 39, 56, 43, 11, 100]. They offer answers where silicon-based electronics cannot provide a solution, such as the possibility of assembling *transparent* electronic components in *flexible* substrates [11], or simply constitute a cheaper and more efficient option to that technology in specific situations, namely large-area applications [11].

One of the great promises of organic electronics is that once the physical requirements

for a certain application are clearly understood, methods of organic synthesis may be employed to produce inexpensive compounds with the desired properties [49]. Those methods have the advantage of being easy to implement in low-temperature procedures, which conjugated with the simplicity of processes such as thin-film deposition or spin-coating cast aside the large-scale facilities necessary for the production and processing of inorganic semiconductors [37]. Organic semiconductors are highly competitive materials from the economical and operational perspectives, since the virtually limitless flexibility of synthetic organic chemistry provides a degree of control over any characteristics of the material which is unattainable with conventional inorganic semiconductors [49, 26].

Several examples of their technological importance exist; for instance, significant advances obtained in a time lapse of less than one decade levelled their electroluminescent capabilities with those of inorganic compounds [14, 39], leading to the development of high efficiency organic light-emitting diodes (OLED) [14, 104, 141]. Their application in another type of optoelectronic device, the organic light-emitting field-effect transistor (OFET), is also envisaged in a near future [78], making use of the fact that organic semiconductors often do not have a preferencial charge-carrier sign and are thus capable of exhibiting ambipolar charge transport [72]. This property is important for the fabrication of complementary logic circuits, allowing the conception of all-organic integrated circuits. Such possibility is further stressed by the late reckoning that, contrary to what was widely accepted, fast switching circuitry may be based in organic devices [127]. Much effort has also been put in the use of organic semiconductors for solar cells; recent accomplishments on organic photovoltaics, OPV, indicate that this type of technology will be able to rival with the industry of amorphous hydrogen-doped silicon in terms of efficiency, while retaining the clear advantage of being significantly cheaper and appropriate for the production of large-scale devices [11, 44]. The success of all these applications obviously depends on the knowledge of the Physics of their behaviour at a fundamental level.

Additionally, particular relevance has been given in the last two years to possible applications which embrace the magnetic properties of these compounds; that interest follows the findings that electron-hole recombination is spin-dependent [94], and the existence of giant magnetoresistivity in certain conjugated polymers [137, 73, 125], both granting entrance of organic semiconductors to the world of spintronics and quantum computing. Again, but now in a many-fold technological perspective, there is an increased interest in having experimental studies which render microscopic information about organic semiconductors.

1.2 A μSR study of organic semiconductors

Local probe techniques present often the best way to convey microscopic information about condensed matter [103]. This work reports the results of a fundamental study of organic semiconductors performed with an experimental technique belonging to that class, Positive Muon Spectroscopy (μSR) (an extensive literature on μSR exists; see *e.g.* [106, 20, 85]). As it will be seen later (Chapter 3), it takes advantage of the technique's unique features to probe at the same time the charge transport properties of organic semiconductors and the effects of hydrogen doping. In itself, the technique involves implanting spin-polarised positive muons in a host material, which may play the role of local magnetic probes sensitive to the transport of spin-carrying carriers in the medium, or act as exotic experimental analogues of protons, mimicking hydrogen behaviour and its doping effects.

Organic semiconductors are traditionally divided in high molecular weight conjugated polymers and low-weight molecular compounds [50]. For the general understanding of organic semiconductors, the second ones are more informative because they can be obtained in higher purity grades more easily, and form highly ordered solids [51]. They are therefore attracting a lot of investigation on semiconducting behaviour, and in this field phthalocyanines are specially favourable and were therefore chosen for this work. They have the advantages of possessing a high thermal stability which allows to employ easy purification processes [50, 37, 51], of being easily doped with other molecular compounds in thin-film form by co-evaporation techniques [86], and of being modified with simple chemical procedures [30].

More specifically, three representative molecules of phthalocyanines were chosen for the experimental μSR study, namely H_2Pc (the metal-free phthalocyanine), ZnPc (Zinc-phthalocyanine) and CuPc (Copper-phthalocyanine), as indicated in Figure 1.2. The choice of these three compounds was based in their structural simplicity, together with the ground-state magnetic properties of each molecule: both H_2Pc and ZnPc are diamagnetic, featuring a closed-shell configuration, while CuPc has one unpaired electronic spin, being paramagnetic. The inclusion of H_2Pc and ZnPc serves the aim of studying the influence of the central atom, which is known to influence the chemical properties of phthalocyanines [50], while the distinction between the diamagnetic molecules H_2Pc and ZnPc, and the paramagnetic one CuPc addresses the influence of unpaired electrons in the material.

The present work aims at characterising the muon states formed in phthalocyanines and the spin dynamics those states undergo. This comprises the definition of the electronic structure

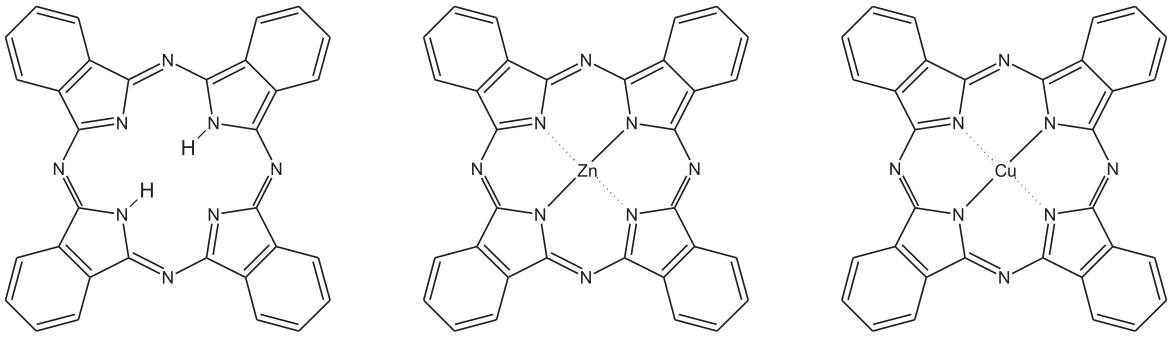

Figure 1.2: Molecular structure of the three model phthalocyanines addressed in this work: H_2Pc, ZnPc and CuPc.

of those states, as well as of their crystalline site, and the identification and characterisation of the dynamical processes which may exist. In parallel, scientific insight regarding the charge carrier properties of this type of compounds and how they behave towards hydrogen doping is also expected to be drawn from the experimental μSR work.

1.3 Layout of this thesis

After having focused the interest of studying phthalocyanines with μSR techniques in this first introductory chapter, a brief presentation of the most important properties of that family of organic semiconductors which relate directly with the interpretation of μSR data is referred in Chapter 2. The rather limited current understanding of how charge transport occurs in phthalocyanines and how it is affected by doping is also referred in that chapter, laying ground for the interpretation of μSR results obtained from measurements targeting spin-dynamics performed later on (Chapter 7). Chapter 3 includes a quite complete account about the μSR technique; it focuses both experimental as theoretical aspects, the latter centred in paramagnetic muon states, and although it was firstly sketched to merely introduce the technique and state important points necessary for the interpretation of the μSR signal in the context of this thesis, it turned out assuming more the shape of a self-consistent textbook chapter on μSR. This outcome was prompted by the fact that μSR is not a well-known technique among those used to investigate condensed matter, and that μSR literature usually tends to be either too short or too detailed for a beginner to grasp a sufficient amount of μSR knowledge in a modest amount of time which enables him to perform a μSR experiment and provide a simple interpretation of its

results. It is hoped also that the capabilities of the technique, the kind of problems it may help solving and its limitations become clear for the reader, assisting in the wide-spreading of μSR. The following chapter, Chapter 4, describes the experimental work carried out in the preparation of samples for the μSR experiments, and lists all samples used together with the specific conditions in which each one was prepared. Chapter 5 is devoted to the spectroscopy of muon states in the three phthalocyanine compounds addressed in this thesis. It establishes simple conclusions about the number of different existing states, and quantifies their relative populations and electronic structure parameters. This information is necessary for the investigation of spin dynamics of those states, reported in Chapter 6, which relate directly with dynamical phenomena involving the host material, namely charge carrier diffusion. The discussion of the experimental results presented in chapters 5 and 6 is finally conducted in Chapter 7, where the conclusions of this work are clearly stated, including those associated with charge transport in phthalocyanines.

Chapter 2

The phthalocyanine organic semiconductor

This chapter constitutes a brief presentation of the physical properties of phthalocyanines which are specially relevant for the work developed in this thesis. It covers mostly the structural and electronic characteristics of the three model molecules chosen for the μSR study performed here, namely the metal-free phthalocyanine (H_2Pc), Zinc-phthalocyanine (ZnPc) and Copper-phthalocyanine (CuPc). They are amongst the simplest phthalocyanines, and also the most widely used ones.

2.1 Molecular structure

Phthalocyanines consist of a planar π-conjugated macrocycle ligand ($C_{32}H_{16}N_8$) often bonded to a central metallic atom [77, 29, 32]. The structure of the ligand closely relates phthalocyanines with porphyrins and other derived macrocycles (Figure 2.1); their common feature is the circular arrangement of 4 pyrrole units linked by C methine or N azamethine bridges, in the centre of which two hydrogen atoms or almost any type of metallic or semimetallic atom may be placed. The size of the inner cavity depends mainly on the type of bridges, being fairly insensitive to the size of the central atom [32]. Relative to the porphyrin ligand, phthalocyanines have benzene rings added to the pyrrole units, and N azamethine bridges instead of C methine ones. The macrocycle of phthalocyanines is an 18 π-electron system, which lends high stability to these compounds; their more specific chemical properties, on the other hand, depend to a large extent on the central atom bonded to the macrocycle [51].

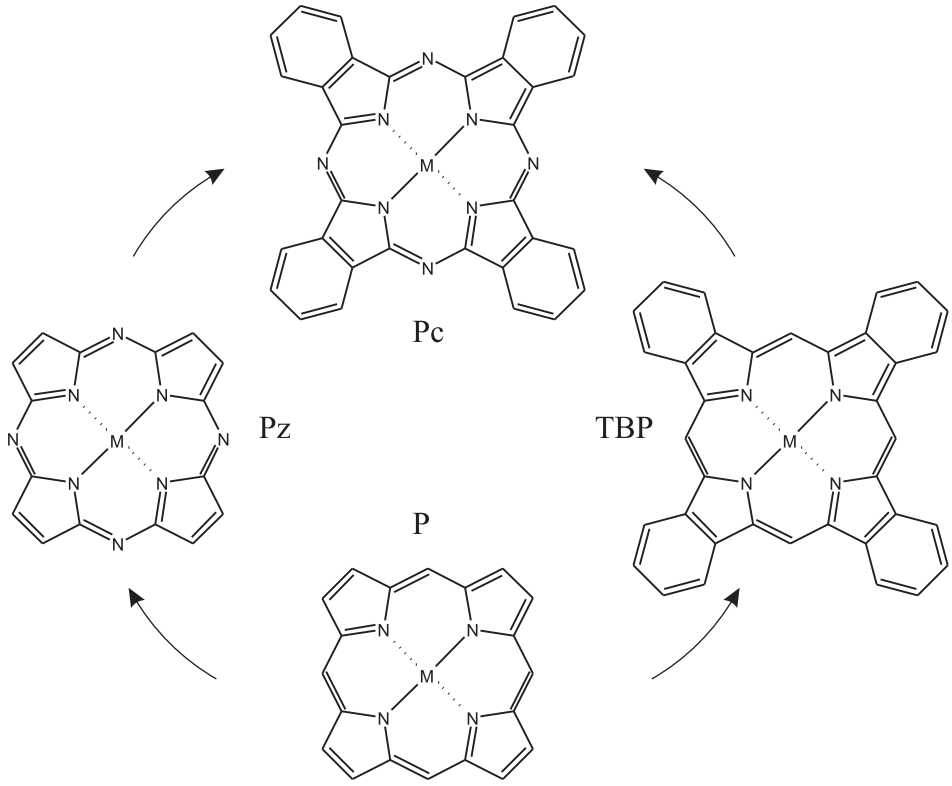

Figure 2.1: Structural relation between phthalocyanines (Pc), porphyrins (P), porphyrazines (Pz) and tetrabenzoporphyrins (TBP). The differences between the four ligands consist in the addition or not of benzene rings to the pyrrole units, and the type of bridge existing between those units.

The *metal-free phthalocyanine*, H_2Pc, is the simplest existing phthalocyanine; it possesses no central metallic atom, which is in this compound substituted by two hydrogen atoms (Figure 2.2*a*). These hydrogen atoms establish alternate bonds with all four isoindole N atoms[1], remaining in the plane of the molecule so that mirror symmetry relative to such plane exists. H_2Pc resembles therefore a large disk-like molecule, capable of originating layered solid state arrangements. The existence of mirror symmetry in the *metallo-phthalocyanines*, MPc, on the other hand, depends on the coordination of their central atom; if the atom has binary coordination, as Zn or Cu, it will stay also in the plane of the molecule, and the molecule will still be fully planar (Figure 2.2*b*). Other coordinations imply the presence of additional ligands at the centre of the molecule with an axial position. The originated structures are no longer fully planar; they may loose the mirror symmetry, as in the case of Titanyl-phthalocyanine, TiOPc (Figure 2.2*c*), promote the formation of dimeric phthalocyanine complexes connected by the axial ligands (Figure 2.2*d*), or even induce a bent macrocycle structure.

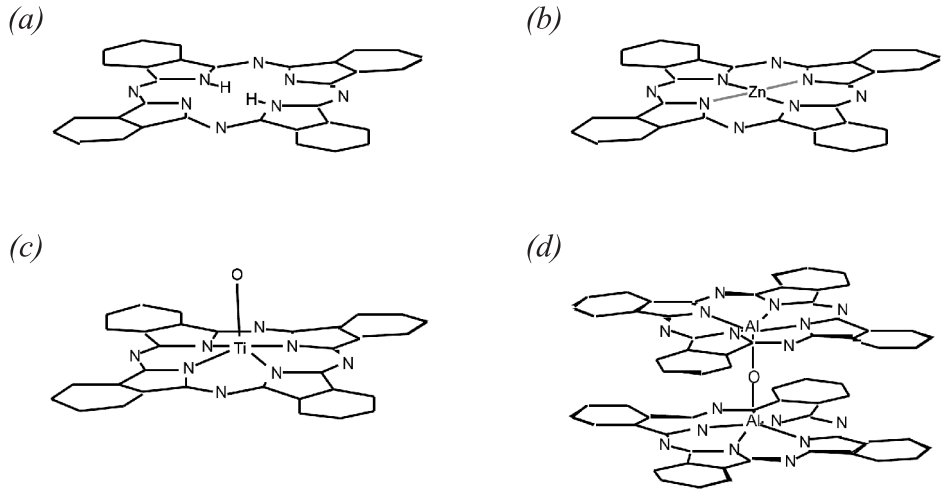

Figure 2.2: Examples of some phthalocyanine structures: *(a)* metal-free phthalocyanine (H_2Pc), *(b)*, Zinc-phthalocyanine (ZnPc) *(c)*, Titanyl-phthalocyanine (TiOPc) and *(d)* the $(AlPc)_2O$ dimer.

Phthalocyanines do not occur naturally, and have been known only since 1907 [77]; as a general rule, they are synthesised using a single step cyclotetramerisation reaction of organic precursors, namely benzoic acid or its derivatives (Figure 2.3) [77, 15]. They are also functionalised at its outer benzene rings quite easily by making the right choice of precursors[2]; since

[1]The isoindole N atoms are the ones belonging to the pyrrole units, as opposed to those in the azamethine bridges.

[2]By functionalisation one understands here the substitution of the hydrogen atoms at the outer benzene rings

phthalocyanines are superbly stable from the chemical point of view, the functionalisation is very difficult post-synthesis and needs to be necessarily considered in the synthesis process. Along with the diversity of choice for the central atom, the simple chemical modification by functionalisation is one of the major reasons why phthalocyanines present such a large potential for applications, since two independent levels of adjustment regarding their chemical and electrical properties are available.

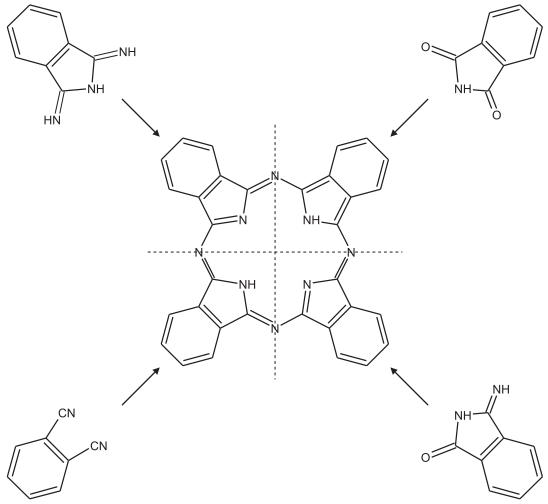

Figure 2.3: General synthesis scheme of phthalocyanines. It is based in a single-step cyclotetramerisation reaction of organic precursors (usually benzoic acid or its derivatives).

2.2 Solid state arrangement

Phthalocyanines form Van-der-Waals solids, with a crystalline arrangement which depends naturally on their specific molecular structure. Many different crystalline geometries exist for phthalocyanines (see [32]), but we will reduce here to the generic description of the solid state layout of those with in-plane central atoms only (which henceforth we will refer to as *planar* phthalocyanines), since these produce the simplest geometries and also because the three compounds focused in the present thesis fall in that class.

The molecular structure of planar phthalocyanines offers an increased range of possibilities for intermolecular interactions, namely between the central atom (a more positively charged region) and the nitrogen atoms (negatively charged regions) [32]. This has as result the fact

by organic chains or other end-groups.

that stable overlap geometries between two molecules in contiguous layers correspond to *slipped* configurations instead of perfectly aligned ones. Figure 2.4 shows the four existing overlap geometries of planar phthalocyanines.

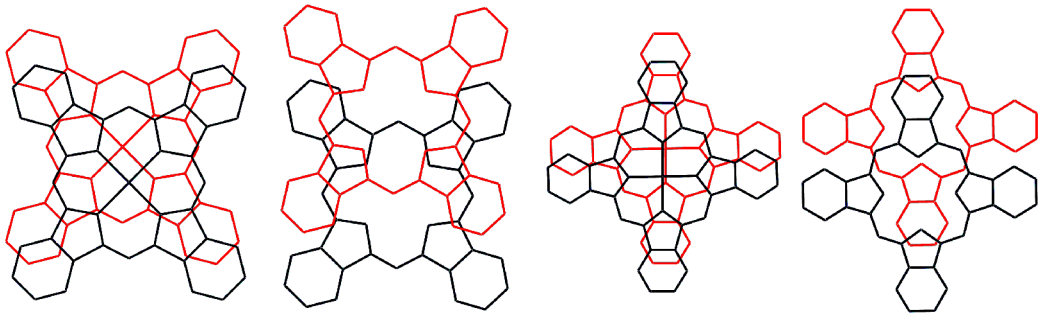

Figure 2.4: The four different overlap geometries of planar phthalocyanines. The most stable of all configurations is the second from the left, which corresponds to the overlap found in the β phase polymorph (see text); its stability stems from the large intermolecular interaction existing between the central atom of one of the molecules and a bridging nitrogen of the other.

Any of the overlaps depicted in Figure 2.4 originates a columnar slipped-stacking of the Pc molecules in solid state[3]. The layout of that stacking (intermolecular distances, stacking angle, *etc.*), however, depends on the specific details of the overlap, giving rise to different metastable phases. This means that phthalocyanines are *polymorphic*, often exhibiting monoclinic and triclinic unit cells. The stable polymorph of planar phthalocyanines is the β-phase, which has a monoclinic crystalline structure with two centro-symmetrical molecules per unit cell [**?**, **?**, 105, 32]. The molecular overlap in this phase corresponds to the second geometry from the left in Figure 2.4; its absolute stability stems from the large intermolecular interaction existing between the central atom of one of the molecules and a bridging nitrogen of the other. Figure 2.5 further elucidates how phthalocyanine molecules interlock in this phase; a cut-view of the slipped-stacked columns (left) reveals a *herring-bone* stacking, where the molecular planes of adjacent columns make an angle of near 90 °. On the right, a tridimensional view along a direction perpendicular to the molecular planes in one of the columns is shown. It should be noted that since the columnar distances are small in the herring-bone stacking, the existence of hydrogen bonding between the benzene hydrogens and the nitrogens of molecules in neighbouring columns is highly favoured. This distorts the benzene rings [74], and pulls the hydrogen atoms away from the molecule.

[3]In slipped-stacked arrangements the overlapping molecules in a stack are slightly displaced in a direction along the stacking axis when observed at perperpendicularly.

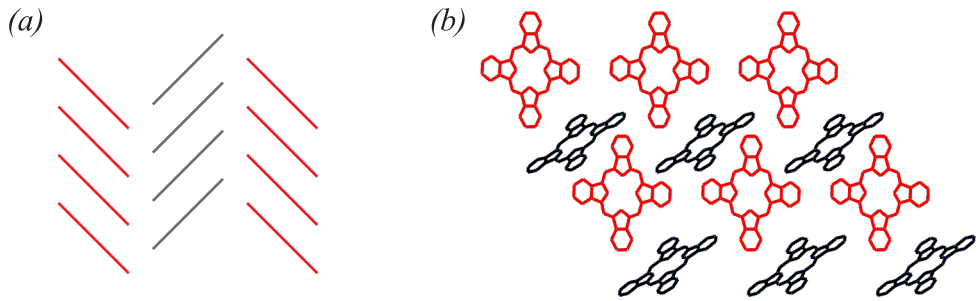

Figure 2.5: Solid state arrangement of phthalocyanine molecules in the β phase: *(a)* cut-view of the slipped-stacked columns, revealing a *herring-bone* layout; *(b)* projection view along a direction perpendicular to the molecular planes of the first column shown in *(a)*.

2.3 Electronic structure

The electronic absorption spectra of closed-shell[4] phthalocyanines, such as H_2Pc or ZnPc, is characterised by the existence of an isolated and intense band between around 650 to 720 nm (Figure 2.6) [15, 79, 97]. This band, known as Q-band, is usually attributed to $\pi \rightarrow \pi^*$ transitions from the highest doubly occupied molecular orbital (HOMO) to one of the lowest unoccupied molecular orbitals (LUMO)[5] of the molecule [15, 79]. A second less intense band is also observed at around 300-400 nm (the B-band), which corresponds to the transition between a molecular orbital deep below the HOMO to the LUMO. The Q-band is responsible by the intense blue to green colours exhibited by phthalocyanines, to which their use as dye pigments is due [29, 77].

Although a large number of atomic valence states exists in a phthalocyanine molecule, the level diagram near the HOMO and the LUMO orbitals is rather simple for planar phthalocyanines, as seen in Figure 2.7 [79, 97, 64]. As a general rule, the LUMO is degenerate, lying about 2 eV ($\approx$ 620 nm, the location of the Q-band) above the HOMO; a different central atom does not change the HOMO, although some influence is exerted in the LUMO's energy. The HOMO orbital is dispersed over the whole spatial extent of the phthalocyanine, possessing a high bonding character (Figure 2.8); the LUMO orbital, on the other hand, his more localised at the N atoms and two opposite benzene rings, and exhibits some π^* anti-bonding character. This basic structure holds for all planar phthalocyanines, including H_2Pc, ZnPc and CuPc.

It may also be seen from Figure 2.7 that the main effect of bonding atoms with unpaired electronic spins to the phthalocyanine ligand relative to the basic structure described above is

[4] *i.e.* having no unpaired spins.

[5] As it is referred below, the LUMO of phthalocyanines is degenerate.

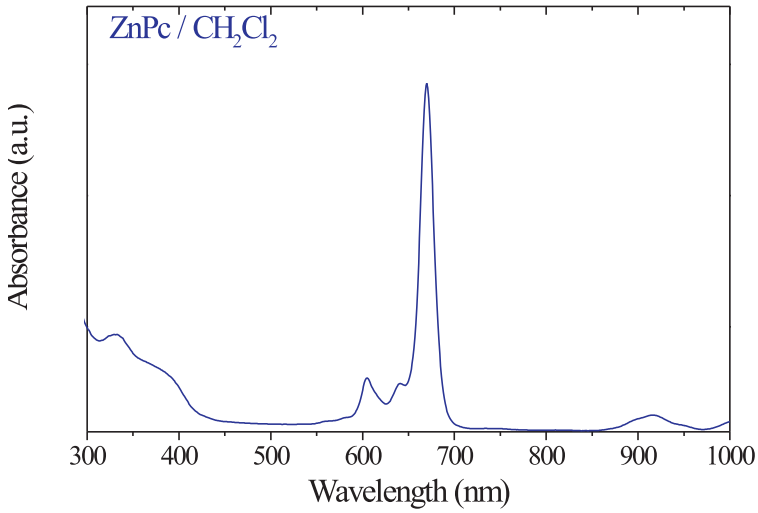

Figure 2.6: Electronic absorption spectrum of ZnPc in dichloromethane, showing the Q-band responsible by the deep colour of phthalocyanines at around 650 nm.

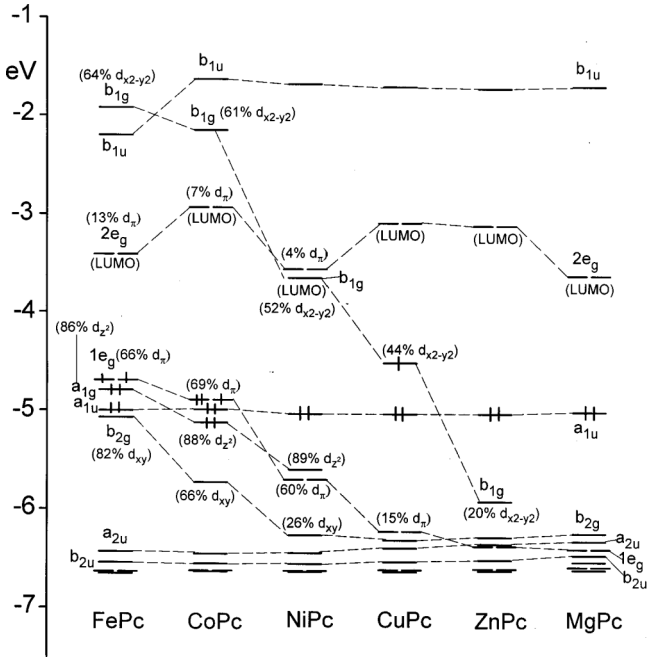

Figure 2.7: Valence energy levels of several planar phthalocyanines. This diagram is the result of an electronic structure calculation using DFT methods, as obtained by Liao and Scheiner [64]. The HOMO orbital is signaled by the doubly occupied levels, and for some molecular orbitals their percentage of $3d$ metal character is indicated by the values in parenthesis. Source: [64]

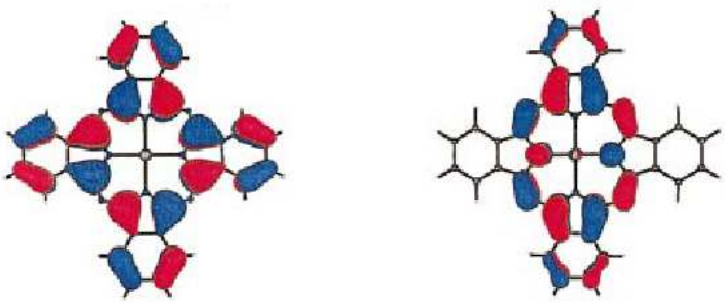

HOMO LUMO

Figure 2.8: Iso-value surface plots of HOMO and LUMO orbitals of ZnPc. The HOMO is dispersed over the whole macrocycle, while the LUMO is more localised at the N atoms in the macrocycle. The red and blue colours indicate the sign of the wave function. Source: [79]

the introduction of a singly occupied molecular orbital (SOMO) level between the HOMO and the LUMO. The SOMO state is invariably localised at the centre of the phthalocyanine molecule, with a character dominated by one of the $3d$ orbitals belonging to the central atom. This is the case *e.g.* of CuPc.

2.4 Semiconducting behaviour

General characteristics of organic semiconductors

The main fundamental difference between organic semiconductors and inorganic semiconductors such as Si, Ge, GaAs or ZnO, resides in the strength of bonding between their basic units. Inorganic semiconductors are usually formed from atoms held together by strong covalent bonds; this gives rise to a large overlap between atomic valence orbitals which, in conjunction with the high spatial regularity of the electrostatic potential also provided by the strong bonding[6], results in the formation of delocalised electronic band states through which electrical conduction may develop [6]. Organic semiconductors, which comprise both conjugated polymers and low molecular weight solids [50], are formed on the other hand from molecules, joined by much weaker Van der Waals forces which produce a significantly smaller overlap between molecular valence orbitals of neighbouring molecules. This sharpens the localisation of charge carriers at the molecules [50, 49], so that charge transport in organic semiconductors occurs *via* hopping

[6]One means here that atomic motion is hampered by the strength of the bonding, which preserves the periodicity of the potential.

between localised states rather than band-like motion. This is certainly true in molecular solids [49], but not so in many conjugated polymers, where band-like motion is also often observed as deduced from their similar electrical properties relative to inorganic semiconductors [130].

Intermolecular interaction forces are nevertheless small, and, for molecular solids, hopping turns out to be an efficient mechanism of charge transport since a high degree of disorder is allowed to exist [50, 49, 130, 5]. Disorder, which may be morphologic (or, in the accepted nomenclature of organic semiconductors, *off-diagonal*), as occurring mainly in conjugated polymers, or due to molecular motion driven by temperature (known as *diagonal* or *energetic* disorder), dominant in molecular compounds, leads to an increased overlap between molecular orbitals of adjacent molecules that in its turn enhances the probability of charge carrier hopping occurring from one molecule to the other [7, 92]. Energetic disorder in molecular solids is therefore the mechanism responsible by the rise of charge-carrier mobilities with increasing temperature observed in these compounds [49], in clear contrast to the well-known mobility decrease seen in inorganic semiconductors and many conjugated polymers due to phonon-scattering [92]. One should note, nevertheless, that the possibilities of the hopping mechanism are still quite limited, as deduced from the typically 100 times lower mobility values measured in organic semiconductors in comparison to inorganic ones [28]. Furthermore, only those materials which possess a conjugated (*i.e.* alternating) structure of double and single bonds capable of contributing in some degree to the delocalisation of molecular orbitals with π-orbitals do exhibit semiconducting behaviour [50, 92]; saturated compounds are invariably insulators, and as such conduct electrical current only under dielectric rupture conditions [92].

Phthalocyanines

Like what happens with many other organic conjugated compounds, the existence of an alternating structure of double and single bonds in the macrocycle of phthalocyanines grants them a behaviour towards electrical conduction which is typically semiconducting. For the solid state arrangement of phthalocyanines, the short intermolecular distances in a slipped column promote the overlap between LUMO and HOMO orbitals of neighbouring molecules, creating an intermolecular charge diffusion path along that column [136]. The overlap conduces to the formation of continuous energy LUMO and HOMO bands analogous to the conduction and valence bands of inorganic solids, although narrower due to the fact that the overlap is poorer and a high degree of electronic localisation in each molecule is retained. The formation of bands

from the LUMO and HOMO orbitals of phthalocyanines is seen *e.g.* in the absorption spectra of phthalocyanine thin-films as a large broadening of the Q-band (Figure 2.9) [74, 30]; the Q-band peak is also shifted in energy, suggesting that the distortion of the outer benzene rings due to hydrogen-bonding plays an important role in the orbital overlap process [74].

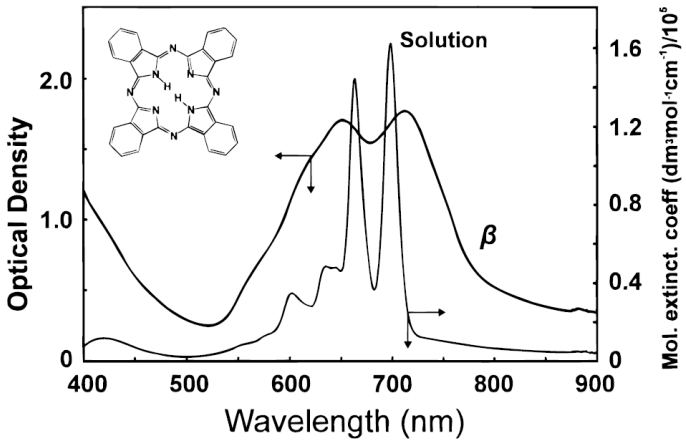

Figure 2.9: Electronic absorption spectra of H_2Pc in solution and thin-film (β phase) forms. The Q-band seen in the solution spectrum is drastically broadened in the thin-film spectrum due to the splitting of the LUMO and HOMO levels into bands, as a result of the overlap promoted by the solid-state stacking. Source: [74]

Phthalocyanines behave in many ways as traditional semiconductors; they possess a HOMO-LUMO transport gap of the order of 2 eV [40, 51], a typical band-gap value for a semiconductor, and their conductivity increases with temperature [50, 86, 51]. Unlike inorganic semiconductors, though, the increase is due to a mobility gain resulting from molecular motion [49]. Typical conductivity values of undoped phthalocyanines at room temperature are usually in the range of 10^{-10} to 10^{-13} S/cm [50, 86, 49].

More importantly, phthalocyanines are easily doped, and its characteristics follow in many ways the standard models used to describe the doping of traditional semiconductors [86, 40, **?**, 49]. In applications, phthalocyanines are usually *p*-doped by oxidising species, such as oxygen or small molecules of high electron affinity as tetrafluoro-tetracyanoquinodimethane, F_4-TCNQ (Figure 2.10). The latter is found to be a very efficient dopant of phthalocyanines, since its LUMO level lies *below* the HOMO of phthalocyanines [86, 40]. The presence of F_4-TCNQ molecules in the Pc media forms charge transfer complexes, where one of the electrons of the phthalocyanine HOMO is transferred to the LUMO of the F_4-TCNQ molecule; this induces the

appearance of holes in the HOMO band of the phthalocyanine, turning it into a hole-conducting medium[7]. Together with the choice for the central atom and the functionalisation of the outer benzenes, doping constitutes the third and last independent mechanism available to control the electrical properties of phthalocyanines.

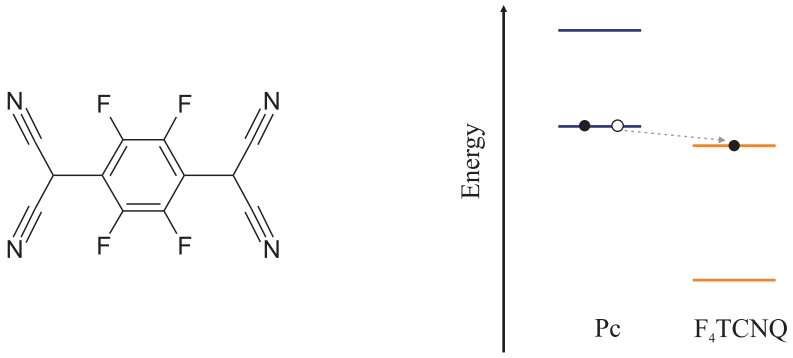

Figure 2.10: *(left)* Molecular structure of the high electron affinity species F_4TCNQ used as a p-dopant for phthalocyanines; *(right)* illustration of the relative level scheme for the HOMO and LUMO of phthalocyanines and F_4TCNQ. Due to its high electron affinity, the LUMO of F_4TCNQ lies *below* the HOMO of phthalocyanines, turning it into a highly successful phthalocyanine dopant.

[7]It should be noted that the recombination of the electron-hole pair formed in the charge transfer complex is hindered by the fact that the two charges remain in different molecules.

Chapter 3

Positive Muon Spectroscopy (μSR)

Positive Muon Spectroscopy, commonly denoted as μSR, is a peculiar member of the nuclear condensed matter techniques realm. Although less known than the traditional techniques, such as Nuclear Magnetic Resonance (NMR), Electronic Spin Resonance (ESR) or Mössbauer Spectroscopy, it has unique features that abide its distinction *inter pares*. Probably the most staggering one is the fact that it uses a probe usually associated with particle physics — the muon —, but it is actually its remarkably high sensitivity to short-range magnetic phenomena what makes it best-known among the condensed matter research community.

This chapter is devoted to the fundamentals of μSR. The technique's basics, typical experimental arrangements for data acquisition and signal processing and short descriptions of the main methods and selected instruments available to the μSR community will be addressed in a first part of the chapter. The second part of the chapter will deal with μSR observables and the way they relate with the charge states and dynamical processes underwent by the muon and its surroundings. It is intended to provide the basic tools for the analysis of μSR data substantiated in subsequent chapters.

The μSR acronym was coined to resemble the NMR and ESR acronyms, and indeed many similarities with these magnetic resonance techniques will become apparent throughout the whole chapter. Nevertheless, and contrarily to the use often given to these techniques in sample characterisation routines, one should make clear that μSR can never play the role of a characterisation technique. Instead, it is always primarily used to investigate fundamental physics problems. Hopefully that will become evident in this chapter, not only because of the type of information μSR yields, but also due to limiting characteristics of the technique, such as the need for an accelerator source or the relatively short lifetime of the muon.

3.1 The role of muons in Condensed Matter Physics research

In the general classification of particles provided by the Standard Model, the muon finds its place, together with the muonic neutrino, in the second generation of the lepton family (Table 3.1). Being a lepton, it is regarded as a fundamental particle, possessing 1/2-spin and no internal structure[1]. Belonging to the second generation, it is an unstable particle, decaying to the lighter (and stable) first generation leptons. Table 3.2 shows a selected list of the muon's properties; its 1/2-spin grants it a non-zero magnetic moment, from which stems the muon's ability to interact with local magnetic environments, and therefore to probe them. This table also displays comparative values of the same set of properties for the electron and the proton; the muon has an intermediate mass between these two particles, and thus intermediate magnetic moment[2].

Table 3.1: The three generations of fundamental particles according to the Standard Model. The electron (e), muon (μ), tau (τ), and respective neutrinos (ν_e, ν_μ and ν_τ) make the lepton family, which does not interact via the strong nuclear force; the up (u), down (d), strange (s), charm (c), top (t) and bottom (b) quarks are the strong interacting particles.

	1st	**2nd**	**3rd**
leptons	e	μ	τ
	ν_e	ν_μ	ν_τ
quarks	u	s	t
	d	c	b

It is usual to take the comparison established in Table 3.2, and infer that a low-energy muon in matter might be regarded either as a heavy electron or a light proton. These two different pictures are in fact what distinguishes the applications of *negative* muons from *positive* muons in condensed matter physics: while negative muons will play the role of heavy (negative)

[1]The absence of internal structure, together with the fact that the muon may be found in a totally unbound state in nature, make it a Dirac particle, which has as direct consequence its 1/2-spin.

[2]For fundamental particles, the magnetic moment is inversely proportional to the particle's mass. This is strictly true for the muon and the electron, but not for the proton. Nevertheless, even for composite particles a loose inverse relation between mass and magnetic moment still holds.

[4]The gyromagnetic ratio is taken here as the proportionality constant between a particle's magnetic moment and its spin angular momentum.

Table 3.2: Properties of the muon, electron and proton. The top sign in the values of the charge, magnetic moment and gyromagnetic ratio[4] refers to the particle state, while the bottom one refers to the anti-particle state. μ_B is Bohr's magneton, $e\hbar/2m_e$. Compiled from [75, 31]

property	**Muon (μ)**	**Electron (e)**	**Proton (p)**
charge (q)	$\pm\, e$	$\pm\, e$	$\pm\, e$
mass (m)	1.8835×10^{-28} kg	9.1094×10^{-31} kg	1.6726×10^{-27} kg
	$206.77\, m_e$	m_e	$1836.2\, m_e$
	$0.11261\, m_p$	$m_p/1836.2$	m_p
spin (s)	1/2	1/2	1/2
magnetic moment (μ)	$\pm\, 4.4904 \times 10^{-26}$ J T^{-1}	$\pm\, 928.48 \times 10^{-26}$ J T^{-1}	$\pm\, 1.4106 \times 10^{-26}$ J T^{-1}
	$\pm\, \mu_B/206.53$	$\pm\, 1.0011\, \mu_B$	$\pm\, \mu_B/657.45$
	$\pm\, 3.1833\, \mu_p$	$\pm\, 658.21\, \mu_p$	$\pm\, \mu_p$
gyromagnetic ratio (γ)	$\pm\, 851.62 \times 10^6$ rad Hz T^{-1}	$\pm\, 176086 \times 10^6$ rad Hz T^{-1}	$\pm\, 267.52 \times 10^6$ rad Hz T^{-1}
mean lifetime (τ)	2.19703×10^{-6} s	$> 4.6 \times 10^{26}$ years	$> 2.1 \times 10^{29}$ years

electrons, positive muons are the ones to behave as light (positive) protons. The μ^- is attracted by atomic nuclei, promptly assuming a $1s$ state by dislodging a lighter (hence higher energy) electron. This muonic $1s$ state has a much smaller Bohr radius than the electron (also due to the mass difference) and will therefore be sensitive mainly to phenomena taking place in the nucleus or the atomic core. The μ^+, on the other hand, is repelled by the nuclei just as the proton does, placing itself well away, in regions rich with delocalised electron density. The fact that the μ^+ probes the delocalised electronic cloud makes it a much better probe for condensed matter physics than the μ^-; positive muon spectroscopy, μ^+SR, is the technique that uses the positive muon in that role [138]. In strict terms, and although negative muons are best suited for atomic and nuclear physics studies, negative muon spectroscopy, μ^-SR, does exist. Nevertheless, it is seldom used, since apart its lesser capabilities for condensed matter studies, it has other technical downsides, namely that negative muons are harder to produce (*cf.* Section 3.2.3) and have their lifetime shortened due to muonic capture ($\mu^- + p \rightarrow n + \nu_\mu$), limiting the muon detection time window in media of high atomic number. Henceforth, we will restrict our discussion mostly to μ^+SR and refer to it simply as μSR, as it is of use.

The positive muon is a very effective probe for magnetism research, and indeed most part of μSR studies are performed in this field [133]. This happens because the magnitude of the muon's gyromagnetic ratio allows the experimental detection of its spin interaction with internal magnetic fields (as described in Section 3.2 further on) over the full range of values found in magnetic phenomena[5] [9]. Examples of studies employing the muon in this 'microscopic magnetometer' role for internal dipolar fields include the investigation of ordering in magnetic media [27], the measuring of internal field distributions in dilute magnetic alloys [67], the depiction of spin dynamics in spin-glass materials [57] and the characterisation of magnetic phase transitions [8]. Many applications of μSR to the broader context of critical phenomena also exist, namely to the study of liquid crystal ordering phase transitions [68], glass transitions in polymeric systems [90] and phase transitions to the superconducting state [2]. Superconductor physics too has benefited deeply from the existence of μSR, especially in the understanding of the superconducting state's nature, where the microscopic character of the muon probe turns it into a high-precision tool to study vortex phenomena [63] and map penetration depth patterns in high-T_c superconductors. The relation between magnetism and superconductivity in several families of superconducting materials is also extensively studied experimentally with μSR, since it is one of the very few techniques to exhibit distinctively clear signals both in the magnetic and the superconducting phase [132]. One should note that in all these applications the muon is a *passive* probe, in the sense that it is external to the system being studied and plays no part (or at most a very small one) in the phenomena addressed.

Other examples of μSR applications which use the positive muon as a passive magnetometer probe arise from the high sensitivity of its magnetic moment to internal *hyperfine* fields. These fields result from the unpaired spin of electronic distributions around and at the muon's site, and allow to probe both local electronic structure and electronic spin dynamics phenomena in many materials. μSR finds use *e.g.* in the investigation of core polarisation and screening effects in metals (see *e.g.* [20]), in the measurement of Knight shifts in metals (see *e.g.* [106]) and charge-carrier diffusion parameters in conducting and semiconducting polymers [87], in structural studies of defects in metals and semiconductors and in the mapping of spontaneous hyperfine fields in ferromagnetic and antiferromagnetic materials [106].

Besides being a natural probe for magnetism, the μ^+ is also specially tailored for hydrogen studies by way of its 'light proton' role. In these studies, the positive muon plays an *active* part,

[5] Zero to a few tesla.

as it is considered to be a lightweight proton, with roughly one ninth of the proton's mass (see Table 3.2). This view is adopted *e.g.* in studies regarding the diffusion of light-interstitials between potential wells; carrying the same electric charge as the proton, the positive muon also assumes the same sites the proton does, independently of host material. So, μSR results often complete proton, deuteron and triton diffusion data, contributing to the testing of theoretical models and the fine-tuning of their parameters [129]. But the highest relevance of this other face of the positive muon becomes evident when it *effectively* takes the place of the proton. Just like protons, positive muons are highly reactive in matter, and often end up binding with a single electron to form a neutral atomic system known as *Muonium*[6], Mu. In vacuum, this hydrogen-like system has properties very similar to the hydrogen atom, as seen in Table 3.3; in concrete terms, it possesses an almost identical electronic structure, since the reduced mass value dictates essentially the same $1s$ electronic wavefunction.

An equivalent similarity occurs for hydrogen and muonium in matter, and for most purposes muonium may be used as an experimental substitute of hydrogen which has the ability to provide information about its local electronic environment *via* the hyperfine field created by the bound electron [99]. This parallel finds many applications in free radical chemistry, where the muon extends the scope of isotopic substitution studies in molecular dynamics, assists in the identification of molecular structures, helps determining reaction rate constants, and provides a way to probe molecular spin dynamics directly, among others.

Yet, the most successful application of the positive muon in the active role of proton substitute has probably been so far the investigation of hydrogen behaviour as an impurity in semiconductors and insulators. In fact, the unique characteristics of μSR provide it with a sensitivity which finds no match among the techniques that are directly sensitive to hydrogen, *viz.* NMR and the EPR variant of ESR. This fact justifies Jess Brewer's well-known statement '*[...] far more is known about isolated H atoms from μSR than from any other method that observes H itself.*' [13] frequently quoted in μSR introductory literature. Furthermore, the limited lifetime of the μ^+ implies that μSR observes muonium in its early stages, hence in isolated form, still far from any reactions with structural defects or other impurities in the host material. μSR is therefore extensively applied to semiconductor and insulator physics in studies regarding the

[6]This is the nomenclature given to this system in a condensed matter physics context; it differs from what would be found in particle physics nomenclature, where muonium is the $\mu^+\mu^-$ bound state, and μ^+e^- is called *muium*.

Table 3.3: Physical properties of muonium (Mu) and hydrogen (H) in vacuum. All properties concerning electronic structure are essentially the same. As will be discussed in Section **??**, the hyperfine coupling constant is a measure of the energy associated with the spin coupling due to Fermi's contact interaction between the muon/proton and the orbiting electron. This parameter is proportional to the electronic density at the muon's/proton's position and the muon's/proton's gyromagnetic ratio. The difference of hyperfine coupling constants between Mu and H corresponds to the difference in gyromagnetic ratios, and is not related with dissimilarities in the electronic wavefunction. a_0 is the Bohr radius for infinite nuclear mass, $4\pi\epsilon_0\hbar^2/m_e e^2$. Compiled from [75]

property	**Muonium** (μ^+e^-)	**Hydrogen** (p^+e^-)
mass (m)	$1.8926 \times 10^{-28}\,\mathrm{kg}$	$1.6735 \times 10^{-27}\,\mathrm{kg}$
	$0.11309\,m_H$	m_H
reduced mass	$9.0655 \times 10^{-31}\,\mathrm{kg}$	$9.1044 \times 10^{-31}\,\mathrm{kg}$
	$0.99519\,m_e$	$0.99946\,m_e$
ground state energy (E)	$-13.540\,\mathrm{eV}$	$-13.598\,\mathrm{eV}$
	$0.99573\,E_H$	E_H
Bohr radius	$0.53174\,\mathrm{Å}$	$0.52947\,\mathrm{Å}$
	$1.0048\,a_0$	$1.0005\,a_0$
hyperfine coupling constant (A)	$4.4633\,\mathrm{GHz}$	$1.4204\,\mathrm{GHz}$
	$3.1423\,A_H$	A_H

electronic structure of interstitial hydrogen [85, 45, 18], to infer the localisation of the proton's site in the host lattice [46], to probe the conversion dynamics between the different charge states the hydrogen possibly assumes [65], and, in selected cases, to address the interaction of hydrogen with electrically active defects. It should be referred that μSR results have a high impact in the semiconductor community, both scientific and industrial. On the industrial side, hydrogen is considered to be an ubiquitous impurity in traditional semiconductors due to their manufacture processes [13]; furthermore, it is often introduced deliberately in semiconducting devices in order to passivate electrically active defects. Information about the 'where' and 'how' hydrogen interacts is thus of the utmost importance for the control of electronic properties via hydrogen incorporation. In fundamental science, μSR contributes to the construction of a systematic view of hydrogen's behaviour in semiconductors and insulators, and allows to test theoretical models that describe hydrogen embedded in those many-particle systems. Being a point-defect, interstitial hydrogen creates an electronic level in the forbidden band-gap which, depending on its position and the existence of other impurity-induced levels, may interfere with the electronic properties of the material. Establishing an universal picture for hydrogen which would describe the properties of that level in semiconductors is a long-desired goal of the semiconductor community. This goal has recently seen considerable advances with several predictions and experimental results consistent with the existence of a universal 'pinning-level', as put forward by Van de Walle [135]. This theory was prompted by the theoretical forecast that, contrary to what had always been observed, hydrogen could form an easily ionised shallow-donor level in some semiconductors [134], and hence become an active dopant instead of a deep-level, passivating impurity. Indeed, the first experimental confirmation of that prediction was obtained in a μSR experiment performed in the II-VI compound zinc oxide by Cox *et al.* [21], but in fact that was at the time already the second experiment confirming the existence of hydrogen shallow-levels, since months earlier Gil and co-workers had found it in cadmium sulfide, cadmium selenide and cadmium telluride [45, 47]. Since then, that theory has been put to severe testing by the muon, namely in the non-magnetic binary oxides, where a systematic search for further examples of these shallow states has been set-up by Cox and co-workers [23, 24]. The use of μSR to model the electronic structure and electrical activity of the hydrogen impurity in electronic materials, cleverly baptised as *muonics* in that work, is thus one fine example that emphasises the importance and the amazing scope of applications muons have in condensed matter research today.

3.2 The μSR essential

μSR is a technique that allows probing the structure and dynamics of condensed matter at the atomic scale. It is based on the implantation of a foreign probe, the positive muon, into the sample being investigated, and observing the effects of local environment and externally applied magnetic fields on the muon's spin direction. Watching those effects is possible because the muon is unstable, and decays to a positron which is preferentially emitted along the muon's spin, as it will be described in Section 3.2.2. The muon's spin direction at the moment of decay is revealed in this way and, many implanted muon decays later, one is usually presented with the time-evolution of that quantity, as the decay events randomly sample all possible decay instants according to Poisson statistics. But to monitor the muon's spin in this manner, two basic assumptions need to be met: that all muons stop in the sample in the same instant of their short lives, which should be as nearest as possible to their birth moment; and that when arriving at the sample, all muons are polarised with the same initial spin direction. Actually, μSR does exist in part because this last requirement is quite easy to accomplish; this will be discussed in Section 3.2.3.

The origin of μSR is not well defined, since it derived naturally from the large amount of experiments using positive muons carried out from the mid-1950's to the 1970's [126, 106]. Those experiments aimed mainly at verifying the V-A weak nuclear interaction theory, for which purpose the interactions experienced by the μ^+ in the target were considered to be at the time an undesired effect. In order to choose the best targets, it became necessary to study in detail those interactions, and by the time this task had been completed, many scientists had already realised the importance the μ^+ could have as a way to investigate the properties of matter. In spite of μSR's clouded origin, its acronym, which stands for *muon spin rotation, relaxation, resonance*, is easily traced back to the 1970's [138], and indicates that the experimental observable is the muon's spin. It also reflects the fact that rather than being a single technique, μSR is instead a collection of methods that use different aspects of the way the muon's spin may interact with its surroundings. This multitude is one part of the reason why μSR finds the amazing number of different applications stated in the last section. The other arises from the universality of μSR. Since μSR uses an implanted probe, it may be applied to virtually any material. It would not be too much to say that μSR is probably the most universal of the condensed matter techniques; its feasibility does not depend on any particular property of the sample, like electrical resistance or the presence of a certain isotope, but only that the sample has a volume big enough for muons

to stop inside it.

3.2.1 The μ^+ as a magnetic probe

The muon has a non-zero magnetic moment (see Table 3.2), and as such is able to interact with magnetic fields. That interaction is of dipolar magnetic nature, and is responsible for lifting the degeneracy of the two possible muon spin states. If one considers a positive muon in the presence of a magnetic field $\vec{B}$ along the z axis of a coordinate system, this system's hamiltonian will be

$$\hat{H} = -\hat{\vec{\mu}}_\mu.\vec{B} = -\gamma_\mu \hat{\vec{S}}_\mu.\vec{B} = -\gamma_\mu \hat{S}_{\mu_z} B = -\omega_\mu \hat{S}_{\mu_z} \ , \tag{3.1}$$

where $\hat{\vec{\mu}}_\mu = \gamma_\mu \hat{\vec{S}}_\mu$ is the positive muon's magnetic moment, $\hat{\vec{S}}_\mu$ is its spin operator and $\omega_\mu = \gamma_\mu B$ is the so called *Larmor frequency* of the muon in the field $\vec{B}$. Choosing the spin quantisation axis to be in the z direction, which means taking for the muon spin basis the spin-up, spin-down $\{|\alpha_\mu\rangle, |\beta_\mu\rangle\}$ eigenvectors of $\vec{S}_\mu^2$ and $\hat{S}_{\mu_z}$,

$$\vec{S}_\mu^2 |\alpha_\mu\rangle = \frac{3\hbar^2}{4} |\alpha_\mu\rangle \quad ; \quad \hat{S}_{\mu_z} |\alpha_\mu\rangle = \frac{\hbar}{2} |\alpha_\mu\rangle \tag{3.2}$$

$$\vec{S}_\mu^2 |\beta_\mu\rangle = \frac{3\hbar^2}{4} |\beta_\mu\rangle \quad ; \quad \hat{S}_{\mu_z} |\beta_\mu\rangle = -\frac{\hbar}{2} |\beta_\mu\rangle \ , \tag{3.3}$$

the eigenvalues E_n and eigenvectors $|n\rangle$ of the hamiltonian (3.1) are

$$E_1 = +\frac{\hbar}{2}\omega_\mu \quad ; \quad |1\rangle = |\beta_\mu\rangle \tag{3.4}$$

$$E_2 = -\frac{\hbar}{2}\omega_\mu \quad ; \quad |2\rangle = |\alpha_\mu\rangle \ . \tag{3.5}$$

The level splitting energy between these two spin eigenstates due to the presence of the magnetic field is $\Delta E = \hbar\,\omega_\mu$, which, as it is shown in Figure 3.1*a*, increases linearly with the field's magnitude. This implies that knowing the energy splitting ΔE between the levels is the same as knowing ω_μ, which in turn is the same as knowing the field's intensity. Indeed, this is the principle of magnetic resonance methods based in the absorption of electromagnetic waves, as Continuous-Wave NMR: the ensemble of nuclei probes is prepared in a state that has a higher occupation of the lower energy eigenstates of their spin hamiltonian, and then is irradiated with a band of RF-frequency waves [103]. The population imbalance causes resonant absorption of those waves at a frequency $\gamma_N B + \Delta\omega$ that matches the total magnetic field felt by the nuclei. Since that magnetic field is the sum between the externally applied field $\vec{B}$ and all internal fields existing locally at the nuclei sites, by measuring the number of different frequencies absorbed

and their shifts $\Delta\omega$ relative to $\gamma_N B$ one is able to determine the number of different local magnetic environments the nuclear probe ensemble experiences and their corresponding internal fields $\Delta B = \Delta\omega/\gamma_N$.

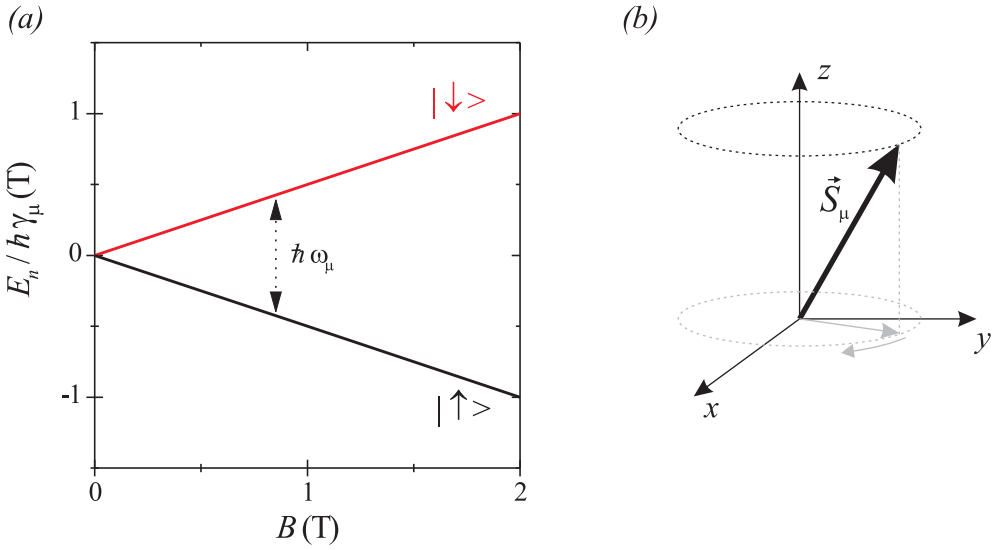

Figure 3.1: *(a)* Energy level scheme of the muon's 1/2-spin as a function of the magnetic field experienced by the muon. *(b)* Spin precession of the muon in a magnetic field.

μSR, nevertheless, uses a different method of determining the total magnetic field at the muon's site. It is based on an important aspect of the interaction of the muon's spin with a magnetic field known as *spin precession*. If the muon's spin starts by having a component perpendicular to the magnetic field $\vec{B}$, that component will rotate clockwise around the field's axis with the Larmor frequency ω_μ (Figure 3.1*b*), often known also as *Larmor precession frequency*. This effect arises from the fact that if the perpendicular component exists, then the spin wavefunction is not one of the eigenstates (3.4), (3.5), but a linear combination of them, and as such will exhibit a time dependence. The direction of the muon spin as a function of time is given by the expectation value of the Pauli spin operator $\hat{\vec{\sigma}}_\mu$,

$$\hat{\vec{\sigma}}_\mu = \frac{\hat{\vec{S}}_\mu}{\hbar/2} \ , \tag{3.6}$$

whose cartesian components can easily be shown to evolve with time in the presence of a magnetic

field according to (see Appendix A)

$$\langle \hat{\sigma}_{\mu_x}(t) \rangle = \cos(-\omega_\mu t + \phi) \sin\theta \tag{3.7}$$

$$\left\langle \hat{\sigma}_{\mu_y}(t) \right\rangle = \sin(-\omega_\mu t + \phi) \sin\theta \tag{3.8}$$

$$\langle \hat{\sigma}_{\mu_z}(t) \rangle = \cos\theta \ , \tag{3.9}$$

where (θ, ϕ) is the pair of polar and azimuthal angles which defines the initial direction of the muon's spin. It becomes clear from these expressions that $\left\langle \hat{\vec{\sigma}}_\mu(t) \right\rangle$ is a unitary vector whose projection on the xy plane rotates *clockwise* with angular frequency ω_μ, maintaining its z-projection constant. This result coincides with the solution obtained from the classic equation describing the precession of the muon's spin angular moment in the magnetic field $\vec{B}$,

$$\frac{d\vec{S}_\mu}{dt} = \vec{\mu}_\mu \times \vec{B} = \gamma_\mu \vec{S}_\mu \times \vec{B} \ , \tag{3.10}$$

and quite often μSR data is conveniently interpreted in classical terms, as it had already implicitly been assumed in Figure 3.1*b*.

The most straightforward method of μSR, muon spin *rotation*, measures the precession frequencies of the implanted muon ensemble by analysing the time-dependence of the ensemble's *spin polarisation vector*, $\vec{P}_\mu(t)$. The muon spin polarisation is defined as the *ensemble's* expectation value of the Pauli spin operator,

$$\vec{P}_\mu(t) = \left\langle \hat{\vec{\sigma}}_\mu \right\rangle \ , \tag{3.11}$$

meaning that it is essentially a vector whose direction follows the net spin direction of the muons in the implanted ensemble. Taking the time dependence of this quantity along a fixed direction in space not collinear to the magnetic field, one gets an oscillating behaviour with the superposition of different frequencies whose values are proportional one by one to the different total fields experienced by the ensemble. This method of assessing internal fields is the same as the one used in Pulsed-NMR, the muon's ensemble polarisation being equivalent to the free-induction decay of the nuclear magnetisation (Figure 3.2).

Regarding equation (3.11), it is important to make a clear distinction between the expectation value of $\hat{\vec{\sigma}}_\mu$ for a single muon spin and the polarisation of an ensemble of muons (expectation value of $\hat{\vec{\sigma}}_\mu$ for that ensemble). The quantum state[7] of an ensemble is generally

[7] By 'quantum state' one means here the maximum-information description of the whole ensemble system; this is not to be confused with the expression 'wavefunction', usually reserved for identifying a linear combination of eigenstates.

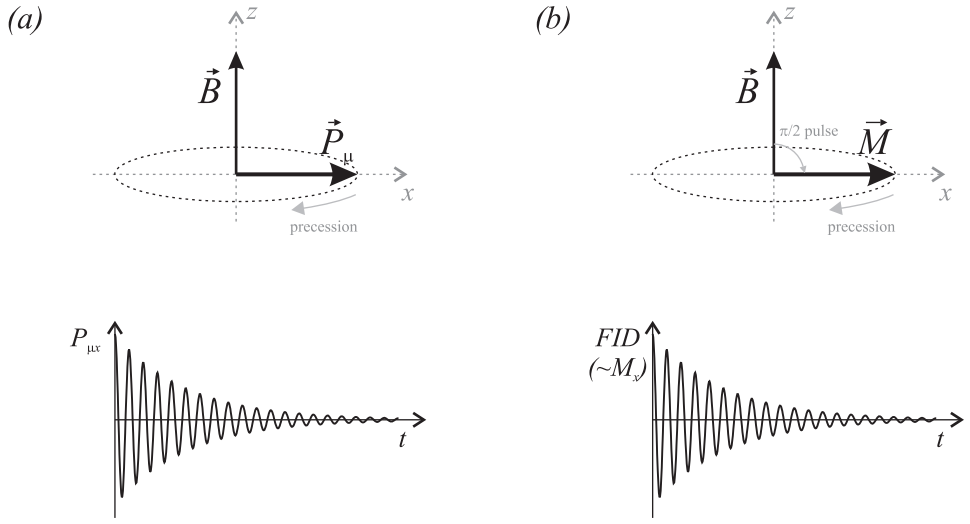

Figure 3.2: *(a)*Typical time dependence of the muon polarisation along a direction non-collinear to the magnetic field in Muon Spin Rotation and *(b)* of the transverse magnetisation free-induction decay in the $\pi/2$-pulse method of Pulsed-NMR (right). The reason why the amplitude of these signals decreases with time is described in the text.

not a wavefunction, since single muons may be in distinct environments, where they experience different hamiltonians with different eigenstates. The description of the ensemble's quantum state is done instead with a *superposition* of single-particle wavefunctions reflecting the statistical distribution of muons between those environments; because that statistics adds to the already statistical nature of the individual quantum states, the whole ensemble system is usually said to be 'doubly statistic' [126]. An ensemble quantum state is usually referred to as a *mixed* or *incoherent* state, in opposition to *pure* or *coherent* states, when there is not a definite, time-independent phase relation between the wavefunctions in the superposition. In that case, its description is usually done with a density matrix, as discussed later on in Section 3.4.3. In practice, the double statistics of the muon ensemble means that the main quantisation axis, which in the most basic picture lies in the direction of the total internal field, is not necessarily the same for all the muons in the ensemble, as it is not the magnitude of that field and the corresponding precession frequencies. As a result, the oscillating behaviour of the muon spin polarisation may loose its coherence, *i.e.* individual muon spins precessing at different frequencies may become out of phase and the magnitude of their ensemble normalised spin-sum lessens with time. Hence, in a mixed state, the loss of coherence decreases the ensemble's polarisation with time, $|\vec{P}_\mu| \leq 1$ (*cf.* Figure 3.2), as the individual spins assume increasingly random di-

rections due to the fact that they are precessing along different quantisation axis and/or with different frequencies. A decrease of polarisation may also exist if there are dynamical processes in the muon's environment capable of changing either the direction or the magnitude of the total internal field with time. Contrary to the loss of coherence, which only decreases the perpendicular, precessing components of the polarisation, dynamics also affects the parallel, non-precessing component of the ensemble's polarisation; that behaviour implies an actual energy transfer from the muon system to the system responsible by the dynamical phenomena. Pure states, on the other hand, correspond to a fully polarised ensemble bearing $|\vec{P}_\mu| = 1$, which may be interpreted classically as all the muon spins being aligned along the same direction in space at any instant. Quite often, the decrease of polarisation in mixed states is proportional to the polarisation itself, and the temporal dependence of the polarisation vector includes a dissipative term just like the well-known Bloch equations of Pulsed NMR, becoming

$$\frac{d\vec{P}_\mu}{dt} = \gamma_\mu \vec{P}_\mu \times \vec{B} - \Lambda \vec{P}_\mu \tag{3.12}$$

were Λ is generally a second-order tensor and its coefficients are usually termed *depolarisation* or *relaxation rates*. The time dependence of equation (3.12) implies an exponential decrease of all components of the ensemble's polarisation, that being the macroscopic effect of the randomisation of the quantisation axis and/or precession frequencies over the whole ensemble, or of any time-dependent spin interactions.

The loss of coherence of the muon ensemble is the basis for another method of μSR, muon spin *relaxation*. Instead of evaluating the time dependence of the muon spin in a direction non-collinear to the magnetic field, this method measures the time dependence of the spin's component which is *parallel* to the magnetic field. According to equation (3.12), if the muon is involved in dynamical phenomena, those will translate to the ensemble's polarisation also as a decrease of the parallel component with time, *i.e.* as its *relaxation* (Figure 3.3). The rate at which the parallel polarisation is lost relates directly with the time structure of the fluctuations associated with the source of dynamics; muon spin relaxation is therefore an appropriate tool to probe dynamic effects, being able to assess phenomena occurring in the muon's environment in any time scale that lies within the limits imposed by the experimental time-resolution (which may be as low as 100 ps) and the exceptionally long lifetime of the muon (up to $10\tau_\mu = 22\,\mu$s)[8].

[8] As it will be seen in Section 3.4.4, the lower limit may be further decreased if the muon experiences the dynamical phenomena via an hyperfine interaction.

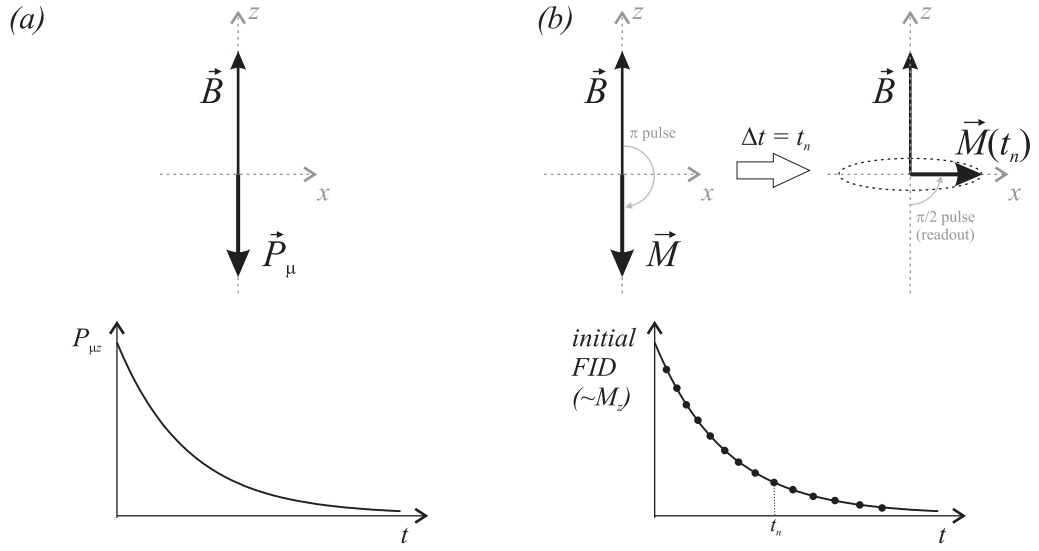

Figure 3.3: *(a)* Typical time dependence of the muon polarisation along a direction parallel to the magnetic field in Muon Spin Relaxation. This method also has an analogue method in Pulsed-NMR, termed *inversion recovery*, as depicted in *(b)*.

Finally, muon spin *resonance* constitutes the third version of the μSR technique, featuring yet another way the muon may be used as a magnetic probe. It relies on one other effect, which is the disappearing of parallel polarisation when the spin wavefunction of a muon transits between two eigenstates of the spin hamiltonian. That transition must be assisted by a perturbation which, to be put simply, may be either a fixed-frequency RF electromagnetic field irradiated on the sample, or an additional term in the hamiltonian related with residual spin interactions underwent by the muon. In the first case, one has the *RF* variation of muon spin resonance; internal fields are measured by the absorption of the RF waves when the resonance condition $\hbar\omega_{RF} = \Delta E$ between the RF frequency ω_{RF} and the eigenstates splitting ΔE is met. This variation is identical to the Continuous-Wave NMR and ESR methods, except that the resonant frequency is signalled by the loss of polarisation, and not by an induced voltage in an RF pick-up coil. The second case is the *level-crossing* variation of muon spin resonance; it is termed like that because the transition occurs between levels that, for a certain externally applied field, would be degenerate (*i.e.* would cross) if it were not for the presence of a residual spin interaction. The exact external field at which the loss of polarisation takes place depends quite sensitively on the coupling constant of the residual spin interaction; knowing that field's value allows to measure the corresponding coupling constant. Just like Continuous-Wave NMR and ESR, muon spin

resonance produces high-precision measurements of internal fields, providing a sensitive tool to distinguish from similar muon environments or obtain coupling constants of the muon's spin hamiltonian with high accuracy.

As it is more than clear by now, the use of the positive muon as a magnetic probe with the μSR technique supposes the ability of following the time dependence of the muon polarisation. The next section is devoted to the physical fundamentals that make it possible.

3.2.2 Muon decay

Although the muon was first artificially produced in 1948 at the Berkeley National Laboratory following its discovery in cosmic rays by Carl Anderson and Seth Neddermeyer [4], it was only after the discovery of parity violation in its decay by Garwin *et al.* [42, 38] that it became a viable magnetic probe. The violation of parity in weak decays is the key for μSR's existence, since it has as a direct consequence the presence of anisotropy in the emitted electron/positron's direction relative to the negative/positive muon's spin (see Figure 3.4). That anisotropy, in turn, provides a way to determine the direction of the muon's spin at the instant of its decay.

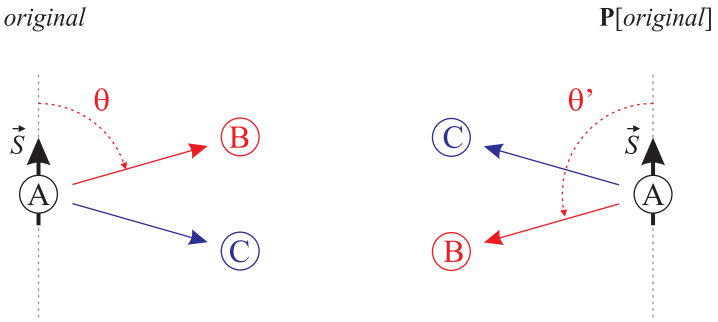

Figure 3.4: The three-body weak decay of a spin-possessing particle A under a parity transformation. The momenta of the daughter particles B and C are *polar* vectors, changing their sign under the parity operation P; on the contrary, the parent's spin angular moment does not change sign because it is an *axial* vector. If parity is not conserved in the decay, the two situations depicted are not equivalent, and will take place in nature with different probabilities. This leads to a biasing in the emission of *e.g.* the daughter particle B, which will occur in a preferential direction relative to the parent's spin.

The muon decay,

$$\begin{aligned} \mu^- &\rightarrow e^- + \bar{\nu}_e + \nu_\mu \\ \mu^+ &\rightarrow e^+ + \nu_e + \bar{\nu}_\mu \ , \end{aligned} \tag{3.13}$$

is a weak interaction process occurring with a mean lifetime of about 2.2 μs. It is a three-body reaction, and as such the electron or positron (in practice the only detectable particle from the decay) will not emerge from it with a single energy. In the rest frame of the muon, it is emitted with a distribution of energies ranging from zero (when the two neutrinos are emitted in opposite directions and the electron/positron remains at rest) to

$$T_e{}^{max} = \frac{1}{2}\, m_\mu\, c^2 \left(1 - \frac{m_e}{m_\mu}\right)^2 = 52.32\,\mathrm{MeV} \tag{3.14}$$

(when the two neutrinos are emitted in the same direction, but antiparallel to the electron's or positron's momentum). Since the muon is a point-like particle and the decay occurs at low energies, the process (3.13) may be quantitatively described by Fermi's theory for weak interactions based on a V-A hamiltonian [106]. The probability per unit time dW that the electron or the positron will be emitted with a certain energy in a solid angle $d\Omega$ can be evaluated in that theoretical framework, giving [106]

$$dW(\epsilon, \theta) = \frac{1}{\tau_\mu}\, \frac{n(\epsilon)}{2\pi}\, (1 + a(\epsilon)\cos\theta)\; d\epsilon\, d\Omega\ , \tag{3.15}$$

where τ_μ is the muon's lifetime, θ is the angle between the direction of emission and the muon's spin, and ϵ is the normalised energy of the electron/positron, $\epsilon = T_e/T_e{}^{max}$. The quantity

$$n(\epsilon) = (3 - 2\epsilon)\epsilon^2 \tag{3.16}$$

is a pre-factor governing the pure energy dependence of the emission probability distribution; that dependence is obtained integrating equation (3.15) over the full 4π solid angle,

$$dW(\epsilon) = \int_{4\pi} \frac{1}{\tau_\mu}\, \frac{n(\epsilon)}{2\pi}\, (1 + a(\epsilon)\cos\theta)\; d\epsilon\, d\Omega = \frac{2}{\tau_\mu}\, n(\epsilon)\, d\epsilon\ , \tag{3.17}$$

leading to the energy distribution shown in the upper part of Figure 3.5, well-known from beta decay. $n(\epsilon)$ is also obviously normalised so that the integration over all energies

$$W = \int_0^1 \frac{2}{\tau_\mu} n(\epsilon)\, d\epsilon = \frac{1}{\tau_\mu}$$

gives the total decay probability per unit time.

The most interesting fact underlying equation (3.15) is the spatial dependence of the probability distribution, which depends on the so called *asymmetry factor*,

$$a(\epsilon) = \mp\, \frac{2\epsilon - 1}{3 - 2\epsilon}\ , \tag{3.18}$$

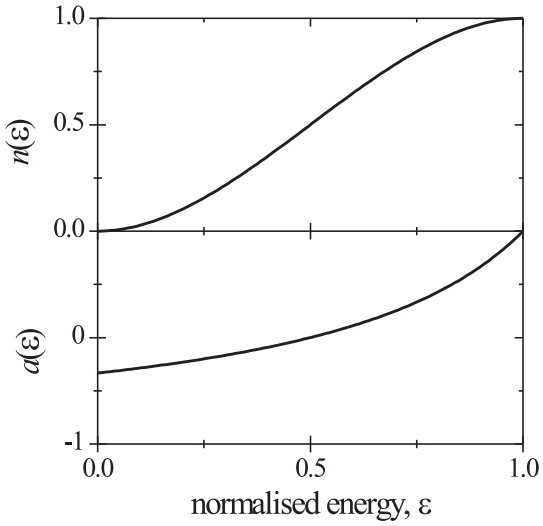

Figure 3.5: *(upper part)* Energy spectrum of the electrons/positrons emitted in muon decay; emission with maximum energy has also maximum probability. *(lower part)* The asymmetry factor as a function of the emitted particle's energy. It increases with energy, also increasing the distortion of the angular emission pattern.

where the $\mp$ signs refer to the negative and the positive muon decays respectively. For each electron/positron energy, the decay probability is axially symmetric with respect to the muon spin, but asymmetric along that same direction (Figure 3.6). The asymmetry factor parameterises the imbalance in the probabilities of emission parallel and antiparallel to the muon spin. Figure 3.6 shows the angular dependence of dW for the positive muon in the case that the positron is emitted with maximum energy ($\epsilon = 1$); as the asymmetry factor here is $+1$, no positrons with that energy will be emitted antiparallel to the positive muon spin. For lower energies, the asymmetry factor decreases (see Figure 3.5), and the emission pattern gets less asymmetric. Averaging equation (3.15) over the electron/positron energy spectrum, one gets a net angular dependence which, although less pronounced than the $\epsilon = 1$ case, is still asymmetric along the muon spin,

$$dW(\theta) = \int_0^1 \frac{1}{2\pi} \, \frac{n(\epsilon)}{\tau_\mu} \, (1 + a(\epsilon) \cos\theta) \; d\Omega \, d\epsilon = \frac{1}{2\pi\tau_\mu} \, \frac{1}{2} \left(1 \mp \frac{1}{3} \cos\theta \right) d\Omega \; , \tag{3.19}$$

with an average asymmetry factor of $\mp 1/3$ (Figure 3.6). The probability of electron/positron emission antiparallel/parallel to the muon spin is therefore double of that in the opposite direction, allowing to statistically determine the direction of the muon's spin at the time of its decay by detecting the bearing of the emitted particle. Thus, for a precessing muon ensemble, the

emitted electron/positron 'beam' works similarly to a lighthouse's light beam. As a concluding remark, one should note that for the positive muon (which is the case of most interest) its spin direction is beaconed by the positron's preferred emission direction, while for the negative muon it is the contrary.

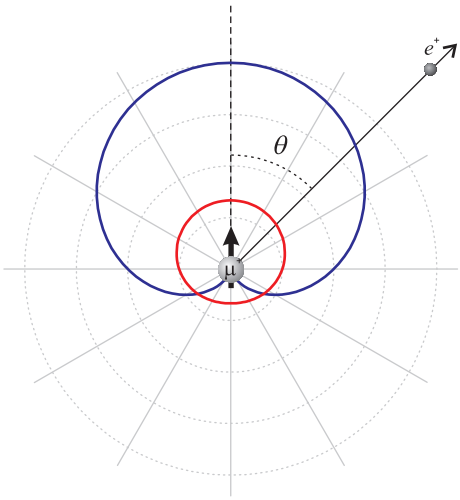

Figure 3.6: Angular dependence of the positron's emission probability relative to the positive muon's spin. The blue curve represents the emission probability for maximum positron energy ($\epsilon = 1$); averaging it over the positron's energy spectrum produces the curve shown in red.

3.2.3 Production of polarised muon beams

Nature produces positive and negative muons in the upper layers of our atmosphere by pair-production reactions. They join other high-energy radiation to form the cosmic rays, and turn out to be its main constituents at ground-level. In the laboratory, muons are born from the decay of charged pions, the lightest exchange mesons responsible for the nuclear strong force in Yukawa's model. Pions are produced in accelerator facilities by the bombardment of low-Z nuclei (usually beryllium or carbon) with high-energy protons; typical reactions yielding charged pions are

$$\begin{aligned} p + p &\rightarrow p + n + \pi^+ \\ p + n &\rightarrow n + n + \pi^+ \\ &\rightarrow p + p + \pi^- \end{aligned} \tag{3.20}$$

which have an energy threshold of 280 MeV in the laboratory (corresponding to a centre-of-mass energy of roughly 140 MeV, the charged pion's rest energy) and are called *single-pion*

production reactions [106]. The cross section for these reactions increases with the incident proton beam energy, reaching a plateau value somewhere between 500 and 1000 MeV; beyond 600 MeV, double-pion production reactions also occur, but exhibit a much lower cross section than the single-pion ones under 1000 MeV.

There are currently four large-scale facilities worldwide using high-intensity pion beams for the production of muons intended for μSR experiments. Three of them, the Paul Scherrer Institut (PSI) in Villigen, Switzerland, the Tri-University Meson Facility (TRIUMF) in Vancouver, Canada, and the Japanese National Laboratory for High Energy Physics (KEK) in Tsukuba, Japan, are dedicated meson factories designed with a proton-beam energy suitable to provide maximum pion and muon fluxes (580 MeV, 520 MeV and 500 MeV respectively). The fourth, placed at the Rutherford-Appleton Laboratory (RAL) in Oxford, United Kingdom, is actually a neutron spallation source oriented for neutron diffraction experiments. Pion production capability at this facility is provided by the fortunate fact that optimum conditions for producing neutrons by spallation of heavy nuclei targets (like uranium, bismuth or tungsten) with a proton beam occur at energies around 800 MeV. As this beam energy is suitable for producing pions with the reactions above, neutron spallation sources are able to parasitically accommodate the production of pion beams at a very small cost (typically less than 3%) of their main proton beam.

Charged pions have a mean lifetime of approximately 26 ns, and decay into muons and muonic neutrinos according to

$$\begin{aligned} \pi^- &\rightarrow \mu^- + \bar{\nu}_\mu \\ \pi^+ &\rightarrow \mu^+ + \nu_\mu \ . \end{aligned} \tag{3.21}$$

Like the muon decay, the disintegration of the pion is a purely weak interaction, although simpler since it involves only two particles being emitted. In the pion's rest frame, this has two major consequences: the muon and the neutrino are emitted *(i)* with opposite momenta due to momentum conservation, and *(ii)* with opposite spins, if one considers that the pion is a spinless particle [31] and angular momentum also has to be conserved. Furthermore, neutrinos and anti-neutrinos are known to have a definite *helicity* [48], *i.e.* there is always a fixed relation between a neutrino's spin and its momentum[9]. Helicity is in fact the only experimental property distinguishing neutrinos from anti-neutrinos: all ν have their spin vectors opposite to their

[9]This happens to be itself a consequence of parity violation in weak interactions.

momentum vectors, which corresponds to a negative helicity, while all $\bar{\nu}$ have spin anti-parallel to momentum, corresponding to positive helicity. As a result, negative muons are forced to have their spin vector parallel to their momentum vector upon pion decay, the contrary standing for positive muons (Figure 3.7).

Figure 3.7: Decay of the positive pion in its rest reference frame. The emitted muonic neutrino has a definite negative helicity, implying that the positive muon's spin $\vec{S}_\mu$is always anti-parallel to its momentum $\vec{p}_\mu$.

The fact that a constant relation between the muon's spin and its momentum exists allows to easily generate a beam of fully polarised muons from the decay of pions. There are actually two different ways of doing that. The first, and most important, is to use pions that have thermalised in the pion production target and subsequently decay there. By collecting all muons emitted from the target along a certain single momentum direction, one gets a 100% polarised beam, which may then be guided to the target sample through a beam-line consisting of bending and quadrupole focusing magnets (Figure 3.8). Muons deriving from pions at rest have an energy of

$$T_\mu = \frac{1}{2}\, m_\pi\, c^2 \left(1 - \frac{m_\mu}{m_\pi}\right)^2 = 4.12\,\mathrm{MeV} \tag{3.22}$$

in the laboratory frame, corresponding to a momentum of about 29 MeV/c; this is a rather low kinetic energy, and because of that the only muons with sufficient range to escape the target are those emitted near the surface of the target (Figure 3.8). Therefore, muon beams produced in this way are called *surface muon beams*, or *Arizona beams*, as they were proposed and produced for the first time by a group from the University of Arizona [106]. The low energy of surface muons is actually an advantage, since their short range in matter (typically a few hundred μm[10]) and consequent small range straggling allows using moderately thin sample targets. The on-sample muon beam-spot size[11] may also be small if the proton beam focus at the pion target is small.

One disadvantage of surface muons is that they are only suitable to produce positive muon beams. This happens because negative pions thermalising in the pion target experience strong

[10] To put it more precisely, the stopping range of 4.1 MeV muons in matter is about 170 mg/cm^2.

[11] The transverse width of the muon beam.

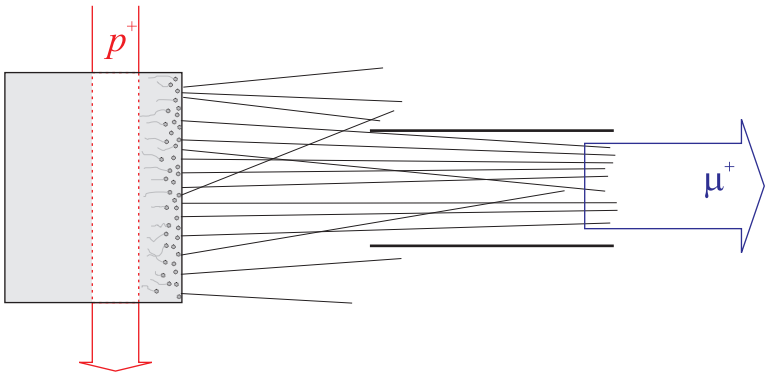

Figure 3.8: Production of surface (or 'Arizona') positive muons. Positive pions thermalising near the pion target surface emit positive muons with a negative helicity, as imposed by momentum and angular momentum conservation laws. By collecting all muons emitted from the target along a single momentum direction, a fully polarised beam of positive muons is produced.

electrostatic attraction forces from the target's nuclei, which drive them into being immediately captured by the nuclei. Pionic capture induces a nuclear disintegration process called a *pionic star*, with the consequent loss of the negative pion. In contrast, high intensity surface beams of positive muons ($\sim 10^7 \mu^+/\mathrm{s}$) are easily accomplished due to the very high stopping density of positive pions in the pion target. In order to produce beams of polarised negative muons, one must use pions that have enough energy to escape the pion target. Those pions are momentum-discriminated and then directed to a region named a *decay channel*, usually several metres in length, where an intense longitudinal magnetic field forces them to go through very long, helical trajectories. If the pion momentum is sufficiently small, most of the pions decay somewhere inside the channel, so that at the channel's exit a diffuse beam primarily composed of muons will exist. The muon beam is then accepted in a momentum selector to choose only those muons that have a momentum parallel to the pion propagation direction inside the decay channel. This is necessary to avoid using muons that suffer an effect known as *kinematic depolarisation*: since the collinearity between a muon's momentum and its spin is only valid in the pion rest reference frame, in the laboratory frame (where the pion is moving) the muon spin gains a component transverse to the muon's momentum whenever the muon is emitted in a direction non-parallel to the pion's velocity, as shown in Figure 3.9. The muons that preserve a collinearity relation between their spin and momentum are only those emitted parallel or anti-parallel to the pion's velocity. In the first case, the muon is said to be emitted in the *forward* direction, and has a velocity larger than the pion's; in the second, it is emitted in the *backward* direction, and

has a velocity smaller than the pion's (see Figure 3.9). The muon momentum selector also distinguishes the two different beams formed from forward and backward muons, selecting one of them.

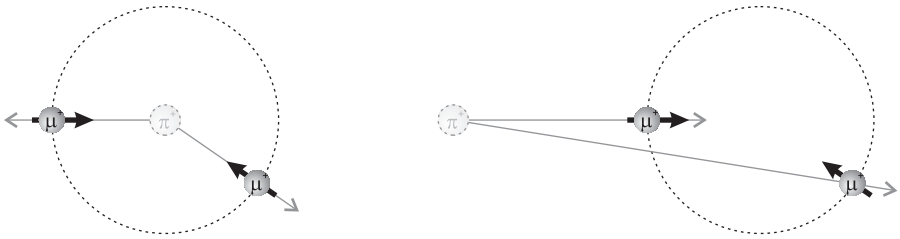

Figure 3.9: The kinematic depolarisation of positive muons emitted from positive pions decaying in flight. On the left, two different pion decays are represented in the centre-of-mass reference frame, where muon momentum and spin are collinear; on the right, the same is represented, but in the laboratory reference frame. Muons emitted parallel to the pion momentum have a velocity larger than the pion's — forward muons — while those emitted anti-parallel have a lower velocity than their parent's — backward muons.

Decay channels are of course not restricted to producing negative muon beams; in fact, a positive muon decay beam is in principle twice brighter than a negative muon decay beam, as the positive pion yield from single-pion reactions (equations (3.20)) is double from the negative pion one. Decay muon beams have some disadvantages towards surface beams: to start with, the cost and maintenance of a decay channel is considerably higher than that of a surface muon set-up, mainly due to the superconducting solenoid needed for the magnetic field along the channel. Secondly, muon momentum, although tunable, is usually larger than the 29 MeV/c momentum of surface muons, implying the use of thicker, hence harder to get, samples. Finally, the polarisation of the resulting muon beam does not go much beyond 80%, since the kinematic depolarisation effect is not completely rejected due to the finite angular acceptance of the muon momentum selector. Still, the polarisation of muon beams, either surface or decay beams, is high enough to render μSR as a superbly sensitive technique when compared to other magnetic resonance techniques. For those other techniques, the spin polarisation of the magnetic probes has always to obey Boltzmann's distribution, and because of that exhibits very low values, typically around 10^{-6}. These are several orders of magnitude below the 0.8-1.0 initial polarisation values used in μSR, which does not rely in the Boltzmann distribution to prepare the spin polarisation of its magnetic probe. Hence, and as μSR is able to detect the decay signal of virtually all muons implanted in the sample (like it will be seen in the next section), far less spins are needed in μSR

($\sim 10^7$) than *e.g.* in NMR ($\sim 10^{17}$) to produce a signal with statistically significant information.

3.2.4 Experimental principles of μSR

A μSR experiment[12] consists in implanting polarised positive muons in a sample, and detect the direction of the positrons emitted from the muon decay. Time-stamping those positrons relative to the instant muons arrive at the sample, it's possible to reconstruct the time evolution of the implanted muon spins thanks to the anisotropic decay properties of the muon (see Section 3.2.2). The simplest experimental arrangement of a μSR time spectrometer is pictured in Figure 3.10. The positive muons are directed to the sample, where they eventually stop after passing through the muon counter M, a thin ($\sim 0.2\,\mathrm{mm}$) scintillation detector which has the ability to distinguish muons from any decay positrons that might possibly be emitted in its direction. This happens thanks to the far higher intensity signals which are generated by the heavier and slower muons in the beam when compared with decay positrons. A signal in M always flags the entrance of a muon in the sample, starting a clock which is stopped when the corresponding decay positron is detected in the positron telescope D[13]. The clock is reset by a logic module whenever a non-valid event occurs, *e.g.* if no outward positron is detected in the telescope before the next muon signal (whenever the decay positron is emitted in a direction out of the solid angle subtended by D). If a valid event does occur, the acquisition electronics translates the clock value to a memory address, incrementing the corresponding channel in a number of positron counts *vs.* time histogram.

The time histogram of positron counts possesses all the experimental information about the time dependence of the muon polarisation's projection along the direction defined by the sample and the positron telescope. As it is shown in Appendix B, the number of positron counts in each time bin in a generic μSR positron detector D is given by

$$\Delta N_{\mathrm{D}}(t_i) = N_0\,\eta_{\mathrm{D}}\,\frac{e^{-t_i/\tau_\mu}}{\tau_\mu}\left(1 + A_{\mathrm{D}}\;\vec{P}_\mu(t_i)\,.\,\hat{r}_{\mathrm{D}}\right)\,\Delta t\;, \tag{3.23}$$

where N_0 is the total number of muons implanted in the sample, η_{D} is the positron telescope detector's efficiency, A_{D} is the detector's asymmetry factor, $\hat{r}_{\mathrm{D}}$ is a unitary vector along the

[12] We focus now only on *positive* μSR, although the contents of this section can be easily translated to negative μSR.

[13] A telescope is a particle counter composed by two scintillators placed consecutively along the direction leading outwards from the sample. This type of double layout is able to distinguish particles moving away from the sample (decay positrons) from those moving towards the sample (surely *not* positrons from muon decays inside the sample), depending on the relative timing of the inside and outside scintillators' signals.

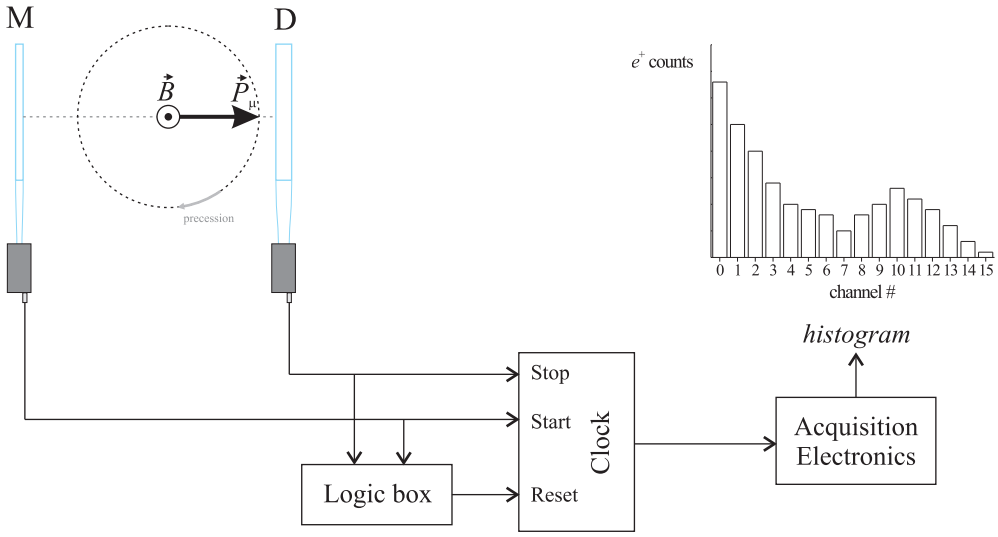

Figure 3.10: Schematic diagram of a simple μSR spectrometer. M is a thin scintillation muon counter that detects muons arriving at the sample; D is a positron telescope, which detects the emitted positrons. The signals of the two detectors trigger the start and stop of an electronic clock, allowing to build a μSR time histogram.

direction defined by the sample and the positron telescope, and Δt is the width of the time bin. The quantity

$$N_{\mathrm{D}} = N_0 \, \eta_{\mathrm{D}} \tag{3.24}$$

is the total number of decay positrons detected in the telescope D, while the time-varying scalar

$$A_{\mathrm{D}}(t) = A_{\mathrm{D}} \; \vec{P}_{\mu}(t) \, . \, \hat{r}_{\mathrm{D}} \; , \tag{3.25}$$

normally referred to as the detector's *asymmetry function*, is the experimental observable of actual interest extracted from the μSR time histogram, since its normalised version $A_{\mathrm{D}}(t)/{A_{\mathrm{D}}}^{max}$ represents the muon polarisation along the detector's direction $\hat{r}_{\mathrm{D}}$. The maximum value ${A_{\mathrm{D}}}^{max} = A_{\mathrm{D}} \, |\vec{P}_{\mu}(t)|^{max}$, which assumes typical values around 0.25, depends on the intrinsic asymmetry of the muon's weak decay (the 1/3 asymmetry factor in A_{D}, see equation (B.12) in appendix B), the detector's efficiency and geometry (the α_{ϵ} and α_g factors in A_{D}, *id.*), and the magnitude of the initial muon polarisation $|\vec{P}_{\mu}(0)|$ (which is the maximum value $|\vec{P}_{\mu}(t)|$ may have if relaxation phenomena exist).

In order to reflect more generally the signal generated in the telescope detector, one should also add a constant number of background counts B_{D} to (3.23). These background counts have several sources, such as muon beam contamination by positive undecayed pions, positrons

emitted by muons decaying in the pion target and in flight, or positrons formed in the muon beam-line by pair-production reactions from gamma photons emitted in the decay of neutral pions produced in the pion target. Figure 3.11 shows an example of a μSR histogram (and corresponding asymmetry) that would be recorded in the positron telescope if the polarisation component parallel to $\hat{r}_{\mathrm{D}}$ would be precessing with a single frequency.

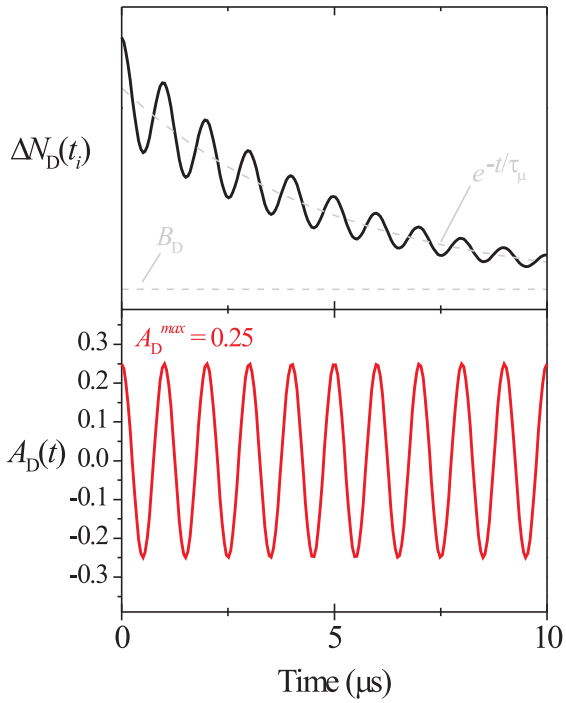

Figure 3.11: An example of a μSR histogram of positron counts versus time that would be recorded with the system of Figure 3.10. Superimposed to the exponential decay, there is an oscillating behaviour if the muon ensemble polarisation precesses around a direction non-collinear to $\hat{r}_{\mathrm{D}}$. A constant background fraction of counts is also represented.

The design of actual spectrometers existing at the facilities which provide muon beams for μSR is not much different from the simple spectrometer shown in Figure 3.10. They have several positron telescopes placed around the sample in order to cover the largest solid angle possible, maximising the spectrometer's sensitivity[14]. Those telescopes are invariably fast plastic scintillators coupled to photomultiplier tubes by light-guides, providing a high timing resolution for the experiment. The photomultipliers have to be at some distance from the sample, so that they are not affected by the large external magnetic fields usually employed in μSR measurements.

[14] *i.e.* the fraction of detected *vs.* emitted positrons.

Although this degrades slightly the timing resolution, because of the sometimes long light-guides needed to do this, resolutions of the order of several hundreds of picoseconds remain achievable. The photomultiplier signals are treated by a set of electronics, basically comprising a standard pulse timing stage of constant fraction discriminators and a TDC (time-to-digital converter) module, a logic stage of coincidence and anti-coincidence units to elect valid muon decay events, and a final acquisition stage of multichannel scalers connected to a read-out computer.

The logic stage's layout highly depends on the time structure of the muon beam, which may either be *continuous*[15] or *pulsed*. The sources at PSI and TRIUMF deliver a continuous beam, meaning that muons arrive at the sample one at a time, in average intervals conditioned by the beam intensity. As each muon enters the sample, it triggers the acquisition by producing a signal in the muon counter (Figure 3.12*a*); if the decaying positron is not detected in any of the positron telescopes around the sample before the next muon arrives, it becomes impossible to distinguish which muon has decayed. Therefore, the muon implantation rate has to be limited to about $5 \times 10^4\,\mu^+/\mathrm{s}$ at these sources in order to avoid multiple muon events in the sample[16]. Even so, the probability that two muons will be present at the sample may not be negligible enough, and since their positrons are uncorrelated this ends up adding to the background. With the lowest beam intensities admitted for acceptable experimental count rates, that background usually renders the μSR histogram unusable after 5 to 10 μs.

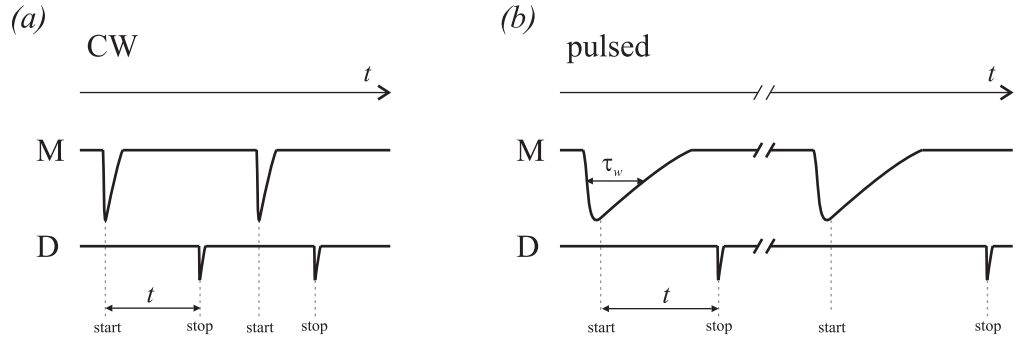

Figure 3.12: Time structure of *(a)* continuous and *(b)* pulsed muon beams. τ_w is the time width of the muon bunch.

In the pulsed sources existing at RAL and KEK, muons enter the sample in very intense

[15]Often denoted by *DC* (direct-current) or *CW* (continuous-wave).

[16]This restriction may be lifted in a type of μSR experiment not yet referred here, called a time-integral measurement. In this type of experiment, one is not interested in the time dependence of the muon polarisation. This method will be further clarified in the next section

and short pulses named *bunches*. The muon detector no longer plays the role of a counter, and is only used to signal the implantation instant of the muon bunch. As muons decay, each detected positron is timed with respect to the arrival of the pulse (Figure 3.12*b*). The time interval between pulses is much larger than the muon's lifetime, so that with a pulsed beam low backgrounds are compatible with high muon implantation rates. It is therefore possible to measure time histograms during many muon lifetimes, typically in a time window going up to 30 μs. Nevertheless, pulsed muon sources have a major drawback relative to continuous sources: the implantation instant for each muon in the bunch suffers from an uncertainty raised by the finite time width of the bunch. Since the width of the bunch ($\sim$ tens of ns) is much larger than the timing resolution of the positron detectors, it folds the time resolution of the positron detection system and limits the maximum resolvable frequency in the time histogram to about 10 MHz. In continuous sources, frequencies up to 400 MHz are resolved, as the timing resolution of the positron detectors is the only limiting factor. Phenomena that imply a rapidly changing polarisation (either precessional or relaxing) can therefore only be observed in laboratories providing continuous muon beams.

The sample's environment conditions are also an important aspect of a μSR experiment. These mainly comprise the control of temperature and the externally applied magnetic field, but sometimes the measurement also involves other variables, such as the usage of RF-fields, an externally applied electric field, laser illumination and high pressures. The external magnetic fields are generated by a fixed pair of Helmholtz coils, which deliver low-fringe fields in a volume with a radius of a few centimetres, as typical μSR samples may be tens of millimetres wide. The magnitude of those fields does not go much farther than 0.5 T; to attain higher fields, a superconducting magnet must be used, but only a very limited number of μSR spectrometers currently in use has this capability. For temperature control one uses either a cryostat or a furnace apparatus. Since these support instruments are normally the bulkiest structures using up the immediate space around the sample, they have to meet some experimental conditions, namely the need to be fitted with a window thin enough not to stop the in-going muons, of being made of non-magnetic materials in order not to disturb the external magnetic field delivered to the sample, and to be designed in a way that there are no muons stopping anywhere else except in the sample. Often this last criterium is difficult to meet, specially when the sample has dimensions smaller than the beam spot. In that case, the muons not hitting the sample must be stopped in a contrasting material that originates a distinct signal from the sample's, which

may then be easily subtracted. A similar problem is faced when the sample is in the liquid or gaseous state, in which case must be placed in a cell; the cell must be designed with the same concerns as those taken for the temperature environment apparatus. It should be noted that no major restrictions in the design of cells, cryostats and furnaces are raised by the out-going positrons, as these have on average quite a high energy, and therefore are penetrating enough to easily reach the positron detectors.

3.2.5 μSR geometries

The recorded μSR time histogram depends directly on the polarisation of the implanted muon ensemble, and in fact it is $\vec{P}_\mu(t)$ the experimental quantity of interest in μSR since it holds all the information about the interactions underwent by the muon inside the sample. As it was referred back in Section 3.2.1, in a simple picture its time evolution is governed by (3.12),

$$\frac{d\vec{P}_\mu}{dt} = \gamma_\mu \vec{P}_\mu \times \vec{B} - \Lambda \vec{P}_\mu \ ,$$

a differential equation whose explicit solution depends on the initial conditions of the experiment, namely $\vec{P}_\mu(0)$, which equals the muon beam polarisation[17]. This fact ends up distinguishing two geometries which yield two distinct types of μSR signals, depending on the relative orientation between the muon beam polarisation, the externally applied field and the direction in which decay positrons are observed. Those are the Transverse-Field (TF) and the Longitudinal-Field (LF) geometries which, along with different signals, normally convey different kinds of information about the local interactions the muons are subjected to.

Transverse-Field (TF) geometry experiments

In transverse-field experiments, the externally applied magnetic field is set perpendicularly to the implanted muon polarisation. Since the external field is normally the main component of the total field felt by the muon, this leads to the precession of the muon's polarisation in a plane perpendicular to the magnetic field's direction, in the way shown back in Figure 3.1*b*. The components of the polarisation perpendicular to the field are therefore the relevant quantities to follow, which are monitored by positron detectors laid in that plane. A scheme of this type of set-up is shown in Figure 3.13.

[17] This assumption is justified in section Section 3.3, where the preservation of the muon polarisation during implantation is discussed.

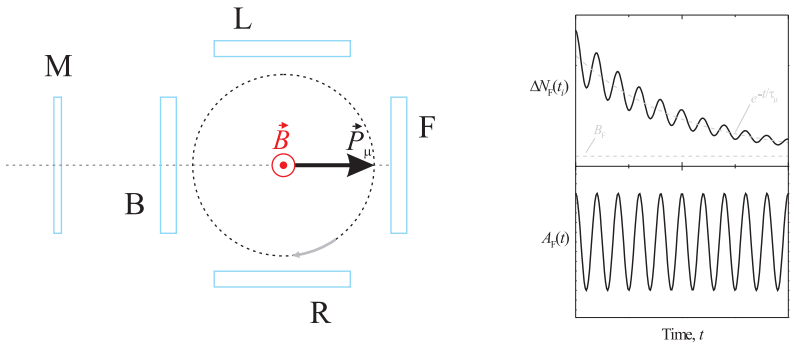

Figure 3.13: *(left)* Layout for transverse-field geometry experiments. The system monitors the muon polarisation components which are perpendicular to the applied field. *(right)* A typical μSR histogram of the Forward detector in a transverse-field experiment, and corresponding asymmetry.

Each detector D records an histogram

$$\Delta N_{\mathrm{D}}(t_i) = e^{-t_i/\tau_\mu} \frac{\Delta t}{\tau_\mu} \; N_{\mathrm{D}} \left(1 + A_{\mathrm{D}}(t_i)\right) + B_{\mathrm{D}} \tag{3.26}$$

having a particular asymmetry function $A_{\mathrm{D}}(t)$ which is generally a sum of damped sinusoidal components of different frequencies. Those components express the precessional (and relaxing) behaviour of the muon polarisation, and are all present in all the detector asymmetries $A_{\mathrm{D}}(t)$ with exactly the same relative spectral amplitude and depolarisation rate. Their initial phases, nevertheless, are different, as the muon polarisation starts precessing at time zero with a different angle relative to each detector.

A typical complete TF-μSR dataset contains several million events, and is analysed by simultaneously least-square fitting all time histograms assuming the same theoretical model for $\vec{P}_\mu(t)$. The unknowns N_{D} and B_{D} are added to the model parameters in this fit. Alternatively, those unknowns may be estimated in an independent way[18], and the simultaneous fit is performed directly on the sampling of the asymmetry functions $A_{\mathrm{D}}(t_i)$ obtained from the detector histograms by the inversion of equation (3.26). Often, Fourier transform methods are used by the experimenter to assist the fitting task, although the fit is always performed in the time do-

[18] It's possible to extract the background counts B_{D} either from the very first histogram channels, since histogram recording usually starts some time before the muon's arrival to the sample, or from the very last channels, when the number of muon decays is very low, already under the background counts. The total decay positron counts N_{D} can then be yielded by a simple exponential decay fit to the background-corrected time histogram divided by $\frac{\Delta t}{\tau_\mu}$ using $1/\tau_\mu$ as the exponential's constant, for the oscillating behaviour of the asymmetry should average it to zero over the full histogram time window (see equation (3.26)).

main. Transverse-field experiments relate directly to muon spin rotation (see Section 3.2.1), and therefore aim mainly at the spectroscopy of the muon states formed in the sample, characterising local environment in terms of properties such as site location and electronic structure.

One important aspect when performing data analysis of a μSR measurement is knowing the value for the maximum asymmetry ${A_{\mathrm{D}}}^{max}$ of each detector. If the muon experiences very strong interactions after being implanted, normally there are components in the asymmetry $A_{\mathrm{D}}(t)$ which oscillate or relax too fast for the timing resolution of the spectrometer to resolve them. When this happens, the total measured asymmetry does not add up to the maximum asymmetry of the detectors, and a *missing fraction* is said to exist. The presence of a missing fraction is information in itself, since it may vary with temperature and the applied magnetic field as the relative amplitudes of the unresolved components change in a behaviour which is characteristic of the interactions giving rise to it. The maximum asymmetry must therefore be measured independently, using a calibration sample in which no missing fraction is known to exist; no internal fields must therefore exist in the calibration sample, which happens when electronic and nuclear magnetism are negligible or non-existent. Since the maximum asymmetry depends sensitively on the experimental conditions, the calibration measurement must reproduce entirely the experiment's set-up. The shape and position of the calibration sample must be the same, as well as the conditions in which the beam is delivered to the sample (identic beam spot size and impact point in the sample; the latter may be affected by the external magnetic field, especially if it is strong). Usually, for solid samples one uses a silver mask cut with the sample's shape, while for liquid and gaseous samples the holding cell is used, but filled with liquid carbon tetrachloride, a well-known non-magnetic electron scavenger [99].

Longitudinal-Field (LF) geometry experiments

The longitudinal-field geometry is characterised by having the externally applied field parallel to the implanted muon polarisation. The parallel component of the polarisation relative to the field is the observable recorded, for which two positron detectors, placed upstream and downstream of the sample, are employed (Figure 3.14). They are the backward (B) and forward (F) detectors, respectively. The usual time dependence of the asymmetry of these two detectors is a non-oscillating relaxing signal. Longitudinal-field experiments are thus employed in muon spin relaxation studies, especially aiming at the dynamical interactions established by muon states with its environment.

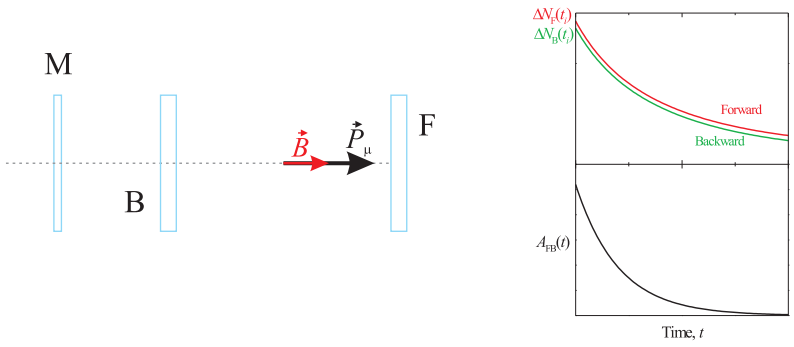

Figure 3.14: *(left)* Layout for longitudinal-field geometry experiments. The muon polarisation component parallel to the applied field is monitored *via* the Forward-Backward asymmetry, which is obtained from the histograms of the Forward and Backward detectors. *(right)* A typical μSR histogram of the Forward and Backward detectors in a longitudinal-field experiment, and corresponding FB-asymmetry function. The translation of forward and backward counts is only possible after an α calibration is carried out (see text).

If surface muons are used, the muon beam is polarised backwards, so the backward detector will initially detect more muons than the forward detector; as the muon polarisation relaxes, the two count rates approach each other as a function of time (see Figure 3.14). This type of signal becomes difficult to analyse by fitting the forward and backward detector histograms in a similar way as what is done with TF signals. Because of that, one instead uses the normalised difference between the background-corrected histogram counts in the backward and the forward detectors, called the *Forward-Backward (FB) asymmetry function*:

$$\begin{aligned} A_{\mathrm{FB}}(t_i) &= \frac{(\Delta N_{\mathrm{B}}(t_i) - B_{\mathrm{B}}) - (\Delta N_{\mathrm{F}}(t_i) - B_{\mathrm{F}})}{(\Delta N_{\mathrm{B}}(t_i) - B_{\mathrm{B}}) + (\Delta N_{\mathrm{F}}(t_i) - B_{\mathrm{F}})} \\ &= \frac{N_{\mathrm{B}}\left(1 + A_{\mathrm{B}}(t_i)\right) - N_{\mathrm{F}}\left(1 + A_{\mathrm{F}}(t_i)\right)}{N_{\mathrm{B}}\left(1 + A_{\mathrm{B}}(t_i)\right) + N_{\mathrm{F}}\left(1 + A_{\mathrm{F}}(t_i)\right)} \,. \end{aligned} \tag{3.27}$$

This combination enhances the asymmetry function's signal, since $A_{\mathrm{F}}(t) = -A_{\mathrm{B}}(t)$ as the two detectors are in opposite directions (see (3.25)). The FB-asymmetry function equals $A_{\mathrm{B}}(t)$, whose normalised version represents the muon's polarisation along its initial direction, provided of course that both detectors have identical efficiencies and asymmetry factors. That, however, is not an experimental reality, but there is a way for the efficiency and asymmetry factor differences to be taken into consideration in the definition of the FB-asymmetry so that it can be made

equal to $A_{\rm B}(t)$. If one defines the quantities

$$\alpha = \frac{\eta_{\rm B}}{\eta_{\rm F}} \tag{3.28}$$

$$\beta = \frac{A_{\rm B}}{A_{\rm F}} = \frac{{A_{\rm B}}^{max}}{{A_{\rm F}}^{max}} \tag{3.29}$$

then

$$\begin{aligned} N_{\rm F} &= N_{\rm B}/\alpha \\ A_{\rm F}(t) &= -A_{\rm B}(t)/\beta \ ; \end{aligned}$$

generally, the forward and backward positron detectors of LF-geometry μSR spectrometers are designed to have equal asymmetry factors[19], being therefore assumed that $\beta = 1$, and it becomes possible to re-define the FB-asymmetry as

$$A_{\rm FB}(t_i) = \frac{(\Delta N_{\rm B}(t_i) - B_{\rm B}) - \alpha\ (\Delta N_{\rm F}(t_i) - B_{\rm F})}{(\Delta N_{\rm B}(t_i) - B_{\rm B}) + \alpha\ (\Delta N_{\rm F}(t_i) - B_{\rm F})}\ , \tag{3.30}$$

a quantity equal to $A_{\rm B}(t)$ as long as α has been independently determined. This is done in a so-called *alpha calibration* run, where a small magnetic field (20 to 100 G) is applied transverse to the beam polarisation. This field induces the precession of the polarisation in a plane containing the forward and backward detectors, with which one can then estimate the value of α that makes the FB-asymmetry (3.30) a zero mean function.

Due to its mainly non-oscillating behaviour, the LF-μSR signal is particularly sensitive to interactions that originate a missing fraction of the polarisation. The dependence of the remnant polarisation (called *initial polarisation*) as a function of the applied field turns out to be quite informative about those interactions; *e.g.* the quenching of hyperfine interactions at high external fields appears as a recovery of the initial polarisation, in what is known as a *repolarisation* behaviour, as discussed later in Section 3.4.3. Any resonant loss of polarisation is also promptly observed, generating an *avoided-level crossing dip* which signals the mixing of spin eigenstates by residual spin interactions in level-crossing muon spin resonance studies (*id.*), or RF-radiation absorption in RF resonance μSR. Hence, LF-geometry measurements also produce rich information for the spectroscopy of muon spin states. Often, initial polarisation studies are done with *time-integral* measurements, as opposed to the *time-differential* measurements that follow the polarisation's time dependence. If the LF signal does not decay significantly with

[19] They are built with the same shape and dimensions, and optimised to have very similar detection efficiency functions.

time during the experimental time window, the number of positrons emitted in the forward and backward directions is proportional to the initial polarisation independently of when they are emitted. This allows one to simply count the total number of positrons detected by the forward and backward detectors in order to obtain the initial polarisation. Time-integral μSR spectrometers are mostly found in laboratories with continuous beams, since the muon implantation rate limitations imposed in time-differential measurements at those sources are lifted, granting the use of the full muon beam ($\sim 10^6\,\mu^+/\mathrm{s}$) and a consequent shortening of run acquisition times.

Similarly to what happens with TF-geometry measurements, the tracking of any missing fraction depends on the knowledge of the maximum FB-asymmetry for all the magnetic fields used in the experiment. In LF-geometry, doing this kind of calibration is vital for amplitude *vs.* field studies, since strong longitudinal fields, besides influencing photomultiplier response, highly distort the emitted positron trajectories, and apparent variations of the total sum of the signal's components may turn out not be true. As a rule, the net effect is a maximum asymmetry decrease with increasing longitudinal field. The distortion of positron trajectories also becomes quite apparent, since one also observes a steep increase in the experiment's count rate. It should be noted that the alpha calibration run never produces the maximum FB-asymmetry of LF-geometry, for it uses a low TF-field geometry which does not take the positron trajectory distortion due to the high longitudinal applied field into consideration.

Finally, a special case of LF-geometry use happens when the applied magnetic field is zero, giving rise to a method called Zero Field μSR (ZF-μSR). In this type of experiment, the muon solely experiences the internal magnetic fields generated by its immediate environment. The time dependence of the muon's polarisation will therefore be strongly influenced by any fluctuations of those fields, *e.g.* if the muon is diffusing through the sample's lattice; in fact, ZF-μSR is specially tailored to address muon diffusion. The ZF-μSR time signal is very sensitive to the presence of even small external fields, requiring the use of an active circuit to generate a compensating field able to counteract earth's magnetic field and any random fields induced by the electric equipment existing around the spectrometer.

3.2.6 μSR instruments

The design of a μSR spectrometer, alongside with the kind of μSR studies it targets, is highly guided by the time-structure of the muon beam it uses. As a rule, spectrometers for continuous beams are built with four to six large positron detectors placed in a box-like geometry around the

sample. Since decay positrons are detected one at a time, it is possible to build a spectrometer that covers a large total solid angle with few detectors. On the contrary, in pulsed sources the acquisition system has to detect a large number of positrons at the same time; in order to cope with this, it is necessary to use segmented positron detectors. Normally, only two segmented detectors in opposite sides relative to the sample are used; the total solid angle covered is also quite restricted, as the segmentation increases the number of channels and complexity of the acquisition electronics[20]. In the following, we restrict ourselves at making a brief description of the three different μSR spectrometers located at PSI and RAL that were used in the context of this thesis. A more thorough review of their layout and specifications may be found in the web pages of those laboratories, as well as of other existing spectrometers.

General Purpose System, GPS, and the DOLLY clone instrument (PSI)

The General Purpose System (Figure 3.15), GPS, permanently installed in one of PSI's 4.1 MeV surface-muon beam-lines, is a time-differential instrument designed for ZF, LF and TF μSR experiments in wide ranges of temperature and external magnetic field. It has five positron detectors placed around the sample's space, two of which are parallel to the beam for use in LF measurements (labelled forward and backward detectors, F and B), and the three others perpendicular for TF measurements (the up, down and right detectors, U, D and R). The backward detector has a 7 mm $\times$ 7 mm hole to allow muon passage into the sample's space; an identical aperture exists in the forward detector which grants it exactly the same shape and dimensions as the backward detector. The size of the beam-spot size at the sample's position, amounting to slightly more than 5 mm FWHM, is mainly determined by the backward detector hole. Two additional scintillators, named backward-veto and forward-veto (B-veto and F-veto), are also present (Figure 3.16). The B-veto detector, a hollow scintillator pyramid connected to the hole in the backward detector, is used to actively collimate the beam by rejecting muons that miss this aperture. The purpose of the F-veto detector, used to investigate very small samples, is to reject muons that have not stopped in the sample; it has a double-cone shape connected on one side to the aperture in the forward detector.

The main magnetic field, oriented longitudinally to the beam's direction, is generated by a pair of Helmholtz coils able to provide fields up to 0.6 T. In LF-geometry operation mode, the muon beam polarisation is kept in its original direction (anti-parallel to the muon momentum),

[20] And, of course, the overall cost of the spectrometer.

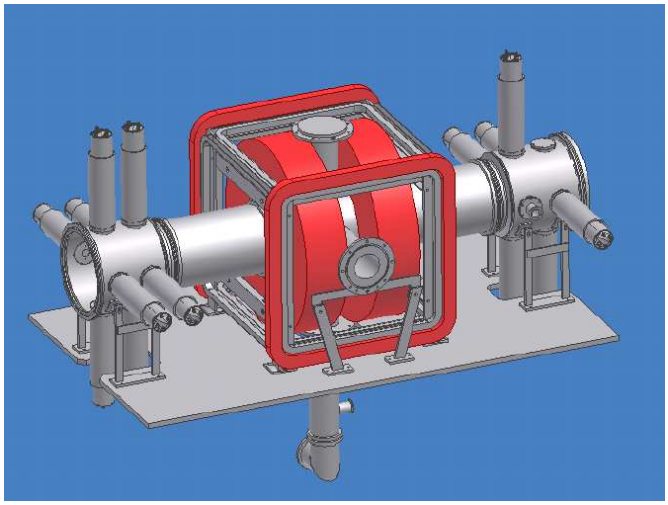

Figure 3.15: The General Purpose System, installed at PSI. It has five positron detectors and a main Helmmoltz pair of coils capable of providing fields up to 0.6 T. (Courtesy of the Swiss Muon Source facility, PSI)

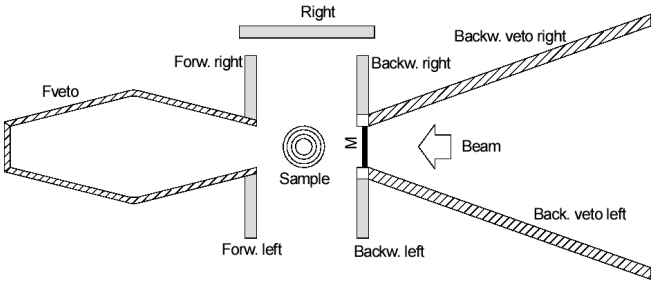

Figure 3.16: Layout of the Forward, Backward and Right detectors of the GPS instrument. Also shown are the veto detectors, forward and backward (see text). (Courtesy of the Swiss Muon Source facility, PSI)

and an auxiliary pair of coils (0-10 mT) along the horizontal direction may be used to create a field perpendicular to the beam for alpha calibration runs. For TF-geometry measurements, the muon beam polarisation is rotated to the vertical direction before entering the spectrometer. This is done in a so-called *spin-rotator*, where a short burst of a circularly polarised RF-field induces the precession of the beam's polarisation in the plane defined by the muon beam and the vertical direction; the RF burst is timed so that the polarisation sweeps a 90 degree angle during its length.

The overall time resolution of the spectrometer is less than 1 ns, allowing histogram counts to be recorded in time-bins ranging from 0.625 ns to 2.5 ns; the standard total time window may be chosen to go from 5 to 10 μs after muon implantation, although a special set-up, baptised as MORE (Muons On REquest), permits to decrease multiple-muon background and measure the time histogram up to 20 μs. This unique set-up, developed at PSI by its μSR group specifically for the GPS instrument, uses an electrostatic deflector triggered by the signal in the muon counter to prevent any incoming muon of reaching the sample until the currently implanted muon has decayed.

A second μSR instrument with the exact same characteristics as GPS[21] also exists at PSI. This clone instrument, named DOLLY, uses a decay-channel muon beam moderated to the same 4.1 MeV energy as GPS's surface beam. Both the GPS and DOLLY spectrometers are fitted with a Quantum Technology continuous-flow ^{4}He evaporation cryostat, which is interchangeable with a common furnace apparatus originally built by a μSR group from Zürich. The combined Quantum cryostat/Zürich furnace set delivers temperatures in the range 2-800 K.

EMU instrument (RAL)

The EMU instrument (Figure 3.17*a*) is a time-differential μSR spectrometer optimised for ZF and LF measurements installed at a surface muon beam-line in the Rutherford-Appleton Laboratory. Its detector arrangement comprises two ring detectors, placed backwards and forwards to the sample along the muon beam direction. Each ring detector is segmented in 16 independent scintillators, summing a total of 32 individual positron detectors for the spectrometer. Two Helmholtz coils create a field of up to 0.4 T parallel to the beam; alpha calibration is performed with a 0-10 mT field generated by a second pair of coils oriented perpendicularly to the beam.

The size of the muon beam-spot is considerably larger than at PSI; its shape is elliptical,

[21] Except for the MORE set-up.

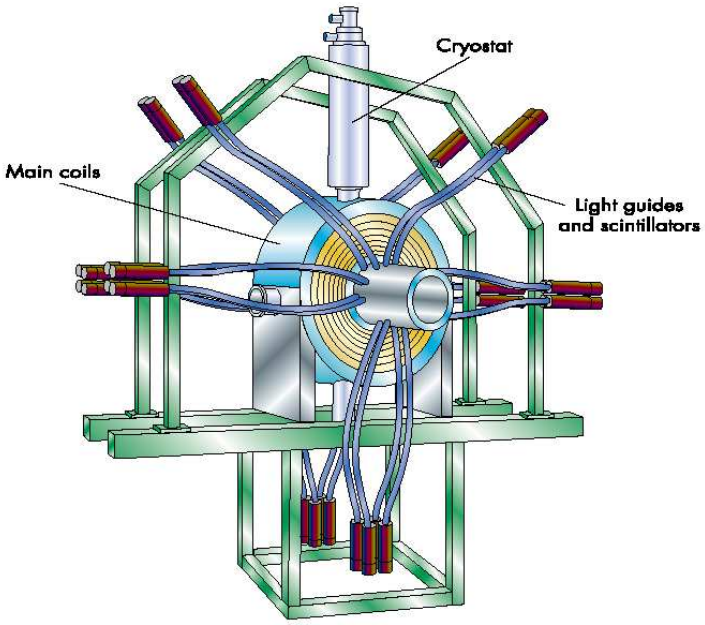

Figure 3.17: The EMU instrument, installed at the ISIS source in the Rutherford-Appleton Laboratory. It is an instrument optimised for LF geometry experiments, with segmented detectors in order to cope with the bunched time structure of the muon beam. (Courtesy of the ISIS Pulsed Muon facility, RAL)

with the major axis in the horizontal direction. Typical dimensions are 10 mm×15 mm (FWHM), although horizontal collimation of the beam is possible using a set of remote slits in order to better adjust the beam-spot to the sample size. In practice, a compromise between a satisfactory count rate and the fraction of the beam hitting the sample must be reached. Small samples can be measured using the so-called *fly-past* mode; it basically consists in the fitting of a long tube in the flange forwards to the sample's space, so that muons not hitting the sample stop away enough from the detectors for their decay positrons not to be detected. Since muon beams at RAL are pulsed, the frequency resolution of this spectrometer is limited to less than 10 MHz, but it becomes possible to record standard time histograms 32 μs wide. Pulsed beams also produce large positron fluxes hitting the scintillators, which make it necessary to correct the positron counts due to the dead-time of the detectors.

Several interchangeable sample environment apparatus are available for use with the EMU spectrometer. For the range below room-temperature, this thesis work used EMU's workhorse cryostat, a closed-cycle refrigerator fitted to the spectrometer's side capable of achieving temperatures as low as 5 K. For high temperatures, a hot-plate furnace able to reach 1000 K was employed; when in use, this furnace is suited in the spectrometer's forward flange, not allow-

ing the fitting of the fly-past tube. Both these apparatus have a fast response to temperature changes between runs, but since the two rely on the thermal exchange between the sample and the sample holder for the cooling/heating process, it is necessary to assure the best contact possible for temperature gradients not to arise, specially when working with powder-form samples. Besides these two apparatus, three additional helium flow cryostats and one irradiation furnace also exist; although thermal equilibrium conditions are much better for these instruments, they have a much slower response, are more difficult to fit in the spectrometer and, in the case of the cryostats, imply the consumption of liquid helium and nitrogen consumables.

3.3 Positive muon implantation and thermalisation in matter

From the muon's point of view, any μSR experiment starts with its implantation in the sample being studied. The few instants the positive muon takes to achieve an equilibrium state inside the sample are divided in three distinct regimes: a stopping stage, where the muon is decelerated from its initial energy to epithermal values, followed by a *charge-exchange* stage, where it cyclicly captures and looses electrons, and a thermalisation process, where it reaches a final state consistent with the electronic properties of the media it was implanted in. All these steps are fast enough not to affect significantly the polarisation of the muon ensemble, nor need to be considered in the experimental recording of the polarisation, as they span a total time interval below the nanosecond range.

3.3.1 The μ^+ stopping process

As it enters the sample, the positive muon promptly interacts with its surroundings, gradually loosing energy until it comes to a halt. Like all charged particles heavier than the electron, the main processes underwent by the muon as it passes through matter are electrostatic collisions with the electrons and the nuclei of the material. The collisions with the nuclei, often referred to as *elastic scattering collisions*, do not contribute relevantly to the energy loss of the muon, since they are quite less probable than the collisions with the clouds of electrons, and the energy transfer per collision is also much smaller due to the heavier mass of the nuclei when compared with the electrons. Instead, these collisions are responsible by the deflection of the muon from its incident direction, causing lateral straggling and the consequent spread of the muon beam as it progresses inside the sample. The muon's kinetic energy is thus almost solely lost to the electrons

in *inelastic collisions*, causing electronic excitation and ionisation along the muon stopping path. The amount of energy transferred in each electronic collision, although considerably larger than that of an elastic scattering collision, is a very small fraction of the muon's kinetic energy, but in normally dense matter the number of inelastic collisions per unit path is so large that this process is in fact extremely efficient in dissipating the muon's kinetic energy. The energy loss is therefore a quasi-continuous process, as summarised in Bethe-Bloch's equation for the stopping power dE/dx, whose cumulative effect renders moderate lengths of material enough to stop the muon completely. In phthalocyanines, for instance, the range of 4.1 MeV surface muons amounts to about 1 mm (Figure 3.18).

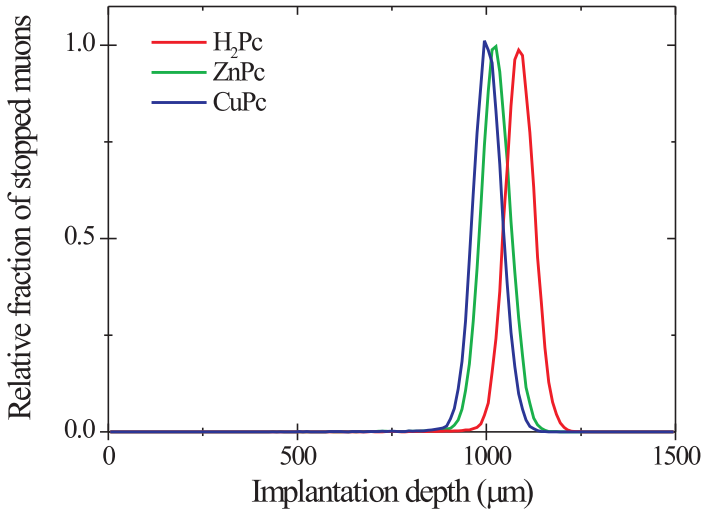

Figure 3.18: Estimated implantation profile of surface positive muons (4.1 MeV) in H_2Pc, ZnPc and CuPc. The three curves were obtained from Monte-Carlo calculations performed with the TRIM program (version SRIM-2003.26), a widely used software code developed by J.P. Biersack and J.F. Ziegler to simulate the interaction of particles with matter [140].

The Bethe-Bloch regime occurs in roughly less than a nanosecond for the implantation energies found in μSR [13]. That time interval is too short for the beam polarisation to suffer any kind of change, which means that the muon is effectively shielded from magnetic interactions during the slowing down. The muon samples a random set of successive non-equilibrium sites in the host material, each possibly with a different total field, but that succession is so fast that the time it persists under the influence of each individual field is too low for the polarisation to precess or relax significantly. Since the typical residence time under each different field's

influence is under one millionth of a ns[22], an interaction capable of changing the polarisation would have to lie in the millions of GHz range[23], a value too high for any type of magnetic interaction to reach. In fact, the largest magnetic interactions the muon may experience are of hyperfine nature, resting at most in the GHz region (*cf.* Table 3.3), but even those are out of consideration here, as down to epithermal muon velocities the electrostatic binding to electrons needed for hyperfine interactions to exist is inhibited by the high kinetic energy of the muon. Hence, up to the point when binding to electrons becomes possible, the muon beam polarisation is considered to be fully preserved.

3.3.2 Charge-exchange, thermalisation and final muon states

When the kinetic energy of the positive muon is of a few keV, the stopping process gets more complex, since the muon velocity becomes comparable to the orbital velocity of the atomic electrons. This causes the electron capture cross-section to be large enough so that muonium formation events may take place. At that point, the muon enters the charge-exchange regime, a stage where it cycles between the bound and the free state as it picks up and releases different electrons along its path. Energy is of course lost in this process, taken away by the electron every time the muon unbinds it. Inelastic collisions with electrons also continue to occur, but are less effective than in the Bethe-Bloch regime due to the screening of the muon's positive charge while it is in the bound muonium species. The energy loss per unit path during the charge-exchange stage is therefore considerably lower, but the overall duration of charge-exchange cycling ends up not going further than the picosecond [106, 13]. Again, the time spent under the influence of internal fields (namely the large hyperfine field caused by the electron coupling in the muonium species for each cycle) is too short for any significant change of the muon polarisation to occur[24]. This process continues until the muon energy reaches a charge-exchange threshold around some eV. The last collision determines whether the muon leaves that regime in a positively charged state or in a neutral state of high hyperfine interaction, but what finally controls the relative

[22] This residence time is comparable to the time the muon spends in each unit cell of the host lattice, which may be crudely estimated to be 10^{-15} s in a 1 nm-parameter lattice if the muon travels for 1 mm during 1 ns until it stops.

[23] We quote here a frequency value for the energy scale; the proper energy scale is of course obtained from this value by multiplying it by Planck's constant h.

[24] Although this may be taken to be true in solids and liquids, where the high density ensures short residence times in the muonium state, in gases some depolarisation may in fact occur due to the on-off cycling of the hyperfine interaction. See *e.g.* [119] for a more complete account of that effect.

epithermal yield of each charge state still remains unknown. Some theoretical evidence suggests that elastic collisions with nuclei may play an unexpected role in the very last part of the charge-exchange process, enhancing the formation of the positively charged state [108, 109]. Low-energy muon implantation studies performed with insulators in the slow-muon beam-line recently built at PSI [91] indicate that such propensity for a positive charge state excess after the charge-exchange regime does exist.

In addition to what happens in the very last phase of the charge-exchange regime, the final muon states and relative yields observed in a μSR experiment depend further on subsequent events that the resulting bare muons or neutral muonium atoms may experience during the thermalisation stage[25]. Both the proton and the hydrogen are known to be quite reactive in matter, the same holding for the positive muon and muonium. Therefore, both fractions resulting from charge-exchange may react with the host environment upon thermalisation to form final states whose charge depends on the properties of that same environment. In condensed matter, both the charge state and site of the positive muon are dictated by the minimisation of the muon's electrostatic energy. With very few exceptions, the muon comes to rest at an interstitial site; it does not trap in vacancies created by the implantation process, since its lighter mass as compared with the lattice atoms forces it to cease atom displacement well before it stops. The diversity and structure of final states it then forms obviously depends on the electronic properties of the implantation media, namely the delocalisation degree, energy and occupation of its electronic states. In metals, for instance, the muon always forms a positively charged Mu^{+}[26] state without any kind of bonded electronic cloud, as it is energetically more favourable for electrons to occupy the highly delocalised (hence low-energy) electronic states of the host metal [106]. It assumes an interstitial site away from nuclear cores, and becomes surrounded by a screening charge of conduction electrons as it polarises the electronic media due to coulombic attraction. In semiconductors and insulators, on the other hand, the existence of a well-defined energy band-gap intensifies the localisation of valence and conduction electrons, commonly leading to the observation of neutral states whenever it is energetically appropriate[27].

[25] It is worth emphasising that a thermalised muon is not necessarily in thermodynamic equilibrium; it merely has a kinetic energy comparable to the thermal energy of its surroundings. This subtle distinction is in fact a weak link in the parallel between muonium and hydrogen, since during the short duration of a μSR measurement one may observe metastable muon states whose hydrogen counterparts do not exist as thermal equilibrium configurations.

[26] We reserve here the μ^{+} notation to refer the high-energetic muons being implanted in the sample. Thermalised or near-thermalised states will be denoted by Mu and a superscript signal to indicate the charge state.

[27] *i.e.* if binding to the positive muon is a lower energy state for the media electrons. That involves comparing

In their simplest form, neutral muonium Mu^0 states have a pure *atomic* character, bearing a compact and isotropic $1s$-type wavefunction. The electronic cloud is trapped inside a wide void, where confinement energy and elastic distortion of the lattice are minimal. The bound electron's spin is coupled to the muon's spin via an hyperfine interaction whose magnitude scales with the electronic density at the muon's position (see Section 3.4.2); depending on the overlap of the muonium's wavefunction with the surrounding host atoms, that hyperfine interaction is reduced relative to its vacuum value (4.4633 GHz, see Table 3.3), varying from one material to another in a range typically going from 100% to 50% of that value. This is the picture for neutral states found in ionic compounds, such as the alkali halides [20], although they are also formed in covalently bonded materials, like oxides, diamond, quartz, the elemental semiconductors Si and Ge, and the III-V and some of the II-VI semiconducting compounds (an extensive literature on the subject exists; see *e.g.* [106, 85, 22]). In these covalent materials, which are often tetrahedrally coordinated, the atomic Mu state is referred to as Mu^0_T, reflecting its localisation at a tetrahedral site[28]. That designation distinguishes it from a second type of neutral state also found in many of those compounds, the *bond-centre muonium*, Mu^0_{BC} [12]. This is a compact molecular-radical state, in which the positive muon sits at the centre of a covalent bond between two neighbouring atoms of the host lattice [35, 61]. The muonium's wavefunction adopts the anti-bonding character of the bond's valence molecular orbital, and therefore is not centred in the muon, being instead divided by the two atoms at both ends of the bond. This feature grants the Mu^0_{BC} state two distinctive characteristics: a low hyperfine interaction value (of the order of 1% of the vacuum value), as the muon is placed at a node of the Mu wavefunction, and the existence of a pronounced anisotropy in that same hyperfine interaction, as it has a large contribution of dipolar origin due to the axially symmetric configuration of the wavefunction. Muonium molecular-radical states are also found in organic media, as revealed from many free-radical chemistry studies performed with μSR [99, 95]. They seem to invariably arise from the addition of atomic muonium to organic molecules [95], which reduces multiple bonds and transfers a substantial part of its electronic cloud to the rest of the molecule. A *muoniated radical* is thus formed which, just as the Mu^0_{BC} state, is characterised by having the most part of its unpaired electronic density dispersed over the molecule and not at the muon site, leading to an equally low (1-5% of the vacuum value) and anisotropic hyperfine interaction. Finally, a third

the energy of the bound state as imbedded in the target material with the media's ionisation potential or Fermi energy, whichever applicable.

[28] This is an interstitial site located at the centre of the cage formed by four neighbouring cations.

and last type of neutral muonium state exists in matter, namely in some of the compound (III-V and II-VI) semiconductors. It is a *shallow-donor* muonium state [45, 21], where the positive muon is believed to be in a position anti-bonding to the anion (the V or VI atom), and whose main characteristic is its extremely dilated electron wavefunction, typically several nanometres in radius. This type of state has a very low hyperfine interaction (less than 0.01% of the vacuum value), since the electronic probability density at the positive muon is vanishingly small even when compared with molecular-radical muonium states. The hyperfine interaction is definitely anisotropic in most cases, indicating that some non-isotropic distortion of the electronic cloud exists; the wavefunction actually stems from conduction band states held together by the small Coulomb attraction promoted by the positive muon, and retains many of the properties of conduction electrons, *viz.* their g-factor value [66]. The formation of an extended wavefunction in shallow muonium enhances the probability that the electron capture event conducing to that state may occur far away from the muon site, and indeed there is evidence that the formation of shallow muonium states directly depends on the capture of electrons 10 to 100 nm away, originating in the radiolytic track[29]. As electron-donor impurities in a semiconductor, shallow muonium centres are apparently well described by the effective mass theory [6]; they have a correspondingly low ionisation energy, of the order of some meV [45, 47, 21], as opposed to the deep centres of atomic and bond-centre muonium, which are ionised at energies of hundreds of meV [85, 18].

Independently of their spatial configuration or exact formation mechanism, the final muon states observed in μSR are usually classified according to the number of unpaired-spin electrons the positive muon binds. If the state is a neutral muonium system, possessing one bound unpaired electron, it is said to be *paramagnetic*; if it is a positively charged state, no bound electron exists, and the state is *diamagnetic*. Diamagnetic muon states also occur when the positive muon binds *two* electrons, originating a negative muonium state Mu^- similar to the hydride ion H^-. In this system, the two electron spins are paired, producing an electronic cloud with zero total magnetic moment and no hyperfine interaction. Mu^- is therefore spectroscopically indistinguishable from Mu^+. This type of negatively charged state is formed in heavily n-doped semiconductors, where the abundance of electrons and the low Fermi energy may cause neutral states to undergo a second electron capture [20, 18].

[29] The trail of ionised atoms and free electrons left behind by the muon as it stops.

3.4 μSR of paramagnetic muon states

The existence of an unpaired electron bound to the positive muon in paramagnetic states produces an hyperfine interaction which couples the muon spin to the electron's spin *via* their magnetic moments. This lifts the degeneracy on the muon's spin coordinates, and splits the energy levels of the (μ^+e^-) system even in the absence of an externally applied field. The electronic structure of the (μ^+e^-) state is often the main factor dictating the properties of that hyperfine interaction; these are quantum mechanically codified in the spin eigenstates of the system, and rule in their turn the time evolution of the muon polarisation. This section is centred on the description of the electronic structure and dynamics of the most common paramagnetic states, and how the μSR observables are affected by it. It therefore constitutes a basic tool for the analysis and interpretation of μSR data performed in subsequent chapters.

3.4.1 The spin hamiltonian

The hamiltonian of a paramagnetic (μ^+e^-) system is usually written as the sum of three components [126],

$$\hat{H} = \hat{H}_C + \hat{H}_{SO} + \hat{H}_S \ , \tag{3.31}$$

where $\hat{H}_C$ describes the kinetic energy and Coulomb interactions of the muon and the electron, $\hat{H}_{SO}$ the electron's spin-orbit coupling, and $\hat{H}_S$ the remaining spin interactions of the system. The energies involving all spin interactions are several orders of magnitude smaller than the kinetic and the Coulomb energy (a few μeV *vs.* some eV), and because of that $\hat{H}_{SO}$ and $\hat{H}_S$ are normally treated as perturbations to $\hat{H}_C$. This turns out to be quite useful, as spin interactions are concerned, since it becomes possible to perform the separation of spatial coordinates from the spin coordinates, and take $\hat{H}_S$ as the effective spin hamiltonian solely responsible for the time-evolution of the spin states. That is of course true whenever the electron is in a state possessing no spin-orbit coupling ($l = 0$), although for states with $l \neq 0$ one may still separate the spatial and spin variables defining an effective spin hamiltonian which does not include the spin-orbit operator. We will not consider those cases here, as they are of very little importance to μSR.

In the absence of dynamical phenomena, the general spin hamiltonian for a paramagnetic (μ^+e^-) system may be written as

$$\hat{H}_S = \hat{H}_{Mu} + \hat{H}_N \ , \tag{3.32}$$

where $\hat{H}_{Mu}$ is the operator that describes spin interactions involving solely the positive muon and/or the electron, and $\hat{H}_N$ includes all remaining spin interactions resulting from the existence of other spin-carrying species which may interact with the paramagnetic state. In the presence of an externally applied magnetic field $\vec{B}$, $\hat{H}_{Mu}$ is given by the dipolar interaction between $\vec{B}$ and the magnetic moment operators $\hat{\vec{\mu}}_e$ and $\hat{\vec{\mu}}_\mu$ of the electron and the muon (often called the electron and muon Zeeman interactions), together with the hyperfine interaction coupling between the electron and muon spin operators, $\hat{\vec{S}}_e$ and $\hat{\vec{S}}_\mu$:

$$\begin{aligned} \hat{H}_{Mu} &= -\hat{\vec{\mu}}_e.\vec{B} - \hat{\vec{\mu}}_\mu.\vec{B} + \frac{2\pi}{\hbar}\ \hat{\vec{S}}_e\mathbf{A}.\ \hat{\vec{S}}_\mu \\ &= -\gamma_e\ \hat{\vec{S}}_e\vec{B} - \gamma_\mu\ \hat{\vec{S}}_\mu\vec{B} + \frac{2\pi}{\hbar}\ \hat{\vec{S}}_e\mathbf{A}.\ \hat{\vec{S}}_\mu\,. \end{aligned} \tag{3.33}$$

Here, γ_e and γ_μ are the gyromagnetic ratios of the electron and muon, and the hyperfine interaction term is presented in the form of a tensorial product between the cartesian components of the electron and the muon spin operators. The second-rank tensor mediating that product is the *hyperfine interaction tensor*, which in the reference frame OX'Y'Z' defined by its principal directions reads[30]

$$\mathbf{A} = \begin{bmatrix} A'_{xx} & 0 & 0 \\ 0 & A'_{yy} & 0 \\ 0 & 0 & A'_{zz} \end{bmatrix}\ ; \tag{3.34}$$

A'_{xx}, A'_{yy} and A'_{zz} are its principal values, whose relative magnitudes reflect the spatial symmetry of the electronic wavefunction, as shown in appendix C. Their absolutes value quantify the coupling energy involved in the interaction, given by hA'_{xx}, hA'_{xx} and hA'_{xx}; h is Planck's constant, and the hyperfine tensor is expressed in units of frequency. For electronic states possessing s character, the principal values of the hyperfine tensor (3.34) are always offset by the *contact hyperfine coupling constant* A_{iso} which parameterises the Fermi contact interaction arising from the finite electron density existing at the muon position (see appendix C). In the simplest case of all, which occurs when the electronic wavefunction is isotropic, that contact interaction is the only contribution for the hyperfine interaction; the principal values of the hyperfine tensor are all equal to A_{iso}, and the tensor has a diagonal representation independently of the reference frame it is expressed in.

As a rule, the external magnetic field is considered to lie along the z-axis direction of the laboratory reference frame OXYZ, i.e. $\vec{B} = B\hat{z}$. That direction is also chosen to be the spin

[30] One should be aware that when considered in the hamiltonian (3.33), the hyperfine tensor is expressed in the laboratory reference frame OXYZ, and in general will not have the diagonal form of (3.34).

quantisation axis, so that the spin-up, spin-down states of the muon and the electron are the usual eigenvectors of $\vec{S}_\mu^2$, $\hat{S}_{\mu_z}$(see equations (3.2),(3.3)) and of $\vec{S}_e^2$, $\hat{S}_{e_z}$(*id.*, but *mutatis mutandis* for the electron). We will follow these two conventions, and adopt a third one often encountered in μSR literature, which is expressing all hamiltonians in angular frequency units. Hence, (3.33) will read from hereon in the more compact notation

$$\begin{aligned} \hat{H}_{Mu}/\hbar &= -\gamma_e \hat{S}_{e_z}/\hbar B - \gamma_\mu \hat{S}_{\mu_z}/\hbar B + \frac{2\pi}{\hbar}\ \hat{\vec{S}}_e/\hbar.\mathbf{A}.\ \hat{\vec{S}}_\mu/\hbar \\ &= \frac{\omega_e}{2}\ \hat{\sigma}_{e_z} - \frac{\omega_\mu}{2}\ \hat{\sigma}_{\mu_z} + \hat{\vec{\sigma}}_e.\frac{2\pi\mathbf{A}}{4}.\hat{\vec{\sigma}}_\mu\ , \end{aligned} \tag{3.35}$$

where the Pauli spin operators of the electron and the muon are used (see appendix A for the definition and properties of the Pauli spin operator of a 1/2-spin particle), and the (absolute) Larmor frequencies of the electron and muon are defined (refer to Table 3.2 for the values of γ_e and γ_μ)[31]:

$$\omega_e = -\gamma_e B = |\gamma_e| B \tag{3.36}$$

$$\omega_\mu = \gamma_\mu B\ . \tag{3.37}$$

Depending on the local environment the muon might be in, the component $\hat{H}_N$ of the spin hamiltonian (3.32) may be simpler or more complex; if spin-carrying nuclei exist near enough, and the electronic unpaired spin density at their positions is not negligible, an hyperfine interaction will develop between those nuclei and the electron of the (μ^+e^-) system. That interaction is known as the *nuclear hyperfine interaction* or *superhyperfine interaction*, and $\hat{H}_N$ will be given by

$$\hat{H}_N/\hbar = \sum_k \left(-\omega_k\, \hat{S}_{k_z}/\hbar + \hat{\vec{\sigma}}_e.\frac{2\pi\mathbf{A}_k}{2}.\ \hat{\vec{S}}_k/\hbar + \ldots \right), \tag{3.38}$$

where ω_k is the Larmor frequency of the k-th nucleus (its definition is analogous to (3.37)), $\hat{\vec{S}}_k$ is its spin operator, and $\mathbf{A}_n^k$ the nuclear hyperfine tensor for the interaction between that nucleus and the unpaired electron. Should it exist, and excepting probably the nuclear Zeeman interaction at higher fields, the nuclear hyperfine interaction will be the largest term in $\hat{H}_N$; nevertheless, smaller contributions arising from coupling of the electron to nuclei having spin larger than 1/2 through the *nuclear quadrupole interaction*, or the direct *dipole-dipole interaction*

[31] Strictly speaking, the electron's g-factor may not be a scalar, meaning that γ_e should have a tensorial form. In fact, if there is any sort of spin-orbit coupling of the unpaired electron to its environment, it will result in the electron's Zeeman energy possessing a value which depends on the direction of the external field. Nevertheless, deviations from its free electron value ($g_e \approx 2$) do not usually produce significant effects in the μSR signal.

between the magnetic moments of the muon and the nuclei (and between themselves) may become important in certain situations (see *e.g.* [126] for a more complete account of these effects).

3.4.2 Hyperfine structure of paramagnetic states

Just as in basic spectroscopy, the hyperfine characterisation of paramagnetic states in μSR is performed using the level splitting induced by an externally applied magnetic field. Given all the spin interactions a paramagnetic state may undergo (see above), its hyperfine structure may be considerably rich; the external field assists at measuring the value of coupling constants (namely the hyperfine interaction, which, as it is discussed in appendix C, conveys information about the spatial distribution of the electron), either by lifting possibly existing degeneracies in some cases, or by simplifying the layout of the energy levels in others. Since knowing the structure of the hyperfine states is essential to characterise the time dependence of the muon's polarisation, as we shall see in Section 3.4.3, we consider it in the following for specific types of paramagnetic states, that are also the commonest.

Isotropic Muonium

Following (3.35), the hamiltonian for an isotropic, atomic-like muonium system in the absence of other nuclei is given by

$$\begin{aligned} \hat{H}_S^{iso}/\hbar &= \frac{\omega_e}{2}\,\hat{\sigma}_{e_z} - \frac{\omega_\mu}{2}\,\hat{\sigma}_{\mu_z} + \hat{\vec{\sigma}}_e.\frac{2\pi\mathbf{A}}{4}.\hat{\vec{\sigma}}_\mu \\ &= \frac{\omega_e}{2}\,\hat{\sigma}_{e_z} - \frac{\omega_\mu}{2}\,\hat{\sigma}_{\mu_z} + \frac{\omega_0}{4}\,\hat{\vec{\sigma}}_e.\hat{\vec{\sigma}}_\mu\ , \end{aligned} \tag{3.39}$$

where the hyperfine tensor reads

$$\mathbf{A} = \frac{1}{2\pi}\begin{bmatrix} \omega_0 & 0 & 0 \\ 0 & \omega_0 & 0 \\ 0 & 0 & \omega_0 \end{bmatrix} \tag{3.40}$$

as a function of the (angular) hyperfine frequency ω_0 (see appendix C for the meaning of all symbols)

$$\omega_0 = 2\pi\, A_{iso} = \hbar\,\frac{\mu_0}{4\pi}\,|\gamma_e|\gamma_\mu\,\frac{8\pi}{3}\,|\psi(0)|^2\ . \tag{3.41}$$

Since one wants to know the hyperfine structure of this state, it is necessary to solve the Schrödinger spin equation to obtain the eigenvalues and eigenvectors of (3.39). We start by

constructing an ordered basis for the eigenvectors' Hilbert space from the four possible combinations of the single-particle spin functions $|\alpha_\mu\rangle$, $|\beta_\mu\rangle$, $|\alpha_e\rangle$ and $|\beta_e\rangle$ that are eigenstates of the $\hat{S}_{\mu_z}$and $\hat{S}_{e_z}$ spin operators:

$$|\alpha_\mu\rangle \otimes |\alpha_e\rangle \equiv |\alpha_\mu\alpha_e\rangle = \begin{bmatrix} 1 \\ 0 \\ 0 \\ 0 \end{bmatrix} \quad ; \quad |\alpha_\mu\rangle \otimes |\beta_e\rangle \equiv |\alpha_\mu\beta_e\rangle = \begin{bmatrix} 0 \\ 1 \\ 0 \\ 0 \end{bmatrix}$$

$$|\beta_\mu\rangle \otimes |\alpha_e\rangle \equiv |\beta_\mu\alpha_e\rangle = \begin{bmatrix} 0 \\ 0 \\ 1 \\ 0 \end{bmatrix} \quad ; \quad |\beta_\mu\rangle \otimes |\beta_e\rangle \equiv |\beta_\mu\beta_e\rangle = \begin{bmatrix} 0 \\ 0 \\ 0 \\ 1 \end{bmatrix}$$

With this choice, and using the properties of the Pauli spin matrices, equations (A.4)-(A.11), the matricial representation $[H^{iso}_{\alpha\beta}]$ of the hamiltonian (3.39) becomes

$$[H^{iso}_{\alpha\beta}]/\hbar = \begin{bmatrix} \omega_- + \frac{\omega_0}{4} & 0 & 0 & 0 \\ 0 & -\omega_+ - \frac{\omega_0}{4} & \frac{\omega_0}{2} & 0 \\ 0 & \frac{\omega_0}{2} & \omega_+ - \frac{\omega_0}{4} & 0 \\ 0 & 0 & 0 & -\omega_- + \frac{\omega_0}{4} \end{bmatrix} , \tag{3.42}$$

where the *positive* quantities

$$\omega_+ = \frac{\omega_e + \omega_\mu}{2} \tag{3.43}$$

$$\omega_- = \frac{\omega_e - \omega_\mu}{2} \tag{3.44}$$

are used. The eigenvalues $\omega_n = E_n/\hbar$ and eigenvectors $|n\rangle$ of (3.42) are obtained solving the secular equation

$$|H^{iso}_{\alpha\beta}/\hbar - \omega\,\delta_{\alpha\beta}| = 0 \ , \tag{3.45}$$

which, in this concrete case, is a degenerate quartic equation; it is therefore solved easily, yielding

$$\omega_1 = \frac{1}{4}\,\omega_0 + \omega_- \quad ; \quad |1\rangle = |\alpha_\mu\alpha_e\rangle \tag{3.46}$$

$$\omega_2 = \frac{1}{4}\,\omega_0 + \Omega \quad ; \quad |2\rangle = s\ |\alpha_\mu\beta_e\rangle + c\ |\beta_\mu\alpha_e\rangle \tag{3.47}$$

$$\omega_3 = \frac{1}{4}\,\omega_0 - \omega_- \quad ; \quad |3\rangle = |\beta_\mu\beta_e\rangle \tag{3.48}$$

$$\omega_4 = -\frac{3}{4}\,\omega_0 - \Omega \quad ; \quad |4\rangle = c\ |\alpha_\mu\beta_e\rangle - s\ |\beta_\mu\alpha_e\rangle \ . \tag{3.49}$$

Here,

$$x = \frac{\omega_e + \omega_\mu}{\omega_0} = \frac{2\omega_+}{\omega_0} = \frac{B}{B_0} \tag{3.50}$$

with

$$B_0 = \frac{\omega_0}{|\gamma_e| + \gamma_\mu} \tag{3.51}$$

is an non-dimensional measure of the externally applied magnetic field,

$$\Omega = \frac{\omega_0}{2}\left(\sqrt{x^2+1} - 1\right) \tag{3.52}$$

is a non-linear field-dependent positive quantity, and

$$c^2 = \frac{1}{2}\left(1 + \frac{x}{\sqrt{x^2+1}}\right) \tag{3.53}$$

$$s^2 = \frac{1}{2}\left(1 - \frac{x}{\sqrt{x^2+1}}\right) = 1 - c^2 \tag{3.54}$$

define the coefficients of the eigenvectors. The eigenvalue equations (3.46)-(3.49) describe the splitting of the energy levels of an hydrogen-like system in an external magnetic field, and are known as *Breit-Rabi equations*; that field dependence is usually plotted in the way of a *Breit-Rabi diagram*, as illustrated in Figure 3.19.

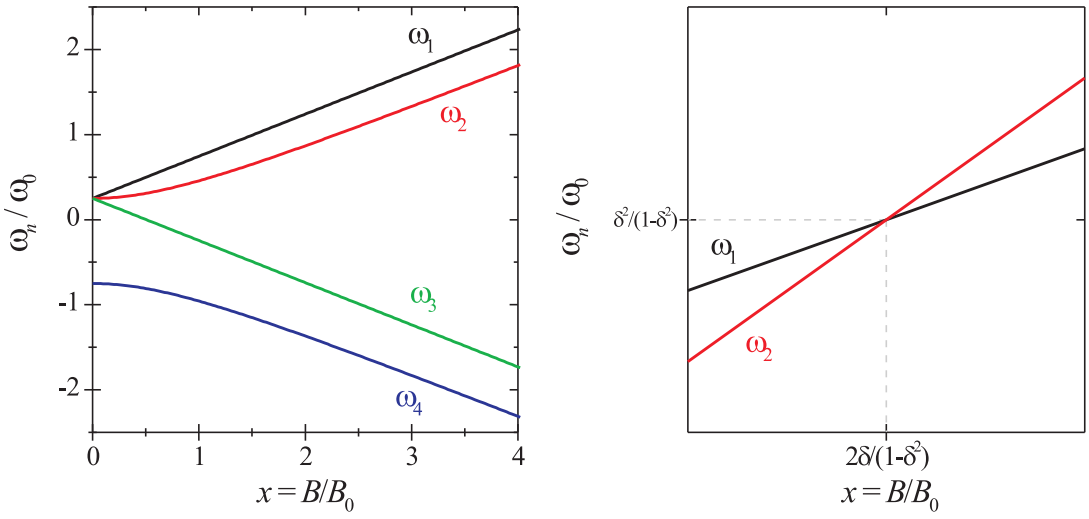

Figure 3.19: Breit-Rabi diagram for an isotropic muonium state. The insert shows in detail the ω_1-ω_2 level-crossing existing at $x^{iso}_{12\,\mathrm{cross}} \approx 103.38$. The energy levels are ordered according to the high-field layout before the crossing.

In the absence of magnetic field, $c = s = 1/\sqrt{2}$ and the four states combine to a triplet ($|1\rangle$-$|3\rangle$) and a singlet ($|4\rangle$) system separated by an energy of $\hbar\omega_0$. The degeneracy of the

triplet is lifted by the external magnetic field: levels ω_1 and ω_3 follow a linear dependence with the field, since they correspond to eigenstates of the spin operators $\hat{S}_{\mu_z}$and $\hat{S}_{e_z}$; levels ω_2 and ω_4, on the other hand, are a mixture of basis states, and their field dependence is non-linear. Nevertheless, these levels are progressively bent as the field magnitude increases, until they reach an asymptotic linear behaviour at $x \gg 1$. In that situation, called the *high-field regime*, the hyperfine interaction between the muon and the electron is decoupled by the large magnetic field; the spin hamiltonian is dominated by the Zeeman energies, states $|1\rangle$ and $|3\rangle$ become eigenstates of the spin operators as $c \to 1$ and $s \to 0$, and the individual magnetic spin quantum numbers m^μ and m^e of the muon and the electron become good quantum numbers. In practice, this regime is attained $x \sim 10$. At higher fields, levels ω_1 and ω_2 eventually cross; this occurs exactly at

$$x^{iso}_{12\,\mathrm{cross}} = \frac{2\delta}{1-\delta^2} \approx 103.38 \ , \tag{3.55}$$

where

$$\delta = \frac{\omega_-}{\omega_+} = \frac{|\gamma_e| - \gamma_\mu}{|\gamma_e| + \gamma_\mu} = 0.990374 \tag{3.56}$$

and

$$\omega_1 = \omega_2 = \frac{\delta^2}{1-\delta^2}\ \omega_0 \approx 51.2\omega_0 \ . \tag{3.57}$$

Furthermore, since the approximation

$$\Omega = \frac{\omega_0}{2}\ \left(\sqrt{x^2-1} - 1\right) \approx \frac{\omega_0}{2}\,(x-1) = \omega_+ - \frac{\omega_0}{2} \tag{3.58}$$

holds at the crossing, and

$$\omega_+ - \omega_- = \omega_\mu \ , \tag{3.59}$$

one gets from $\omega_1 = \omega_2$ the relation

$$\omega_\mu = \frac{\omega_0}{2} \ . \tag{3.60}$$

As in high field $\langle \hat{\sigma}_{\mu_z} \rangle = \left\langle \hat{\vec{\sigma}}_e . \hat{\vec{\sigma}}_\mu \right\rangle = 1$, (3.60) means that at the ω_1-ω_2 level crossing, *the absolute value of the muon's Zeeman interaction energy equals the hyperfine interaction energy.* This is an important remark, since when that happens the hamiltonian (3.39) is stripped from all interactions figuring the muon spin; therefore, the least perturbation to (3.39) involving the muon will be the dominant factor influencing its polarisation at the crossing, giving rise to prominent features, as it will be seen later in the cases of axially symmetric and radical states.

Axially symmetric Muonium

For an axially symmetric muonium state, the hamiltonian

$$\hat{H}_S^{ax}/\hbar = \frac{\omega_e}{2}\ \hat{\sigma}_{e_z} - \frac{\omega_\mu}{2}\ \hat{\sigma}_{\mu_z} + \hat{\vec{\sigma}}_e.\frac{2\pi\mathbf{A}}{4}.\hat{\vec{\sigma}}_\mu \tag{3.61}$$

holds, but with an hyperfine tensor which, when expressed in the OX'Y'Z' reference frame of its principal axis, reads

$$\mathbf{A} = \begin{bmatrix} A_{iso} - D/2 & 0 & 0 \\ 0 & A_{iso} - D/2 & 0 \\ 0 & 0 & A_{iso} + D \end{bmatrix}\ , \tag{3.62}$$

D being the dipolar contribution brought to the hyperfine interaction by the axial symmetry of the electron's wavefunction (see appendix C). To compute the tensorial product with the Pauli spin operators of the muon and the electron figuring in the hyperfine interaction, however, it is necessary to express $\mathbf{A}$ and those operators in the same reference frame, which we will choose here to be the OXYZ coordinate system of the laboratory. If the system OX'Y'Z' defines the Euler angles (ϕ, θ, ψ) in the ZYZ convention relative to OXYZ, the transformation is performed according to

$$\mathbf{A} = \mathbf{R} \begin{bmatrix} A_{iso} - D/2 & 0 & 0 \\ 0 & A_{iso} - D/2 & 0 \\ 0 & 0 & A_{iso} + D \end{bmatrix} \mathbf{R}^{-1}\ , \tag{3.63}$$

where $\mathbf{R}(\phi, \theta, \psi)$ is an orthogonal transformation matrix given by

$$\mathbf{R} = \begin{bmatrix} \cos\psi & \sin\psi & 0 \\ -\sin\psi & \cos\psi & 0 \\ 0 & 0 & 1 \end{bmatrix} \begin{bmatrix} \cos\theta & 0 & -\sin\theta \\ 0 & 1 & 0 \\ \sin\theta & 0 & \cos\theta \end{bmatrix} \begin{bmatrix} \cos\phi & \sin\phi & 0 \\ -\sin\phi & \cos\phi & 0 \\ 0 & 0 & 1 \end{bmatrix}\ . \tag{3.64}$$

It is not difficult to prove that the axial symmetry of the hyperfine tensor renders the rotations along ψ and ϕ irrelevant, leading to a final form which depends solely on the angle θ defined by the symmetry axis and the z-axis direction; that form reads explicitly

$$\begin{aligned} \mathbf{A} &= \begin{bmatrix} A_{iso} + \frac{1-3\cos 2\theta}{4} D & 0 & -\frac{3\sin 2\theta}{4} D \\ 0 & A_{iso} - D/2 & 0 \\ -\frac{3\sin 2\theta}{4} D & 0 & A_{iso} + \frac{1+3\cos 2\theta}{4} D \end{bmatrix} \\ &= \begin{bmatrix} \omega_0 + \frac{\omega_D}{2} - \omega_c & 0 & -\omega_s \\ 0 & \omega_0 - \frac{\omega_D}{2} & 0 \\ -\omega_s & 0 & \omega_0 + \omega_c \end{bmatrix} \times \frac{1}{2\pi}\ , \end{aligned} \tag{3.65}$$

where the quantities

$$\omega_D = 2\pi D \tag{3.66}$$

$$\omega_c = 2\pi D \frac{1+3\cos 2\theta}{4} = \omega_D \frac{3\cos^2\theta - 1}{2} \tag{3.67}$$

$$\omega_s = 2\pi D \frac{3\sin 2\theta}{4} = \omega_D \frac{3\sin\theta\cos\theta}{2} \tag{3.68}$$

are used. The hamiltonian matrix becomes

$$[H^{ax}_{\alpha\beta}]/\hbar = \begin{bmatrix} \omega_- + \frac{\omega_0}{4} + \frac{\omega_c}{4} & -\frac{\omega_s}{4} & -\frac{\omega_s}{4} & \frac{\omega_D}{4} - \frac{\omega_c}{4} \\ -\frac{\omega_s}{4} & -\omega_+ - \frac{\omega_0}{4} - \frac{\omega_c}{4} & \frac{\omega_0}{2} - \frac{\omega_c}{4} & \frac{\omega_s}{4} \\ -\frac{\omega_s}{4} & \frac{\omega_0}{2} - \frac{\omega_c}{4} & \omega_+ - \frac{\omega_0}{4} - \frac{\omega_c}{4} & \frac{\omega_s}{4} \\ \frac{\omega_D}{4} - \frac{\omega_c}{4} & \frac{\omega_s}{4} & \frac{\omega_s}{4} & -\omega_- + \frac{\omega_0}{4} + \frac{\omega_c}{4} \end{bmatrix} , \tag{3.69}$$

whose eigenvalues $\omega_n = E_n/\hbar$ and eigenvectors $|n\rangle$ are again obtained by solving the secular equation, now a full quartic equation. Although that equation may be solved analytically (see [120]), the solution is hard to find, and in practice the numeric diagonalisation of (3.69) is performed,

$$[H^{ax}_{\alpha\beta}] \equiv \mathbf{H} = \mathbf{U}\ \mathbf{D}\ \mathbf{U}^\dagger\ ; \tag{3.70}$$

the eigenvalues are then the elements of its diagonal representation $\mathbf{D}$, and the corresponding eigenvectors the columns of the (unitary) diagonalising matrix $\mathbf{U}$:

$$\omega_n = D_{nn}/\hbar \tag{3.71}$$

$$|n\rangle = U_{1n}|\alpha_\mu\alpha_e\rangle + U_{2n}|\alpha_\mu\beta_e\rangle + U_{3n}|\beta_\mu\alpha_e\rangle + U_{4n}|\beta_\mu\beta_e\rangle\ . \tag{3.72}$$

Figure 3.20 shows three Breit-Rabi diagrams as a function of the dimensionless field parameter x for an axially symmetric muonium state with $D = A_{iso}/2$ for the two limiting cases $\theta = 0$ and $\theta = \pi/2$, and an intermediate orientation $\theta = \pi/4$. The relative layout of the energy levels is strongly influenced by the value of θ, as the anisotropy in zero field lifts the degeneracy of one of the three states involved in the triplet found for the isotropic case. Which state it is, and how much it is shifted, depends on the specific value of θ. All levels follow non-linear dependencies with the field as a general rule, although all end up reaching also a linear asymptotic behaviour at high fields, corresponding to the high-field decoupling of the hyperfine interaction. The level crossings are affected by the existence of anisotropy as well; in the case shown, an additional low-field level crossing exists at $\theta = 0$ between levels ω_2 and ω_3, while for $\theta = \pi/4$ the ω_1-ω_2 crossing no longer exists, but is *avoided* at the field for which the muon Zeeman energy

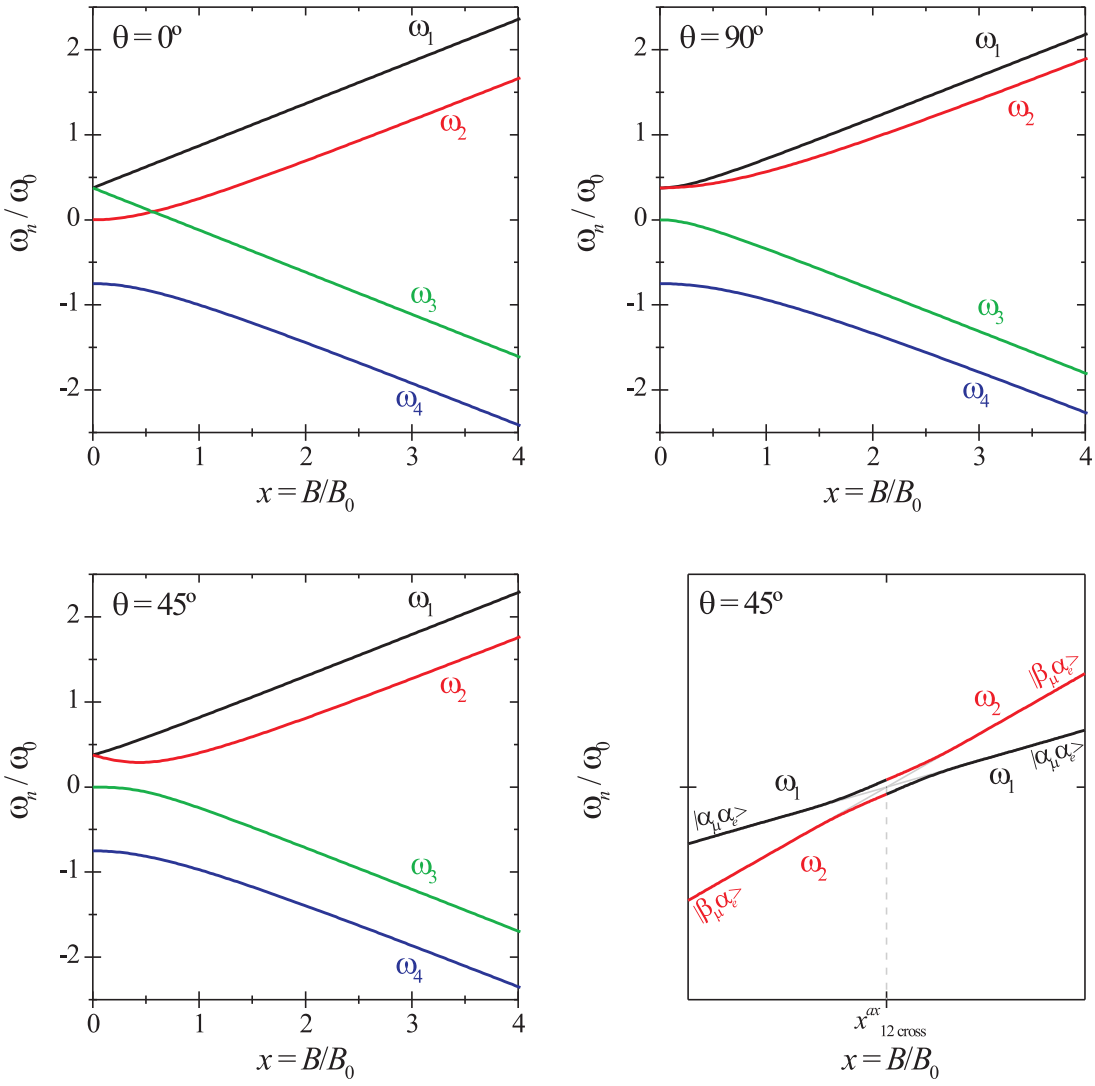

Figure 3.20: Breit-Rabi diagrams for an axially symmetric muonium state with $D = A_{iso}/2$ at three different orientations. The evolutions of the levels ω_1 and ω_2 at their (avoided) level-crossing is also shown in detail, emphasising the mixing of these two near-degenerate levels.

matches the hyperfine interaction energy (or, put in another way, when the total muon energy — the sum between its Zeeman energy and the hyperfine interaction energy — is zero). Taking into account this happens in high field, the avoided crossing occurs when

$$\begin{aligned} \left\langle \frac{\omega_\mu}{2}\,\hat{\sigma}_{\mu_z} \right\rangle &= \left\langle \hat{\vec{\sigma}}_e.\frac{2\pi\mathbf{A}}{4}.\hat{\vec{\sigma}}_\mu \right\rangle \\ &\Downarrow \\ \omega_\mu &= \frac{\omega_0+\omega_c}{2}\ , \end{aligned} \tag{3.73}$$

which corresponds to the orientation-dependent field

$$x^{ax}_{12\,\mathrm{cross}}(\theta) = x^{iso}_{12\,\mathrm{cross}}\left(1+\frac{\omega_D}{\omega_0}\,\frac{3\cos^2\theta-1}{2}\right)\ . \tag{3.74}$$

Near this field, the anisotropy causes the two levels to exhibit a highly non-linear behaviour, indicating the enhanced mixture of basis states in the corresponding hamiltonian eigenvectors. This corresponds to the mixing of the two near-degenerate levels $|1\rangle$ and $|2\rangle$ in such a way that the highest energy level gradually shifts from the $|\alpha_\mu\alpha_e\rangle$ state to the $|\beta_\mu\alpha_e\rangle$ one, while the lowest energy traverses the inverse path $|\beta_\mu\alpha_e\rangle$ to $|\alpha_\mu\alpha_e\rangle$. That evolution is shown in Figure 3.20, where the level numbering scheme is changed through the avoided crossing so that away from it state $|1\rangle$ always corresponds to $|\alpha_\mu\alpha_e\rangle$ and state $|2\rangle$ to $|\beta_\mu\alpha_e\rangle$.

The existence of a level crossing avoidance between states $|1\rangle$ and $|2\rangle$ may be understood in terms of perturbation theory considering the anisotropy to be a disturbance of the isotropic hamiltonian (3.39). In that framework, the $|n\rangle$ states of (3.61) are given in first-order by (see *e.g.* [76])

$$|n\rangle = |n^{(0)}\rangle + \sum_{\substack{m=1\\ m\neq n}}^{4} \frac{\langle m^{(0)}|\Delta\hat{H}^{ax}|n^{(0)}\rangle}{E^{(0)}_n - E^{(0)}_m}|m^{(0)}\rangle\ , \tag{3.75}$$

where $|n^{(0)}\rangle$ are the eigenstates of the isotropic hamiltonian (3.39), equations (3.46)-(3.49), and $\Delta\hat{H}^{ax}$ is the traceless perturbation hamiltonian

$$[\Delta\hat{H}^{ax}_{\alpha\beta}]/\hbar = \frac{1}{4}\begin{bmatrix} \omega_c & -\omega_s & -\omega_s & \omega_D-\omega_c \\ -\omega_s & -\omega_c & -\omega_c & \omega_s \\ -\omega_s & -\omega_c & -\omega_c & \omega_s \\ \omega_D-\omega_c & \omega_s & \omega_s & \omega_c \end{bmatrix}\ . \tag{3.76}$$

The perturbation treatment, nevertheless, breaks down for a given $|n\rangle$ state if the non-perturbed $|n^{(0)}\rangle$ state is degenerate with any of the other $|m^{(0)}\rangle$ states,

$$E^{(0)}_n = E^{(0)}_m\ ,$$

and the condition

$$\langle m^{(0)}|\Delta\hat{H}^{ax}|n^{(0)}\rangle \neq 0$$

is met. If that does happen, *degenerate* perturbation theory has to be used, giving rise to the splitting of the two degenerate levels under the action of the perturbation, which we name here as *level-avoidance*. The matrix elements $\langle m^{(0)}|\Delta\hat{H}^{ax}|n^{(0)}\rangle$ are therefore what determine if a crossing occurs *de facto* or is avoided; in our concrete case, they read

$$\langle 1^{(0)}|\Delta\hat{H}^{ax}/\hbar|2^{(0)}\rangle = -\omega_s/4 \tag{3.77}$$

$$\langle 1^{(0)}|\Delta\hat{H}^{ax}/\hbar|3^{(0)}\rangle = (\omega_D-\omega_c)/4 \tag{3.78}$$

$$\langle 1^{(0)}|\Delta\hat{H}^{ax}/\hbar|4^{(0)}\rangle = -\omega_s/4 \tag{3.79}$$

$$\langle 2^{(0)}|\Delta\hat{H}^{ax}/\hbar|3^{(0)}\rangle = \omega_s/4 \tag{3.80}$$

$$\langle 2^{(0)}|\Delta\hat{H}^{ax}/\hbar|4^{(0)}\rangle = -\omega_s/4 \tag{3.81}$$

$$\langle 3^{(0)}|\Delta\hat{H}^{ax}/\hbar|4^{(0)}\rangle = \omega_s/4\ . \tag{3.82}$$

Hence, for $\theta \neq 0, \pi/2, \pi$ *all* level-crossings are avoided. Particularly for the ω_1-ω_2 avoided level-crossing, the use of degenerate perturbation theory leads to the (new) non-degenerate states (see *e.g.* [76])

$$|1\rangle = s_\chi\ |\alpha_\mu\alpha_e\rangle + c_\chi|\beta_\mu\alpha_e\rangle \tag{3.83}$$

$$|2\rangle = c_\chi\ |\alpha_\mu\alpha_e\rangle - s_\chi|\beta_\mu\alpha_e\rangle \tag{3.84}$$

before the crossing ($\omega_\mu < \frac{\omega_0+\omega_c}{2}$) and

$$|1\rangle = c_\chi\ |\alpha_\mu\alpha_e\rangle - s_\chi|\beta_\mu\alpha_e\rangle \tag{3.85}$$

$$|2\rangle = s_\chi\ |\alpha_\mu\alpha_e\rangle + c_\chi|\beta_\mu\alpha_e\rangle \tag{3.86}$$

after the crossing ($\omega_\mu > \frac{\omega_0+\omega_c}{2}$), separated by an energy gap given by

$$\begin{aligned}
|\omega_1-\omega_2| &= \frac{1}{\hbar}\sqrt{\left(\langle 1^{(0)}|\hat{H}_S^{ax}|1^{(0)}\rangle - \langle 2^{(0)}|\hat{H}_S^{ax}|2^{(0)}\rangle\right)^2 + 4\,\langle 1^{(0)}|\Delta\hat{H}^{ax}|2^{(0)}\rangle^2} \\
&\approx \sqrt{\left(\omega_- - \omega_+ + \frac{\omega_0}{2} + \frac{\omega_c}{2}\right)^2 + \left(\frac{\omega_s}{2}\right)^2} \\
&= \sqrt{\omega_x^2+\omega_G^2} \\
&= \omega_G\sqrt{\chi^2+1}
\end{aligned} \tag{3.87}$$

where

$$\omega_x = \omega_- - \omega_+ + \frac{\omega_0}{2} + \frac{\omega_c}{2} = \omega_\mu - \frac{\omega_0+\omega_c}{2} \tag{3.88}$$

is a quantity vanishing at the field where the crossing was supposed to exist,

$$\omega_G = \frac{\omega_s}{2} \tag{3.89}$$

is the minimum gap value, and

$$c_\chi^2 = \frac{1}{2}\left(1 + \frac{\chi}{\sqrt{\chi^2+1}}\right) \tag{3.90}$$

$$s_\chi^2 = \frac{1}{2}\left(1 - \frac{\chi}{\sqrt{\chi^2+1}}\right) = 1 - c_\chi^2 \tag{3.91}$$

are the mixture coefficients in the wavefunctions, with

$$\chi = \frac{\omega_x}{\omega_G} \tag{3.92}$$

being a dimensionless field parameter centred at the crossing (note that at the crossing one has $\chi = 0$). As it will be seen later, the existence of a finite gap between levels ω_1 and ω_2 is an important feature of the avoided level-crossing which originates a characteristic oscillation of the muon polarisation in longitudinal geometry at high fields.

Muoniated radicals

Muoniated molecular-radical states formed in organic media are characterised by having a considerable number of other spin-carrying nuclei in the molecule which couple to the state's unpaired electron *via* the nuclear hyperfine interaction. Indeed, it was realised quite soon in μSR's history that this mechanism had to be included in the interpretation of data obtained with organic molecules [98, 99, 126]. This is due to the large population of protons (1/2 spins) normally found in those compounds, and to the fact that the main part of the radical's electron density does not reside at the muon, but is distributed over the whole molecule. According to (3.35) and (3.38), the hamiltonian of a muoniated organic radical is given by

$$\begin{aligned}\hat{H}_S^{rad}/\hbar &= \frac{\omega_e}{2}\,\hat{\sigma}_{e_z} - \frac{\omega_\mu}{2}\,\hat{\sigma}_{\mu_z} + \hat{\vec{\sigma}}_e.\frac{2\pi\mathbf{A}}{4}.\hat{\vec{\sigma}}_\mu + \\ &\quad - \sum_k \omega_k\,\hat{S}_{k_z}/\hbar + \sum_k \hat{\vec{\sigma}}_e.\frac{2\pi\mathbf{A}_k}{2}.\,\hat{\vec{S}}_k/\hbar\ ,\end{aligned} \tag{3.93}$$

where, for the sake of simplicity, we will consider all hyperfine interactions to be isotropic[32], and, for the time being, that all nuclei are equivalent. The nuclear terms in this hamiltonian are normally of lesser importance[33], and the eigenvalues and eigenvectors may be obtained by treating them as perturbations to the isotropic muonium hamiltonian (3.39). If we collect the equivalent nuclei in a group with spin and magnetic quantum numbers J and M_J, corresponding to the eigenvectors $|J, M_J\rangle$ of the total spin operators $\vec{J}^2$ and $\hat{J}_z$,

$$\vec{J}^2 \ |J, M_J\rangle = \hbar^2 J(J+1) \ |J, M_J\rangle \tag{3.94}$$

$$\hat{J}_z \ |J, M_J\rangle = \hbar \ M_J \ |J, M_J\rangle \ , \tag{3.95}$$

and consider the common Larmor frequency and isotropic hyperfine interaction to be ω_N and $\omega_{0_N}/2\pi$ respectively, the perturbation hamiltonian in (3.93) will read

$$\hat{H}_N^{rad}/\hbar = -\omega_N \ \hat{J}_z/\hbar + \frac{\omega_{0_N}}{2} \ \hat{\vec{\sigma}}_e.\hat{\vec{J}}/\hbar \ ; \tag{3.96}$$

the zeroth-order eigenstates of the whole system will be simple products of the non-perturbed solutions (3.46)-(3.49) with the nuclear state $|J, M_J\rangle$,

$$|1, M_J\rangle = |1\rangle|J, M_J\rangle = |\alpha_\mu \alpha_e\rangle|J, M_J\rangle \tag{3.97}$$

$$|2, M_J\rangle = |2\rangle|J, M_J\rangle = (s \ |\alpha_\mu \beta_e\rangle + c \ |\beta_\mu \alpha_e\rangle)|J, M_J\rangle \tag{3.98}$$

$$|3, M_J\rangle = |3\rangle|J, M_J\rangle = |\beta_\mu \beta_e\rangle|J, M_J\rangle \tag{3.99}$$

$$|4, M_J\rangle = |4\rangle|J, M_J\rangle = (c \ |\alpha_\mu \beta_e\rangle - s \ |\beta_\mu \alpha_e\rangle)|J, M_J\rangle \ , \tag{3.100}$$

and the corresponding first-order corrections to the energy values

$$\langle 1, M_J| \ \hat{H}_N^{rad}/\hbar \ |1, M_J\rangle = -\omega_N M_J + \frac{\omega_{0_N}}{2} M_J \tag{3.101}$$

$$\langle 2, M_J| \ \hat{H}_N^{rad}/\hbar \ |2, M_J\rangle = -\omega_N M_J + \frac{\omega_{0_N}}{2} \ (c^2 - s^2) M_J \tag{3.102}$$

$$\langle 3, M_J| \ \hat{H}_N^{rad}/\hbar \ |3, M_J\rangle = -\omega_N M_J - \frac{\omega_{0_N}}{2} M_J \tag{3.103}$$

$$\langle 4, M_J| \ \hat{H}_N^{rad}/\hbar \ |4, M_J\rangle = -\omega_N M_J - \frac{\omega_{0_N}}{2} \ (c^2 - s^2) M_J \ , \tag{3.104}$$

[32]This is usually a reasonable assumption since most μSR experiments with organic radicals are done in liquid samples, where the anisotropic contributions to the hyperfine interaction are averaged to zero due to rapid tumbling of the radicals. Nevertheless, the generalisation to anisotropic interactions may be easily performed in what follows using the corresponding non-diagonal hyperfine tensor in the hamiltonian, and numerically diagonalising it to obtain the eigenvalues ω_1 through ω_4 and eigenstates $|1\rangle$ through $|4\rangle$.

[33]All nuclei are composite, heavy particles, and therefore possess gyromagnetic ratios quite smaller than those of elementary particles such as the muon or the electron. Hence, both the nuclear Zeeman energies as the nuclear hyperfine interactions will be considerably lower than the Zeeman interactions of the electron and the muon and the hyperfine interaction.

where the relations

$$\langle M_J|\ \hat{\vec{J}}/\hbar\ |M_J\rangle = M_J\ \hat{z} \tag{3.105}$$

$$\langle 1|\ \hat{\sigma}_{e_z}\ |1\rangle = 1 \tag{3.106}$$

$$\langle 2|\ \hat{\sigma}_{e_z}\ |2\rangle = c^2 - s^2 \tag{3.107}$$

$$\langle 3|\ \hat{\sigma}_{e_z}\ |3\rangle = -1 \tag{3.108}$$

$$\langle 4|\ \hat{\sigma}_{e_z}\ |4\rangle = s^2 - c^2 \tag{3.109}$$

were used. The final expressions for the energy levels are

$$\omega_1(M_J) = \frac{1}{4}\,\omega_0 + \omega_- - \omega_N M_J + \frac{\omega_{0_N}}{2} M_J \tag{3.110}$$

$$\omega_2(M_J) = \frac{1}{4}\,\omega_0 + \Omega - \omega_N M_J + \frac{\omega_{0_N}}{2}\ (c^2 - s^2) M_J \tag{3.111}$$

$$\omega_3(M_J) = \frac{1}{4}\,\omega_0 - \omega_- - \omega_N M_J - \frac{\omega_{0_N}}{2} M_J \tag{3.112}$$

$$\omega_4(M_J) = -\frac{3}{4}\,\omega_0 - \Omega - \omega_N M_J - \frac{\omega_{0_N}}{2}\ (c^2 - s^2) M_J\ , \tag{3.113}$$

which in reality is a set of $4 \times (2J+1)$ different values since one has to account for the possible $2J+1$ different values of M_J. These expressions can be easily generalised for situations having more than one group of equivalent nuclei, in which case

$$\omega_1(M_J^1, M_J^2, \ldots) = \frac{1}{4}\,\omega_0 + \omega_- + \sum_p \left(-\omega_N^p M_J^p + \frac{\omega_{0_N}^p}{2} M_J^p \right) \tag{3.114}$$

$$\omega_2(M_J^1, M_J^2, \ldots) = \frac{1}{4}\,\omega_0 + \Omega + \sum_p \left(-\omega_N^p M_J^p + \frac{\omega_{0_N}^p}{2}\ (c^2 - s^2) M_J^p \right) \tag{3.115}$$

$$\omega_3(M_J^1, M_J^2, \ldots) = \frac{1}{4}\,\omega_0 - \omega_- + \sum_p \left(-\omega_N^p M_J^p - \frac{\omega_{0_N}^p}{2} M_J^p \right) \tag{3.116}$$

$$\omega_4(M_J^1, M_J^2, \ldots) = -\frac{3}{4}\,\omega_0 - \Omega + \sum_p \left(-\omega_N^p M_J^p - \frac{\omega_{0_N}^p}{2}\ (c^2 - s^2) M_J^p \right)\ , \tag{3.117}$$

where the subscript p identifies each different group.

Figure 3.21 depicts the Breit-Rabi diagram for the isotropic muonium state shown in Figure 3.19, but now coupled to a single 1/2-spin proton. The levels are seen to be doubly split by the nuclear hyperfine interaction with the extra spin; at high fields, the splitting attains a constant value of ω_{0_N} and the levels become linearly dependent on the field. This simple situation is once again provided by the electron Zeeman interaction dominating the hamiltonian, and decoupling both the hyperfine and the nuclear hyperfine interactions.

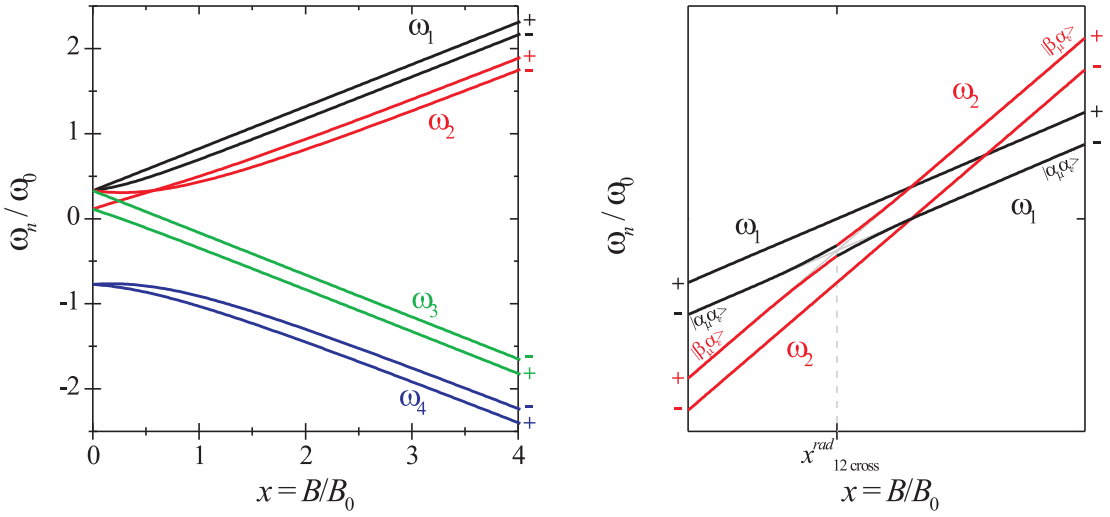

Figure 3.21: Breit-Rabi diagram for a muoniated radical state with isotropic hyperfine interaction coupled to a 1/2-spin proton via an isotropic nuclear hyperfine interaction $\omega_{0_N} = \omega_0/10$. The plot on the right shows in detail the ω_1-ω_2 (avoided) level crossing. All the curves presented were extracted from calculations using the full hamiltonian.

Similarly to what happens with the case of an axially symmetric $(\mu^+ - e^-)$ state, the ω_1-ω_2 level crossing is also highly affected by the presence in the hamiltonian of terms in addition to the isotropic hyperfine interaction. In this case, the analysis of the matrix elements $\langle m, M_J|\ \hat{H}_N^{rad}\ |n, M'_J\rangle$ figuring in the expansion of the first-order eigenstates yields crossing avoidance between states that satisfy [85, 99]

$$\Delta M = 0\ , \tag{3.118}$$

where M is the total spin magnetic quantum number of the system, as given by the sum of the individual magnetic quantum numbers m^μ, m^e and M_J. Hence, and since levels ω_1 and ω_2 in high fields exhibit both $m^e = +\frac{1}{2}$, level-crossings will be avoided only between split levels corresponding to the simultaneous flip of the muon's and the nuclei total spin, *i.e.* $|1, M_J - 1\rangle$ and $|2, M_J\rangle$. In the case of Figure 3.21, where the possible values of M_J are $\pm\frac{1}{2}$, the crossing is avoided between levels ω_1^- $(M_J = -\frac{1}{2})$ and ω_2^+ $(M_J = +\frac{1}{2})$. The ω_1-ω_2 crossing is avoided at a field $x_{12\,\mathrm{cross}}^{rad}$ meeting the condition $\omega_1(M_J - 1) = \omega_2(M_J)$, which from equations (3.110) and (3.111) in the high field regime leads to (compare with (3.60) and (3.73))

$$-\omega_\mu + \frac{\omega_0}{2} = -\omega_N + \frac{\omega_{0_N}}{2}\ , \tag{3.119}$$

i.e. it occurs when the total muon energy matches the total nuclear energy; the explicit value of $x^{rad}_{12\,\mathrm{cross}}$ is

$$x^{rad}_{12\,\mathrm{cross}} = x^{iso}_{12\,\mathrm{cross}} \left(1 - \frac{\omega_{0_N}}{\omega_0}\right) \frac{1}{1 - \gamma_N/\gamma_\mu} \,. \tag{3.120}$$

It is also easy to show that the degenerate perturbation theory states are (compare with equations (3.83)-(3.86))

$$|1, M_J - 1\rangle = s_\chi \, |\alpha_\mu \alpha_e\rangle |J, M_J - 1\rangle + c_\chi |\beta_\mu \alpha_e\rangle |J, M_J - 1\rangle \tag{3.121}$$

$$|2, M_J\rangle = c_\chi \, |\alpha_\mu \alpha_e\rangle |J, M_J\rangle \quad - s_\chi |\beta_\mu \alpha_e\rangle |J, M_J\rangle \tag{3.122}$$

and

$$|1, M_J - 1\rangle = c_\chi \, |\alpha_\mu \alpha_e\rangle |J, M_J - 1\rangle - s_\chi |\beta_\mu \alpha_e\rangle |J, M_J - 1\rangle \tag{3.123}$$

$$|2, M_J\rangle = s_\chi \, |\alpha_\mu \alpha_e\rangle |J, M_J\rangle \quad + c_\chi |\beta_\mu \alpha_e\rangle |J, M_J\rangle \tag{3.124}$$

before ($\omega_\mu - \omega_N < \frac{\omega_0}{2} - \frac{\omega_{0_N}}{2}$) and after ($\omega_\mu - \omega_N > \frac{\omega_0}{2} - \frac{\omega_{0_N}}{2}$) the avoided crossing, and that the energy gap is (compare with (3.87))

$$|\omega_1(M_J - 1) - \omega_2(M_J)| = \sqrt{\omega_x^2 + \omega_G^2} \,. \tag{3.125}$$

The quantities c_χ and s_χ are defined in terms of $\chi = \omega_x/\omega_G$ according to equations (3.90) and (3.91), but now with ω_x and ω_G being given for $-J + 1 \leq M_J \leq J$ by

$$\begin{aligned} \omega_x &= \langle 1| \, \hat{H}^{rad}_S/\hbar \, |1\rangle - \langle 2| \, \hat{H}^{rad}_S/\hbar \, |2\rangle \\ &= (\omega_\mu - \omega_N) - \left(\frac{\omega_0}{2} - \frac{\omega_{0_N}}{2}\right) \end{aligned} \tag{3.126}$$

and

$$\begin{aligned} \omega_G &= 2 \, \langle 1, M_J - 1| \, \hat{H}^{rad}_N/\hbar \, |2, M_J\rangle \\ &= 2 \, s \, \omega_{0_N} \, \sqrt{J(J+1) - M_J(M_J - 1)} \\ &\approx \frac{\omega_{0_N}}{x} \, \sqrt{J(J+1) - M_J(M_J - 1)} \,, \end{aligned} \tag{3.127}$$

where the angular momentum relations

$$\hat{\vec{\sigma}}_e . \hat{\vec{J}} = \frac{1}{2}\left(\hat{\sigma}_+ \, \hat{J}_- + \hat{\sigma}_- \, \hat{J}_+\right) + \hat{\sigma}_{e_z} \, \hat{J}_z \tag{3.128}$$

$$\hat{J}_\pm = \hat{J}_x \pm i \, \hat{J}_y \tag{3.129}$$

$$\hat{J}_\pm |n, M_J\rangle = \hbar \sqrt{J(J+1) - M_J(M_J \pm 1)} \, |n, M_J \pm 1\rangle \tag{3.130}$$

and the high-field approximation

$$s \approx \frac{1}{2x} \tag{3.131}$$

were used. The similarities with the electronic structure of an axially symmetric paramagnetic state are evident, and indeed the finite gap between levels ω_1 and ω_2 will likewise originate a characteristic LF oscillation of the muon polarisation in high fields.

3.4.3 Time dependence of the muon's polarisation

The analysis of the time dependence of the muon polarisation is essential for the interpretation of μSR data. In fact, the electronic structure and dynamical interactions underwent by a paramagnetic state are reflected in the μSR signal as characteristic precession frequencies and/or relaxations. The fact that one is able to explicitly compute that time dependence for specific physical models allows to establish comparisons between the experimental data and the signal expected from a given model. It thus becomes possible to assess the adequacy of that model in describing the targeted phenomena, and measure its unknown parameters. In practice, this is done by chi-square fitting the experimental data to the theoretical function derived from the model for the polarisation observable. The fitting is invariably performed in the time domain, although whenever a signal with precession frequencies is involved, auxiliary Fourier transform methods are also employed.

In the following, we present two methods of computing the time evolution of the muon polarisation. The first employs a formalism derived from quantum statistics, using a dynamical equation for the density matrix of the $(\mu^+ - e^-)$ paramagnetic system; it involves the *a priori* knowledge of the system's energy levels and eigenstates. The second is based on the simultaneous solution of a set of coupled motion equations for all the polarisations of the system. The two methods are equivalent, and obviously yield the same results; the reason why both are presented is related with the fact that they correlate to physical descriptions of the $(\mu^+ - e^-)$ system which are based on different, but complementary, concepts. While the density matrix formalism links the system's electronic structure more clearly to the muon polarisation, interpreting it in terms of energy transitions, the formalism using the equations of motion deals with individual polarisations which may easily be interpreted classically.

After getting acquainted with the methods that allow to compute the time evolution of the muon polarisation, several practical examples of its use are shown and discussed. In these examples, we focus mainly on states with electronic structures relevant to this thesis.

Density matrix formalism

The muon polarisation, defined as the expectation value of the muon's Pauli spin operator, equation (3.11),

$$\vec{P}_\mu(t) = \left\langle \hat{\vec{\sigma}}_\mu \right\rangle \ ,$$

will evolve in time according to the time-evolution operator of the whole muonium system. If a statistic distribution of different ensemble states exists, a density matrix needs to be used in order to reflect the double statistics on the time-evolution operator; this is especially necessary if one wants to compute an observable which does not depend on all of the system's coordinates, like, for instance, the muon spin polarisation in a muon-electron bound system. In the quantum formalism of density matrices, the expectation value of any operator in a doubly statistical system is given by the trace of the product between that operator and the system's density operator $\hat{\rho}$; in the specific case of the muon's Pauli spin operator one therefore has

$$\vec{P}_\mu(t) = \left\langle \hat{\vec{\sigma}}_\mu \right\rangle = \mathrm{Tr}\left\{ \hat{\rho}_{Mu}(t)\, \hat{\vec{\sigma}}_\mu \right\} \tag{3.132}$$

in each time instant t. The explicit time dependence of the density operator indicates the assumption that all dynamical features of the system are included in that operator. We are therefore expressing $\hat{\rho}$ in Heisenberg's notation, which means that it must obey the dynamical equation

$$-i\,\hbar\,\frac{\partial}{\partial t}\,\hat{\rho}_{Mu}(t) = \left[\, \hat{H}_{Mu}\,,\, \hat{\rho}_{Mu}(t) \right] \ , \tag{3.133}$$

often known as *Liouville's equation*; its formal integration yields

$$\hat{\rho}_{Mu}(t) = e^{\frac{i}{\hbar}\hat{H}_{Mu}t}\ \hat{\rho}_{Mu}(0)\ e^{-\frac{i}{\hbar}\hat{H}_{Mu}t} \ , \tag{3.134}$$

implying the necessary knowledge of $\hat{\rho}_{Mu}(0)$ and the eigenvalue spectrum of the hamiltonian $\hat{H}_{Mu}$. For a 1/2-spin particle, it so happens that it is possible to write the density operator at time zero as a function of its initial polarisation:

$$\hat{\rho}(0) = \frac{1}{2}\left(\hat{1} + \vec{P}(0).\hat{\vec{\sigma}}\right) \ ; \tag{3.135}$$

for a system consisting of two 1/2-spin particles, namely the muon and the electron, the density operator at $t = 0$ will be given by the direct product between individual density operators with

the form of (3.135),

$$\begin{aligned}\hat{\rho}_{Mu}(0) &= \frac{1}{2}\left(\hat{1}+\vec{P}_{\mu}(0).\hat{\vec{\sigma}}_{\mu}\right)\otimes\frac{1}{2}\left(\hat{1}+\vec{P}_{e}(0).\hat{\vec{\sigma}}_{e}\right)\\ &= \frac{1}{4}\left(\hat{1}+\vec{P}_{\mu}(0).\hat{\vec{\sigma}}_{\mu}+\vec{P}_{\mu}(0).\hat{\vec{\sigma}}_{e}+\vec{P}_{\mu}(0).\hat{\vec{\sigma}}_{\mu}\ \vec{P}_{\mu}(0).\hat{\vec{\sigma}}_{e}\right)\\ &= \frac{1}{4}\left(\hat{1}+\vec{P}_{\mu}(0).\hat{\vec{\sigma}}_{\mu}+\vec{P}_{\mu}(0).\hat{\vec{\sigma}}_{e}+\sum_{\alpha,\beta=x,y,z}P_{\alpha\beta}(0)\sigma_{\mu_{\alpha}}\sigma_{\mu_{\beta}}\right)\end{aligned} \tag{3.136}$$

where

$$P_{\alpha\beta}(0)=P_{\mu_{\alpha}}(0)P_{e_{\beta}}(0)\qquad(\alpha,\beta=x,y,z) \tag{3.137}$$

are called the initial *mixed polarisations* of the spin system. As it is generally assumed that upon the last electronic capture in the charge-exchange stopping regime the muon binds electrons of each spin direction with equal probabilities, the electron's initial polarisation may be considered zero, and $\hat{\rho}(0)$ is simplified to

$$\hat{\rho}(0)=\frac{1}{4}\left(\hat{1}+\vec{P}_{\mu}(0).\hat{\vec{\sigma}}_{\mu}\right)\ . \tag{3.138}$$

Having written the density operator as a function of time, the hamiltonian eigenvalue spectrum and the muon's initial polarisation, one may finally evaluate the trace in (3.132) to calculate the explicit time dependence of the muon's polarisation, using $\hat{H}_{Mu}$'s eigenstates $\{\,|n\rangle, n=1,..,4\}$ as a basis for Hilbert's spin-space:

$$\mathrm{Tr}\left\{\hat{\rho}_{Mu}(t)\,\hat{\vec{\sigma}}_{\mu}\right\}=\frac{1}{4}\sum_{n=1}^{4}\langle n|\ e^{\frac{i}{\hbar}\hat{H}_{Mu}t}\ \left(\hat{1}+\vec{P}_{\mu}(0).\hat{\vec{\sigma}}_{\mu}\right)\ e^{-\frac{i}{\hbar}\hat{H}_{Mu}t}\ \hat{\vec{\sigma}}_{\mu}\ |n\rangle\ . \tag{3.139}$$

Making use of the identity operator $\hat{1}=\sum_{m=1}^{4}|m\rangle\langle m|$ one has therefore

$$\begin{aligned}\vec{P}_{\mu}(t) &= \frac{1}{4}\sum_{n=1}^{4}\langle n|\ e^{\frac{i}{\hbar}\hat{H}_{Mu}t}\ \hat{\vec{\sigma}}_{\mu}\ e^{-\frac{i}{\hbar}\hat{H}_{Mu}t}\ |n\rangle\ +\\ &\quad+\frac{1}{4}\sum_{n,m=1}^{4}\langle n|\ e^{\frac{i}{\hbar}\hat{H}_{Mu}t}\ (\vec{P}_{\mu}(0).\hat{\vec{\sigma}}_{\mu})\ e^{-\frac{i}{\hbar}\hat{H}_{Mu}t}\ |m\rangle\ \langle m|\hat{\vec{\sigma}}_{\mu}|n\rangle\\ &= \frac{1}{4}\sum_{n=1}^{4}e^{i\omega_{nn}t}\langle n|\hat{\vec{\sigma}}_{\mu}|n\rangle\ +\\ &\quad+\frac{1}{4}\sum_{n,m=1}^{4}e^{i\omega_{nm}t}\langle n|(\vec{P}_{\mu}(0).\hat{\vec{\sigma}}_{\mu})|m\rangle\ \langle m|\hat{\vec{\sigma}}_{\mu}|n\rangle\ ,\end{aligned} \tag{3.140}$$

where

$$\omega_{nm}=\omega_{n}-\omega_{m} \tag{3.141}$$

is the transition frequency between states $|m\rangle$ and $|n\rangle$. Since by definition the spin operators are traceless, the first summation in (3.140) is zero, and one has finally $\vec{P}_{\mu}(t)$ as the sum of precessing

components with frequencies matching the transition frequencies between the system's energy levels,

$$\begin{aligned} \vec{P}_\mu(t) &= \frac{1}{4} \sum_{n,m=1}^{4} \langle n|(\vec{P}_\mu(0).\hat{\vec{\sigma}}_\mu)|m\rangle \ \langle m|\hat{\vec{\sigma}}_\mu|n\rangle \ e^{i\omega_{nm}t} \\ &= \sum_{n,m=1}^{4} \vec{a}_{nm} \ e^{i\omega_{nm}t} \ , \end{aligned} \tag{3.142}$$

in which

$$\vec{a}_{nm} = \frac{1}{4} \ \langle n|(\vec{P}_\mu(0).\hat{\vec{\sigma}}_\mu)|m\rangle \ \langle m|\hat{\vec{\sigma}}_\mu|n\rangle \tag{3.143}$$

is the complex amplitude of the precession with frequency ω_{nm}. The complex amplitudes depend on the geometry of the system[34] through the hamiltonian eigenvectors, the initial direction of the muon polarisation (the first factor in (3.143), which essentially defines the system's initial state), and the direction along which the polarisation is monitored (the second factor, since $\vec{P}_\mu(t)$ borrows its direction from it). Thus, they may give rise to selection rules (*i.e.* unobserved frequencies, $\vec{a}_{nm} = 0$) depending on the geometry, the initial polarisation and the observation direction.

For an isolated muonium state, there are four different energy levels, which produces a maximum of six different precession frequencies. A non-precessing component may also exist if any of the complex amplitudes having $n = m$ are non-zero. This is easily seen when one considers that the precession frequencies ω_{nm} and ω_{mn} correspond actually to a single precession component. In fact,

$$\omega_{mn} = -\omega_{nm} \ ,$$

meaning that

$$e^{i\omega_{mn}t} = \left(e^{i\omega_{nm}t}\right)^* \ ;$$

furthermore, the spin operators are hermitian, so

$$\vec{a}_{mn} = \vec{a}^*_{nm} \ ,$$

[34] Basically the relation between concurring quantisation axis existing in the system, such as the external applied field or the principal axis of the hyperfine tensor.

and it becomes possible to transform (3.142) into

$$\begin{aligned}
\vec{P}_\mu(t) &= \sum_{n,m=1}^{4} \vec{a}_{nm}\, e^{i\omega_{nm}t} \\
&= \sum_{\substack{n=1\\m=n}}^{4} \vec{a}_{nm}\, e^{i\omega_{nm}t} + \sum_{\substack{n,m=1\\m\neq n}}^{4} (\vec{a}_{nm}\, e^{i\omega_{nm}t} + \vec{a}_{mn}\, e^{i\omega_{mn}t}) \\
&= \sum_{n=1}^{4} \vec{a}_{nn}\, e^{i\omega_{nn}t} + \sum_{n=1}^{3}\sum_{m=n+1}^{4} \left(\vec{a}_{nm}\, e^{i\omega_{nm}t} + \left(\vec{a}_{nm}\, e^{i\omega_{nm}t}\right)^*\right) \\
&= \sum_{n=1}^{4} \vec{a}_{nn} + \sum_{n=1}^{3}\sum_{m=n+1}^{4} 2\,\mathrm{Re}\left\{\vec{a}_{nm}\, e^{i\omega_{nm}t}\right\} \ . \qquad (3.144)
\end{aligned}$$

If we monitor the polarisation along a given direction $\hat{r}$, the time-evolution of that projection will be

$$\begin{aligned}
\vec{P}_\mu(t).\hat{r} &= \sum_{n=1}^{4} \vec{a}_{nn}.\hat{r} + \sum_{n=1}^{3}\sum_{m=n+1}^{4} 2\,\mathrm{Re}\left\{\vec{a}_{nm}.\hat{r}\, e^{i\omega_{nm}t}\right\} \\
&= a_0^{(\hat{r})} + \sum_{n=1}^{3}\sum_{m=n+1}^{4} a_{nm}^{(\hat{r})} \cos(\omega_{nm}t + \phi_{nm}^{(\hat{r})}) \ , \qquad (3.145)
\end{aligned}$$

i.e. it will be the sum of one non-oscillating component

$$a_0^{(\hat{r})} = \sum_{n=1}^{4} \vec{a}_{nn}.\hat{r} \qquad (3.146)$$

with a maximum of six cosines of frequency, amplitude and initial phase given by

$$\omega_{nm} = \omega_n - \omega_m \qquad (3.147)$$

$$a_{nm}^{(\hat{r})} = 2\,|\vec{a}_{nm}.\hat{r}| \qquad (3.148)$$

$$\phi_{nm}^{(\hat{r})} = \arg\{\vec{a}_{nm}.\hat{r}\} \ , \qquad (3.149)$$

where $n = 1, .., 3$, $m = n, .., 4$ and

$$\vec{a}_{nm}.\hat{r} = \frac{1}{4}\, \langle n|(\vec{P}_\mu(0).\hat{\vec{\sigma}}_\mu)|m\rangle\, \langle m|\hat{\vec{\sigma}}_\mu.\hat{r}|n\rangle \ . \qquad (3.150)$$

Equations of motion formalism

This method directly considers the dynamical equations for all the polarisations of the muonium system, namely the muon's, equation (3.132), but also the electron's and that for the

mixed polarisations:

$$\vec{P}_e(t) = \mathrm{Tr}\left\{\hat{\rho}_{Mu}(t)\,\hat{\vec{\sigma}}_e\right\} \tag{3.151}$$

$$P_{\alpha\beta}(t) = \mathrm{Tr}\left\{\hat{\rho}_{Mu}(t)\,\sigma_{\mu_\alpha}\sigma_{e_\beta}\right\} \qquad (\alpha,\beta = x,y,z)\ . \tag{3.152}$$

It starts by considering the Liouville equation for the density operator of the system, (3.133),

$$-i\,\hbar\,\frac{\partial}{\partial t}\,\hat{\rho}_{Mu}(t) = \left[\,\hat{H}_{Mu}\,,\,\hat{\rho}_{Mu}(t)\,\right]\ ,$$

and the time-dependent density operator as a function of those polarisations for any instant t, obtained in analogy with (3.136) by

$$\hat{\rho}_{Mu}(t) = \frac{1}{4}\left(\hat{1} + \vec{P}_\mu(t).\hat{\vec{\sigma}}_\mu + \vec{P}_\mu(t).\hat{\vec{\sigma}}_e + \sum_{\alpha,\beta=x,y,z} P_{\alpha\beta}(t)\sigma_{\mu_\alpha}\sigma_{\mu_\beta}\right)\ . \tag{3.153}$$

Since we know the general form of the hamiltonian for an isolated paramagnetic (μ^+e^-) system, equation (3.35),

$$\hat{H}_{Mu}/\hbar = \frac{\omega_e}{2}\,\hat{\sigma}_{e_z} - \frac{\omega_\mu}{2}\,\hat{\sigma}_{\mu_z} + \hat{\vec{\sigma}}_e.\frac{2\pi\mathbf{A}}{4}.\hat{\vec{\sigma}}_\mu\ ,$$

the commutator

$$\left[\,\hat{H}_{Mu}\,,\,\hat{\rho}_{Mu}(t)\,\right] = \hat{H}_{Mu}\hat{\rho}_{Mu}(t) - \hat{\rho}_{Mu}(t)\hat{H}_{Mu}$$

in Liouville's equation may be explicitly evaluated as a function of the hyperfine tensor's components $A_{xx},\ldots,A_{zz}$ in the laboratory frame of reference,

$$\mathbf{A} = \begin{bmatrix} A_{xx} & A_{xy} & A_{xz} \\ A_{yx} & A_{yy} & A_{yz} \\ A_{zx} & A_{zy} & A_{zz} \end{bmatrix}\ ; \tag{3.154}$$

using the result in Liouville's equation, one obtains an expression that relates the time derivatives of the polarisations on the left hand side of the equation to the values of those polarisations at each instant on the right hand side. The algebra is lengthy, and therefore not reproduced here, but by considering the linear independence of the x,y,z components of the muon's and the electron's spin operators, and of their mixed products, the result may be cast as a set of 15 coupled differential equations for *(i)* the three cartesian components of the muon's polarisation, $P_{\mu_x}, P_{\mu_y}, P_{\mu_y}$, *(ii)* the three cartesian components of the electron's polarisation, $P_{e_x}, P_{e_y}, P_{e_y}$, and *(iii)* the nine distinct mixed polarisations $P_{xx}, P_{xy},\ldots,P_{zz}$. All the equations have the form

$$\frac{dP_j(t)}{dt} = f_j\left(\vec{P}_\mu(t), \vec{P}_e(t), P_{\alpha\beta}(t)\right) \qquad (j = 1,..,15)\ , \tag{3.155}$$

where P_j denotes any of the 15 components of the polarisations referred above, and each function f_j does not depend explicitly on the component $P_j(t)$. To solve these 15 coupled equations, one may define a 15-component vector $\mathbf{P}$ where the first three components correspond to the cartesian components of $\vec{P}_\mu$, the following three to the cartesian components of $\vec{P}_e$, and the last nine to the mixed polarisations $P_{\alpha\beta}$:

$$\mathbf{P} = \begin{bmatrix} P_{\mu x} \\ \vdots \\ P_{\mu x} \\ \vdots \\ P_{xx} \\ \vdots \end{bmatrix} \; ; \tag{3.156}$$

the coupled equations (3.155) are then written as

$$\dot{\mathbf{P}}(t) = \mathbf{Q}\ \mathbf{P}(t)\ , \tag{3.157}$$

where $\mathbf{Q}$ is a time independent 15×15 matrix depending solely on the parameters figuring in the hamiltonian and the direction we took for the quantisation of spin. The explicit expression for $\mathbf{Q}$ is shown in the last appendix of this work. The solution of the vectorial equation (3.157) implies transforming it to the coordinate system in $\mathbf{Q}$'s space where this matrix is diagonal; if

$$\mathbf{Q} = \mathbf{U}\ \mathbf{D}\ \mathbf{U}^{-1}\ , \tag{3.158}$$

where $\mathbf{D}$ is the diagonal representation of $\mathbf{Q}$, whose components are the eigenvalues of $\mathbf{Q}$, and $\mathbf{U}$ is the diagonalising matrix[35], whose columns are the eigenvectors of $\mathbf{Q}$, then it is easy to show that the formal solution of (3.157) is given by

$$\mathbf{P}(t) = \mathbf{U}\ e^{\mathbf{D}t}\ \mathbf{U}^{-1}\ \mathbf{P}(0)\ , \tag{3.159}$$

which in terms of the individual components P_j reads

$$P_j(t) = \sum_{k=1}^{15} \sum_{l=1}^{15} U_{jk}\ e^{D_{kk}t}\ U^{-1}_{kl}\ P_l(0)\ . \tag{3.160}$$

[35]Although we use here the symbol $\mathbf{U}$ to denote the diagonalising matrix of $\mathbf{Q}$, that does not mean it is a unitary matrix; quite the contrary, $\mathbf{Q}$ is in general a non-normal matrix, *i.e.* $\mathbf{Q}^\dagger\,\mathbf{Q} \neq \mathbf{Q}\,\mathbf{Q}^\dagger$, meaning that the adjoint of $\mathbf{U}$ does not equal $\mathbf{U}$'s inverse.

This equation describes the time evolution of all the system's polarisations in the absence of external perturbations; its solution is equivalent to the one obtained by the density matrix formalism. It should be made clear that $\mathbf{Q}$ is a real, anti-symmetric matrix, and so its eigenvalues are necessarily either pure imaginary numbers or zero; this means that each polarisation will be the sum of purely (*i.e.* non-damped) oscillating components with (also non-damped) non-oscillating ones. Furthermore, (3.157) is formally equivalent to the equations of motion of a classical system of two coupled oscillators; for such a system, six normal modes of oscillation are expected, together with three translational ones. Therefore, each polarisation will be the sum of up to six different oscillations with up to three constant values which sum to give a single non-oscillating component. Just as we did in the case of the density matrix formalism, we may group the products having $D_{kk} = i\,\omega_k$,

$$U_{jk}U_{kl}^{-1}e^{D_{kk}t} = U_{jk}U_{kl}^{-1}e^{i\,\omega_k t}$$

with their conjugates ($D_{k'k'} = i\,\omega_{k'} = -i\,\omega_k$)

$$U_{jk'}U_{k'l}^{-1}e^{D_{k'k'}t} = U_{jk'}U_{k'l}^{-1}e^{-i\,\omega_k t} = \left(U_{jk}U_{kl}^{-1}e^{i\,\omega_k t}\right)^* \ ,$$

since it follows from $\mathbf{Q}$ being a real matrix that

$$U_{jk'}U_{k'l}^{-1} = \left(U_{jk}U_{kl}^{-1}\right)^*$$

whenever $D_{k'k'} = -D_{kk}$. Hence, (3.160) may be written as

$$\begin{aligned}
P_j(t) &= \sum_{\substack{k \\ D_{kk}=0}} \left(\sum_{l=0}^{15} U_{jk}U_{kl}^{-1}\,P_l(0)\right) + \\
&\quad + \sum_{\substack{k \\ D_{kk}=+i\,\omega_k}} \left\{ \left(\sum_{l=0}^{15} U_{jk}U_{kl}^{-1}\,P_l(0)\right) e^{i\,\omega_k t} + \left(\sum_{l=0}^{15} U_{jk}U_{kl}^{-1}\,P_l(0)\right)^* e^{-i\,\omega_k t} \right\} \\
&= \sum_{\substack{k \\ D_{kk}=0}} \left(\sum_{l=0}^{15} U_{jk}U_{kl}^{-1}\,P_l(0)\right) + \sum_{\substack{k \\ D_{kk}=+i\,\omega_k}} 2\,\mathrm{Re}\left\{ \left(\sum_{l=0}^{15} U_{jk}U_{kl}^{-1}\,P_l(0)\right)\ e^{i\,\omega_k t} \right\} \\
&= a_0^{(j)} + \sum_{i=1}^{6} a_i^{(j)}\,\cos(\omega_i t + \phi_i^{(j)}) \ , \qquad (3.161)
\end{aligned}$$

where the non-oscillating component is

$$a_0^{(j)} = \sum_{\substack{k \\ D_{kk}=0}} \left(\sum_{l=0}^{15} U_{jk}U_{kl}^{-1}\,P_l(0)\right) \qquad (3.162)$$

with k running the three indexes that satisfy $D_{kk} = 0$, and the frequencies, amplitudes and initial phases of the oscillating components are

$$\omega_i = \omega_k = \mathrm{Im}\{D_{kk}\} \tag{3.163}$$

$$a_i^{(j)} = \sum_{l=0}^{15} 2\,|U_{jk}U_{kl}^{-1}|\,P_l(0) \tag{3.164}$$

$$\phi_i^{(j)} = \arg\left\{\sum_{l=0}^{15} U_{jk}U_{kl}^{-1}\,P_l(0)\right\} \tag{3.165}$$

with k restricted to the six indexes conforming to $\mathrm{Im}\{D_{kk}\} > 0$.

In μSR we are only able to monitor the muon's polarisation, and so $\mathbf{P}$'s components of interest will be

$$\begin{aligned}
P_{\mu_x}(t) &\equiv P_1(t) = a_0^{(1)} + \sum_{i=1}^{6} a_i^{(1)}\,\cos(\omega_i t + \phi_i^{(1)}) \\
P_{\mu_y}(t) &\equiv P_2(t) = a_0^{(2)} + \sum_{i=1}^{6} a_i^{(2)}\,\cos(\omega_i t + \phi_i^{(2)}) \\
P_{\mu_z}(t) &\equiv P_3(t) = a_0^{(3)} + \sum_{i=1}^{6} a_i^{(3)}\,\cos(\omega_i t + \phi_i^{(3)})
\end{aligned}$$

Again, selection rules may exist depending on the geometry (through the shape of $\mathbf{Q}$), the initial polarisation of the whole system (the $P_l(0)$ factors) and the direction along which the polarisation is monitored. We should also note that the expressions (3.162)-(3.165) for the amplitudes and phases are considerably simplified in a typical μSR experiment, since the initial values for the polarisation of the electron and the mixed polarisations is normally zero. Only one or two of the elements of $\mathbf{P}(0)$ will be non-zero, depending if the experiment is performed in longitudinal field geometry ($P_3(0) = 1$, all others zero) or transverse-field geometry ($P_1^2(0) + P_2^2(0) = 1$, all others zero).

$\vec{P}_\mu(t)$ of isotropic muonium states

Transverse-field geometry

Using equations (3.145)-(3.150), one can derive the explicit time dependence of the μSR signal both in TF and LF geometries for the case of an isotropic muonium state. We start by considering the first geometry, for which the operators figuring in the precession amplitudes,

equation (3.150), read

$$\vec{P}_\mu(0).\hat{\vec{\sigma}}_\mu = \hat{x}.\hat{\vec{\sigma}}_\mu = \hat{\sigma}_{\mu_x} \tag{3.166}$$

$$\hat{\vec{\sigma}}_\mu.\hat{r} = \hat{\vec{\sigma}}_\mu.\hat{x} = \hat{\sigma}_{\mu_x} \tag{3.167}$$

if the implanted muon beam is polarised along the x-axis, which we take also to be the observation direction $\hat{r}$. Evaluating the matrix elements of $\hat{\vec{\sigma}}_\mu$ and the corresponding precession frequencies (3.141) with the analytical expressions for the eigenstates (3.46)-(3.49) of isotropic Mu, one chiefly obtains

$$a_0^x = 0 \tag{3.168}$$

$$a_{12}^x = \frac{c^2}{2} \longrightarrow \omega_{12} = \omega_- - \Omega \tag{3.169}$$

$$a_{13}^x = 0 \tag{3.170}$$

$$a_{14}^x = \frac{s^2}{2} \longrightarrow \omega_{14} = \omega_- + \Omega + \omega_0 \tag{3.171}$$

$$a_{23}^x = \frac{s^2}{2} \longrightarrow \omega_{23} = \omega_- + \Omega \tag{3.172}$$

$$a_{24}^x = 0 \tag{3.173}$$

$$a_{34}^x = \frac{c^2}{2} \longrightarrow \omega_{34} = -\omega_- + \Omega + \omega_0 \ ; \tag{3.174}$$

the non-oscillating component is zero because the eigenstates of (3.39) are orthogonal to the eigenstates of $\hat{\sigma}_{\mu_x}$, and out of the possible six transition frequencies only four turn out to be actually observed. The transverse-field muon polarisation of an isotropic muonium state is therefore written as

$$P_{\mu_x}(t) = \frac{s^2}{2}\left(\cos\omega_{23}t + \cos\omega_{14}t\right) + \frac{c^2}{2}\left(\cos\omega_{12}t + \cos\omega_{34}t\right) \ , \tag{3.175}$$

where it should be noted that the quantities ω_{14}, ω_{23} and ω_{34} are positive at all the values of the external field, while ω_{12} changes to negative values at the level crossing field $x_{12\,\mathrm{cross}}^{iso}$, equation (3.55), and the four observed frequencies satisfy the two sum rules

$$\omega_{14} - \omega_{23} = \omega_0 \tag{3.176}$$

$$\omega_{12} + \omega_{34} = \omega_0 \ . \tag{3.177}$$

Figure 3.22 shows the amplitudes and absolute frequency values (in units of ω_0) of $P_{\mu_x}(t)$ as a function of the dimensionless field parameter x. In zero field, the polarisation is equally divided by the four components, two of them having zero frequency (ω_{12} and ω_{23}), while the other

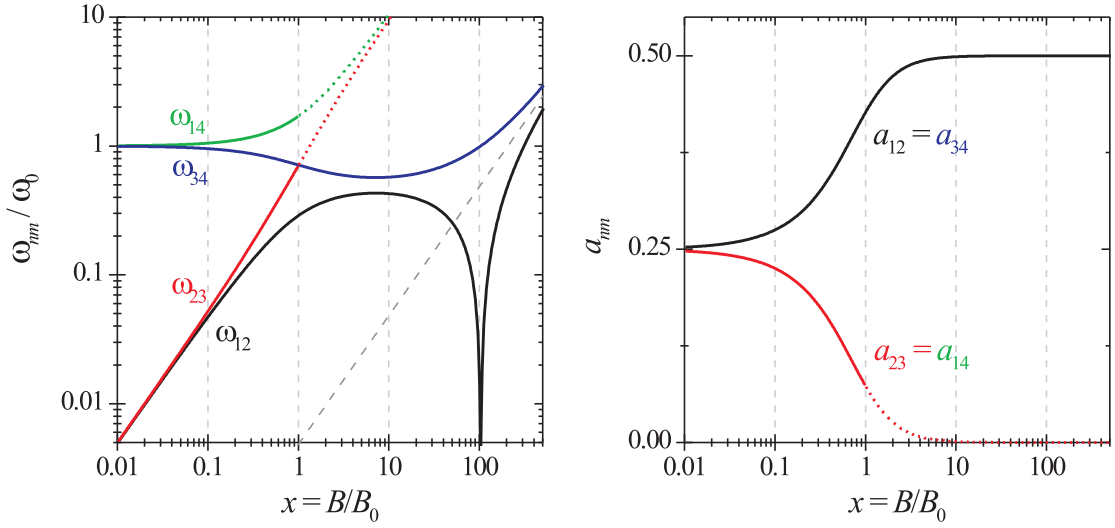

Figure 3.22: Expected amplitudes and absolute frequency values (in units of ω_0) of $P_{\mu_x}(t)$ as a function of the dimensionless field parameter x for an isotropic muonium state in transverse-field geometry. The dotting indicates a region where that component is no longer visible. The dashed gray line follows the muon's Larmor frequency.

(ω_{34} and ω_{14}) match the hyperfine frequency. At finite fields, the signal shows quite different features depending on the magnitude of x. For $x < 0.1$, in the so-called *low field regime*, the four frequencies keep approximately the same amplitude as in zero field, but their values shift as the hyperfine interaction is perturbed by the external field; for ω_{12} and ω_{23} the relative shift is considerable, since $\Omega \sim 0$ and

$$\omega_{12} \approx \omega_{23} \approx \omega_- = \frac{\omega_0}{2}\,\delta\,x\ ; \tag{3.178}$$

ω_{12} and ω_{23} grow linearly with the field at a rate proportional to the hyperfine interaction, giving rise to a single component of amplitude 1/2 known as the *triplet muonium precession* signal. In this region, (3.175) may therefore be written in the form

$$P_{\mu_x}(t) = \frac{1}{2}\cos\omega_- t + \frac{1}{4}\left(\cos\omega_{14}t + \cos\omega_{34}t\right) \quad (x < 0.1)\ , \tag{3.179}$$

where ω_{14} and ω_{34}, which have values of the order of ω_0, slowly increase and decrease respectively with the field. For states of high hyperfine interaction, these frequencies are not observed since they are not resolved experimentally. At intermediate fields, between $x \sim 0.1$ and $x \sim 1$, the weight of the low-frequency ω_{23} and the high frequency ω_{14} is successively transferred to the

low-frequency ω_{12} and high frequency ω_{34} components. Above $x \sim 1$, they cease to be observed as the *high-field regime* sets in; the signal becomes

$$P_{\mu_x}(t) = \frac{1}{2}\left(\cos\omega_{12}t + \cos\omega_{34}t\right) \quad (x > 1) \ , \tag{3.180}$$

with both frequencies presenting now a much slower dependence on the field. At $x < 10$, a region where the two observed frequencies do not vary with the field exists; beyond $x \sim 10$, ω_{12} and ω_{34} start to respectively decrease and increase linearly with the field according to

$$\omega_{12} = \omega_- - \omega_+ + \frac{\omega_0}{2} = -\omega_\mu + \frac{\omega_0}{2} \tag{3.181}$$

$$\omega_{34} = \omega_0 - \omega_- + \omega_+ - \frac{\omega_0}{2} = \omega_\mu + \frac{\omega_0}{2} \ , \tag{3.182}$$

where (3.58) and (3.59) were used. The value of ω_{12} eventually reaches zero when $\omega_\mu = \frac{\omega_0}{2}$, which corresponds to the crossing of the ω_1 and ω_2 energy levels at the value of $x^{iso}_{12\,\mathrm{cross}}$ given in (3.55). Above it, it flips sign and assumes a negative value. Its absolute value, however, will be

$$|\omega_{12}| = \omega_\mu - \frac{\omega_0}{2} \ ; \tag{3.183}$$

hence, in the high field regime, the sum rule (3.177) may be used to determine the hyperfine interaction of a paramagnetic state by the sum of the absolute values of the ω_{34} and ω_{12} frequencies below $x^{iso}_{12\,\mathrm{cross}}$, or its difference above $x^{iso}_{12\,\mathrm{cross}}$:

$$\omega_0 = |\omega_{34}| + |\omega_{12}| \quad (x > 10,\ \omega_\mu < \omega_0/2) \tag{3.184}$$

$$\omega_0 = |\omega_{34}| - |\omega_{12}| \quad (x > 10,\ \omega_\mu > \omega_0/2) \ . \tag{3.185}$$

Comparing the absolute values of ω_{34} and ω_{12}, equations (3.182) and (3.183), and taking into account the sum rule (3.185) after the crossing, one sees that the two absolute frequencies will be evenly spaced around the diamagnetic muon Larmor frequency with a splitting equal to the hyperfine interaction value at fields beyond $x^{iso}_{12\,\mathrm{cross}}$. This feature is most striking whenever diamagnetic states are formed in addition to muonium states, since in a power Fourier spectrum the three corresponding lines (the Larmor diamagnetic precession, see appendix A or Section **??** ahead, and the two paramagnetic frequencies) will move solidary as the field is increased. When the paramagnetic state is in this situation, the *Paschen-Back regime* is said to have been attained. That characteristic splitting is shown in Figure 3.23, where the field dependence of the four frequencies in a power Fourier spectrum throughout the successive regions of x is depicted.

As a last remark, it must be referred that care should be taken when analysing plots as a function of the reduced field x such as those in Figure 3.22. In particular, the actual fields

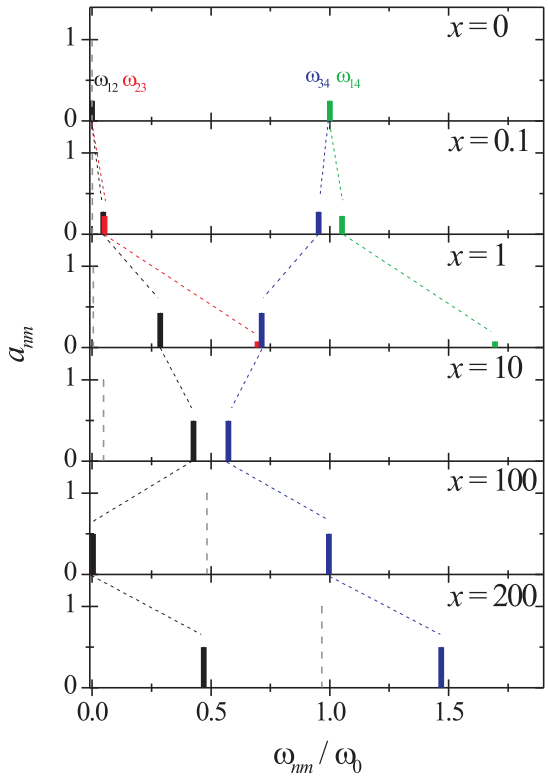

Figure 3.23: Fourier field dependence of the four precession components observed for an isotropic muonium state. The relative position and amplitude of each line is represented in the three different field regions (low field, high-field and Paschen-Back regime) usually defined in magnetic resonance.

at which the transition from the low field ($x \ll 1$) to the high field ($x \gg 1$) regime operates depends strongly on the hyperfine constant of the state under consideration. In fact, for atomic muonium states, whose hyperfine constant lies in the GHz range, B_0 is of the order of 0.1 T; the decoupling of the hyperfine interaction is only attained in fields of a few tesla, which are hard to obtain experimentally. The investigation of this type of states is thus normally performed in the low field regime, using the triplet precession signal to determine the hyperfine constant from (3.178). In the case of molecular radicals, B_0 is only several tens of gauss, and the high-field regime is fully reached at fields of some perfectly attainable kG; for these states, the hyperfine interaction may be accurately measured in the high-field regime through the sum-rules (3.184) and/or (3.185). Finally, shallow states are almost always in the high-field regime, since for them B_0 is less than a gauss. Transverse-field measurements are mostly performed in the Paschen-Back regime, where (3.185) holds and the time spectrum shows a slow beating pattern due to the superposition of the close ω_{12} and ω_{34} components.

Longitudinal-field geometry

In longitudinal-field geometry, the spin operators involved in the computation of the precession amplitudes correspond to $\hat{\sigma}_{\mu_z}$, since the initial polarisation and the observation direction lie in the direction of the externally applied field:

$$\vec{P}_\mu(0).\hat{\vec{\sigma}}_\mu = \hat{z}.\hat{\vec{\sigma}}_\mu = \hat{\sigma}_{\mu_z} \tag{3.186}$$

$$\hat{\vec{\sigma}}_\mu.\hat{r} = \hat{\vec{\sigma}}_\mu.\hat{z} = \hat{\sigma}_{\mu_z} \ . \tag{3.187}$$

The hamiltonian eigenvalues and eigenstates are of course the same as those used in the case of transverse fields; only two of the polarisation components have non-zero amplitudes, namely the non-oscillating component and the ω_{24} frequency:

$$a_0^z = 1 - 2\,s^2\,c^2 = \frac{1+2x^2}{2(x^2+1)} \tag{3.188}$$

$$a_{24}^z = 2\,s^2\,c^2 = \frac{1}{2(x^2+1)} \quad \longrightarrow \quad \omega_{24} = 2\Omega + \omega_0 = \omega_0\sqrt{x^2+1} \tag{3.189}$$

The time dependence of the muon polarisation of an isotropic paramagnetic state in longitudinal fields is then rather simpler than in transverse fields, assuming the expression

$$P_{\mu_z}(t) = \frac{1+2x^2}{2(x^2+1)} + \frac{1}{2(x^2+1)}\,\cos\omega_{24}t \ . \tag{3.190}$$

For states having a large hyperfine constant, though, the oscillating component is often not resolved, being averaged to zero, and the μSR signal is reduced to a residual static polarisation given by a_0^z.

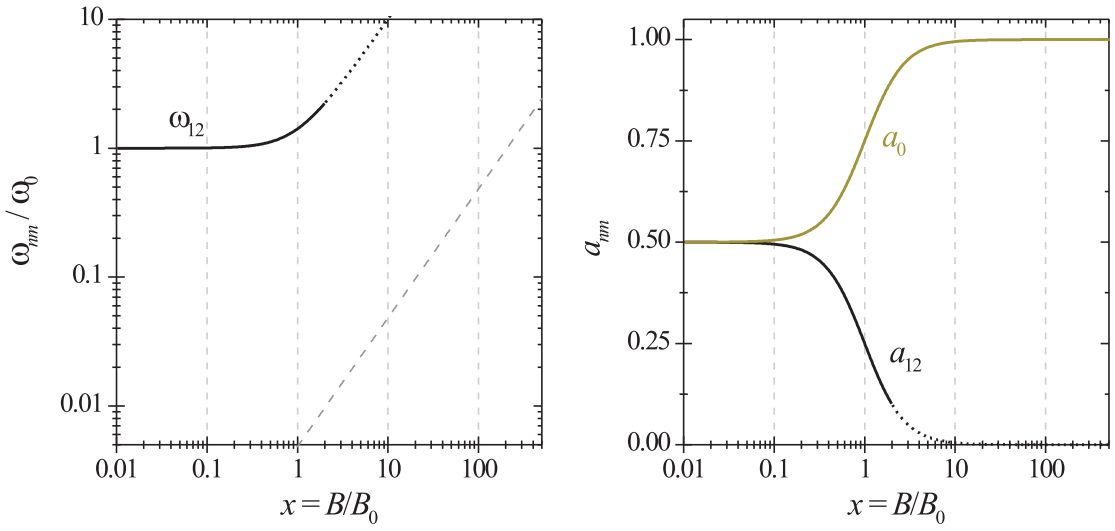

Figure 3.24: Expected amplitudes and absolute frequency values (in units of ω_0) of $P_{\mu_z}(t)$ as a function of the dimensionless field parameter x for an isotropic muonium state in longitudinal-field geometry.

The field dependence of the LF signal is shown in Figure 3.24, again as a function of x. At zero field, the total amplitude is divided by both components, with the oscillating one having a frequency ω_0. This is consistent with the description of the zero-field signal in transverse-field geometry, where half the total amplitude was ascribed to a zero-frequency component (the ω_{12} and ω_{23} frequencies) and the other half to a frequency with the hyperfine interaction (the ω_{14} and ω_{34} frequencies). As the field increases from $x > 0.1$, the amplitude of the non-oscillating term is incremented at the expense of the oscillating one, reaching the full polarisation value at the onset of the high-field regime, $x > 1$. This behaviour, termed *repolarisation*, expresses the gradual decoupling of the hyperfine interaction by the applied field towards a situation in which the muon retains its fully polarised initial state. In fact, assuming that the muon binds to unpolarised electrons upon Mu formation, the initial spin state of the $(\mu^+ - e^-)$ system in LF geometry, expressed in the same quantisation axis as the hamiltonian, will be an equal mixture of the $|\alpha_\mu \alpha_e\rangle$ and $|\alpha_\mu \beta_e\rangle$ individual spin states. Since the second one is not an eigenvector of the Mu hamiltonian at the lower fields, the $(\mu^+ - e^-)$ spin state will evolve with time, departing from

its initial value[36]. As the field increases, however, the same $|\alpha_\mu\beta_e\rangle$ state eventually becomes an eigenstate of the Mu hamiltonian, and the $(\mu^+ - e^-)$ spin state quits its time-dependent behaviour. The repolarisation of the non-oscillating component of the muon polarisation with the applied field may be used to estimate the hyperfine interaction of the paramagnetic $(\mu^+ - e^-)$ state just by measuring the field at which that component has completed half-way of its total rise, since that occurs precisely at $x = 1$. Although this is a feasible way of determining the hyperfine interaction, it is seldomly used, since any perturbation to the hamiltonian (even a dynamical one) will drastically reduce the zero-field value of the non-oscillating polarisation, as it is referred in the next paragraphs.

$\vec{P}_\mu(t)$ of axially symmetric muonium states

Transverse-field geometry

For axially symmetric muonium states described by the hamiltonian (3.69), the evaluation of the precession amplitudes for a generic orientation of the symmetry axis in the same way as what was done for isotropic states yields now non-zero values for all the possible transitions. Even the non-oscillating amplitude is in general different from zero, since the enhanced mixture of basis states in the hamiltonian's eigenvectors, equation (3.72), produces eigenvectors which may no longer orthogonal be to the initial spin state of the $(\mu^+ - e^-)$ system. The transverse-field muon polarisation of an axially symmetric muonium state is therefore written in the quite generic form

$$\begin{aligned} P_{\mu_x}(t) = a_0^x \quad &+ \quad a_{12}^x \cos\omega_{12}t + a_{13}^x \cos\omega_{13}t + a_{14}^x \cos\omega_{14}t \\ &+ \quad a_{23}^x \cos\omega_{23}t + a_{24}^x \cos\omega_{24}t + a_{34}^x \cos\omega_{34}t \ . \end{aligned} \tag{3.191}$$

Figure 3.25 shows the absolute values of the precession frequencies and amplitudes of (3.191) as a function of the dimensionless field x for the situation considered in Figure 3.20. Depending on the orientation of the hyperfine symmetry axis, one may have several frequencies at zero field, corresponding to transitions between the non-degenerate hyperfine levels which are made possible by the perturbative effect of the anisotropy on the hamiltonian. Just as

[36] We should make clear that the situation in transverse field is quite different; the initial spin-state of the muon-electron system is *never* an eigenstate of the hamiltonian due to the fact that the muon is polarised in a direction *perpendicular* to the quantisation axis of the hamiltonian. Because of that, no static components exist in the TF signal of an isotropic state.

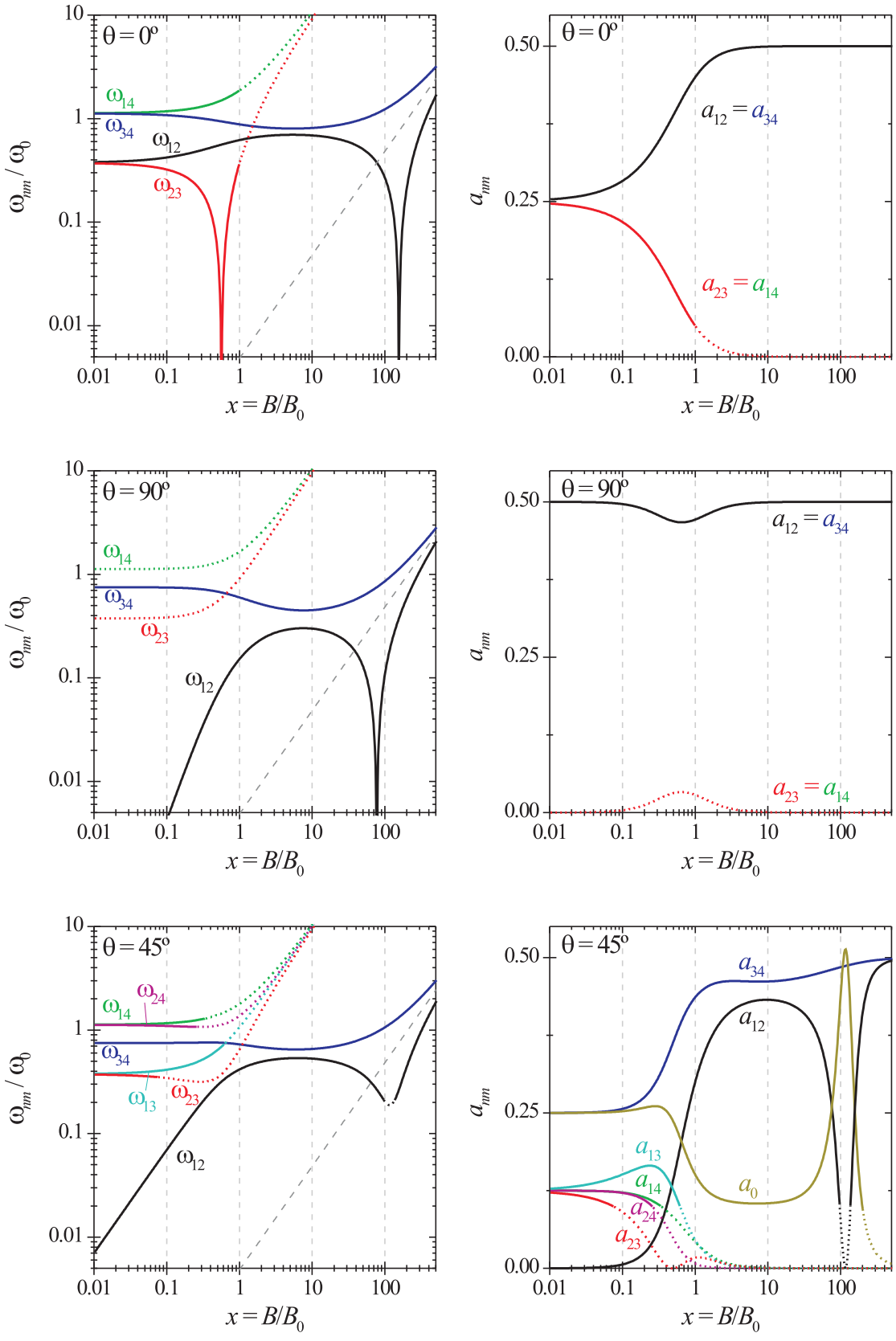

Figure 3.25: Expected amplitudes and absolute frequency values (in units of ω_0) of $P_{\mu_x}(t)$ as a function of the dimensionless field parameter x for the axially symmetric muonium state of Figure 3.20 in transverse-field geometry.

in the isotropic muonium case, it is possible to consider the existence of a low-field region at $x < 0.1$, where a maximum number of frequencies is observed for each orientation. Likewise, the amplitudes of the frequencies ω_{12} and ω_{34} grow at the cost of the other components over an intermediate field region up to $x \sim 1$, were now low-field level crossings may exist (as for $\theta = 0$), and a non-oscillating component appears for intermediate orientations. The high-field regime onsets at $x \sim 1$; again, a region at $x < 10$ exists where ω_{12} and ω_{34} are field independent for all orientations, but after that, near the ω_1-ω_2 level crossing region, drastic changes relative to the isotropic case for $0 < \theta < \pi/2$ occur. This happens as a result of the avoided level crossing between the two near-degenerate states $|1\rangle$ and $|2\rangle$, implying the finiteness of ω_{12} and the decrease of ω_{12}'s transverse-field amplitude to zero due to the mixture of those states, from which a transverse-field non-oscillating amplitude develops also. Using the non-degenerate states (3.83)-(3.86) and the energy gap (3.87) in the region of the avoided crossing, it's easy to show that the ω_{12} and non-oscillating polarisation components will be given by[37]

$$a_0^x = 2\, s_\chi^2\, c_\chi^2 = \frac{1}{2(\chi^2+1)} \tag{3.192}$$

$$a_{12}^x = \frac{1}{2}\left(c_\chi^2 - s_\chi^2\right)^2 = \frac{\chi^2}{2(\chi^2+1)} \quad \longrightarrow \quad \omega_{12} = \pm\, \omega_G \sqrt{\chi^2+1} \tag{3.193}$$

for $x \sim x_{12\,\mathrm{cross}}^{ax}$. Above the avoided level crossing, $x > 100$, the system enters the Paschen-Back regime, and the absolute values of the two observed paramagnetic lines ω_{12} and ω_{34} follow the muon's Larmor frequency splitted by the hyperfine interaction value just as in the isotropic muonium case.

The high-field splitting of the ω_{12} and ω_{34} frequencies depends on the orientation of the hyperfine symmetry axis relative to the field, and may be used to experimentally distinguish isotropic muonium states from states possessing axial symmetry. In high fields, and away from the avoided level crossing, the off-diagonal terms of the hamiltonian's matrix representation for an axially symmetric state, equation (3.69), may be neglected relative to the diagonal ones,

[37] We remember that according to the level numbering scheme shown in Figure 3.20, ω_{12} is positive before the avoided crossing and negative after.

leading directly to the high-field energy levels and eigenstates

$$\omega_1 = \omega_- + \frac{\omega_0}{4} + \frac{\omega_c}{4} \quad ; \quad |1\rangle = |\alpha_\mu \alpha_e\rangle \tag{3.194}$$

$$\omega_2 = \omega_+ - \frac{\omega_0}{4} - \frac{\omega_c}{4} \quad ; \quad |2\rangle = |\beta_\mu \alpha_e\rangle \tag{3.195}$$

$$\omega_3 = -\omega_- + \frac{\omega_0}{4} + \frac{\omega_c}{4} \quad ; \quad |3\rangle = |\beta_\mu \beta_e\rangle \tag{3.196}$$

$$\omega_4 = -\omega_+ - \frac{\omega_0}{4} - \frac{\omega_c}{4} \quad ; \quad |4\rangle = |\alpha_\mu \beta_e\rangle \ . \tag{3.197}$$

The high-field non-zero amplitudes and frequencies are immediately given by (note that $\omega_+ - \omega_- = \omega_\mu$)

$$a_{12}^x = \frac{1}{2} \ \longrightarrow \ \omega_{12} = -\omega_\mu + \frac{\omega_0 + \omega_c}{2} \tag{3.198}$$

$$a_{34}^x = \frac{1}{2} \ \longrightarrow \ \omega_{34} = \omega_\mu + \frac{\omega_0 + \omega_c}{2} \ , \tag{3.199}$$

and again a sum rule identical to (3.184) and (3.185) exists:

$$\omega_0 + \omega_c = |\omega_{34}| + |\omega_{12}| \quad (\omega_\mu < \tfrac{\omega_0+\omega_c}{2}) \tag{3.200}$$

$$\omega_0 + \omega_c = |\omega_{34}| - |\omega_{12}| \quad (\omega_\mu > \tfrac{\omega_0+\omega_c}{2}) \ . \tag{3.201}$$

With this rule, and knowing that

$$\omega_0 + \omega_c = 2\pi \left(A_{iso} + \frac{D}{2} \left(3\cos^2\theta - 1 \right) \right) \ , \tag{3.202}$$

it is possible to determine the hyperfine constants A_{iso} and D and the crystalline direction of the hyperfine interaction's symmetry axis by measuring the high-field angular dependence of the ω_{12} and ω_{34} frequencies.

Longitudinal-field geometry

Like what happens in the case of transverse field geometry, all possible transitions plus a non-oscillating component will in general be visible in the longitudinal field muon polarisation. Figure 3.26 depicts what is expected again for the situation of Figure 3.20, but now in longitudinal field geometry. In zero field, the non-oscillating component of the polarisation depends strongly on the orientation, departing from 50% of the full polarisation at $\theta = 0$ to zero at $\theta = \pi/2$. The decoupling of the hyperfine interaction in high fields is clearly observed as that component repolarises to unity at $x > 1$ for all orientations, but deep into the high-field regime, at the ω_1-ω_2 avoided crossing for the intermediate orientations $0 < \theta < \pi/2$, the non-oscillating

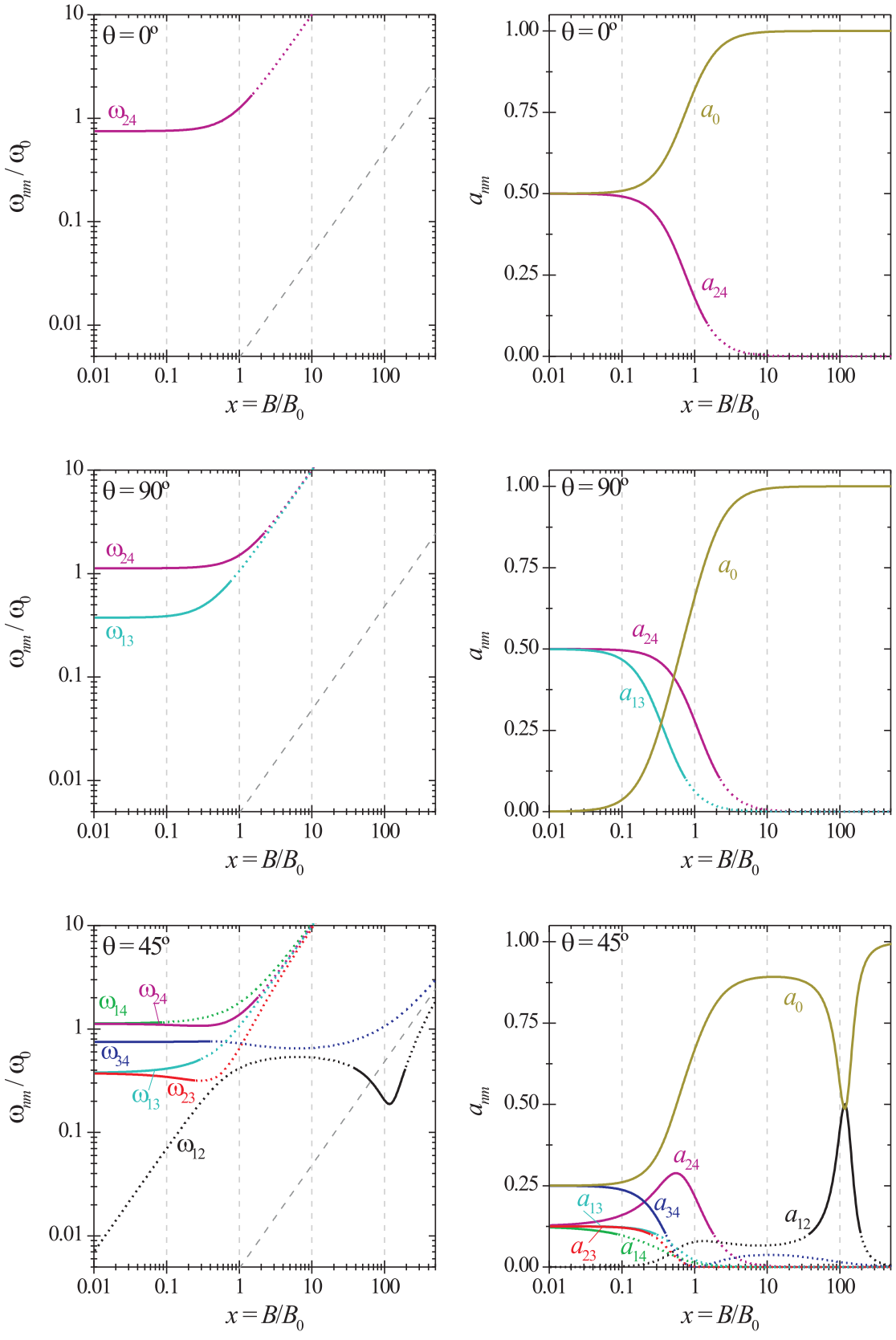

Figure 3.26: Expected amplitudes and absolute frequency values (in units of ω_0) of $P_{\mu_z}(t)$ as a function of the dimensionless field parameter x for the axially symmetric muonium state of Figure 3.20 in longitudinal-field geometry.

component presents a dip from nearly 100% to 50% as states $|1\rangle$ and $|2\rangle$ mix. The dip occurs in an orientation-dependent field given by (3.74), and is accompanied by the appearance of the ω_{12} frequency which, at the avoided crossing, matches the ω_1-ω_2 minimum gap ω_G, equation (3.89). At that field, the full amplitude is *evenly divided* between the non-oscillating component and the ω_{12} component. This is easily seen using again the non-degenerate states (3.83)-(3.86), from which one obtains in the region of the avoided crossing

$$a_0^z = 1 - 2\,s_\chi^2\,c_\chi^2 = \frac{2\chi^2+1}{2(\chi^2+1)} \tag{3.203}$$

$$a_{12}^z = 2\,s_\chi^2\,c_\chi^2 = \frac{1}{2(\chi^2+1)} \qquad \longrightarrow \quad \omega_{12} = \pm\,\omega_G\,\sqrt{\chi^2+1}\;; \tag{3.204}$$

the first expression also allows to compute the full-width at half minimum of the non-oscillating dip, leading to

$$\begin{aligned} \Delta\chi &= 2 \\ &\Downarrow \\ \Delta x &= \frac{\omega_D}{\omega_0}\,\frac{3\sin\theta\cos\theta}{2}\left(1+\frac{|\gamma_e|}{\gamma_\mu}\right) \end{aligned} \tag{3.205}$$

This dip at high-fields in LF geometry is characteristic of the ω_1-ω_2 avoided-level crossing; its position and width give direct information about the state's anisotropy in axially symmetric muonium systems, providing an experimental way to measure it if the anisotropy is not decoupled by dynamical phenomena[38].

$\vec{P}_\mu(t)$ of muoniated radicals

Transverse-field geometry

The transverse-field muon polarisation of a muoniated radical is considerably more complex than that of isolated muonium states, since the nuclear hyperfine interaction increases the total number of possible precession frequencies as a result of the level splitting it produces in the system's Breit-Rabi diagram. This is especially true in low fields ($x < 0.1$), as both the Mu and the nuclear hyperfine interactions promote the mixing of basis states in the system's eigenstates, giving rise to many non-zero oscillating components. At high-fields ($x > 1$), the

[38] Dynamical interactions with effective coupling constants larger than the anisotropic parameter D destroy the mixing effect of the anisotropy on states $|1\rangle$ and $|2\rangle$, leading in general to the disappearance or distortion of the non-oscillating dip.

field decouples those interactions, and one falls in a case similar to isotropic Mu, where the only observed frequencies correspond to ω_1-ω_2 and ω_3-ω_4 transitions. The magnetically allowed transitions in this regime imply the conservation of the nuclear magnetic spin quantum numbers M_J^p, leading to the non-zero components

$$a_{12}^x(M_J^1,\ldots) = \frac{1/2}{\prod_p 2J^p+1} \quad \longrightarrow \quad \omega_{12}(M_J^1,\ldots) = \omega_- - \Omega + s^2 \sum_p \omega_{0_N}^p \, M_J^p \tag{3.206}$$

$$a_{34}^x(M_J^1,\ldots) = \frac{1/2}{\prod_p 2J^p+1} \quad \longrightarrow \quad \omega_{34}(M_J^1,\ldots) = -\omega_- + \Omega + \omega_0 - s^2 \sum_p \omega_{0_N}^p \, M_J^p \tag{3.207}$$

where the perturbation-theory energy levels (3.114)-(3.115) for different groups of equivalent nuclei and the corresponding high-field eigenstates ($c \approx 1, s \approx 0$) were used. Hence, the two ω_{12} and ω_{34} lines are broadened in a number of components which depends on the nuclear spins and their hyperfine interactions; the component splitting, however, decreases with the applied field due to the s^2 factor, and around $x \sim 10$ all components collapse to produce two clean ω_{12} and ω_{34} components of amplitude 1/2 and frequency equal to the isotropic frequencies

$$\begin{aligned} \omega_{12} &= -\omega_\mu + \frac{\omega_0}{2} \\ \omega_{34} &= \omega_\mu + \frac{\omega_0}{2} \, . \end{aligned}$$

Similarly to the case of axially symmetric muonium, this high-field picture also fails at the ω_1-ω_2 avoided level-crossing, and an amplitude dip occurs due to the mixing of eigenstates.

Figure 3.27 depicts the field dependence of the amplitudes and frequencies expected for the muoniated radical state of Figure 3.21 in the high-field region. The evolution of the ω_{12} and ω_{34} frequencies, split in only two components by the 1/2 proton spin, shows a gradual merging of those components as the field approaches $x = 10$, beyond which the splitting is no longer visible with a finite frequency resolution. This is also clearly seen in Figure 3.28, where the field dependence is represented in terms of a Fourier diagram. The region near the ω_1-ω_2 avoided level-crossing is shown in detail in the two lower plots of Figure 3.21; one may see that the transitions involving the proton spin only become visible at the crossing, an effect that in principle could be used to measure nuclear hyperfine constants. The width of this resonance, however, is too small to be usually observed, and ends up being very difficult to make use of it in regular μSR studies.

Longitudinal-field geometry

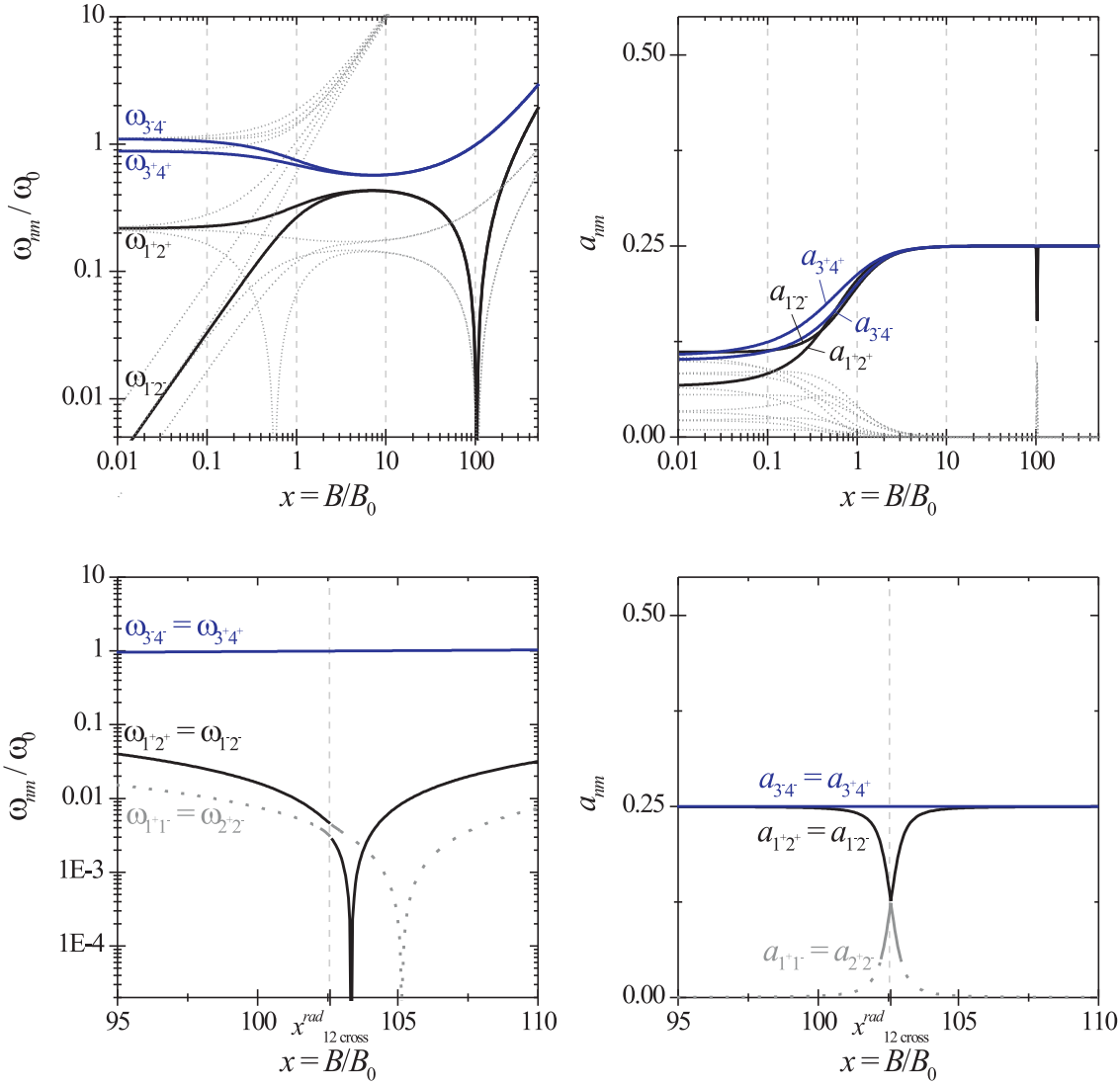

Figure 3.27: Expected amplitudes and absolute frequency values (in units of ω_0) of $P_{\mu_x}(t)$ as a function of the dimensionless field parameter x for the muoniated radical state of Figure 3.21 in transverse-field geometry. The two lower plots depict in detail the region of the ω_1-ω_2 avoided level-crossing.

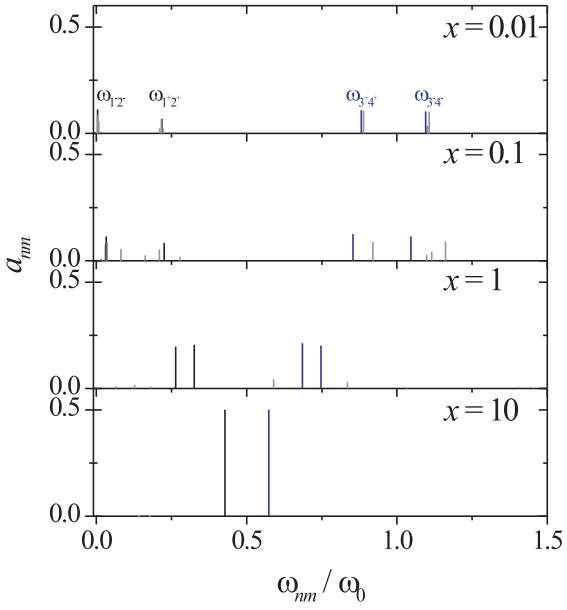

Figure 3.28: Fourier field dependence of the high-field precession components observed for the muoniated radical state of Figure 3.21. The relative position and amplitude of each line is represented in the three different field regions (low field, high-field and Paschen-Back regime) usually defined in magnetic resonance.

The muon polarisation in longitudinal-field geometry for a muoniated radical state having an isotropic hyperfine interaction is again complex at the lower fields, becoming considerably simpler in high fields as soon as the nuclear hyperfine interaction is decoupled, where it presents a repolarisation behaviour typical of an isotropic muonium state, as what may be observed in Figure 3.29. Near the avoided-level crossing, however, this behaviour breaks down due to the presence of the additional term in the hamiltonian brought by the nuclear hyperfine coupling; one finds a situation similar to what is known for an axially symmetric state, with the appearance of a dip in the non-oscillating component of the muon polarisation. The computation of amplitudes and precession frequencies at the level crossing produces a result similar to equations (3.203)-(3.205). The lower part of Figure 3.29 shows in detail the dip at the avoided crossing; here, the resonance is large enough to be observed, and its regular use for the investigation of muoniated radicals constitutes a sub-technique of μSR known as *Avoided Level Crossing Resonance* (ALCR).

Axially symmetric states in polycrystalline samples

More often than one would like, appropriate single-crystal samples are not available for μSR experiments, and polycrystalline samples in the form of pressed powder pellets have to be used alternatively. This sample casting corresponds to a random sampling of all crystalline directions relative to the fixed geometry defined by the externally applied magnetic field and the initial beam polarisation. If the paramagnetic muon states formed in the sample are isotropic, this does not constitute a problem, but if they have any anisotropy at all, the principal axis of the hyperfine tensor will assume a random orientation. Since the precession frequencies of a non-isotropic paramagnetic state depend on the orientation of the principal axis relative to the magnetic field, this implies that the polarisation signal will in general exhibit up to six distinct frequency distributions instead of the six sinusoidal frequencies detected for single-crystalline samples.

In high transverse field, the situation is nevertheless simpler, since only the ω_{12} and ω_{34} frequencies are observed. If, in addition, the hyperfine tensor has axial symmetry, they give rise to two symmetrical frequency distributions governed by the sum rules (3.200)-(3.201) and equation (3.202), where

$$\omega_c = \frac{\omega_D}{2}\left(3\cos^2\theta - 1\right)$$

goes over the full $[0, \pi[$ range of possible values for the angle θ. Hence, one may derive the shape

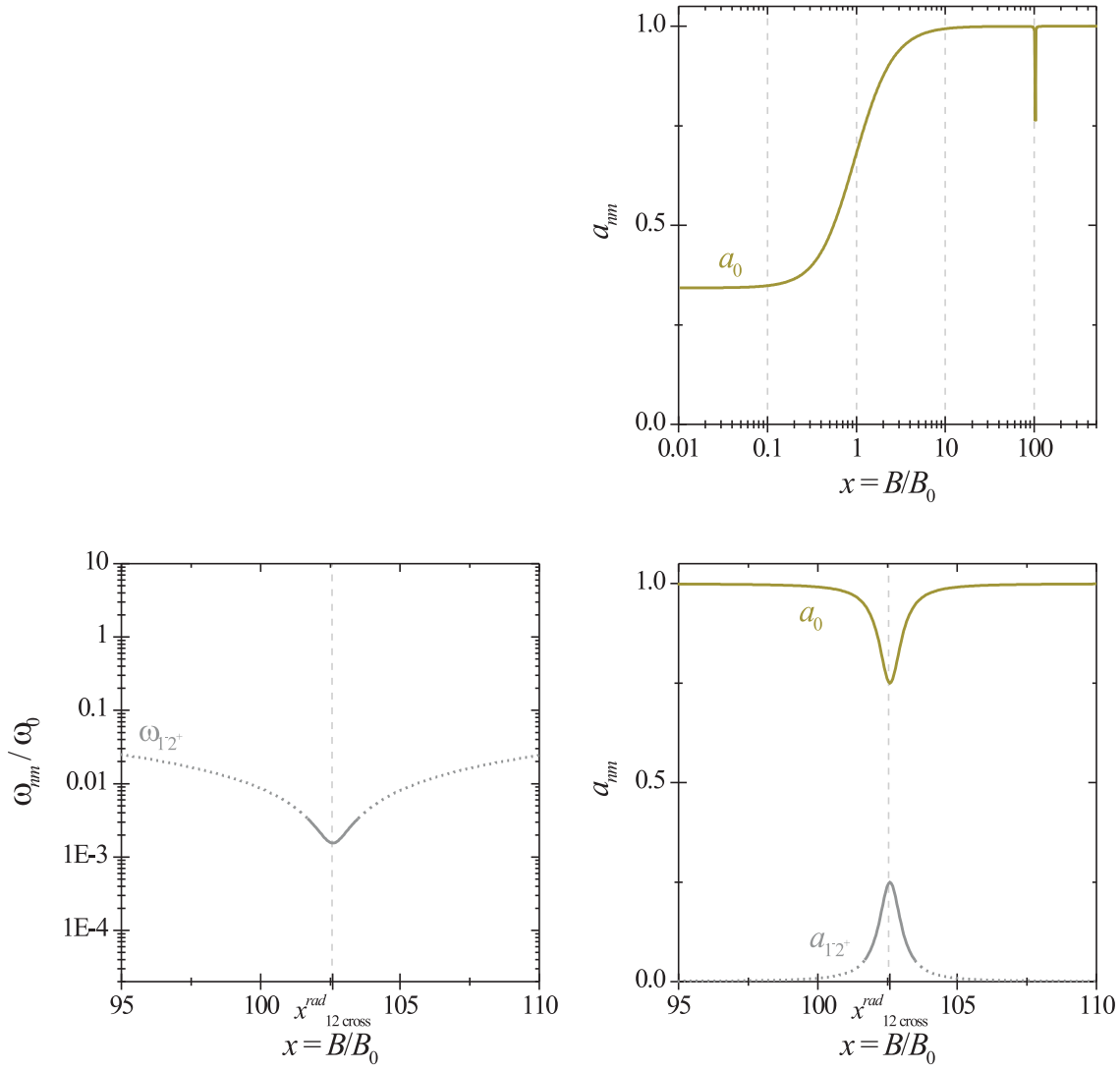

Figure 3.29: Expected amplitudes and absolute frequency values (in units of ω_0) of $P_{\mu_z}(t)$ as a function of the dimensionless field parameter x for the muoniated radical state of Figure 3.21 in longitudinal-field geometry.

of the precession frequency distribution from the splitting

$$\omega(\theta) = \omega_0 + \omega_D \ \frac{3\cos^2\theta - 1}{2} \tag{3.208}$$

taking into account the purely geometrical weight that each possible value of θ has in the overall distribution. The precession frequency distribution will thus be given by

$$\frac{dp}{d\omega} = \frac{dp}{d\theta} \ \frac{1}{\left|\frac{d\omega}{d\theta}\right|} \ , \tag{3.209}$$

where $\frac{dp}{d\theta} = \sin\theta$, and $\frac{d\omega}{d\theta}$ is easily computed from (3.208) as being

$$\frac{d\omega}{d\theta} = -3 \ \omega_D \sin\theta\cos\theta \ . \tag{3.210}$$

With a straightforward algebra manipulation using the fact that (see (3.208))

$$\cos\theta = \frac{1}{\sqrt{3}} \ \sqrt{2 \ \frac{\omega - \omega_0}{\omega_D} + 1} \ , \tag{3.211}$$

one gets

$$\frac{dp}{d\omega} = \frac{1}{\sqrt{3}} \ \sqrt{2\,\omega_D\,(\omega - \omega_0) + \omega_D^2} \ ; \tag{3.212}$$

this distribution is depicted in Figure 3.30. In this figure, it becomes apparent that for the splitting corresponding to $\theta = \pi/2$ ($\omega = \omega_0 - \omega_D/2$), which is the most probable orientation of all, two cusps where $dp/d\omega \to \infty$ exist, while for $\theta = 0$ ($\omega = \omega_0 + \omega_D$) the distribution's value remains finite at $1/(3\,\omega_D)$; also, the width of each individual line distribution scales directly with ω_D by

$$\Delta\omega = \frac{3}{4}\,\omega_D \ . \tag{3.213}$$

By way of the sum-rules (3.200)-(3.201) and the probability distribution (3.212), it is not difficult to show that the probability density function of both ω_{12} and ω_{34} distributions expressed explicitly as a function of frequency is given by

$$\frac{dp}{df}(f) = \frac{1}{\sqrt{3D\,(2(|f - f_\mu| - A_{iso}) + D)}} \ , \tag{3.214}$$

where the $f_\mu = \omega_\mu/2\pi$ is the muon Larmor frequency in non-angular units, and f is restricted to the interval $]A_{iso} - D/2, A_{iso} + D]$ [39]. It is a matter of algebra to integrate (3.214) in order to obtain the explicit time dependence of the high transverse field muon polarisation of an axially

[39] Depending on the relative signs of A_{iso} and D, this interval may have to be reversely written, *i.e.* as $[A_{iso} + D, A_{iso} - D/2[$.

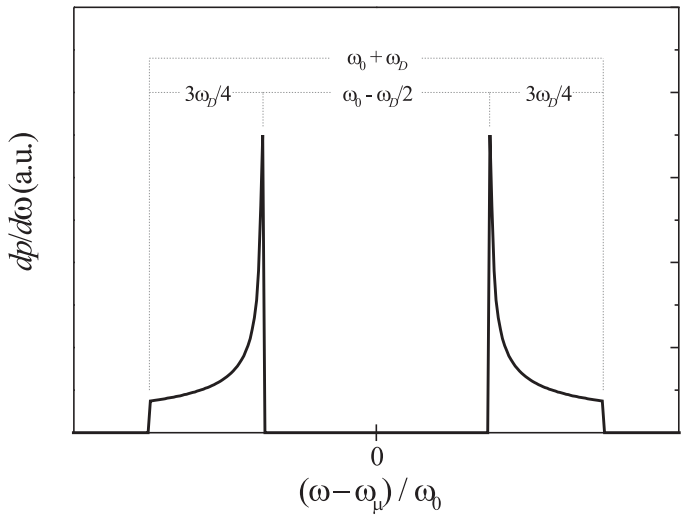

Figure 3.30: Probability distribution pattern for the precession frequencies of an axially symmetric muonium state with $\omega_D = +\omega_0/2$ in a polycrystalline environment at high fields. The frequency axis is shown in units of ω_0, and relative to the Larmor precession frequency of the muon ω_μ.

symmetric paramagnetic state; the result, which has never been published in μSR literature before, reads

$$\begin{aligned} P_{\mu_x}(t) &= \cos(-\omega_\mu t)\left(\frac{\mathrm{FC}(\sqrt{3|D|t})}{\sqrt{3|D|t}}\cos\left(2\pi\left(\frac{A_{iso}}{2}-\frac{D}{4}\right)t\right)+\right. \\ &\left.-\mathrm{sgn}(D)\frac{\mathrm{FS}(\sqrt{3|D|t})}{\sqrt{3|D|t}}\sin\left(2\pi\left(\frac{A_{iso}}{2}-\frac{D}{4}\right)t\right)\right)\ , \end{aligned} \tag{3.215}$$

where sgn means the sign function, and

$$FC(z) = \int_0^z \cos(\pi t^2/2)dt \tag{3.216}$$

$$FS(z) = \int_0^z \sin(\pi t^2/2)dt \tag{3.217}$$

are the Fresnel cosine and sine integral functions. The extension of the frequency distribution (3.214) to the case of a fully anisotropy hyperfine tensor is much more complex, and no analytic expressions exist for it neither for the time dependence of the muon polarisation. Hence, the values of these two expressions need to be obtained by a numeric integration considering all the possible orientations of the three principal axis of the hyperfine tensor.

The random orientation of the symmetry axis for an axially symmetric muonium state also affects the longitudinal field signal, and in particular the non-oscillating amplitude, since

each polarisation is located at a different field (which we recall to be located at the ω_1-ω_2 level-crossing) (left side of Figure 3.31). The resulting repolarisation curve is therefore given by

$$a_0^z(\text{powder}) = \int_0^{\pi/2} a_0^z(\theta) \sin\theta \; d\theta \; , \tag{3.218}$$

as shown in the right-hand side plot of Figure 3.31. it should be noted that the convolution of all the dips at different orientations assumes a characteristic asymmetric shape, also with a cusp, situated at

$$\begin{aligned} x_{\text{cusp}} &= \frac{1}{2\pi} \int_0^{\pi/2} x_{12\,\text{cross}}^{ax}(\theta) \; \sin\theta \; d\theta \\ &= x_{12\,\text{cross}}^{iso} \; ; \end{aligned}$$

hence, the cusp relates directly the isotropic hyperfine parameter of the state at hand, and may be used to infer its value.

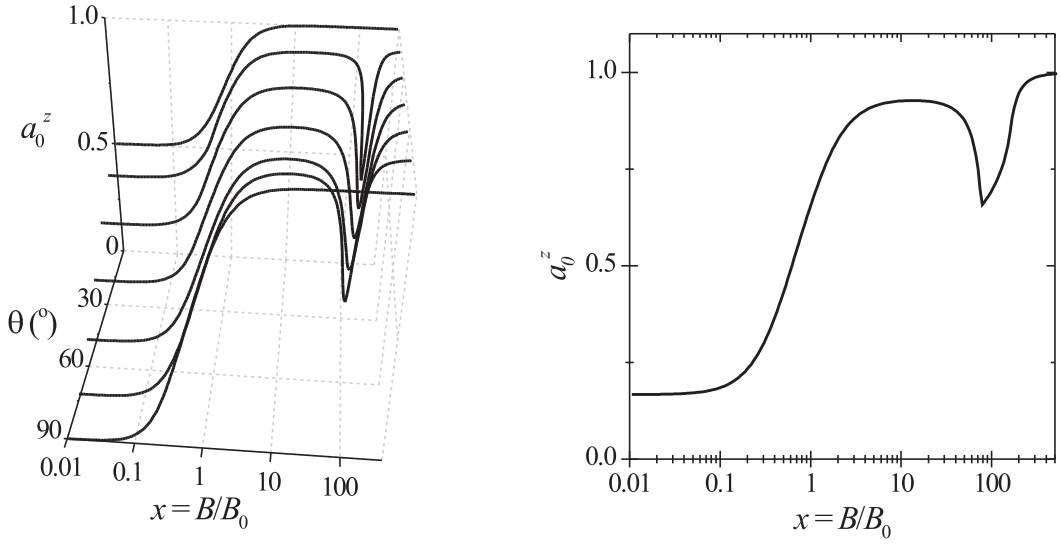

Figure 3.31: *(left)* Repolarisation curves at different orientations of the symmetry axis of an axially axially symmetric muonium state with $\omega_D = +\omega_0/2$ in a polycrystalline environment. *(right)* The weighted integral of all repolarisation curves for that same muonium state; the weight is given by the solid angle factor $\sin\theta$. The convolution of dips forms a characteristic asymmetric dip shape.

3.4.4 Spin exchange dynamics of paramagnetic states

In matter, muon states may undergo dynamical interactions with the surrounding media. As it was mentioned in Section 3.2.4, this results generally in a depolarising effect of the muon

polarisation whose time structure relates with that of the dynamical phenomena giving rise to it. In the specific case of paramagnetic states, further changes occur, namely shifts in the amplitudes, phases and frequencies of the polarisation components which depend also on the time structure of the dynamical interactions experienced by the bound muon-electron system. That time structure may either correspond to a persistent interaction, in the sense that it is a randomly repeated phenomenon, or to an irreversible interaction, if it is an unique event during each muon's lifetime. Persistent interactions may be further classified in spin exchange and cycle exchange processes, depending if they arise from the relative motion between the state and a paramagnetic species (such as free electrons or holes diffusing in the material, or static spin-carrying nuclei as muonium diffuses in the host material), or from the modulation of the hyperfine interaction driven by a cyclic change between two different states[40]. Here, we will concern ourselves only with spin exchange dynamics, and relegate the subjects of cycle exchange and irreversible interactions to the literature [85, 106].

In the simplest approach, a spin exchange process may be roughly interpreted as a magnetic field whose direction and/or magnitude randomly fluctuates according to a correlation time τ. The effect of that fluctuating magnetic field on the muon spin is primarily conveyed not by the muon Zeeman interaction, but *via* the hyperfine interaction, since the muonium electron is much more sensitive to the field in view of its significantly larger gyromagnetic ratio (*cf.* Table 3.2). The fluctuating character of the field directly depolarises the muonium electron, which in turn depolarises the muon because their spins are coupled by the hyperfine interaction. The actual relaxation rate imparted on the muon polarisation depends on the relation between τ, which commands the electron depolarisation, the hyperfine interaction ω_0 coupling both spins, and the electron Larmor frequency ω_e, which determines the magnitude of the electron's static Zeeman interaction due to the externally applied magnetic field B. Some general trends may nevertheless be guessed in asymptotic situations, namely the slow and fast spin exchange regimes. In the slow spin exchange regime, *i.e.* $1/\tau \ll \omega_0$, the muon spin follows the electron spin, reacting promptly to any changes through the hyperfine coupling; the muon depolarisation rate increases with the electron depolarisation rate, and hence with $1/\tau$. The ability to react, though, lessens with the external static field, as the electron spin gets successively more coupled to that field and less

[40] In reality, the nomenclature of 'cycle exchange' does not exist in μSR literature and is introduced here for the first time. It refers to processes in which the muon cycles between states with different configurations, such as charge exchange processes ($Mu^+ \rightleftharpoons Mu^0$ cycling) or the diffusion among inequivalent sites in a crystalline lattice.

coupled to the muon spin. In high fields, i.e. $\omega_e \gg \omega_0$, the muon depolarisation rate decreases with the field and the dynamical interaction is said to be quenched. For the fast spin exchange case, $1/\tau \gg \omega_0$, the electron spin changes too fast for the muon spin to keep up with; as $1/\tau$ and the electron depolarisation rate increase, the muon depolarisation rate decreases. In the limit of very short correlation times, the hyperfine interaction is said to be dynamically decoupled, and the muon behaves as if it was in a diamagnetic environment; therefore, no variation of the muon depolarisation rate exists with the field. Fast spin exchange is the mechanism responsible for μSR's sensitivity to dynamical phenomena occurring with correlation times much shorter than the experimental time resolution; it is analogous to the motional narrowing effect found in NMR, since the line widths in the Fourier spectrum of TF data are seen to decrease with increasing temperature.

A more realistic description of spin exchange is based on the direct quantum spin flip interaction between the muonium electron and the paramagnetic species. Considering it to be *e.g.* free electrons, a 1/2-spin species, with concentration n and average velocity v relative to the muonium state, one has for the encounter rate per unit area between muonium and electrons

$$\frac{1}{\tau} = n\ v\ . \tag{3.219}$$

While each single encounter lasts, the electronic wavefunctions of the passing free electron and of the muonium state overlap, and a finite probability that the two electrons are exchanged exists. If they are exchanged or not depends on the spatial configuration and spin of both wavefunctions, but whenever it does happen and the electrons have opposite spins, the relative populations between the hyperfine eigenvectors of the muonium system are changed. This enhances the mixing of eigenvectors of the Mu hamiltonian in the spin wavefunction of the muonium state, and as encounters repeatedly occur at random, the muon polarisation gets depolarised.

The probability that a spin flip event occurs is the *spin flip cross section*, σ_{SF}, given by [112]

$$\sigma_{SF} = \sin^2\left(\frac{\Delta}{2}\right)\ , \tag{3.220}$$

where Δ is a phase factor related with the partial-wave collision phase shifts $\delta_l^{s/t}$ of the singlet (s) and the triplet (t) configurations of the 2-electron subsystem, which may be written in terms of the interaction energies V_s and V_t by the time integral [112, 122]

$$\Delta = -\frac{1}{\hbar}\int (V_s - V_t)\, dt\ . \tag{3.221}$$

A *spin non-flip cross section*, σ_{NF}, may also be defined using this parameter,

$$\sigma_{NF} = 1 - \sigma_{SF} = \cos^2\left(\frac{\Delta}{2}\right) \ , \tag{3.222}$$

but its existence has been shown not to affect the muon polarisation whenever the distribution of collision instants is Poissonian[41] [112, 113, 115]. In this situation, spin exchange may be treated as if all encounters are of spin flip type and occurring at a reduced rate [112]

$$\lambda_{SF} = \frac{1}{\tau}\,\sin^2\left(\frac{\Delta}{2}\right) = n\,v\,\sigma_{SF} \ ; \tag{3.223}$$

this is the effective rate which will rule the spin exchange process and the muon polarisation. Its determination may yield important information about dynamical properties of the scattering species; for instance, λ_{SF} is proportional to the electrical conductivity in semiconductors due to the movement of charge carriers (electrons or holes), or to the muonium slowing down time after the charge exchange regime in paramagnetic gases [112, 117].

The first theoretical treatment of the effects of spin exchange in the μSR signal was performed by Nosov and Yakovleva [82, 83] and Ivanter and Smilga [52, 53]. These authors modelled the dynamics with a phenomenological parameter ν related with the relaxation rate of the muonium *electron's* polarisation. They start by describing the muonium polarisation in terms of the equations of motion mentioned in the last section, equation (3.157),

$$\dot{\mathbf{P}}(t) = \mathbf{Q}\ \mathbf{P}(t) \ ,$$

and postulate an exponential decrease of the electronic components with rate ν:

$$\vec{P}_e(t) \sim e^{-\nu t} \ . \tag{3.224}$$

This behaviour is forced on $\vec{P}_e(t)$ quite easily if the time derivatives of all polarisation components involving the electron ($\vec{P}_e$ and the mixed polarisations $P_{\alpha\beta}$) are in each instant proportional to a negative constant times their own values,

$$\dot{P}_j(t) = \left[\mathbf{Q}\ \mathbf{P}(t)\right]_j - 2\,\nu\,P_j(t) \ , \ j = 4, \ldots, 15 \ , \tag{3.225}$$

[41] It should nonetheless be made clear that if the distribution of collision instants is not random, or if the scattering species is polarised, the spin non-flip cross section may influence the μSR signal. See [118] and [117, **?**] respectively for the effects of non-randomness and the polarisation of the scattering species in the μSR signal.

where the appropriate constant is straightly found to be $2\,\nu$[42]. Given an electronic depolarisation rate ν, one just needs therefore to solve (3.157) using an accordingly modified matrix $\mathbf{Q}^{NY}$. Although it remains real, $\mathbf{Q}^{NY}$ is no longer antisymmetric, and because of that its eigenvalues will in general be three *negative* reals rather than zeros (non-oscillating components) plus six conjugated pairs of *negative* real part rather than pure imaginary numbers (oscillating components):

$$D_{kk} = -\lambda_k \qquad \text{(3 components)} \tag{3.226}$$

$$D_{kk} = -\lambda_k \pm i\,\omega_k \qquad \text{(6 components)} \tag{3.227}$$

Non-zero relaxations and non-zero initial phases may therefore appear as a general rule in all the components of $\mathbf{P}(t)$, equation (3.160),

$$\begin{aligned} P_j(t) &= \sum_{k=1}^{15}\sum_{l=1}^{15} U_{jk}\; e^{D_{kk}t}\; U_{kl}^{-1}\; P_l(0) \\ &= \sum_{i=1}^{3} a_{0i}^{(j)}\, e^{-\lambda_i t} \;+ \sum_{i=1}^{6} a_i^{(j)}\, e^{-\lambda_i t}\cos(\omega_i t + \phi_i^{(j)}) \;, \end{aligned} \tag{3.228}$$

with the now separated non-oscillating amplitudes

$$a_{0i}^{(j)} = \sum_{l=0}^{15} U_{jk} U_{kl}^{-1}\, P_l(0) \;, \tag{3.229}$$

where k satisfies $\mathrm{Im}\{D_{kk}\} = 0$, and

$$\lambda_i = -\mathrm{Re}\{D_{kk}\} \tag{3.230}$$

for all k. Figure 3.32 shows demonstrative results computed with Nosov and Yakovleva's theory relative to the polarisation an isotropic muonium centre undergoing spin exchange dynamics in longitudinal field geometry.

More sophisticated and fundamental approaches of spin exchange were introduced by Turner and Snider [131], Celio and Meier [16], and Senba (see [121] and references therein) to

[42] The factor 2 here may seem confusing, but it is in fact necessary in order to have the electron polarisation proportional to $e^{-\nu t}$. Just as (3.157) is analogous to the equations of two coupled harmonic oscillators, also (3.225) corresponds to the equations of two coupled *damped* oscillators. In the description of the damped oscillator, a dissipative component $\gamma\dot{x}$ is added to the equation $\ddot{x} + \omega_0^2\, x = 0$ of the harmonic oscillator; the resulting expression may be cast as $\dot{x} = -\omega_0^2 \int x dt - \gamma x$ (compare with equation (3.225)), whose oscillating solution is $x(t) = A\, e^{-\gamma/2\, t}\cos(\sqrt{\omega_0^2 - \gamma^2/4}\;\, t + \phi)$. The exponential constant is thus proportional to half the damping constant γ.

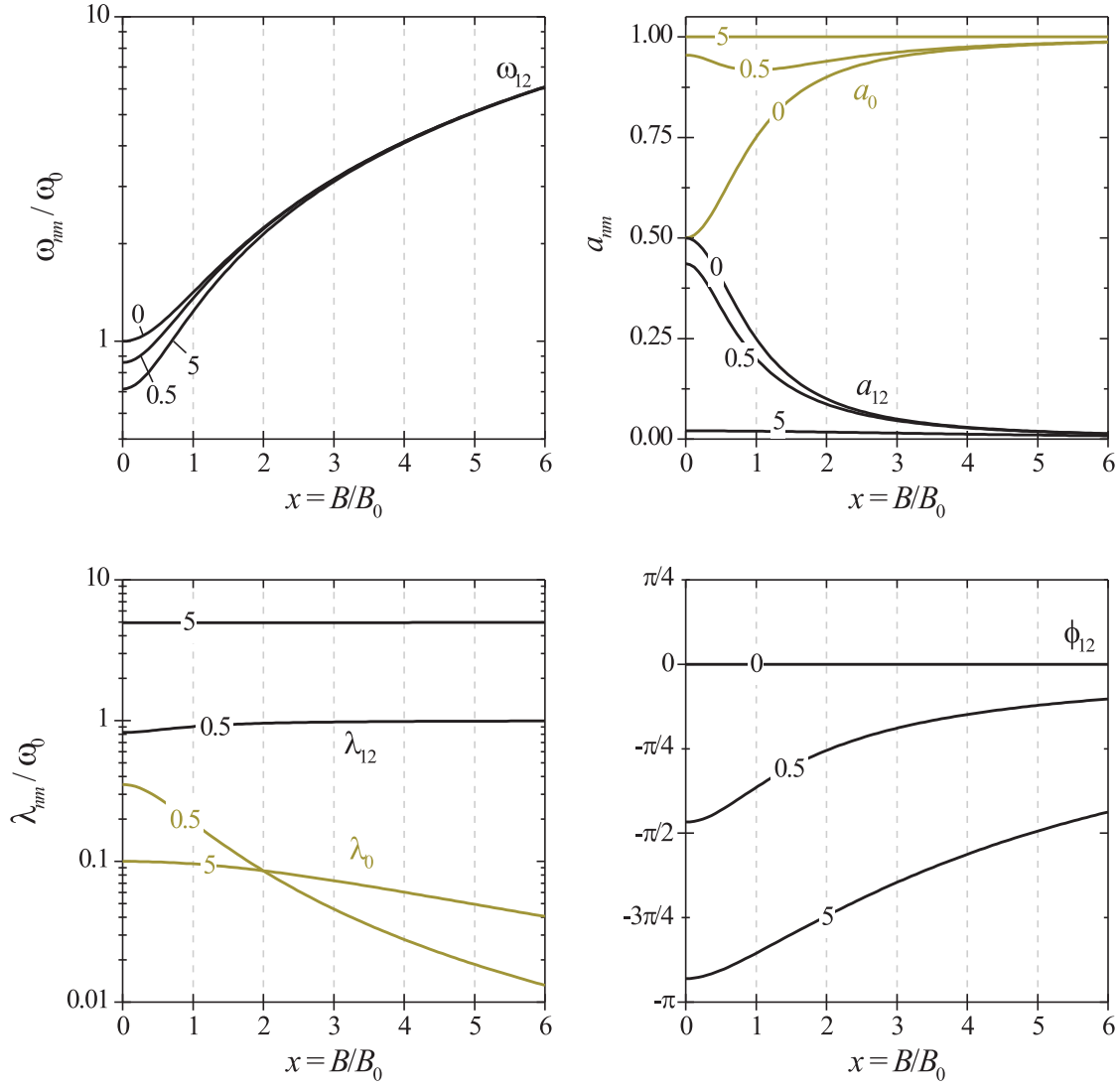

Figure 3.32: LF polarisation components of an isotropic muonium state undergoing spin exchange dynamics, as obtained using the Nosov-Yakovleva's theory. Three distinct situations are shown, depending on the ratio ν/ω_0 (indicated as simple numbers): absence of dynamics (0), slow spin-flip regime (0.5) and fast spin-flip regime (5).

describe the muon polarisation in terms of the quantum-mechanical spin-flip cross section σ_{SF}. Turner and Snider used a method based on the Boltzmann equation for the spin degrees of freedom of a spin-colliding system, while Celio and Meier solved a master equation for muonium subjected to a fluctuating magnetic field, and Senba developed the so-called *time-ordered stochastic method*. Senba's procedure, which is based in a step-by-step description of random, Poisson-distributed spin flipping encounters averaged over time and the total number of collisions, has been applied by that author to investigate the connection between the muon spin relaxation rates, initial amplitudes, transverse-field frequencies and transverse-field phases observed in μSR with the spin-flip rate λ_{SF} in a multitude of situations differing in the spin flip rate range, the μSR geometry configuration and the magnitude (and symmetry) of the hyperfine interaction tensor. We do not go into many details here, since his bibliography is extensive and the actual deduction of some of the final results is situation-dependent, but we nevertheless summarise the general expressions he obtains for the most important cases and produce very brief comments. We also leave out of this discussion the transition regime between fast spin exchange and slow spin exchange, since its analysis is considerably more complex, and has only recently been addressed in the literature.

Fast spin exchange

Transverse field geometry

When a muonium state is undergoing spin exchange with a paramagnetic species at a rate much larger than any of its hyperfine periods, the hyperfine interaction is dynamically decoupled. The muonium state behaves therefore as a diamagnetic positive muon, which in transverse field leads to a muon polarisation signal composed by a single precession with frequency ω_T and relaxation λ_T given by ($\lambda_{SF} \gg \omega_{nm}$)

$$\omega_T = -\lambda_{SF}^2 \sum_{n,m=1}^{4} \frac{\omega_{nm}}{\lambda_{SF}^2 + \omega_{nm}^2}\, a_{nm}^{+} \tag{3.231}$$

$$\lambda_T = \lambda_{SF} \sum_{n,m=1}^{4} \frac{\omega_{nm}^2}{\lambda_{SF}^2 + \omega_{nm}^2}\, a_{nm}^{+} \ , \tag{3.232}$$

where ω_{nm} are the transition frequencies of the muonium state, and a_{nm}^{+} is the TF amplitude

$$a_{nm}^{+} = \frac{1}{4}\, \langle n|(\vec{P}_{\mu}(0).\hat{\vec{\sigma}}_{\mu})|m\rangle\, \langle m|\hat{\sigma}_{\mu_+}|n\rangle \ , \tag{3.233}$$

$\hat{\sigma}_{\mu_+}$ being the raising ladder operator for the muon's spin. The dependence of ω_T and λ_T on the field and spin-flip rate is depicted in Figure 3.33 for an isotropic muonium state and an axially symmetric state. It should be noted that the absolute value of ω_T rapidly approaches the muon Larmor precession frequency with increasing spin-flip rate, while the relaxation λ_T tends to zero *via* an asymptotic behaviour given by

$$\lambda_T \rightarrow \frac{\omega_0^2}{2\lambda_{SF}} \tag{3.234}$$

i.e., the relaxation becomes field independent and scales with the inverse of λ_{SF}; also, at high fields it can be shown that λ_T assumes the limiting value λ_{SF}, corresponding to the absolute decoupling of the hyperfine interaction.

Longitudinal field geometry

In longitudinal field geometry, the muon polarisation will consist in a full polarisation signal, in accordance with the signal produced by a diamagnetic positive muon, but damped with a relaxation rate

$$\lambda_L = \lambda_{SF} \sum_{n,m=1}^{4} \frac{\omega_{nm}^2}{\lambda_{SF}^2 + \omega_{nm}^2} \; a_{nm}^z \; , \tag{3.235}$$

where $a_{nm}^z = \vec{a}_{nm}.\hat{z}$ is the LF amplitude corresponding to the transition nm. Figure 3.34 shows the field and spin-flip rate dependence of (3.235) for an isotropic muonium state and an axially symmetric one. One feature clearly visible in that figure is the field dependence at high fields, which can be shown to exhibit a $1/B^2$ character; this fact is often used to identify the fast regime of spin exchange dynamics, together with the expected lowering of the LF relaxation rate as the spin-flip rate λ_{SF} increases.

Slow spin exchange

Transverse field geometry

In the slow spin exchange regime, the μSR TF signal is considerably more complex than in the fast regime, since depending on the external field, all the allowed spin precessions ω_{nm} might be resolved. In general, for an isotropic or axially symmetric muonium state, the four precession frequencies ω_{12}, ω_{23}, ω_{34} and ω_{14} will exhibit field-dependent relaxations given by

$$\lambda_{12} = \lambda_{34} \;=\; \frac{\lambda_{SF}}{4}\left(3 - \frac{x}{\sqrt{1+x^2}}\right) \tag{3.236}$$

$$\lambda_{23} = \lambda_{14} \;=\; \frac{\lambda_{SF}}{4}\left(3 + \frac{x}{\sqrt{1+x^2}}\right) \; , \tag{3.237}$$

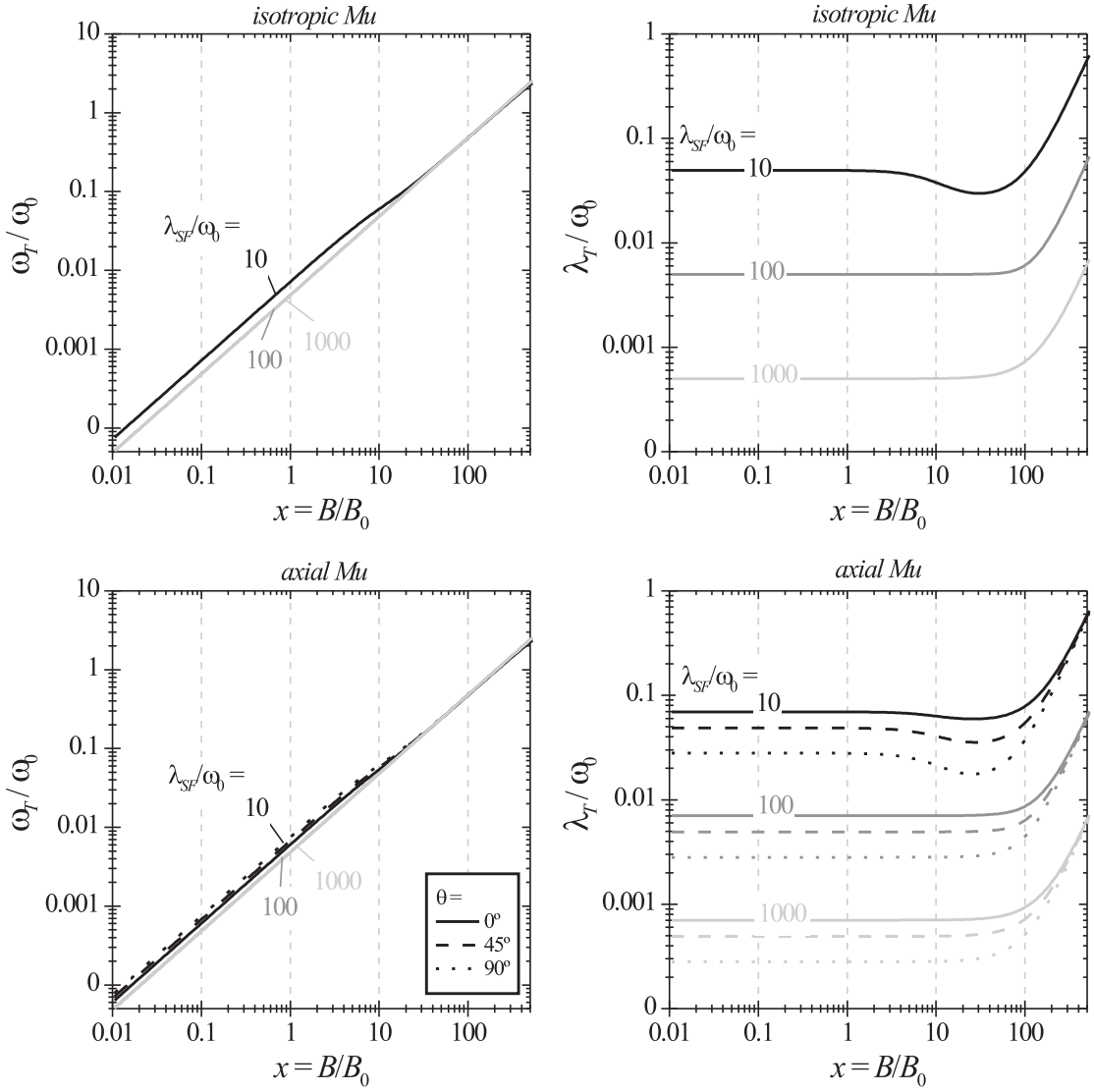

Figure 3.33: Apparent TF diamagnetic frequency and corresponding relaxation rate in the fast spin exchange regime for an isotropic muonium state, and an axially symmetric muonium state with $D = A_{iso}/2$.

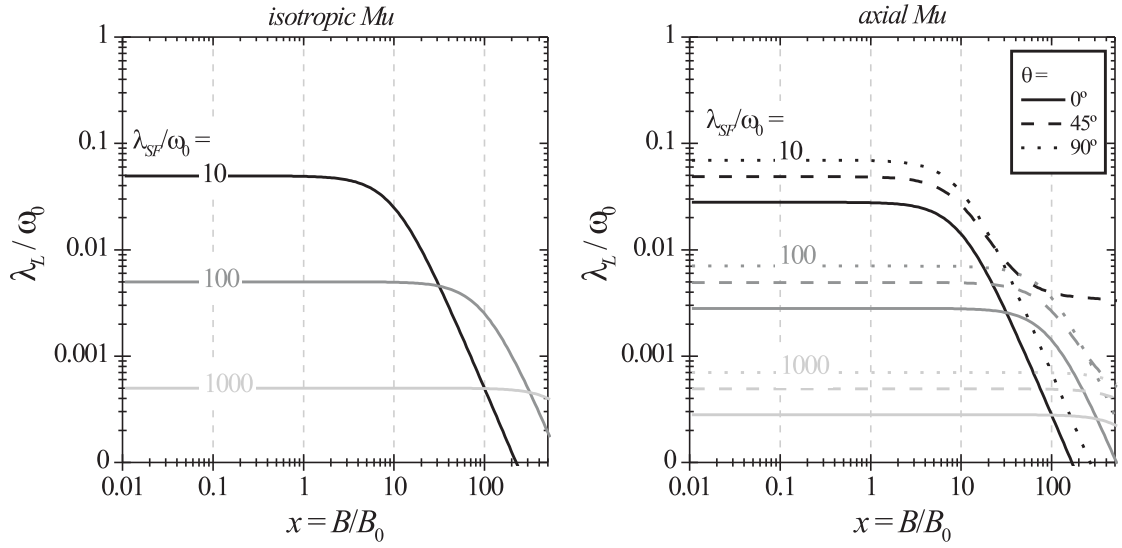

Figure 3.34: LF relaxation for the non-oscillating polarisation in the fast spin exchange regime for an isotropic muonium state, and an axially symmetric muonium state with $D = A_{iso}/2$.

where x is the reduced field parameter defined in (3.50). The corresponding amplitudes and precession frequencies are still given by the expressions obtained in Section 3.4.3 for the case of the absence of dynamics. As it becomes quite apparent, as the field increases, the relaxations of the high-field precessions ω_{12} and ω_{34} decrease from $3\lambda_{SF}/4$ to $\lambda_{SF}/2$, while the relaxations of the low field precessions increase from $3\lambda_{SF}/4$ to λ_{SF}.

Slow spin exchange

In longitudinal field, the situation is again simple, and the non-oscillating polarisation will be damped with a relaxation given by an expression identical to the one shown for the fast spin exchange regime, *i.e.*

$$\lambda_L = \lambda_{SF} \sum_{n,m=1}^{4} \frac{\omega_{nm}^2}{\lambda_{SF}^2 + \omega_{nm}^2} \, a_{nm}^z \ ;$$

however, and in spite the computation being performed using the same expression, the behaviour of the LF relaxation is quite different from that in the fast exchange regime, since it *increases* with the spin-flip rate λ_{SF} in slow spin exchange, whereas it *decreases* with λ_{SF} in the fast regime. This type of variation may be observed in Figure 3.35, where an important feature for axially symmetric states is also revealed: at the $\omega_1 - \omega_2$ level crossing, there is a relaxation peak whenever the external field is not aligned with any of the hyperfine tensor's axis ($0 < \theta < \pi/2$).

This peak does not exist in the fast spin exchange regime, as in that case the hyperfine interaction is decoupled. Thus, the LF relaxation peak at the level-crossing is a clear signature for the existence of spin exchange dynamics in the low spin-flip regime, offering an easy way to identify this type of dynamics.

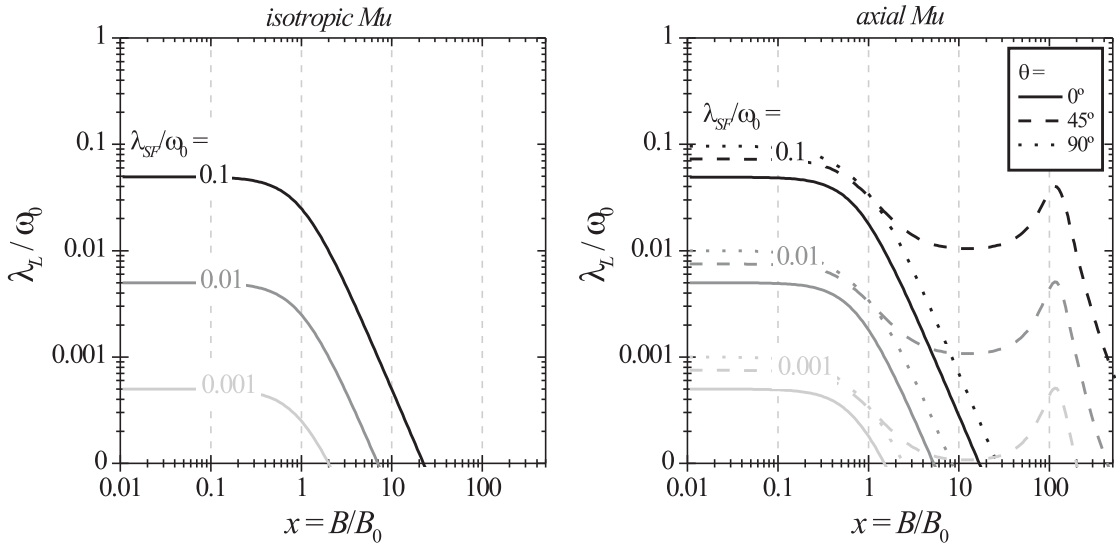

Figure 3.35: LF relaxation for the non-oscillating polarisation in the slow spin exchange regime for an isotropic muonium state, and an axially symmetric muonium state with $D = A_{iso}/2$. For axially symmetric states undergoing slow spin exchange phenomena, an important feature is the existence of a relaxation peak at the $\omega_1 - \omega_2$ (avoided) level crossing.

Chapter 4

Preparation of samples for μSR experiments

One of the major drawbacks of μSR is that one needs large samples when compared to most of the other condensed matter techniques. The implantation depth of surface muons in phthalocyanines is about 1 mm (see Figure 3.18), which, given the typical FWHM beam-spot sizes of the muon beams at PSI (5 mm) and ISIS ($>$ 10 mm), implies using samples with dimensions of approximately 2 mm thickness by 10 mm (PSI) or 20 mm (ISIS) diameter. This is not a strict requirement, as the three instruments chosen to perform the μSR experiments have the capability to measure samples smaller than the beam-spot size (see Section 3.2.6), but since that is done at the cost of having smaller count rates, in ideal conditions the samples should comply to those dimensions. Taking into account that the densities of H_2Pc, ZnPc and CuPc are all around 1.5 g cm^{-1} [77], this traduces to using samples with masses of at least 0.25 g (PSI) and 1 g (ISIS).

Further optimum conditions for a μSR experiment with solid samples are the use of single-crystals as opposed to polycrystalline material. The reason is two-fold: firstly, muon interactions often depend on the relative orientation between the crystalline axis of the material and the externally applied field. That is the case for axially-symmetric molecular-radical states (see Section 3.4.2), which are expected to be formed *a priori* in phthalocyanines; using polycrystalline material implies the necessary consideration of powder pattern distributions in the analysis of the μSR signal. Secondly, the fraction of muons which are stopped in the surface of the sample and form non-bulk states is negligible in a single-crystal, whereas in a polycrystalline sample

it may be quite noticeable, depending on the grain size. That fraction obviously produces a highly undesired component of unknown character[1] in the μSR signal; to limit its existence, the surface/volume ratio of the polycrystalline sample has to be minimal.

Both the spectroscopic and the dynamical studies of muon states in phthalocyanines would therefore benefit from using single-crystal samples, but it so happens that no phthalocyanine single-crystals with the required dimensions for μSR are currently commercially available[2]. Hence, all phthalocyanine samples used in this work took the form of pressed pellets of polycrystalline material. This means that some concern should be devoted to preparing samples with the largest possible crystalline grains, as well as considering the directional averaging of possible anisotropies in muon interactions at the time of data analysis. Powder pattern distributions are taken to be a nuisance in the analysis of the μSR signal[3], since they are a source of line-broadening which may seclude the dynamics of paramagnetic muon states. In μSR studies of organic compounds which are impossible to get as single-crystals, this is usually discarded by performing measurements with the compound in a liquid solution, where the rapid thermal tumbling motion of the molecules averages out the anisotropy of the hyperfine interaction; after subtracting the solvent's μSR signal, the muon interactions are considered to be effectively isotropic. For our study, nevertheless, this option is cast aside, since phthalocyanines are highly insoluble[4] in the solvents whose μSR signal is well-known. Moreover, the study of charge-carrier diffusion dynamics in phthalocyanines cannot be performed in any other form than in its solid-state arrangement.

4.1 Undoped samples

Since the model phthalocyanine molecules chosen for this work (H_2Pc, ZnPc and CuPc) are readily available from most major chemical manufacturers, all samples were prepared from commercially acquired material in polycrystalline form. The original material was all bought from AlfaAesar in a nominally pure grade (100% for H_2Pc and CuPc, and $> 98\%$ for ZnPc).

[1] It may be anything from a diamagnetic state to a paramagnetic one, but most probably it will be a mixture whose characteristics may change with temperature and the externally applied field.

[2] And neither are they non-commercially existent, as far as what is known.

[3] In some cases, nevertheless, they actually prove to be extremely useful in the spectroscopic characterisation of muon states.

[4] The solubility of phthalocyanines is further discussed in Section 4.2.3.

4.1.1 Phthalocyanine purification

All the material received was purified in a first stage inside a long quartz tube by vacuum temperature gradient sublimation (Figure 4.1). In certain cases, up to three cycles of the sublimation procedure were performed, as indicated in the sample lists shown later on in Tables 4.1 to 4.3 (see Section 4.3). In mild sublimation conditions, *i.e.* when the temperature of the hot end of the gradient is not high above the sublimation temperature of the substance being purified and the gradient is not too steep, the material gets slowly recondensed along the direction of the temperature gradient. For a given molecular compound, the exact spot where recondensation takes place corresponds to the point in the tube where the temperature matches the compound's (vacuum) sublimation temperature. The separation of the different molecular components existing in an initial mixture is thus performed by physical deposition in different locations, allowing to recover the compound of interest by collecting all material deposited in its specific condensation location. In our case, the identification of the place where the purified phthalocyanine is deposited was quite easy to do, since it necessarily corresponds to the location where most of the recondensed material is. Furthermore, mild conditions also assure a slow sublimation rate at the hot end of the gradient, meaning that the material will slowly recondensate in a stable crystalline phase. Optimum conditions for the growth of large needle-like phthalocyanine crystallites in the ovens used at Coimbra (Figure 4.2) and Berlin were found to be reached when the hot end of the temperature gradient (chosen to be in the centre of the oven) was kept at 490, 480 and 490 °C for H_2Pc, ZnPc and CuPc respectively. The mass yield of the purified phthalocyanines was also seen to be maximised in these conditions, taking values of 60-70% for sublimation times of 1-2 hours and initial masses on the order of 1 g. Most of the purification cycles was performed with the plain original powder being placed at the hot end of the temperature gradient; in some cases, it was pressed into pellets with a small-size pellet dye before being sublimated. The earliest sublimations were done at the HMI laboratory in Berlin during one visit planned for the acquisition of experimental know-how in the handling of phthalocyanines, but the largest part of the purification tasks was actually performed at the laboratories of the FNMC group in Coimbra.

4.1.2 Crystalline phase of the purified material

As planar phthalocyanines are polymorphic [32], possessing two distinct phases (the α, or brickstone arrangement, and the β, or herringbone configuration, see Chapter 2), the crystalline

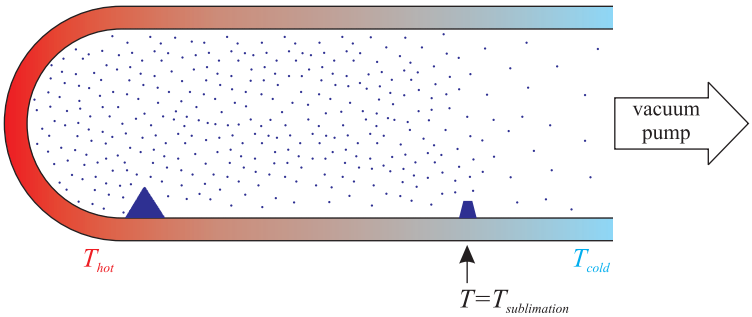

Figure 4.1: Schematic representation of the vacuum gradient sublimation principle. The material to be purified is placed at the hot end of the temperature gradient, where it is sublimated. It then condenses at the position along the gradient that matches its vacuum sublimation temperature. This is a standard technique used in the purification of solid molecular materials which do not decompose upon sublimation.

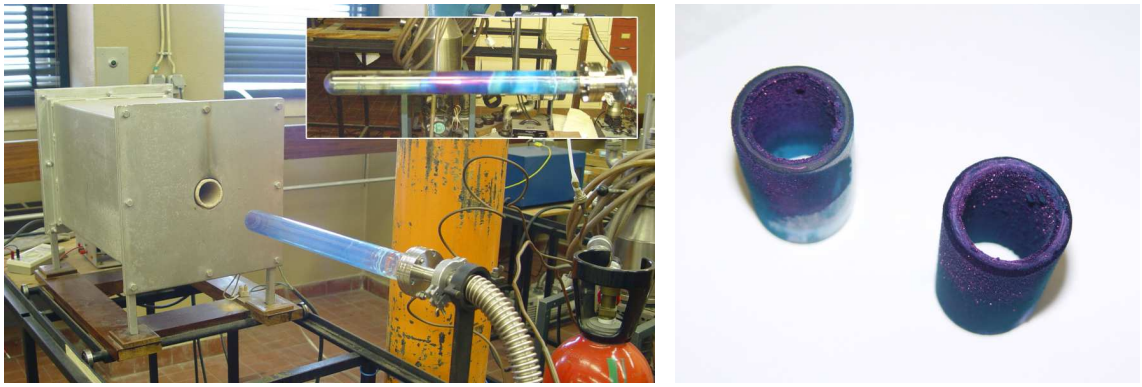

Figure 4.2: *(left)* The vacuum gradient sublimation apparatus used for phthalocyanine purifications in Coimbra. It consists in a long and wide quartz tube and a cylindrical induction oven where the tube is inserted until its tip matches the centre of the oven. On the other end, the quartz tube is connected to a high vacuum system ($p < 10^{-3}$ Pa) driven by a turbo-molecular pump. The temperature gradient inside the oven is naturally established by the cold spot created at the tube's entrance. *(right)* Detail of the deposited material after a sublimation run. The phthalocyanine crystallisation takes actually place in short quartz cylinders fitted successively inside the tube; these cylinders ease the collection of the deposited material.

structure of the material obtained by the purification procedure under optimum growth conditions was ascertained in a quick X-ray powder diffraction measurement using the Debye-Scherrer method[5]. Figure 4.3 shows the diffraction spectrum of H_2Pc along with simulated spectra for both the α and the β phases. As expected, the purification produces the β configuration, which is known to be the stable phase of planar phthalocyanines formed under mild sublimation conditions.

4.1.3 Sample shaping and thermal annealing treatments

All samples were shaped into a circular pellet pressed from the purified material with an hydraulic press and a pellet-dye of the required size (Figure 4.4). Diameters between 12 and 19 mm were chosen for samples which would be measured at PSI, while for those measured exclusively at ISIS the preferred diameter size was 27 mm.

The undoped pellet samples used in μSR measurements which involved direct comparisons with doped or non-annealed ones were also subjected to a thermal annealing treatment in vacuum before being taken to PSI and ISIS. That treatment served the purpose of freeing the sample from possibly absorbed or adsorbed gases which could in principle form states with some ability to influence the number of free charge carriers in the material; although phthalocyanine compounds are superbly stable from the chemical point of view, the incorporation of molecular oxygen in thin-film phthalocyanines, for instance, is known to substantially enhance their conductivity (see the next section for references and a more detailed discussion of this effect). The sublimation set-up was used for the vacuum thermal annealing, with the oven set to a temperature lower than the sublimation temperature of phthalocyanines. The annealing temperature was chosen to be 300 °C, and the treatment duration of 2 hours, after which the sample was rapidly cooled to room temperature by irrigating the quartz tube with water while using a small pressure of helium inside the tube as a heat exchanger gas. The choice of the annealing conditions was based on the results relative to the oxygen doping procedures discussed in the next section. As soon as the cooling process was complete, the sample was transferred to a sealed container and

[5] We choose not to make any attempt at describing the theoretical and experimental aspects of X-ray diffraction methods due to the onetime character of this measurement, and the fact that X-ray diffraction is probably the best-known technique used in the investigation of condensed matter. A full description of X-ray diffraction techniques and methods may be found *e.g.* in [6]. The same attitude is adopted for several other ancillary techniques used throughout this thesis which are of common knowledge, like resistivity measurements or electronic absorption spectroscopy (both referred to in Section 4.2.3).

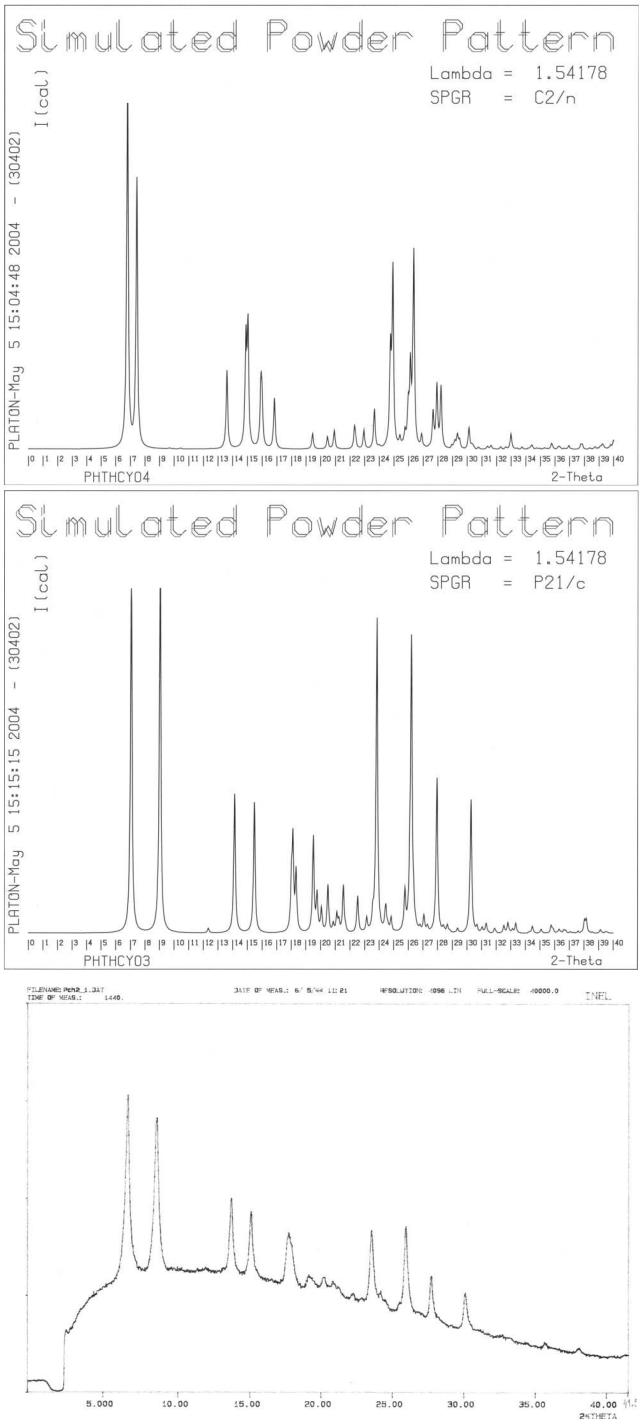

Figure 4.3: Simulated X-ray powder diffraction spectra for H_2Pc in the α (top) and β (centre) phases. The bottom spectrum is the experimentally obtained data for H_2Pc sublimated under the optimum growth conditions referred in the text, showing the formation of β phase phthalocyanine.

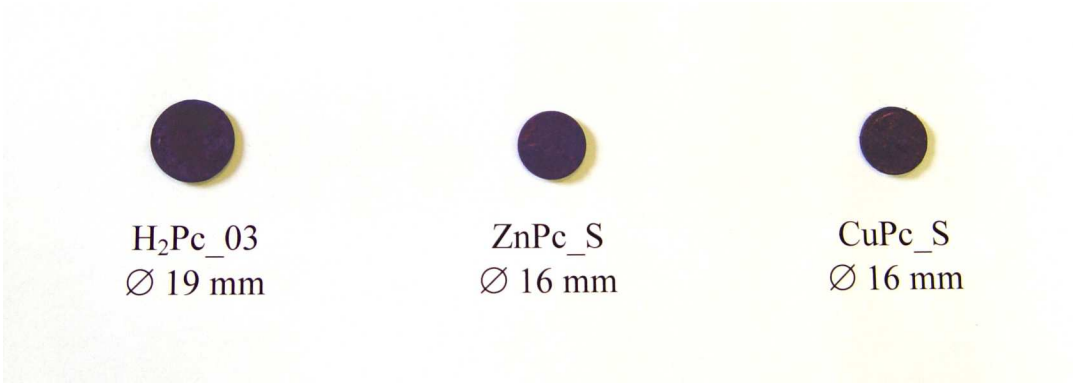

Figure 4.4: Phthalocyanine pellets with different sizes for μSR experiments. These pellets were produced in an hydraulic press using a pellet-dye of the required size.

transported under vaccum to the μSR laboratories.

4.2 Doped samples

One of the purposes of this work involves employing μSR as a tool to investigate the microscopic properties of charge carrier diffusion in phthalocyanines through the dynamics rendered by spin-scattering events between charge carriers and the muon states. Performing spin-dynamics measurements with doped samples in addition to undoped ones is therefore a valuable asset, as μSR results may be directly related with the concentration of free charge carriers depending on the larger or smaller dopant-to-phthalocyanine ratio of each sample. Thus, the preparation of doped samples for μSR was considered. Since phthalocyanines are normally used as p-conducting channels in the manufacture of devices, the choice of dopants was aimed at producing polycrystalline material also p-doped by hole donor[6] species. This implies using high electron affinity species, such as the full fluorinated of tetracyanoquinodimethane, F_4-TCNQ (see Chapter 2), or simple oxidising gases.

The local character of the positive muon probe conjugated with the polycrystalline form of the material requires the dopant-phthalocyanine mixture to be the most homogeneous possible. No domains with substantially different charge-carrier concentrations should exist, as the distribution of stopped muons through different environments would contribute to the incoherence of the muon polarisation in a way which is uncorrelated with the intrinsic characteristics of spin-scattering interactions. Having a perfect mixture is also an issue for the optimisation of

[6] *i.e.* electron acceptor.

thin-film devices based in phthalocyanines, since inhomogeneities degrade ordering and decrease the conductivity [26]. But while for doped thin-films of phthalocyanine it is easy to attain satisfactory dopant-phthalocyanine mixtures at the microscopic level, in bulk material the same is very difficult due to the fact that the long-range solid-state packing of phthalocyanines tends to highly segregate the dopant species [51]. Doping of thin-films with small organic molecules is usually performed by co-evaporation [50, 37]; the two compounds are slowly and independently sublimated from different sources in a high-vacuum chamber, physically mixing with a ratio controlled by the sublimation rates as they simultaneously reach the deposition substrate. Doped polycrystalline material could probably be obtained by traditional co-evaporation methods, but the mass yield rate would be too small to deliver a gram-sized amount of material in a reasonable time scale; also, the grain-size might not be large enough to ensure a small surface/volume ratio. An equivalent method to co-evaporation where a large-mass mixing phase exists prior to the crystallisation of the material would in principle be the most adequate to prepare polycrystalline material in suitable amounts for μSR samples of controlled doping[7]. One other alternative to the doping of polycrystalline phthalocyanine is the exposure to oxydising gases, which may diffuse inside the crystallites and create doping states in already grown material. This method has been successfully employed as a p-doping method following the deposition of thin-films [51], although diffusion phenomena end up creating non-stable doping profiles in many situations.

In the following, the three attempts at creating doped samples for μSR measurements performed in this thesis work are described.

4.2.1 Molecular doping by mechanical ball milling

The first method considered for obtaining phthalocyanine doped samples with a high mixture degree at the molecular level was the mechanical incorporation of dopant molecules *via* ball milling. This is a method often used in materials science to make alloys and induce mixtures at the sub-micrometric scale, with which some members of the FNMC group are well acquainted. It consists in the mixing of two (or more) powder substances by the mechanical action of hard steel spheres inside a closed container. The spheres are continuously propelled against each other and the container's walls, acting as pounders to grind and mix the substances by impact

[7] We should make clear that such phase cannot be an equilibrium gas phase of the two compounds from which the final material would be obtained by crystallisation upon cooling. The compounds are bound to have different sublimation temperatures, and thus would not condensate simultaneously.

and friction (Figure 4.5).

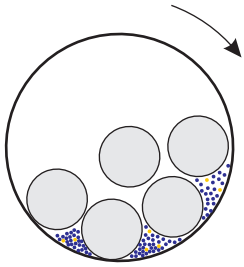

Figure 4.5: Schematic representation of the ball milling principle. The powder substances to be alloyed are inclosed in a sealed container together with hard steel spheres. The spheres are driven by the periodic motion of the container, which may be rotational, vibrational, or a combination of both. This forces the spheres to repeatedly hit each other and the container's walls, grinding and mixing the powders until a mixture at sub-micrometric scale exists.

The eventual use of mechanical ball milling with phthalocyanines in polycrystalline form raised nevertheless some concerns which had to be evaluated beforehand. Firstly, the milling procedure potentially grinds the crystalline grains to sizes in the nanometre scale, highly increasing the total surface/volume ratio of the sample. This may enhance the formation of muon surface states, affecting the μSR signal of doped samples. Secondly, it may induce modifications of the crystalline structure, deforming the initial phase by shear stresses or forming totally different phases. This will surely affect the local muon environment, changing the structure of muon states, and denying the comparison between doped and undoped data. To assess the existence of any of these effects, two undoped samples of H_2Pc (samples H_2Pc_03 and H_2Pc_03m15) were prepared from the same batch of purified material. The first sample (H_2Pc_03) was pressed directly as all other undoped samples, while the material used for the second one (H_2Pc_03m15) was subjected to soft milling conditions before the pellet pressing procedure. The milling was carried out in an inert atmosphere of Ar at room temperature for 15 hours, using the single-sphere vibratory mill existing in the laboratory of the FNMC group (a FRITSCH Vibratory Micro Mill pulverisette 0) set to a low amplitude. As it is discussed in Chapter 5, high transverse-field μSR measurements done on both samples came to indicate substantial changes in the μSR signal which disabled the viability of this method for doping purposes. No further work on this subject was therefore engaged.

4.2.2 Oxygen doping

The exposure of phthalocyanine thin-films to molecular oxygen is known to induce a dramatic increase of hole conductivity in those structures [59]. The oxygen oxidises the phthalocyanine molecules, removing electrons from the film and acting as a p-dopant species. The production of oxygen-doped phthalocyanine samples for μSR measurements by pressure-charging procedures of previously purified material was thus considered as a viable alternative in addition to doping by incorporation of small dopant molecules.

In order to perform the controlled oxygen doping of the rather large quantity ($\sim 1\,\mathrm{g}$) of polycrystalline phthalocyanine needed for μSR samples, it was first necessary to establish an experimental relation between oxygen charging conditions (essentially oxygen pressure and charging temperature) and the number of free charge-carriers induced by the doping. Assuming that bulk polycrystalline material behaves in a similar manner to thin-films, such relation may be extracted from conductivity measurements of phthalocyanine thin-films under different oxygen charging conditions. Since phthalocyanine in thin-film form crystallises in randomly oriented β-phase grains [26], matching the crystalline structure of the bulk crystallites obtained from the purification procedure, conductivity results may qualitatively carry over to polycrystalline material provided that oxygen is able to diffuse deep enough inside the bulk crystallites so that its average concentration is similar to the one in a thin-film for the same charging conditions.

Thin-film doping

Conductivity measurements were performed in a single 400 nm thin-film sample of ZnPc as a function of oxygen pressure and temperature. The sample was prepared in a high-vacuum ($p < 10^{-3}\,\mathrm{Pa}$) Veeco evaporation chamber which was adapted for the deposition of organic thin-films at the HMI institute and brought to the laboratory of the FNMC group in Coimbra for the experiment (Figure 4.6). For the oxygen charging, a gas admission system consisting of a needle valve, an absolute low pressure gauge (0-2 bar piezoresistive absolute pressure sensor from Kistler, model 4043A2) readout by a micro-voltmeter and a high-purity ($> 99.995\%$) oxygen gas source was fitted to one of the available ports on the chamber.

The film was grown on a 100 °C-heated fused silica substrate possessing two microstructured aluminium electrodes (Figure 4.7) that allowed the *in situ* measurement of its electrical resistance in coplanar contact geometry using an electrometer with leak current cancelling features (Keithley 6517A). The substrate was cleaned prior to the deposition with a 15-minute

Figure 4.6: The evaporation chamber for organic thin-film deposition at the laboratory of the FNMC group in Coimbra, based in a bell-glass high-vacuum Veeco chamber driven by a diffusion pump. It possesses two resistively heated crucibles for the sublimation of organic materials, of which only one is currently connected to a power supply plus temperature controller set capable of reaching a maximum temperature of around 700 °C. The sample substrate holder may be heated up to 150 °C with a wrapped up resistive thermocoax filament connected to a low power supply source. Deposition control is performed with shutters for the ovens and sample, and the deposition rate is monitored with a quartz oscillator. The fact that a single oven power supply and a single quartz oscillator exist allows so-far the sublimation of one type of material at a time only.

acetone bath followed by another 15-minute ethanol bath and an in-place 15-minute heating to 100 °C under vacuum conditions. The growth rate was adjusted to a slow value of 2 Å/s by heating the crucible containing previously purified ZnPc to a temperature of 450 °C. Following deposition, the circuit resistance measured in the electrometer was 25 GΩ[8], a value which remained unaltered after a single vacuum annealing of the film at 100 °C for an half-hour period. The conductivity of the sample in undoped conditions was therefore (see Figure 4.7*b* for details on the calculation)

$$\sigma = \frac{1}{35 \times R_m} \, \frac{33\,\mu\text{m}}{3\,\text{mm} \times 400\,\text{nm}} = 3.1 \times 10^{-10}\,\text{S/cm} \ ,$$

lying well within the order of magnitude known for conductivities of undoped phthalocyanines (*cf.* Chapter 2).

The first oxygen uptake experiment was performed with the sample being kept at room temperature (21 °C) under a constant oxygen pressure of $p_{O_2} = 100\,\text{mbar}$. The film electrical resistance was seen to react promptly to oxygen presence, rapidly lowering on a minute timescale, after which it kept falling at a much slower rate (Figure 4.8); at the end of one day, it had dropped to 1.6 GΩ ($\sigma = 4.9 \times 10^{-9}$ S/cm). The evaporation chamber was then evacuated with the sample at 21 °C, and again the resistance reacted with a similar time pattern (Figure 4.8), rising fast to 6.8 GΩ after 1 minute and slower to 22 GΩ after 1 day. At 21 °C, the original 25 GΩ resistance was only attained with the sample under vacuum conditions during about 1 week.

These results are consistent with the oxygen-doping of thin-film ZnPc being performed by two different fractions of oxygen, as proposed by Kerp and Faassen [58]. In their work, they find that one oxygen fraction is rapidly desorbed in vacuum (which they call the 'mobile' fraction), while the other (the 'fixed' fraction) only diffuses out when the temperature is taken above 90 °C. After sample exposure to air at room temperature, they estimate the mobile and fixed oxygen contents to be of respectively 2 and 1 molecules per 30 ZnPc molecules. In our results, the mobile fraction is responsible by the fast time evolution of the conductivity upon oxygen charging and de-charging of the sample, while the fixed one produces the slow behaviour. The fraction of interest for oxygen doping of phthalocyanine samples to be used in μSR is of course the second one, as μSR experiments are usually performed with the sample in vacuum. The incorporation and stability characteristics of that fraction were therefore targeted in measurements of the film's electrical resistance after charging periods of 2 hours at different

[8]No experimental errors will be quoted in the text for the resistance measurements; they were nevertheless estimated to be of about 10% of the measured value, and are indicated as error bars in the plots shown below.

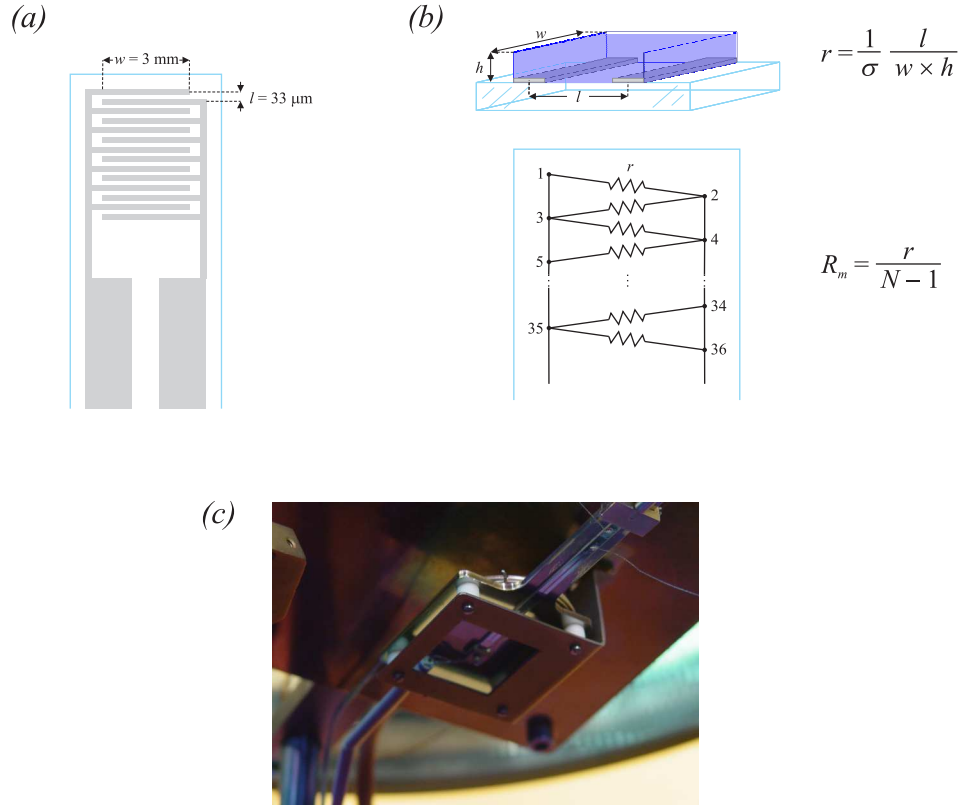

Figure 4.7: *(a)* Scheme of the structured microelectrodes used for *in situ* resistance measurements in coplanar contact geometry. Each electrode is composed by 18 filaments of Al 3 mm long. The spacing between filaments is 33 μm. *(b)* Illustration of the electrical resistance r between 2 adjacent filaments as a function of filament length w, filament spacing l and film thickness h, and the equivalent resistance of the whole microelectrode structure, R_m (N is the total number of filaments in the two electrodes). *(c)* Detail of a ZnPc thin-film evaporated onto a microstructured substrate at the evaporation chamber shown in Figure 4.6.

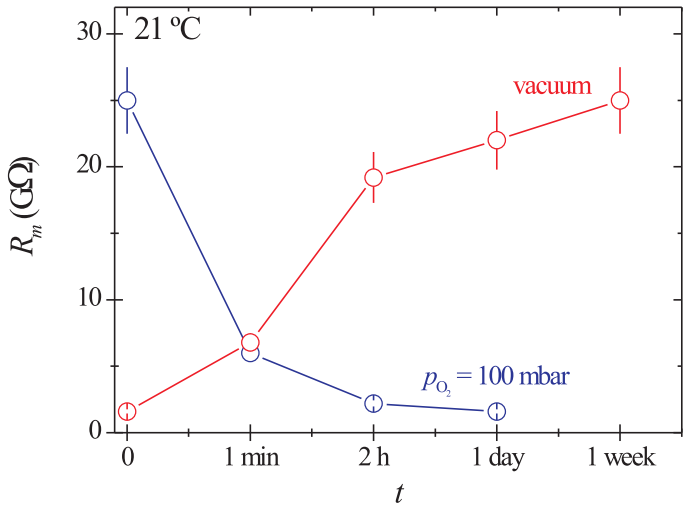

Figure 4.8: Time dependence of the electrical resistance in the ZnPc thin film sample prepared for oxygen pressure-charging experiments during oxygen uptake (blue data points) and oxygen effusion (red data points). The lines are mere guides to the eye.

pressures and temperatures. Between each measurement, the sample was subjected to a vaccum annealing treatment at 100 °C for 1 hour, since those conditions were found to clearly reset the film's resistance to its post-deposition value of 25 GΩ. A short dependence of the resistance at 21 °C with the oxygen charging pressure is depicted in Figure 4.9; no variation is seen, seeming to indicate that oxygen pressure is irrelevant for the doping process in the considered range.

Temperature, on the other hand, does influence the electrical resistance at a constant charging pressure of $p_{O_2} = 100$ mbar, decreasing with increasing charging temperature, as seen in Figure 4.10. Although at first sight this may suggest that higher temperatures induce an easier oxygen uptake and consequent larger hole concentration, the fact is that studies with other dopants of phthalocyanines attribute the temperature behaviour of the conductivity in lightly-doped thin-films mainly to a rise in the hole mobility and not of its concentration [86]. We are therefore inclined to conclude that the number of holes induced by oxygen does not change significatively with temperature in the range measured. Figure 4.10 also shows the film's resistance after 2 hours in vacuum, taken before the resetting 100 °C, 1 hour vacuum annealing at each of the temperatures measured under $p_{O_2} = 100$ mbar. For that time lapse, oxygen effusion increases with temperature, as already hinted by the conditions of the resetting vacuum annealing. At room temperature, a substantial part of the fixed oxygen fraction is still inducing

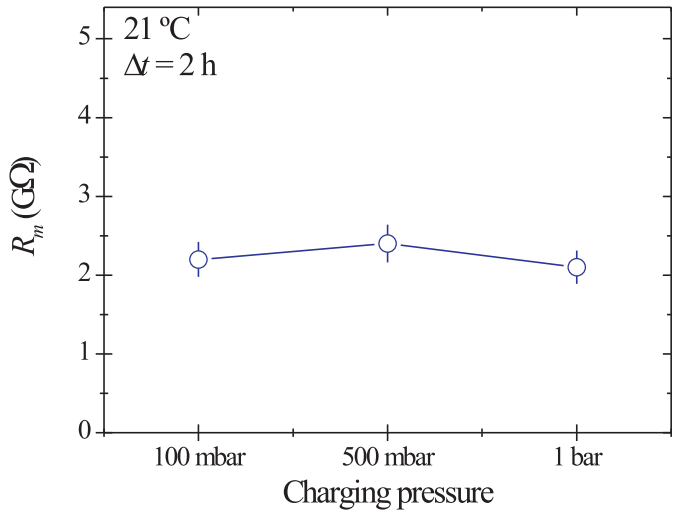

Figure 4.9: Pressure dependence of the electrical resistance at 21 °C for the ZnPc thin film sample prepared for oxygen pressure-charging experiments.

free charge-carriers in the sample; taking into account Figure 4.8, we estimate it to be about half of its initial value.

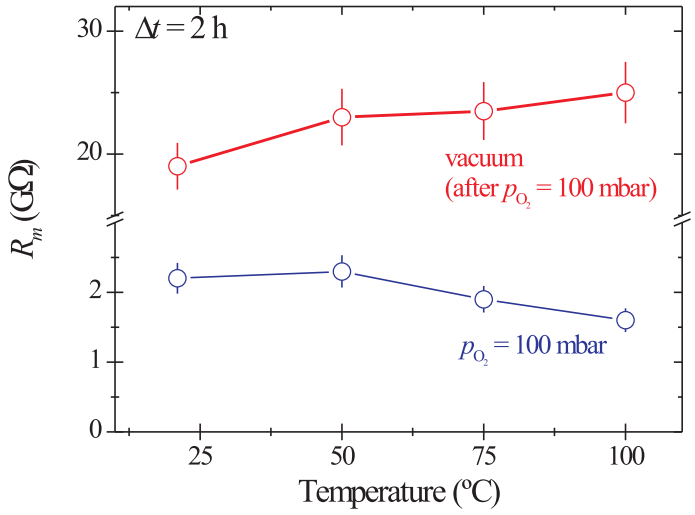

Figure 4.10: Temperature dependence of the electrical resistance for the ZnPc thin film sample prepared for oxygen pressure-charging experiments. Blue and red data points correspond to measurements taken in an oxygen pressure of 100 mbar and in vacuum after the 100 mbar period, respectively.

In view of obtaining a pragmatic set of oxygen doping conditions for polycrystalline samples, the results presented above for the fixed oxygen fraction are in agreement with the sample being oxygen-saturated already at low charging pressures, and the slow effusion in vacuum (performed in a timescale of many hours) at room temperature. The oxygen saturation, unfortunately, disables any quantitative control of doping[9], so one is limited to producing a single oxygen-doped μSR sample with a mild concentration of free charge-carriers. Furthermore, the doping will only be stable in vacuum at temperatures around room temperature (and presumably also at lower temperatures) during a limited period of time.

Doping of polycrystalline material

The oxygen doping of the polycrystalline material for μSR samples was performed in the gradient sublimation apparatus on a single already pressed pellet of ZnPc (sample ZnPc_oxy) by coupling the gas admission system to the apparatus vacuum system. The charging was done in a pure oxygen atmosphere at a pressure of 1 bar and a temperature of 200 °C for 1 hour, followed by slow cooling in oxygen-rich conditions. Although the thin-film results indicate that the doping efficiency depends very weakly on the temperature and oxygen pressure, it was thought to be preferable using a high temperature and pressure to ensure the successful doping of the larger crystallites found in the polycrystalline material. Efforts to observe the charging and outgasing process directly in polycrystalline samples were also made at the time this oxygen-doped sample was prepared, but the pressure variations induced as a result of oxygen uptake and release by the sample were too small to yield quantitative values conclusive within errors for the amount of oxygen absorbed or desorbed.

4.2.3 F_4-TCNQ doping

Since the results of oxygen-doping showed the impossibility to control the number of charge-carriers induced in phthalocyanines by gas charging procedures, the doping with small molecules bearing acceptor character was again considered, namely with F_4-TCNQ. With this type of compound, dopant-to-phthalocyanine ratios on the order of 1:50 to 1:500 are known to induce weak p-doping of thin-film samples [86]. The controlled incorporation of F_4-TCNQ in purified

[9]One could try to use small charging pressures for which oxygen saturation would not be reached, but the effect of the fixed oxygen in saturation conditions is already low (after 2 hours in vaccum the resistance is just 10% below its final value, see Figure 4.10), which means that no changes would probably be seen in the μSR data.

polycrystalline phthalocyanine material with similar ratios would therefore produce suitably p-doped samples for μSR measurements.

A method to surpass the problem of attaining a random microscopic mixture at the molecular level between phthalocyanine and F_4-TCNQ molecules was devised, consisting in the vacuum evaporation of the desired phthalocyanine–F_4-TCNQ mixture in liquid solution by an atomising noozle (a vacuum-spraying method, Figure 4.11). If the solvent is volatile enough, the phthalocyanine and F_4-TCNQ molecules present in the minute quantities of solution passing through the noozle into a small vacuum chamber should preserve the random solution mixing as the solvent vaporises. When a target is placed in front of the noozle, the phthalocyanine–F_4-TCNQ mixture will be deposited there with a rate in principle much higher than that obtained in a coevaporation chamber, surmounting the time limitation problems presented by the coevaporation for the production of the massive quantity of doped phthalocyanine necessary for the preparation of a μSR sample. The question of which phthalocyanine solid-state phase would be formed in such situation is of course an important issue here, but that may be solved in an X-ray diffraction measurement of post-deposited doped material.

The experimental set-up for the vacuum-spraying was assembled in the laboratory at Coimbra using a small stainless steel chamber built on purpose by the workshop of the High Energy Physics and associated Instrumentation group (LIP). The chamber was connected on one side to a needle valve which acted as the atomising noozle, and on the other to a vacuum system ended by a rotary pump ($p \sim 10^{-1}$ Pa) (Figure 4.11*b*). The needle valve was fed by a large container, while the vacuum line possessed a trapping device for the collection of the evaporated solvent before it reached the pump, preventing any damage of occurring to it. A third port in the chamber was fitted with an electrical feed-through for the connection of a substrate with microstructured electrodes identical to the ones used for the *in situ* measurement of the electrical resistance of evaporated films (see the last section); that substrate was used as a simple way to monitor the deposition in the chamber. Finally, a glass beaker was fitted to the inside of the chamber with its opening facing the needle valve in order to collect the sprayed material.

Choice of the solvent

In parallel with the design and assembly of the spraying system, the choice of an adequate solvent was also conducted. Phthalocyanines have extremely low solubilities in the most common

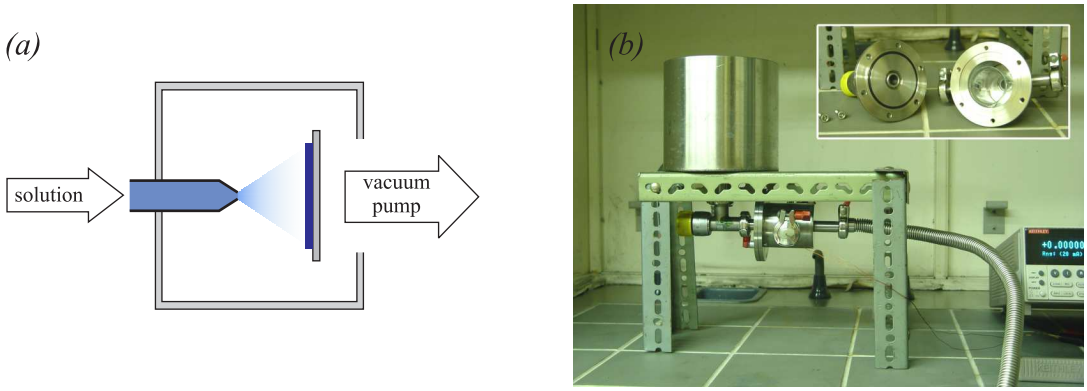

Figure 4.11: *(a)* Working principle of the vacuum-spraying method devised in this thesis to obtain a solid molecular mixture between phthalocyanine and F_4-TCNQ from solution. The solution is sprayed into a vacuum chamber by an atomising noozle; as the solvent vaporises, the phthalocyanine–F_4-TCNQ mixture is deposited onto a target placed in front of it. *(b)* The vacuum-spraying system assembled in Coimbra according to the principle of *(a)*.

volatile organic solvents, as ethanol or acetone, and are only well solubilised by polar aprotic solvents. From that class of solvents, N,N-dimethylformamide (DMF, $HCON(CH_3)_2$) has the lowest boiling point (153 °C), and was therefore considered to be the best one to perform the vacuum-spraying experiments. A short series of solubilisation experiments allowed to estimate a value of about 0.5 g/L for the solubility of ZnPc in DMF. The chemical stability of the ZnPc and F_4-TCNQ molecules in DMF solution was also looked into; Figure 4.12 shows electronic absorption spectra in quartz cells for DMF solutions of pure ZnPc and pure F_4-TCNQ, as compared with spectra obtained in dichloromethane (CH_2Cl_2). The two ZnPc spectra exhibit essentially a Q-band with the same shape (see Chapter 2), which does not present itself as a surprise in view of the well-known high chemical stability of phthalocyanines, but the two F_4-TCNQ spectra turn out to be quite different. The simple band spectrum in CH_2Cl_2 at 400 nm changes to a more complex one in DMF, with several additional intense bands between 680 and 870 nm. Since no electronic absorption data was found for F_4-TCNQ in the literature, these results were compared with data obtained by Jonkman and Kommandeur [55] on non-fluorinated TCNQ and its mono- and di-valent anions in a mixture of dimethoxy ethane and acetonitrile (Figure 4.13). The CH_2Cl_2 spectrum of F_4-TCNQ is almost the same as the one they measure for TCNQ, while the DMF one compares superbly to their data on the $TCNQ^-$ anion. This means that negative charge is transferred from the DMF molecules to F_4-TCNQ in solution. The formation of charge-transfer complexes between the oxidised DMF molecules and the reduced

F_4-TCNQ ones constitutes a factor of reduction in the *p*-doping efficiency of F_4-TCNQ, since upon vacuum-spraying some of the DMF^+/F_4-$TCNQ^-$ complexes might not get dissociated and would certainly end up being incorporated in the deposited mixture. Although charge transfer does exist, the hypothesis that DMF^+/F_4-$TCNQ^-$ complexes are formed in DMF solution is nevertheless unlikely, taking into account the high similarity between the spectra of $TCNQ^-$ and F_4-TCNQ+DMF. If a charge-transfer complex would be formed, the electrical dipole induced by the transferred negative charge would substantially change the shape and energy of the bands observed in the absorption spectra, distinguishing the F_4-TCNQ+DMF spectrum from the $TCNQ^-$ one. Therefore, in the DMF solution of a ZnPc and F_4-TCNQ mixture, we take the ZnPc to be in a neutral-charge state, while the F_4-TCNQ is in the form of its mono-anion. After deposition, charge neutrality will of course set in, forcing the excess negative charge to leave the material and promoting the formation of $ZnPc^+/F_4$-$TCNQ^-$ charge-transfer complexes.

Vacuum-spraying experiments

In spite of all the work strived to assemble the apparatus and optimise the spraying conditions[10], the first experiments with plain DMF revealed that the spraying rate had to be kept vanishingly small in order for its efficient vaporisation to occur. DMF is a solvent with a viscosity and surface tension significantly larger than water, and that turns it into a substance hard to evaporate. The unforeseen effect of viscosity was tentatively mended by heating the container-valve-chamber system to near the (atmospheric-pressure) boiling point of DMF using a ribbon heater, but still the rate was experimentally estimated to be too slow for this method to give positive results within a reasonable time period. It was decided not to pursue this course any further within the time scope of this thesis, although the possibility of finding success using a more volatile solvent remains open. The same procedures for finding the solubility and assessing the stability of solubilised phthalocyanine and F_4-TCNQ as the ones performed for DMF will of course have to be followed once that other solvent is chosen.

4.3 Samples list

As a concluding paragraph regarding samples, Tables 4.1, 4.2 and 4.3 shown below present a systematic account of all H_2Pc, ZnPc and CuPc samples prepared for the μSR experiments.

[10]Including the temperature of the pre-pump trap, which was cooled to about -78 °C (a temperature close to the atmospheric-pressure melting point of DMF) with a bath of solid ice.

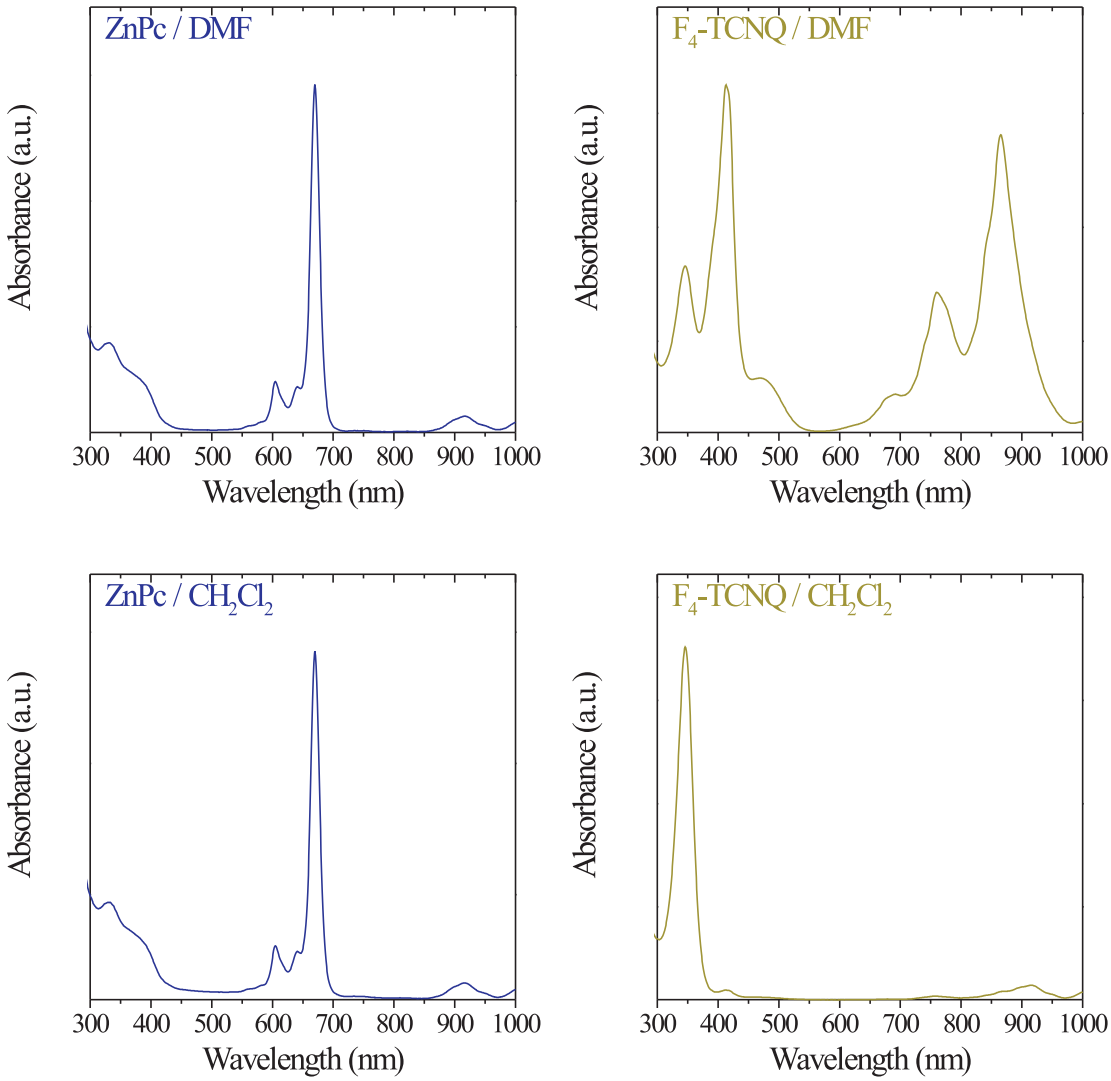

Figure 4.12: Visible-UV absorption spectra of ZnPc (left) and F_4-TCNQ (right) in DMF (upper figures) and CH_2Cl_2 (lower figures). The two ZnPc spectra are essentially the same, while large changes are observed between the two F_4-TCNQ datasets.

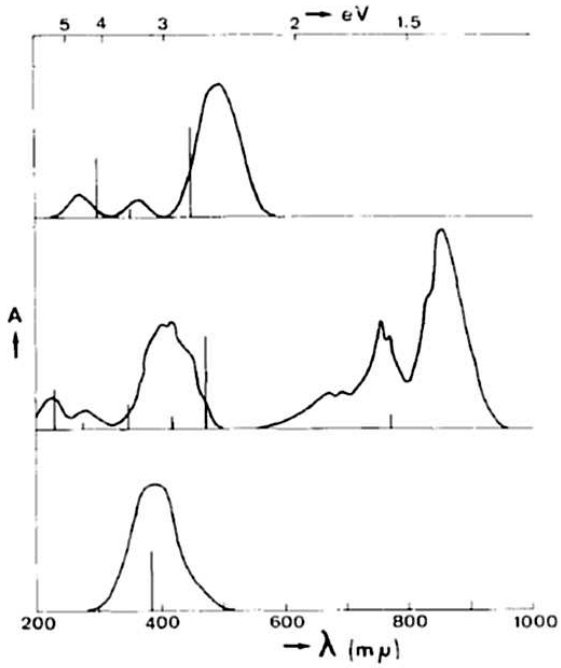

Figure 4.13: Visible-UV absorption spectra of the TCNQ molecule (lower), the $TCNQ^-$ anion (middle) and the $TCNQ^{2-}$ anion (upper) measured by Jonkman *et al.* in a mixture of dimethoxy ethane and acetonitrile. Source: [55]

Relevant characteristics, namely if they were subjected to any type of treatment or doping procedure, are indicated.

Table 4.1: List of H_2Pc pellet samples for μSR measurements, indicating each sample's dimensions (diameter), number of sublimation cycles underwent by the material before pellet pressing (sublimation), if they were subjected to any type of doping or annealing before the measurements (treatment) and the manufacturer of the original material (origin).

name	*diameter*	*sublimation*	*treatment*	*origin*
H_2Pc_S	16 mm	3 cycles	—	AlfaAesar
H_2Pc_03	19 mm	1 cycle	—	AlfaAesar
H_2Pc_03m15	12 mm	1 cycle	ball milled	AlfaAesar
H_2Pc_06	27 mm	2 cycles	vacuum annealed	AlfaAesar

Table 4.2: List of ZnPc pellet samples for μSR measurements. See the legend of Table 4.1 for the meaning of each entry.

name	*diameter*	*sublimation*	*treatment*	*origin*
ZnPc	16 mm	1 cycle	—	AlfaAesar
ZnPc_S	16 mm	3 cycles	—	AlfaAesar
ZnPc_vac	19 mm	2 cycles	vaccum annealed	AlfaAesar
ZnPc_oxy	19 mm	2 cycles	oxygen doped	AlfaAesar
ZnPc_p3	19 mm	2 cycles	vaccum annealed	AlfaAesar
ZnPc_06	27 mm	2 cycles	vacuum annealed	AlfaAesar

Table 4.3: List of CuPc pellet samples for μSR measurements. See the legend of Table 4.1 for the meaning of each entry.

name	*diameter*	*sublimation*	*treatment*	*origin*
CuPc_S	16 mm	3 cycles	—	AlfaAesar
CuPc_03	27 mm	1 cycle	—	AlfaAesar
CuPc_p1	19 mm	2 cycles	vacuum annealed	AlfaAesar

Chapter 5

Spectroscopy of muon states in the model phthalocyanines ZnPc, H_2Pc and CuPc

This chapter reports experimental μSR results regarding the spectroscopic characterisation of muon states in ZnPc, H_2Pc and CuPc. Some immediate conclusions drawn from the experimental data are also referred here, although the main discussion is left for Chapter **??**. The measurements were performed over a broad temperature range (2-600 K[1]) using the GPS and DOLLY spectrometers in transverse-field geometry. Fields above0.1 T were employed in order to have any signals corresponding to typical paramagnetic muoniated radicals in the high field regime, allowing the easy identification of different states. As it will be seen, at least three distinct states of paramagnetic origin are formed in ZnPc and H_2Pc, with hyperfine interactions on the order of 125-140 MHz for two of them, and of about 25 MHz for the third. All three states exhibit anisotropic hyperfine tensors, as expected for muoniated radicals, and do not ionise below the sublimation temperature of phthalocyanines. In CuPc, only Larmor precession signals are found.

Due to the intrinsic richness of paramagnetic states, the results presented focus on measurements performed in ZnPc and H_2Pc. These comprise the determination of hyperfine pa-

[1] Although planar phthalocyanines exhibit typical sublimation temperatures on the order of 500 °C = 773 K [29], an upper temperature limit of 600 K was used for the μSR experiments. This choice was based on the purification procedures referred in Section 4.1.1, where some sublimation was seen to occur already at around 420 °C = 693 K.

rameters for each state, of its relative population and stability characteristics, and finally of its molecular addition site. The lack of frequency structure in the signal obtained with CuPc, on the other hand, shortens the allowed insight one may have about the states formed in this compound. Therefore, a simple presentation in terms of distinguishable components is adopted here, leaving a more complete discussion about this subject for Chapter 7.

5.1 ZnPc

5.1.1 Number and nature of muon states

The number, nature and stability of the muon states formed in undoped ZnPc where investigated with temperature dependent measurements in high-transverse fields using samples ZnPc and ZnPc_S (see sample descriptions in Chapter 4). At all temperatures, the implantation of positive muons produces a μSR signal whose main feature is the existence of three distinct pairs of precession frequencies, signaling the formation of three muoniated paramagnetic radicals. This is seen in the left-hand side of Figure 5.1, where the FFT amplitude transform of a typical time spectrum, obtained for sample ZnPc_S in a high-statistics measurement (640 million μ^+ decay events) at 500 K, 0.4 T, is displayed. Besides the sharp Larmor precession signal at 54.2 MHz, representing the fraction of muons which form diamagnetic states, three pairs of frequencies labelled I, II and III, corresponding to the ω_{12} and ω_{34} transition frequencies expected in high fields for paramagnetic states (*cf.* Section 3.4.3), are observed. A broad frequency distribution denoted by IV and centred with the diamagnetic line is also present; this component of the signal might be related either to the formation of states possessing a low hyperfine constant, or the existence of a paramagnetic state undergoing fast spin exchange.

The hyperfine interactions of states I-III are seen to be 140, 125 and 25 MHz from the frequency pair correlation transform shown in the right-hand side of Figure 5.1 (exact values at 500 K, considering isotropic hyperfine interactions)[2]. As a first approach, we choose to ignore the existence of anisotropy in the states observed, although its presence is apparent (a thorough

[2]The frequency pair correlation transform is a visual aid created by Ivan Reid to quickly identify pairs of frequencies in a μSR signal. It is based on the fact that in the high transverse-field regime the splitting between the ω_{12} and ω_{34} precession frequencies of an isotropic muonium state relates directly with the hyperfine coupling constant via the sum-rules (3.184) and (3.185). Hence, knowing the applied magnetic, it is possible to calculate the autocorrelation of the FFT transform in search of periodicities in the FFT transform itself. See *e.g.* [10] for a more thorough discussion about frequency pair correlation transforms.

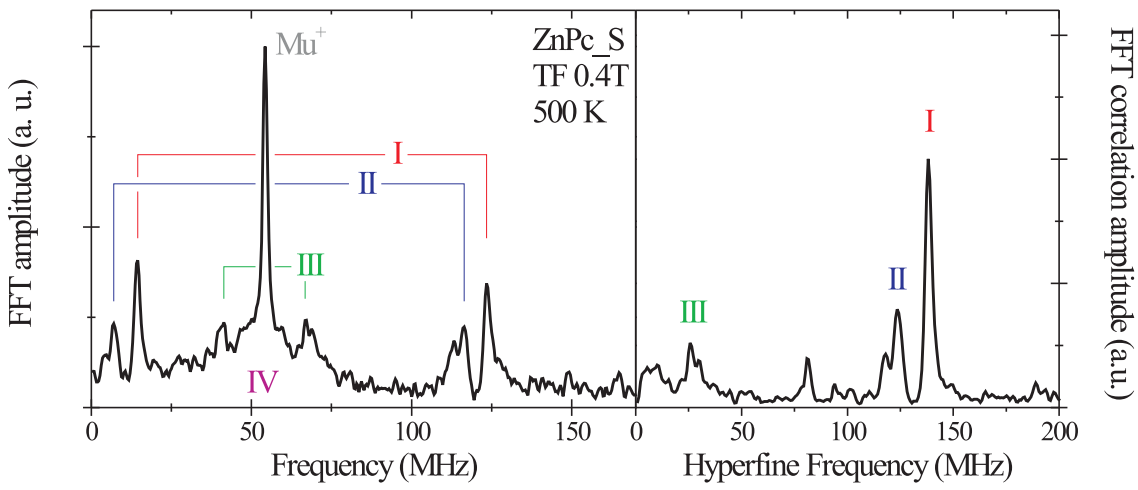

Figure 5.1: Fourier (left) and frequency pair correlation (right) transforms of ZnPc obtained at 500 K under an applied transverse field of 0.4 T. The three pairs of lines I, II and III observed in addition to the Larmor precession of diamagnetic muons at 54.2 MHz show the formation of three different paramagnetic muon states in ZnPc. A fourth paramagnetic signal consisting in a broad frequency distribution below the diamagnetic line also exists; this component has been denoted by IV. The hyperfine interaction values of states I-III are of about 140, 125 and 25 MHz, as seen in the frequency pair correlation spectrum.

analysis taking into account the anisotropy of muon states will be discussed later). The ω_1-ω_2 level crossings[3] of these states (as given by equation (3.55)) should therefore roughly take place at 0.51, 0.46 and 0.09 T. This qualitatively agrees with the field dependence of the line pair positions presented in Figure 5.2; state III is clearly in the Paschen-Back regime above 0.3 T (the lowest field used for measurements with ZnPc samples), while the level crossings of states I and II occur respectively above 0.5 T and between 0.45 and 0.5 T.

The three paramagnetic states I-III are stable (*i.e.* do not ionise) in the investigated temperature range, as seen in the temperature dependence of the frequency pair correlation transform, Figure 5.3. This figure also shows that the hyperfine interaction of states I and II red-shifts[4] with temperature, the decrease being considerably larger for the highest coupling state, while no evolution with temperature exists for state III.

[3] At which the frequency ω_{12} decreases to zero and rises again with increasing field; see Section 3.4.3.

[4] With *red-shift*, one means a shift to lower frequency values; conversely, a shift to higher frequency values is a *blue-shift*.

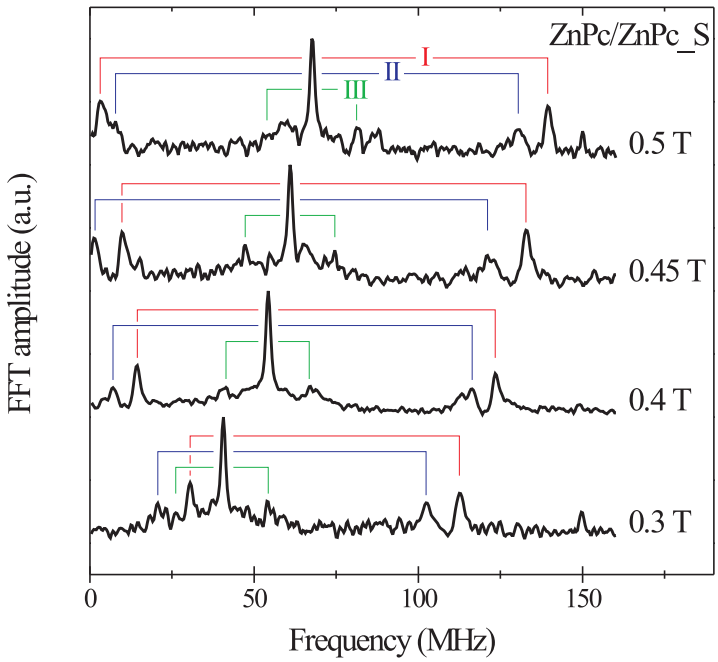

Figure 5.2: Fourier power spectra of ZnPc at different fields. The field dependence of the three pairs of paramagnetic lines shows that all states are in the high-field regime. The ω_1-ω_2 level crossings of states I and II occur respectively between 0.45 T and 0.5 T, and slightly above 0.5 T.

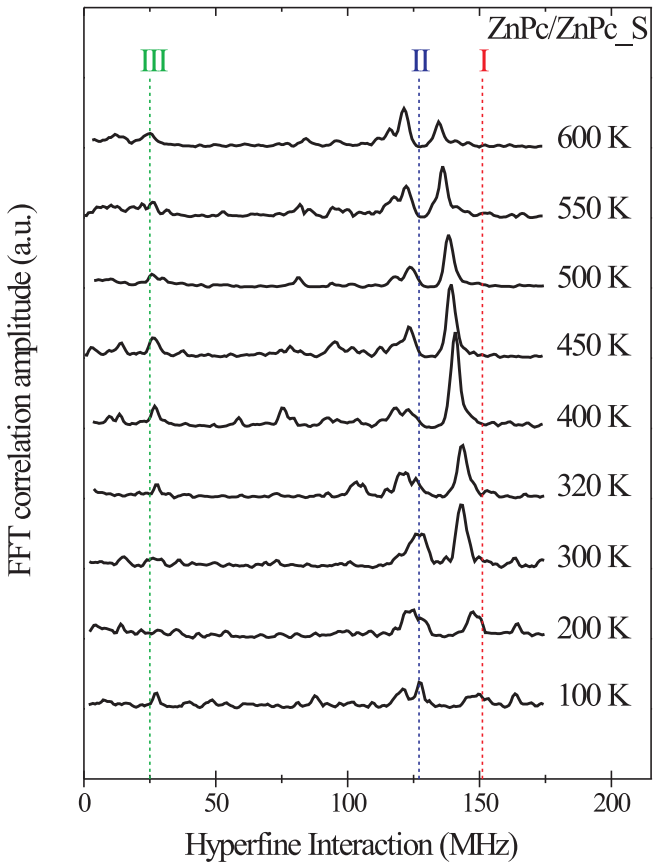

Figure 5.3: Frequency pair correlation spectra of ZnPc at different temperatures. The dotted lines indicate the $T = 0\,\mathrm{K}$ values obtained from the temperature activated fits to the hyperfine interaction shown below in Figure 5.6.

5.1.2 Relative populations and hyperfine parameters

First analysis - isotropic hyperfine tensors

In order to quantitatively extract the relative populations of the five components found in high-transverse field, and measure the hyperfine parameters of the three paramagnetic states I-III, time domain fits to the temperature-dependent data referred in the last section were performed. Although the asymmetric shapes of the three pairs of paramagnetic lines indicate the existence of anisotropy (see Section 3.4.3), in a first analysis their hyperfine interactions were considered to be isotropic. The effects of the powder pattern were included using a simple line broadening Lorentzian relaxation of the form $e^{-\lambda t}$, allowing to qualitatively follow the temperature evolution of the dipolar parameter D for each state, since the relaxation λ scales with the width of the precession lines . A relaxation function $e^{-\sigma^2 t^2/2}$ of Gaussian shape was also tried, but its results showed no relevant differences relative to the Lorentzian ones, and are not reproduced here. This course of action was chosen taking into account the foreseen difficulties in performing a full analysis from scratch which included anisotropy in the hyperfine tensors of the three states observed. Hence, this first analysis served as the most sensible starting point for the full analysis discussed in the following section. Furthermore, it proves to be useful as a means of comparison with the results obtained for states I and II in H_2Pc (Section 5.2.2), where it was only possible to analyse the signal of those states with a pair of high-field precession lines instead of a powder frequency pattern. The paramagnetic component IV was fitted with a diamagnetic precession broadened also by a Lorentzian relaxation; for this component, however, a Gaussian relaxation function was found to produce unreasonable goodness-of-fit χ^2 values.

Figures 5.4 and 5.5 show the fitted amplitudes and relaxations as a function of temperature obtained for the five asymmetry components. Only half the full experimental asymmetry is accounted for[5]; states I and II possess similar average populations, amounting to about 10% of the full asymmetry each, a very small fraction of diamagnetic muons exists (less than 2.5% of the full asymmetry), and the asymmetries of states III and IV sum to give a roughly constant value corresponding to a population of about 30% of the full asymmetry. The relaxation of state IV is substantially decreased with temperature, apparently accompanied by the increase of state III's relaxation. As for states I and II, a decrease with temperature of their fitted relaxations is observed, hinting the averaging of the dipolar part of the hyperfine interaction presumably due

[5]The maximum asymmetry of the GPS and DOLLY detectors in high transverse-field is of about $0.20 = 20\%$.

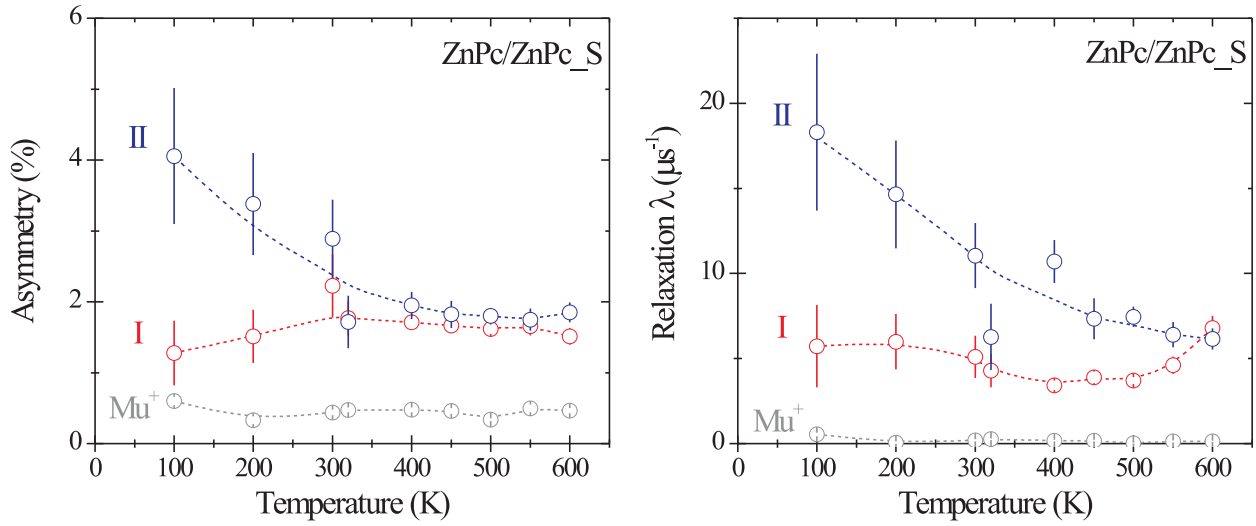

Figure 5.4: Temperature dependence of the asymmetries and relaxations of the diamagnetic fraction and states I and II considering isotropic hyperfine interactions in ZnPc. The dashed lines are mere visual guides indicating the qualitative variation of the quantities shown.

to a motional narrowing effect.

The average hyperfine interaction of these two states, Figure 5.6, also lessens with temperature, in agreement with the frequency pair correlation spectra shown in Figure 5.3. The variation is consistent with a temperature-activated behaviour given by

$$A(T) = A(0) + (A(\infty) - A(0))\, e^{-\frac{E_a}{k_B T}} \ , \tag{5.1}$$

where T is the absolute temperature, k_B is Boltzmann's constant, $A(0)$ and $A(\infty)$ are the $T = 0\,\mathrm{K}$ and $T \to \infty$ limiting values of the hyperfine interaction, and E_a is the activation energy of the process responsible for the temperature dependence. The values of the parameters fitted with (5.1) to the hyperfine interaction of states I and II are shown in Table 5.1; both states have their interactions red-shifted following the same activation energy within errors. In contrast, the hyperfine interaction of state III does not fit well with a temperature-activated function, and indeed does not seem even to exhibit any significant temperature dependence[6]. Its average value is also indicated in Table 5.1.

[6]The lack of information at 200 K is of course conditioning the certainty with which one is allowed to make this statement.

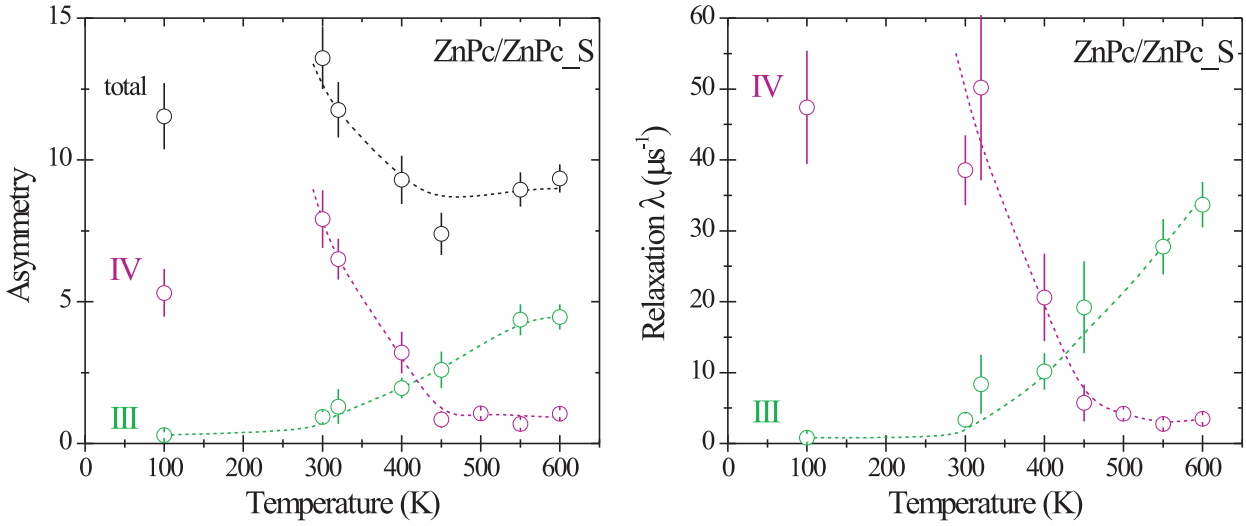

Figure 5.5: Temperature dependence of the asymmetries and relaxations of state III considering an isotropic hyperfine interaction and of the signal component IV in ZnPc. The dashed lines are mere visual guides indicating the qualitative variation of the quantities shown. The data labelled as 'total' refers to the sum of all the asymmetries composing the TF polarisation signal, including those relative to states I and II. The fit results obtained for the temperature of 200 K are not shown in these two plots, since at this temperature the two components III and IV are highly correlated, producing unreasonable values for their asymmetries and relaxations. In spite of this, the signals of states I and II at this same temperature are discernible from states III and IV, and were therefore shown in Figure 5.4.

Table 5.1: Summary of the temperature activated fits to the hyperfine interaction of states I and II with equation (5.1). The average value of the hyperfine interaction of state III is quoted in the last row.

state	$A(0)$ (MHz)	$A(\infty)$ (MHz)	E_a (meV)
I	150(1)	115(2)	44(4)
II	127(1)	117(2)	42(8)
III	21(1)		—

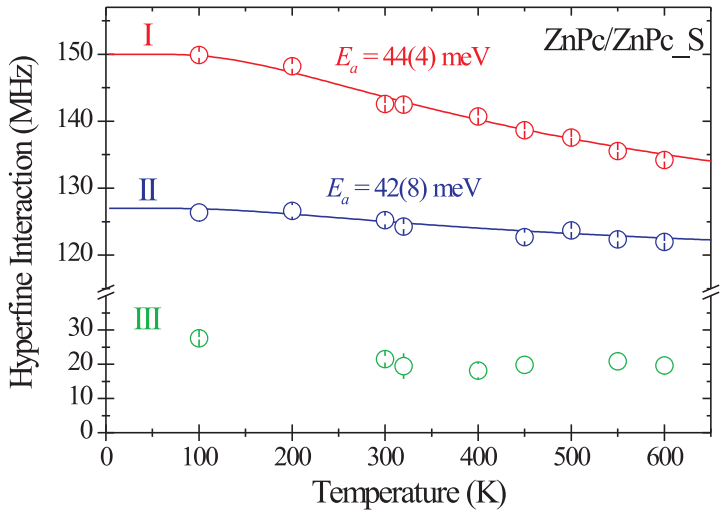

Figure 5.6: Temperature dependence of the hyperfine interaction of states I, II and III in ZnPc. The solid lines are fits obtained with a temperature activation function, equation (5.1). State III does not fit well with that type of temperature dependence.

Full analysis - axially symmetric hyperfine tensors

The hyperfine tensor of muoniated radicals often has dipolar character due to the highly directional nature of the chemical bond established by the muonium adduct with the rest of the molecule [99, 126, 10]. This is true also for the paramagnetic states I-III formed in ZnPc, since their pairs of precession lines in the Fourier transform spectra exhibit the characteristic powder pattern expected from the integration over all possible directions between the hyperfine tensor's symmetry axis and the applied magnetic field (see Section 3.4.3). The generic shape of those powder patterns is enlightened with Figure 5.7, in which simulated distributions with appropriately chosen isotropic and dipolar parameters for all three states were superimposed to the spectra of Figure 5.1. States I and II have distributions with dipolar parameters of respectively positive and negative signs, while state III reveals a rather uncommon overlapped pattern originated by a dipolar parameter in absolute value larger than the isotropic one and opposite in sign.

Simulations as the one presented in Figure 5.7 were taken as the starting point for another set of fits to the same ZnPc data previously analysed, but now using the powder muon polarisation function (3.216) instead of a pair of ω_{12} and ω_{34} precession frequencies to describe the signal of states I-III. State IV and the diamagnetic fraction were fitted in the same way as

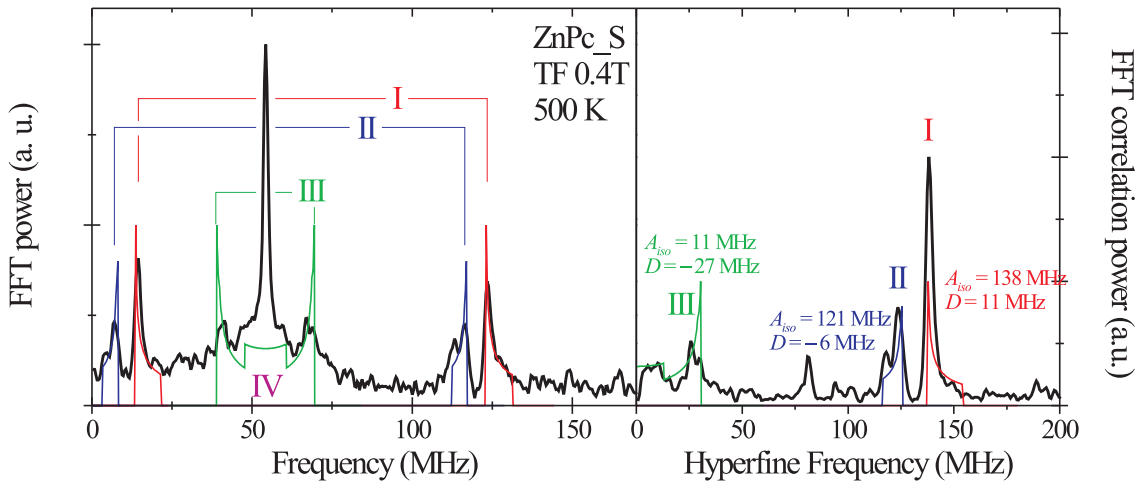

Figure 5.7: Simulated frequency distributions considering axially symmetric hyperfine interactions in ZnPc. The Fourier and frequency pair correlation transforms already shown in Figure 5.1 are consistent with all states exhibiting anisotropy. The hyperfine parameters used for the simulations were extracted from the fit performed at 500 K, and shown later in Figure 5.10.

before, *i.e.* with Lorentzian relaxed Larmor precessions. The motivation for considering this second course of analysis was raised by the necessity in characterising as best as possible the hyperfine structure of these three states, in order to correctly interpret the μSR data relative to the study of spin dynamics performed in Chapter 6.

The fit results are shown in figures 5.8-5.10. More than half of the initial muon polarisation is still unaccounted for; the populations of states I and II were decreased to about 5% of the full asymmetry each, exhibiting again a weak temperature dependence. The average asymmetry of state III is slightly lower than before, but is now approximately constant, being decoupled from the variation of the fourth component's asymmetry. The relaxation of this component still follows the same trend in the highest temperatures, but below room temperature the fitted values exhibit a fast decrease in close similarity to what is observed for its asymmetry. From a close inspection of the Fourier transform spectra of the low temperature data, it seems reasonable to assume that this double behaviour might traduce the loss of sensitivity to this component conveyed by a fast increase of its relaxation under the limited time resolution of the spectrometer.

Most importantly, all hyperfine parameters of states I and II, Figure 5.10, exhibit again a variation consistent with a temperature-activated behaviour following equation (5.1). The results of the fits with this expression are shown in tables 5.2 and 5.3; for the dipolar parameters, the

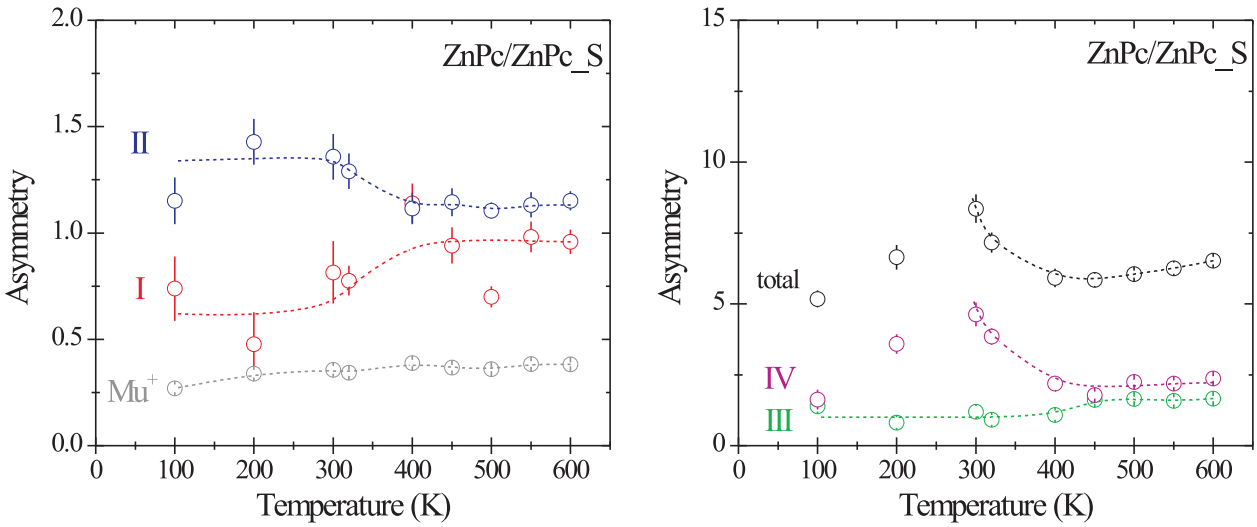

Figure 5.8: Temperature dependence of the fitted asymmetries for all the signal components considered in ZnPc using axially symmetric hyperfine interactions. The dashed lines are mere visual guides indicating the qualitative variation of the quantities shown. In this and the next figures, the data at 200 K relative to state III and component IV are indicated, as with the full analysis no unreasonable values were obtained for their asymmetries and relaxations.

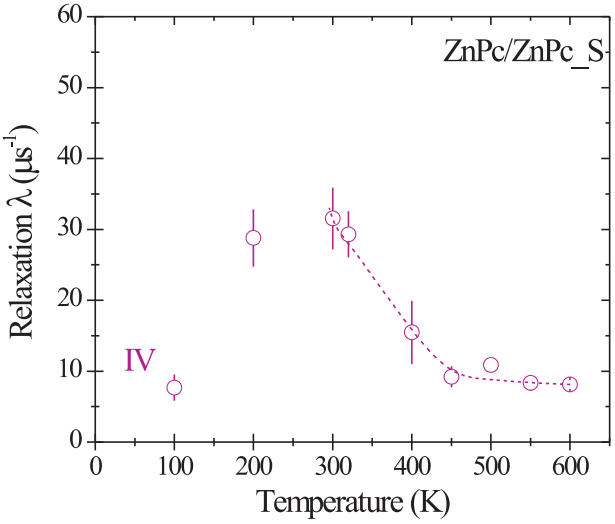

Figure 5.9: Relaxation of the component IV for the temperature dependent time fits of ZnPc considering axially symmetric hyperfine interactions for states I, II and III. The dashed line is a mere visual guide indicating the qualitative variation of component's IV relaxation.

value of $D(\infty)$ was fixed to zero. The activation energies of all four parameters agree superbly to an average value of 42(6) meV. Both hyperfine parameters of state III are also seen not to depend on temperature; their average values are quoted in those two tables.

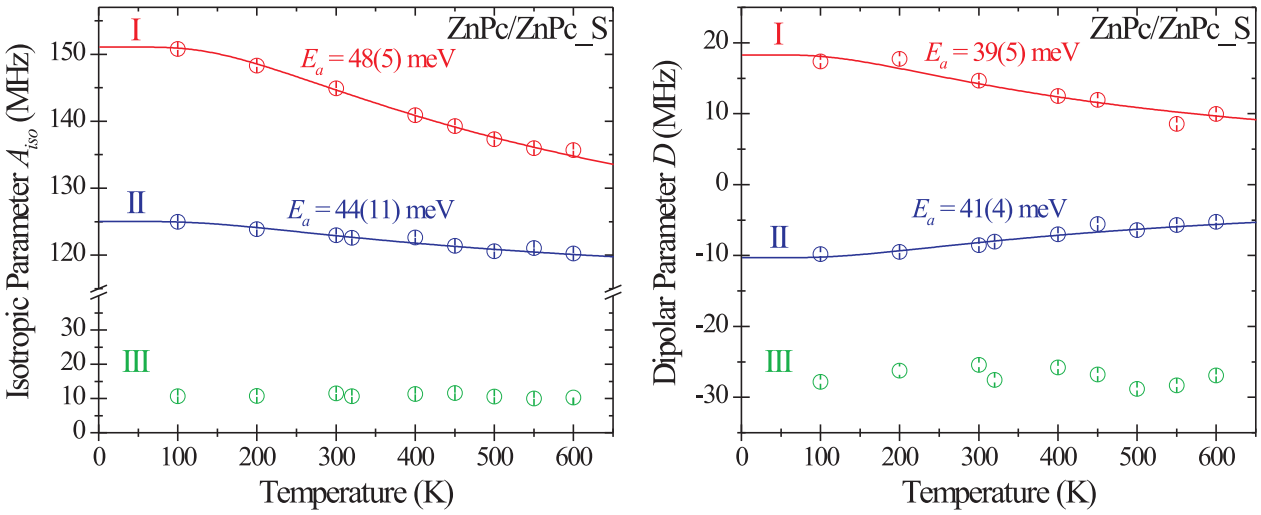

Figure 5.10: Temperature dependence of the hyperfine parameters of states I, II and III in ZnPc considering axially symmetric interactions. The solid lines are fits obtained with the temperature activated function of (5.1). The hyperfine parameters of state III do not exhibit a significative temperature dependence, and again do not fit well with that equation.

Table 5.2: Summary of the temperature activated fits to the hyperfine isotropic parameter of states I and II with equation (5.1). The average value of the isotropic parameter of state III is quoted in the last row.

state	$A(0)$ (MHz)	$A(\infty)$ (MHz)	E_a (meV)
I	151(1)	110(4)	48(5)
II	125(1)	114(2)	44(11)
III	10.8(1)		—

Table 5.3: Summary of the temperature activated fits to the hyperfine dipolar parameter of states I and II with equation (5.1), setting $D(\infty) = 0$. The average value of the dipolar parameter of state III is quoted in the last row.

state	$D(0)$ (MHz)	E_a (meV)
I	+18(1)	39(5)
II	-10(1)	41(4)
III	-27.1(1)	—

5.1.3 Site assignment

In order to deduce the crystalline site of the positive muon for each of the muoniated radicals identified in ZnPc, density-functional theory electronic structure calculations envisaging the hyperfine properties of hydrogen adducts to the isolated ZnPc molecule were performed. The trial sites used in the computation, see Figure 5.11, included all possible additions to unsaturated bonds (sites *a*-*f*) together with a position favourable for bonding with the central Zn atom (site *g*). The full procedure, implemented using the well-known GAUSSIAN 98 code [41], consisted in a first step of geometry optimisation using the B3LYP electron exchange-correlation functional [36], followed by a single-point calculation of the adduct's hyperfine interaction with the B3PW91 functional. This particular combination, often seen in μSR literature [69], brings together the efficiency of the B3LYP functional in geometry optimisations of large molecules with the known superior performance of B3PW91 for the determination of hyperfine parameters [33, 34, 69]. Carbon and nitrogen atoms were described using the combination of pseudopotentials from Pacios and Christiansen [84] and the valence basis set from Stevens *et al* [128] commonly applied for cyclic compounds having C and N atoms. The compact effective potential CEP-31G with double-zeta splitting on the valence was used for the zinc atom, while for hydrogen atoms and the extra H adduct the 3-21G and the 6-31++G basis sets were taken for the geometry and the hyperfine computations respectively. The initial geometry of the ZnPc molecule was obtained from x-ray diffraction values found in references [32], while downstream the calculation standard

convergence criteria on the energy and forces were used.

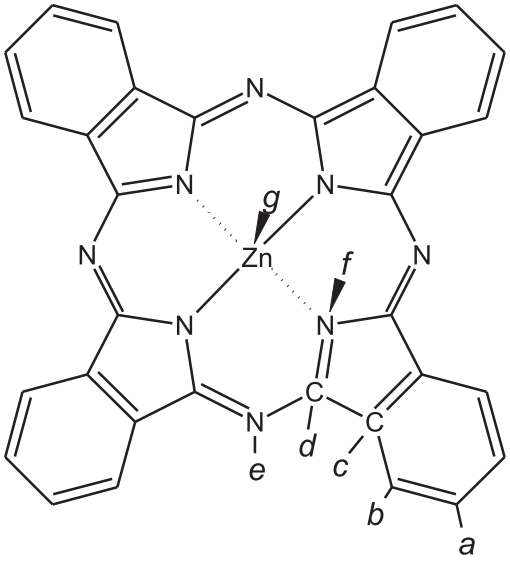

Figure 5.11: Trial ZnPc addition sites for hyperfine interaction calculations. All possible additions to unsaturated bonds (sites *a*-*f*) together with a position favourable for bonding with the central Zn atom (site *g*) are included.

From all the addition positions considered, only sites *a*, *b* and *g* were found to yield electrostatically stable configurations. The solution for site *g* corresponds to a dissociated ZnPc + H state[7], while sites *a* and *b* possess calculated hyperfine interactions with an order of magnitude typical of radical states. The results of the calculation are given in Table 5.4 for sites *a* and *b* only, where the relative formation energy of each configuration is indicated and the calculated (hydrogen) hyperfine values were scaled to muonium values by the proton and muon gyromagnetic ratios,

$$A_\mu = \frac{\gamma_p}{\gamma_\mu} A_p \ .$$

These two sites have very similar hyperfine interactions, in close resemblance to what happens with the muoniated states I and II. Based on this fact, we assign *a* and *b* as being the sites of states I and II respectively, where we also take into account that state I has the largest hyperfine interaction of the two, the same happening to site *a* when compared to *b*. The assignment is made clear in Table 5.4 by quoting additionally the experimentally determined $T = 0\,\mathrm{K}$ values for states I and II. It should be noted that this result is not surprising, since the similarity of

[7]The resulting hyperfine interaction of this hydrogen adduct was identical to the vacuum value shown in Table 3.3.

values for states I and II was already a strong hint that they were bound to unpaired electrons with alike spatial distributions.

Table 5.4: Calculated hyperfine interactions (A_{calc}) and relative formation energies (ΔE_{calc}) of muon addition sites a and b to the ZnPc molecule. The last two columns display the experimentally determined $T = 0\,\mathrm{K}$ values for states I and II ($A(0)$) and the ratio between the experimental and the calculated hyperfine couplings.

site	A_{calc} (MHz)	ΔE_{calc} (meV)	*state*	$A(0)$ (MHz)	$A(0)/A_{\mathrm{calc}}$
a	279	0	I	151(1)	0.54
b	274	+186	II	125(1)	0.46

The computed hyperfine interactions are about a factor of 2 larger than the experimentally measured ones, in complete contradiction with the hyperfine isotope effect expected between proton and muon couplings. The difference could arise from the nature of the mechanism with which an hyperfine interaction exists at the positive muon upon muonium addition to a double bond in an organic molecule, and consequent sharing of electronic density. This mechanism, called σ-π *hyperconjugation* [20, 99, 95, 10], explains the small hyperfine interactions observed in muoniated radicals when compared to the isolated muonium state; the positive muon assumes a position near a carbon atom, known as the α-carbon, establishing a covalent C—Mu σ bond with it by suppressing one of the electrons the α-carbon shared in a C—C π bond with its neighbouring carbon atoms, known as β-carbons. An unpaired electron occupying a p_z orbital is therefore left localised at a β-carbon, which may overlap with the doubly occupied C—Mu σ orbital, giving rise to a small unpaired density at the muon's site. Nevertheless, σ-π hyperconjugation is also the mechanism occurring when an hydrogen atom adds to an organic molecule, and in fact the smaller zero-point energy of the muon is a factor that *enhances* σ-π hyperconjugation in organic muoniated radicals[8], giving rise to muon hyperfine couplings about 1.4 times *larger* than scaled proton constants. The discrepancy observed in Table 5.4 is thus not due to an isotope effect, but has rather to do with geometric constraints related with the solid-

[8]This happens because the overlap between the C_α—Mu σ and the C_β p_z orbitals decreases when the relative motion between the two orbitals becomes faster.

state packing of β-phase phthalocyanines. In fact, in the β phase the phthalocyanine molecules are stacked in tilted columns of layers separated by a small distance of about 3.2Å (Figure 5.12). This develops intercolumnar hydrogen bonding interactions which pull the hydrogen atoms at the outer benzene rings radially away from the molecule [32]. Muoniated radicals located at those sites will therefore take part in the hydrogen bonding, producing an increase in the angle defined by the C–Mu σ bond and the p_z orbital at the β carbons (Figure 5.12). As a result, a decrease of hyperconjugation and thus of unpaired spin density at the muon occurs. The same bending effect may also arise due to the presence of the molecule stacked on top of the radical, which will force it to adopt a more planar configuration in view of the short inter-layer distance.

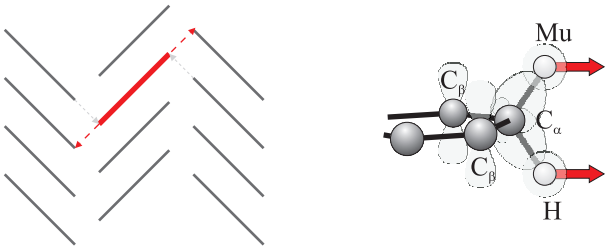

Figure 5.12: Decrease of hyperconjugation effects for muoniated radicals formed in solid-state pthalocyanines. On the left, the herring-bone stacking of β phase Pcs is shown; this configuration enhances hydrogen-bonding between adjacent columns, pulling the outer hydrogens away from the molecule. On the right, the effect of hydrogen bonding in a muoniated radical formed at sites a and b is illustrated; the overlap between the C-Mu σ bond and the p_z orbitals of the β carbons is decreased relative to what would happen in an isolated Pc molecule.

The nonexistence of any other stable addition sites leading to bonded states leaves the assignment of state III open. One may only infer that the muon is either located at an addition site which becomes stabilised with the solid state arrangement of ZnPc, or assumes an interstitial position between molecules. This subject will be discussed in more detail in Chapter 7.

5.1.4 States in doped samples

The muon states in the tentatively oxygen-doped sample ZnPc_oxy (Section 4.2) were also briefly investigated in a single high-transverse field measurement at low temperature (100 K). Figure 5.13 compares the correlation frequency spectrum of that run with data collected at the same temperature using sample ZnPc_S. The four paramagnetic components are still observed with no apparent significant changes; the same is revealed by the time fit, where the parameters extracted (Table 5.5) are essentially equal to the ones obtained for the undoped ZnPc_S sample.

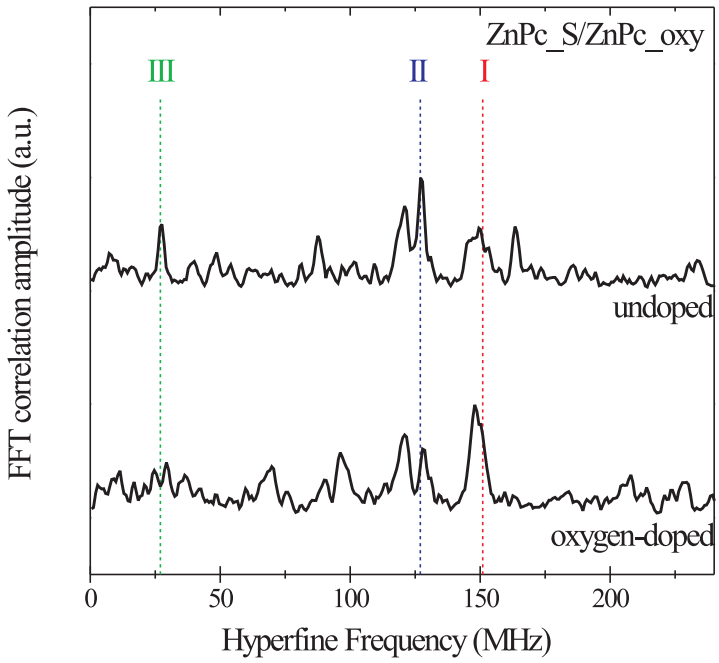

Figure 5.13: Correlation frequency spectrum of the oxygen-doped sample ZnPc_oxy in high transverse field, compared with an equivalent spectra taken with ZnPc_S at the same temperature. No significant changes exist between both spectra. The dashed lines are guides to the eye.

Table 5.5: Summary of the fitted parameters to the polarisation of ZnPc_oxy. The values for data taken with the undoped sample ZnPc_S at the same field and temperature are also shown.

		ZnPc_oxy	ZnPc_S
State I	*asymmetry* (%)	0.8(2)	0.7(2)
	A_{iso} (MHz)	150.7(2)	150.8(1)
	D (MHz)	17.2(3)	17.4(2)
State II	*asymmetry* (%)	0.6(1)	1.2(1)
	A_{iso} (MHz)	124.6(1)	125.0(2)
	D (MHz)	-10.0(2)	-9.8(3)
State III	*asymmetry* (%)	1.3(2)	1.4(2)
	A_{iso} (MHz)	10.6(1)	10.7(2)
	D (MHz)	-28.1(3)	-27.8(3)
State IV	*asymmetry* (%)	1.7(1)	1.6(2)
	λ (μs^{-1})	8(1)	8(2)
Diamagnetic	*asymmetry* (%)	0.28(2)	0.27(2)

5.2 H_2Pc

5.2.1 Number and nature of muon states

A shorter version of the high-transverse field measurements performed in ZnPc was employed to investigate the nature and number of muon states formed in H_2Pc. The experiments, carried out with sample H_2Pc_S, included only temperatures at and above room temperature. The four signal components (along with a diamagnetic precession) observed in ZnPc also exist in H_2Pc_S at all measured temperatures, as depicted in Figure 5.14. The relative populations and hyperfine interactions have slightly different values; the population of state III seems to dominate over states I and II more clearly than in ZnPc, exhibiting now lower and harder to resolve hyperfine interactions. Their values amount to *ca.* 112 and 106 MHz for the run presented (550 K), while state III appears to have a coupling constant roughly around 16 MHz. The ω_1-ω_2 level-crossing of states I-II occurs therefore nearby 0.4 T. In addition, the anisotropy of states I and II seems to be quite low when compared with what was determined in ZnPc.

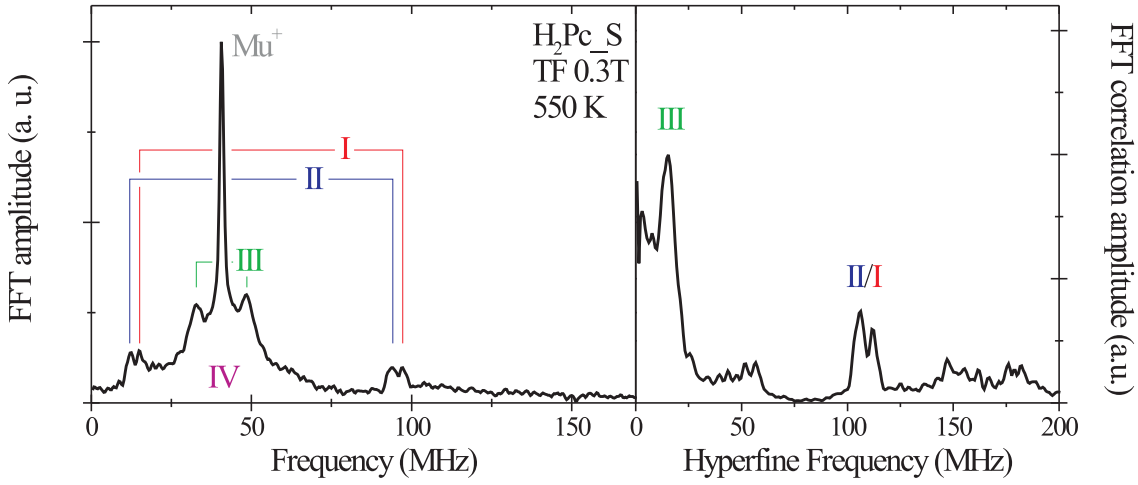

Figure 5.14: Fourier (left) and frequency pair correlation (right) transforms of H_2Pc obtained at 550 K under an applied transverse field of 0.3 T. Similarly to ZnPc, the three pairs of lines I, II and III observed in addition to the Larmor precession of diamagnetic muons at 40.6 MHz show the formation of three different paramagnetic muon states in H_2Pc. The fourth broad paramagnetic signal is also present here.

Again, all states are visible throughout the investigated temperature range (Figure 5.15), suggesting that they do not ionise below sublimation temperatures for H_2Pc. The temperature dependence of the frequency pair correlation spectra also reveals a red-shift of the hyperfine

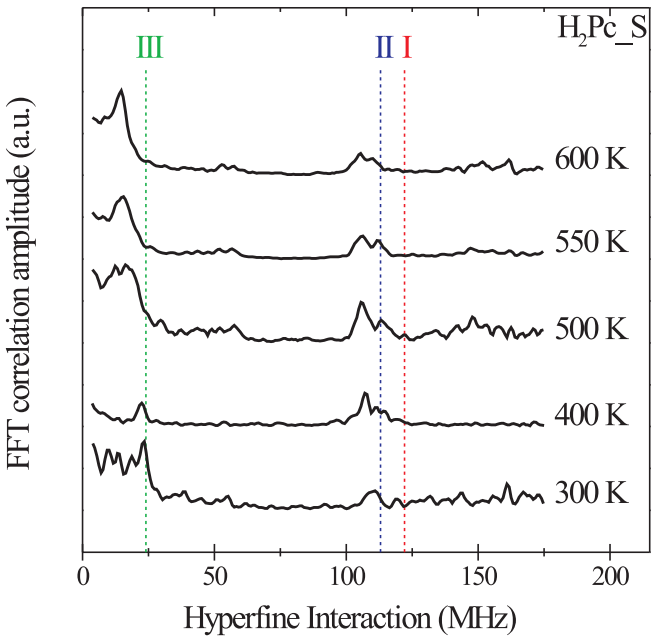

Figure 5.15: Frequency pair correlation spectra of H_2Pc at different temperatures. For states I and II, the dotted lines indicate the $T = 0\,\mathrm{K}$ values obtained from the temperature activated fits to the hyperfine interaction shown in Figure 5.18; for state III, it indicates the value of $A_{iso} - D/2$ at room temperature.

couplings of states I and II. A decrease with temperature of state III's hyperfine interaction is now clearly observed too.

5.2.2 Relative populations and hyperfine parameters

The quantitative analysis of the temperature dependent data shown in Figure 5.15 was done using a variation of the overall polarisation function employed for the time spectra of ZnPc. The change, which consisted in fitting the polarisation of states I and II with a pair of high-field frequencies instead of the frequency distribution function characteristic of axially symmetric states in policrystalline samples, was prompted by practical difficulties in independently resolving the two components. The small anisotropy apparent from the Fourier transform spectra for these two states was described using a lorentzian relaxation of fixed width ($\lambda = 1\,\mathrm{MHz}$, a value chosen taking into account the small population of those components and the line width observed in the Fourier transform spectra). State III was still fitted with a powder polarisation function; the results of the time fits are shown in figures 5.16-5.18.

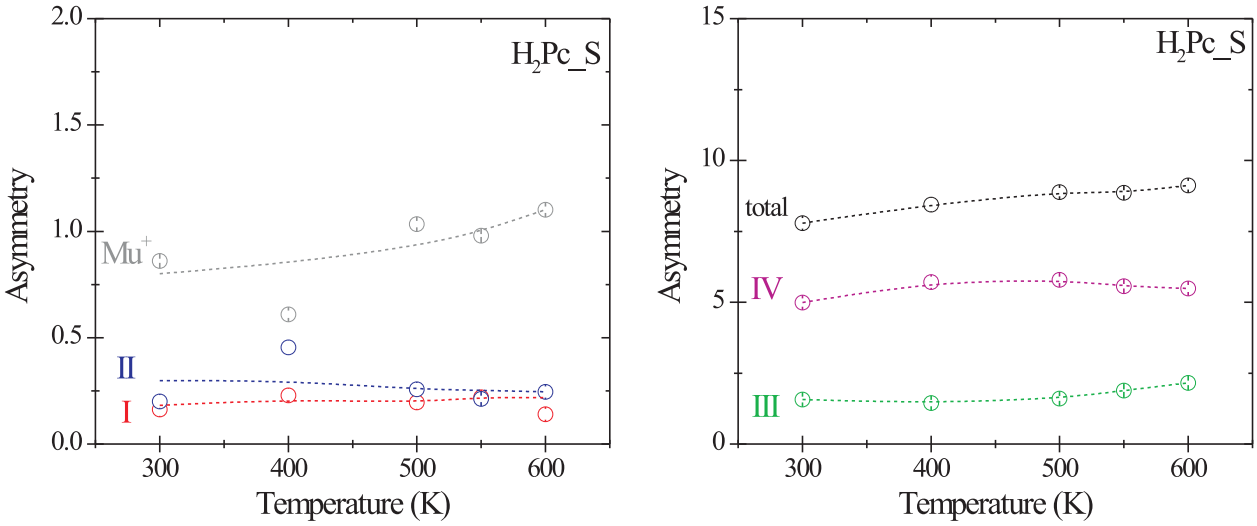

Figure 5.16: Temperature dependence of the fitted asymmetries for all the signal components observed in H_2Pc. The dashed lines are mere visual guides indicating the qualitative variation of the quantities shown.

Also in H_2Pc a large fraction of the initial muon polarisation is missing (more than 50%). States I and II have fairly constant populations in the addressed temperature range, but which are less than half their values observed in ZnPc. The diamagnetic fraction, on the contrary,

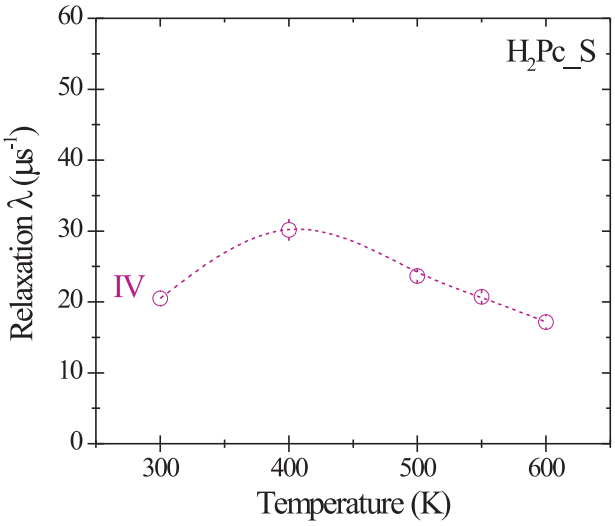

Figure 5.17: Relaxation of the component IV in H_2Pc. The dashed line is a mere visual guide indicating its qualitative variation.

is more than the double measured in ZnPc. The population of components III and IV is approximately constant, with the relaxation of the paramagnetic state IV decreasing at high temperatures.

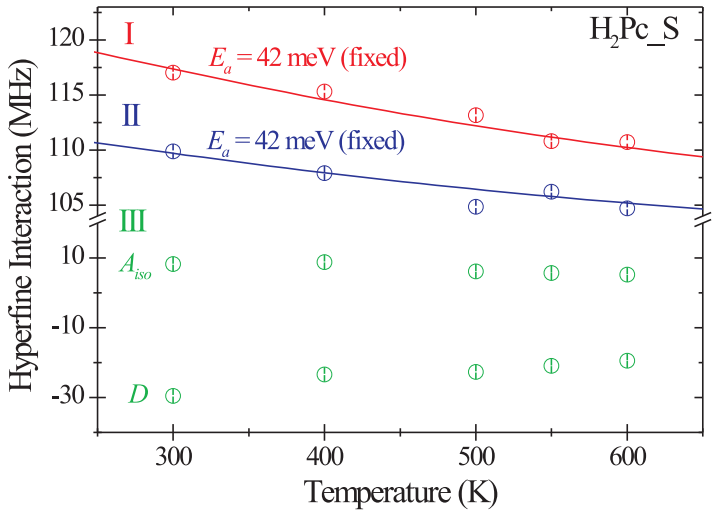

Figure 5.18: Temperature dependence of the hyperfine parameters of states I, II and III in H_2Pc. The solid lines are temperature activated fits to states I and II fixing the activation energy to 42 meV. No equivalent fit was performed to the hyperfine parameters of state III (see text for details).

The temperature variation of the hyperfine parameters drawn from the fits is shown in Figure 5.18. The number of different temperature points is not enough to quote reliable activation energies from unambiguous fits with equation (5.1), but the temperature variation of states I and II seems at least to be consistent with an activation energy similar to the energies found in ZnPc. The hyperfine interactions of states I and II were therefore fitted using the average value of 42 meV determined for ZnPc; the corresponding values of $A(0)$ and $A(\infty)$ are quoted in Table 5.6. As for state III, the lack of data did not allow to clarify if the hyperfine parameters followed or not a temperature activated dependence. Nevertheless, the clear change observed indicates that if an activated behaviour is to exist, an energy larger than 42 meV is necessary to describe it.

Table 5.6: Summary of the temperature activated fits to the hyperfine parameter of states I and II in H_2Pc. The fit was done fixing the activation energy to 42 meV.

state	$A(0)$ (MHz)	$A(\infty)$ (MHz)	E_a (meV)
I	123(1)	94(2)	42 (fixed)
II	113(2)	95(3)	42 (fixed)
III	—	—	—

5.2.3 Site assignment

In close parallel to what was done with ZnPc, electronic structure calculations of hydrogen adducts to H_2Pc were performed in order to assign the observed paramagnetic states I-III to addition sites in the molecule. The trial sites were the same as the ones indicated in Figure 5.11, although in the case of H_2Pc two different calculations per site need to be performed in order to account for the two isomeric forms the molecule may have for the same adduct, depending if it is in the benzene ring corresponding to the pyrrole unit bonding one of the two central hydrogens ($\parallel$ isomer), or if it is in a perpendicular one ($\perp$ isomer). The exact same calculation strategy, exchange and correlation potentials, and pseudo-potentials for the C and N atoms where used.

Once more, the only stable configurations found correspond to sites *a*, *b* and *g*, the latter

Table 5.7: Calculated hyperfine interactions (A_{calc}) and relative formation energies (ΔE_{calc}) of muon addition sites a and b to the H_2Pc molecule. The last two columns display the experimentally determined values at ($T = 0\,\mathrm{K}$) for states I and II, and the ratio between the experimental and the calculated hyperfine couplings.

site	A_{calc} (MHz)	ΔE_{calc} (meV)	*state*	$A(0)$ (MHz)	$A(0)/A_{\mathrm{calc}}$
a	273	0	I	122(2)	0.45
b	262	+77	II	93(3)	0.36

being again a dissociated state. The results for the bound states are given in Table 5.7 following the same conventions used for the case of ZnPc; the values quoted are already the average of the two isomeric forms for each adduct. The hyperfine parameter of site a is again the highest one, and also the most stable. It therefore corresponds to state I, as indicated in Table 5.7, while state II is formed at site b. An anomalous hyperfine isotope ratio is present in the H_2Pc results as well due to the reduction of σ-π hyperconjugation by one (or both) the mechanisms referred for ZnPc. The site of state III in H_2Pc did not stem from these calculations either, but will be further discussed later.

5.2.4 States in doped samples

No genuinely doped samples of H_2Pc where prepared in this work, but a pair of milled and non-milled samples (see Chapter 4) were prospectively measured in high-transverse field to assess the effect of mechanical ball milling in the μSR signal. Two runs of high statistics were taken with samples H_2Pc_03 and H_2Pc_03m15 at 400 K with an applied field of 0.4 T. Their FFT amplitude transforms are shown in Figure 5.19; as it is easy to see, the population of all paramagnetic states is severely decreased by the milling process. This result ruled out the viability of mechanical ball milling for the doping of phthalocyanines.

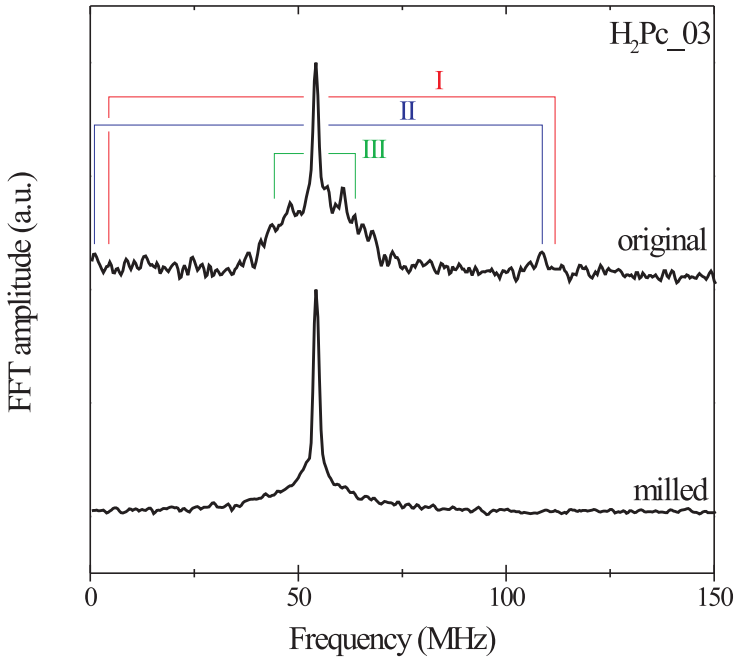

Figure 5.19: Effect of ball-milling in the Fourier transform of H_2Pc. The population of all paramagnetic states is severely decreased by the milling process.

5.3 CuPc

Similarly to what was done with ZnPc and H_2Pc the formation of muon states in CuPc was addressed with temperature dependent measurements in high-transverse fields using sample CuPc_S. Since CuPc has originally an unpaired electron from the Cu atom, the addition of muonium is expected to generate a diamagnetic environment for the muon, as the total number of electrons in the muoniated molecule becomes even. The typical μSR time spectrum of CuPc (Figure 5.20) shows indeed a precession signal with the muon Larmor frequency, but clearly two distinct components bearing different relaxation rates are present. This type of signal is found throughout the whole investigated temperature range (2-600 K), with both components getting slightly less relaxed as temperature rises. The time-dependent muon polarisation is well described by two lorentzian-shaped Larmor precession components, one fast and another slowly relaxing; fit results for data collected with an applied field of 0.45 T are shown in Figure 5.21.

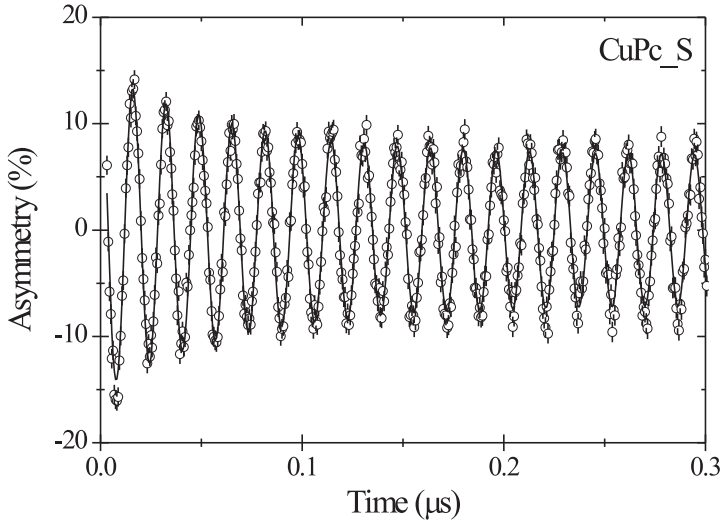

Figure 5.20: μSR time spectrum of CuPc in a transverse field of 0.45 T at 320 K. The solid line is a fit performed with two precession components at the muon Larmor frequency, but with different lorentzian relaxations.

At low temperatures, a missing fraction of about 50% of the full muon polarisation exists; this missing fraction is gradually recovered as temperature increases, reaching almost zero at 600 K. The amplitudes of the two fitted components also evolve with temperature; a shift of weight from the fast to the slow relaxing component is seen above 200 K, while below this

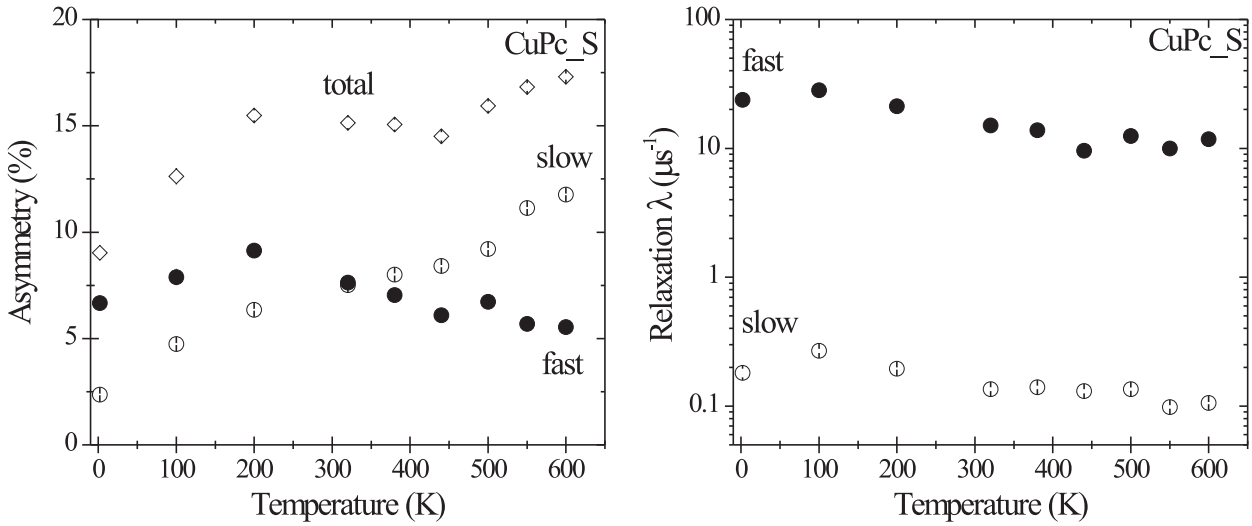

Figure 5.21: Temperature dependence of the asymmetries and relaxations for the two components observed in CuPc. Both relaxations exhibit a very weak dependence.

temperature an additional asymmetry transfer is apparently played between the fast component and the missing fraction. The relaxation rates, on the other hand, show a very weak, but congruent, temperature dependence. Their ratio is constant within errors for all temperatures, with a value of about 1:100. The temperature dependence of both relaxations is well fitted with a temperature-activated behaviour given by

$$\lambda(T) = \lambda(0)\ e^{+\frac{E_a}{k_B T}}\ , \tag{5.2}$$

as shown in the Arrhenius plot of Figure 5.22. The pre-exponential factors $\lambda(0)$ are related by the 1:100 ratio already mentioned, and the activation energies are identical. Their value is rather small, amounting to an average between both of 10(2) meV.

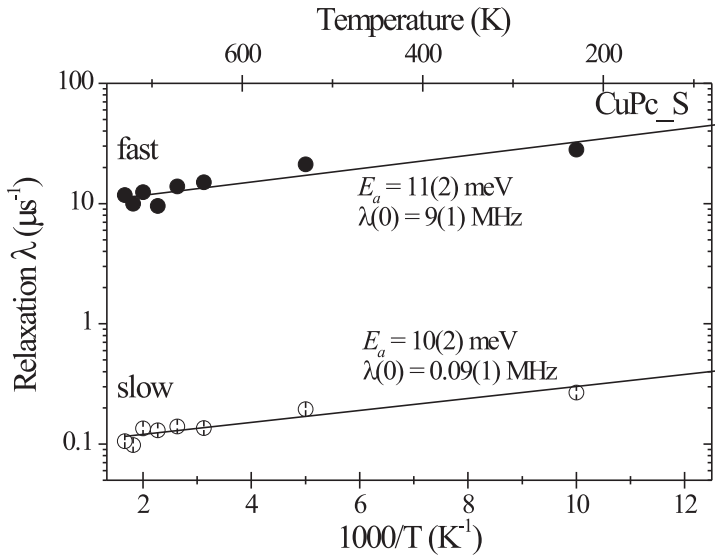

Figure 5.22: Arrhenius plot of the two relaxations observed for CuPc. The solid lines are fits with the temperature-activated function (5.2). The activation energies have a value around 10 meV.

Chapter 6

Spin dynamics of muon states in ZnPc and H_2Pc

Experimental results concerning the spin dynamics of the muon states identified in the three phthalocyanines addressed with this work are presented in this chapter. This study was performed with μSR measurements in longitudinal-field (LF) geometry using the GPS, DOLLY and EMU spectrometers. The field dependence of the μSR LF signal at selected temperatures was used to infer about the nature of the dynamics, while its temperature dependence over a wide range (5-650 K) was analysed to extract the relevant dynamical parameters of the physical processes involved in the muon spin dynamics.

In ZnPc and H_2Pc, the signal is seen to be dominated by spin-exchange features which relate directly to the muon state labelled as state III in the last chapter. For these two compounds, the time-domain data was firstly described in terms of a restricted number of simple relaxing components, as reported in the first two sections of the chapter. Those components were then interpreted in terms of a model that takes into account the directional averaging of the spin-relaxation rate for a paramagnetic state undergoing spin-exchange dynamics in a polycrystalline sample. The third section of the chapter describes this analysis model, and presents quantitative results regarding the temperature dependence of the spin-flip rate underwent by state III in the investigated samples.

6.1 ZnPc

The spin dynamics of the muon states identified in the last chapter for ZnPc was investigated with time-dependent longitudinal-field measurements using the undoped samples ZnPc_S and ZnPc_p3 (refer to Chapter 4 for sample descriptions). The spectra obtained allowed no individual distinction of the four components observed in transverse-field, although in general terms a relaxed behaviour bearing a time scale around $1\,\mu$s exists. This indicates the presence of dynamical features which give rise to relaxation rates of the order of $1\,\mu s^{-1}$, a magnitude that confirms a paramagnetic origin for the dynamics. Indeed, nearly all muon states formed in ZnPc are paramagnetic, being therefore particularly sensitive to dynamical phenomena via their unpaired electronic spin. As it is argued later in Section 7.2.1 (Chapter 7), the spin dynamics of the LF muon polarisation in ZnPc is attributed to spin-exchange scattering between one of the paramagnetic muon states formed in this compound (state III) and diffusing charge carriers (see Section 3.4.4).

Since it was not possible to easily relate the LF signal to the paramagnetic states observed in transverse-field, the description of the data was performed using a phenomenological fit model consisting in two exponentially decaying components and a third constant component. This combination was found to be the one that produced the best fits to the time dependence of the muon polarisation throughout the whole investigated range of fields and temperatures, not only regarding goodness-of-fit chi-squared values, but also the smoothness of variation of the parameters involved both with the applied field and the temperature[1]. It also presents the advantage of making a clear distinction between rapidly varying signals, described by the component having the highest relaxation rate, henceforth referred to as the *fast* component, from slowly relaxing ones, described by the *slow* component, and from *very* slowly relaxing ones, accounted with the *constant* component[2]. As an example, Figure 6.1 shows the time fit obtained with this model to the FB-asymmetry spectrum of ZnPc_p3 collected with the GPS instrument at 600 K using an applied field of 0.1 T.

[1]This criterium was judged from the visual inspection of the relaxation and amplitude *versus* field and temperature graphics obtained with the fit model. A similar consistency, with comparable chi-squared values, was also found with a model composed by a single stretched exponential of the form $a\ e^{-(\lambda t)^{\beta}}$, but the total polarisation values were not matched as satisfactorily as with the two-relaxation, one-constant model eventually adopted.

[2]The distinction between slowly and very slowly relaxing signals is made in a sense that the μSR histogram, while being long enough to attribute a finite relaxation to slow signals within experimental errors, is too short to distinguish very slowly relaxing signals from absolutely non-relaxing ones.

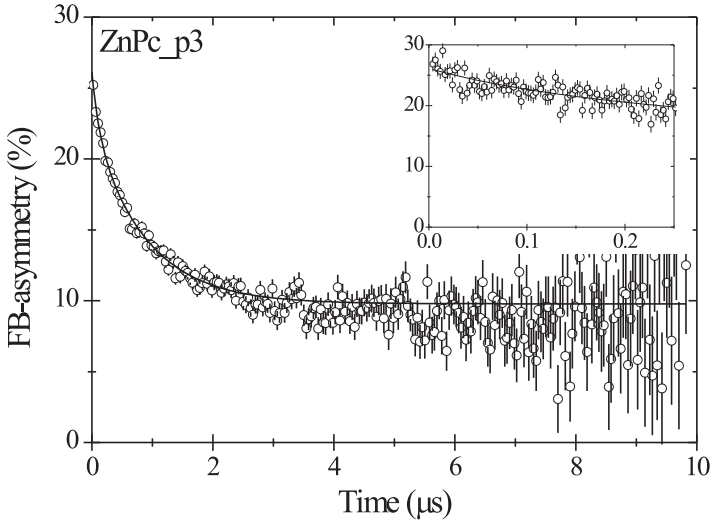

Figure 6.1: μSR time spectrum of ZnPc in a longitudinal field of 0.1 T at 600 K. The solid line is a chi-squared fit performed with two exponentially relaxed components plus a constant component; the insert shows it in detail for the earliest instants. The fitted values are $A_{\text{fast}} = 3.6(6), \lambda_{\text{fast}} = 9(3)\,\mu\text{s}^{-1}$; $A_{\text{slow}} = 12.7(5), \lambda_{\text{slow}} = 1.14(6)\,\mu\text{s}^{-1}$; $A_{\text{constant}} = 9.8(1)$. Translation of asymmetries A to initial fractions a using the maximum FB-asymmetry value ${A_{\text{FB}}}^{max} = 27.7(1)\%$ determined for this measurement using a silver mask yield the values $a_{\text{fast}} = 0.13(2)$; $a_{\text{slow}} = 0.46(2)$; $a_{\text{constant}} = 0.35(1)$.

6.1.1 Field-dependent signal

Figures 6.2 and 6.3 present the field dependence of the LF signal obtained for ZnPc at 150 K and 600 K respectively. The first set of data does not exhibit information relative to the fast component, since it was measured with a pulsed-beam instrument (EMU) and therefore lacks the necessary time resolution to observe fast-decaying signals[3].

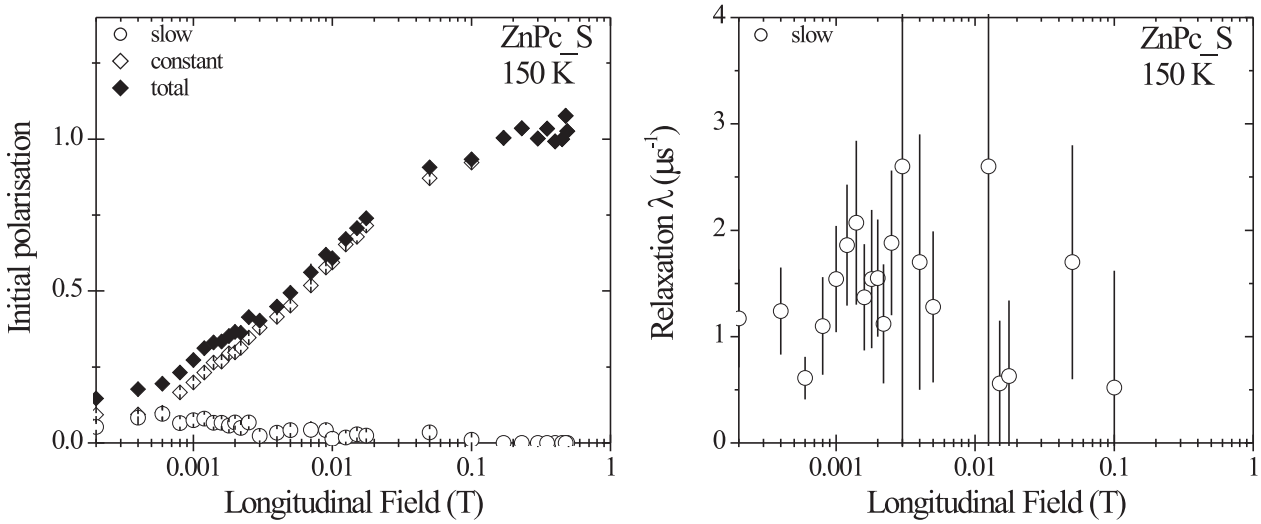

Figure 6.2: Field-dependence of the LF signal for ZnPc at 150 K. The slow component's relaxation appears to be constant, with a value of about $1\,\mu s^{-1}$. No information about the fast component exists at this temperature since this set of data was obtained with the EMU instrument (see text).

At 150 K, the slow component exhibits a very small fraction, which decreases with field. The slow relaxation is poorly defined due to this fact, but seems to be constant to about $1\,\mu$s. The signal is fully repolarised beyond 0.1 T, although none of the two observed components (slow and constant) matches any of the expected repolarisation curve shapes for the non-oscillating polarisation of the three states identified in ZnPc, as depicted by the simulated curves in the left plot of Figure 6.4. At 600 K, the slow component's fraction is considerably larger, and its relaxation becomes well defined. A relaxation peak is clearly observed around 0.08 T, a value in agreement with the ω_1-ω_2 level-crossing field of state III obtained from the analysis using isotropic hyperfine interactions performed in the first part of Section 5.1.2 (refer to Table 5.1 for the fitted value of the hyperfine interaction, and to equations (3.55) and (3.51) for the definitions

[3]The typical time resolution attained with the muon beams at RAL is of the order of 0.1 μs (*cf.* Section 3.2.6).

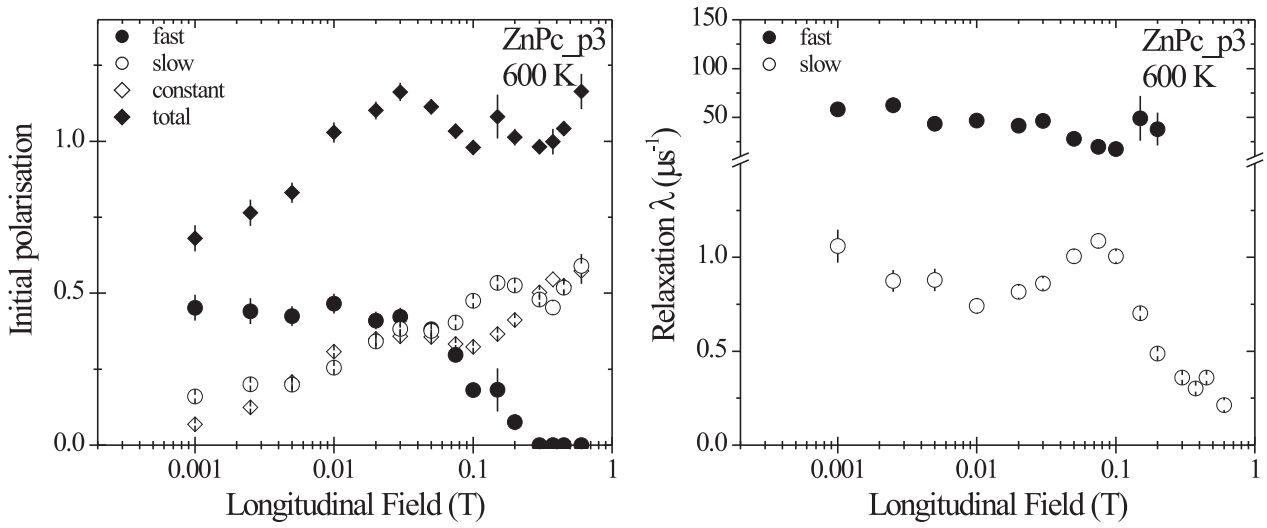

Figure 6.3: Field-dependence of the LF signal for ZnPc at 600 K. The slow component's relaxation exhibits a peak at around 0.08 T, a value which matches the level-crossing field of state III.

of $x^{iso}_{12\,\mathrm{cross}}$ and B_0 respectively),

$$B_{\mathrm{cross}} = x^{iso}_{12\,\mathrm{cross}} \times B_0(\mathrm{III}) = 0.077(4)\,\mathrm{T}\ .$$

This is a distinct indication that for the high temperature range, state III plays the main role in the LF signal of ZnPc, dominating the slow component and exhibiting a feature typical of spin-exchange processes for anisotropic paramagnetic states (Section 3.4.4, Chapter 3).

The slow component, however, does not provide a full description of the LF signal generated by state III, as its field dependence is not readily consistent with the repolarisation curve that state III should exhibit (right side of Figure 6.4), even though similar trends are clearly recognised in the region around and above 0.1 T. The shape of the fast component, on the other hand, is complementary to the shape expected for the repolarisation curve of that state. Since the complementary of the repolarisation curve is the expected *oscillating* amplitude in longitudinal-field geometry (Section 3.4.3, Chapter 3), it becomes clear that the fast component is parameterising the rapidly oscillating polarisation of state III. The reason why this fraction of polarisation appears as an exponentially damped constant signal instead of a relaxed oscillating function is due to the distribution of oscillating frequencies generated by the highly anisotropic character of state III, as the powder pattern imprinted by the sample's polycrystalline environment produces a width larger than the distribution's average value (Figure 6.5). The width of

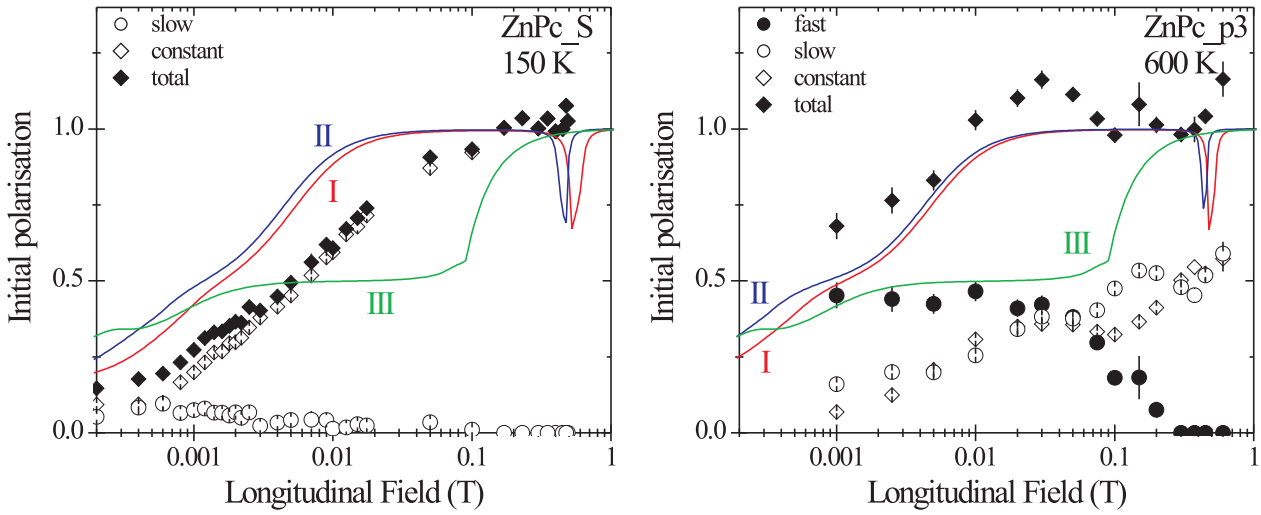

Figure 6.4: Initial polarisation values of LF components *vs.* expected repolarisation curves of states I, II and III in ZnPc at 150 K (left) and 600 K (right). The simulated repolarisation curves shown here were obtained using hyperfine parameters given by Equation (5.1) with the fitted values of Tables 5.2 and 5.3 for states I and II, and by the average values quoted in those same tables for state III. The simulation also took into account the geometric averaging of the non-oscillating polarisation for all possible directions of the hyperfine tensor's symmetry axis in a polycrystalline environment.

that distribution, estimated to be of the order of $15\,\mu s^{-1}$, is also in accordance with the measured relaxation rate of the fast component (refer to the caption of Figure 6.5).

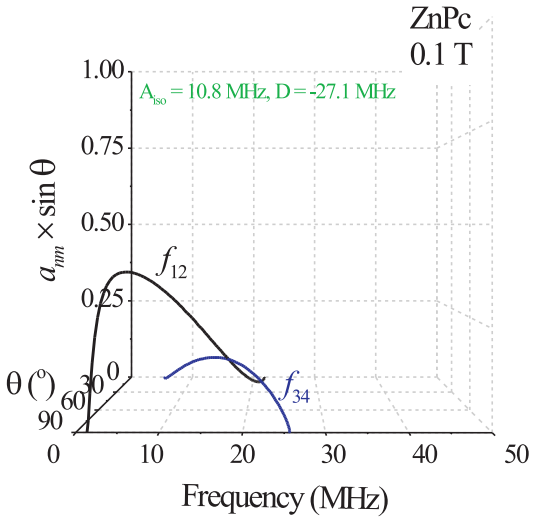

Figure 6.5: Frequency distribution of the expected LF oscillating components in ZnPc for state III in a field of 0.1 T as a function of the angle θ defined by the hyperfine tensor's symmetry axis and the external field. The overall distribution, properly weighted by the geometric averaging in a polycrystalline environment, is given by $a(f) = \sum_{n,m} \int_0^{2\pi} a_{nm} \sin\theta \; d\theta$. $a(f)$ is a left-lobbed function with a width of the order of $15\,\mu s^{-1}$ and average value around 10 MHz; its time-domain representation is therefore consistent with a non-oscillating exponentially damped signal bearing a relaxation rate roughly given by[5] $3 \times 15 = 45\,\mu s^{-1}$, a value which is in accordance with the measured relaxation rate of the fast component (see Figure 6.3). The two curves shown assume the absence of spin dynamics.

6.1.2 Temperature-dependent signal

The temperature behaviour of the LF signal in ZnPc was followed near the slow component's relaxation peak field, with measurements at a field of 0.1 T for samples ZnPc_S and ZnPc_p3. Figures 6.6 and 6.7 show the results of those measurements in terms of the three phenomenological components used to describe the data (the set of data regarding sample ZnPc_S was again measured with the EMU instrument, allowing no access to the fast component). The slow component's relaxation increases with temperature in both samples, as would be expected for

[5] It is straightforward to show that the time-domain relaxation of a lorentzian frequency distribution is $\lambda = \pi \times \Delta f$, Δf being the FWHM of the distribution; for a generic single-lobed distribution, the same relation should also approximately stand.

the LF relaxation produced by a spin-exchange process in the slow spin-flip regime of dynamics (Section 3.4.4, Chapter 3). The specific growth, however, is distinct for the two samples: while in sample ZnPc_S the slow relaxation onsets at around 200 K from zero, attaining a value of $0.5\,\mu s^{-1}$ at 500 K, in ZnPc_p3 it departs from a value of about $0.65\,\mu s^{-1}$ sitting in a temperature plateau spanning from room temperature to *c.* 500 K, and increases significantly only above this temperature to around $1.2\,\mu s^{-1}$ at 600 K. This difference in behaviour might be correlated with the different preparation procedures employed for each sample, as described in Chapter 4: ZnPc_S did not undergo any type of treatment, while sample ZnPc_p3 was annealed in vacuum immediately prior to the μSR experiments. Hence, the vacuum annealing treatment apparently leads to larger μSR relaxation values, and a relaxation plateau below 500 K.

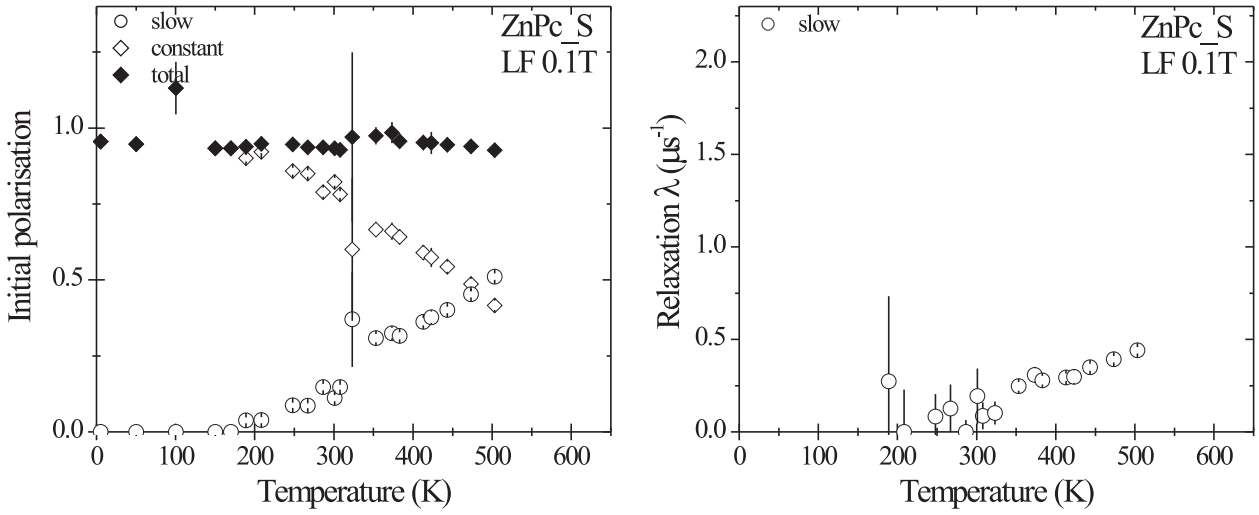

Figure 6.6: Temperature-dependence of the LF signal for sample ZnPc_S at 0.1 T. The slow relaxation is seen to increase with temperature. No information about the fast component exists since this set of data was obtained with the EMU instrument; also, the absolute values of the initial polarisations are affected by an undetermined systematic error (see text).

The initial polarisation values of the constant, slow and fast components, on the other hand, exhibit a very similar temperature variation between the two samples, with the slow component's fraction increasing with temperature at the expense of the decrease of the constant component. The crossing point between these two fractions occurs in the region 500-550 K for both samples, with the total summed polarisation remaining constant throughout the investigated temperature range. In ZnPc_p3, the fast component's fraction is fairly temperature

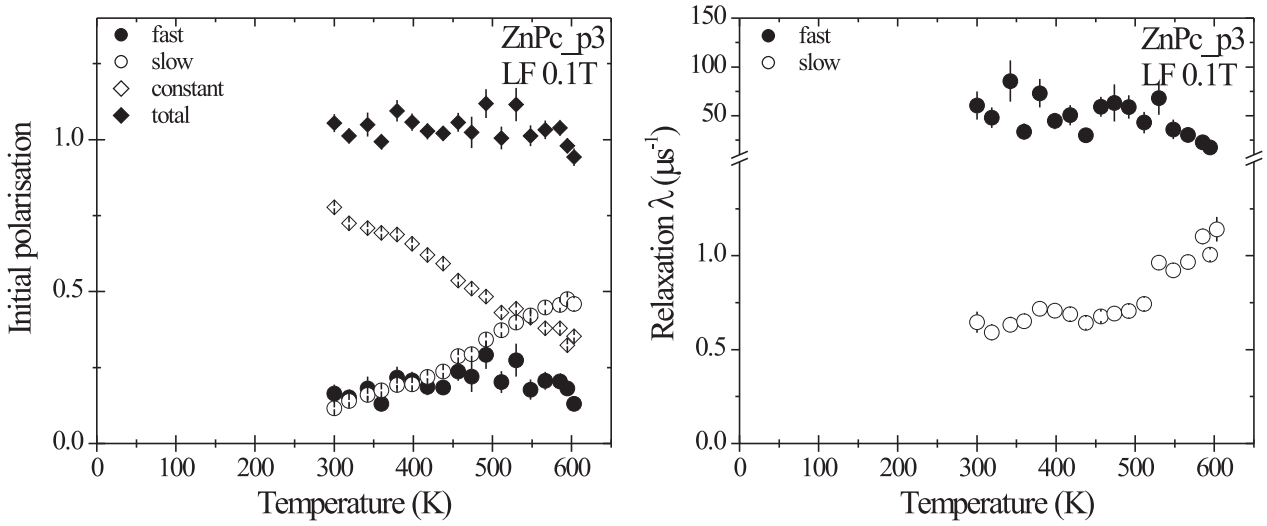

Figure 6.7: Temperature-dependence of the LF signal for sample ZnPc_ p3 at 0.1 T. Again, the slow relaxation increases with temperature, but with values considerably larger than the ones observed in sample ZnPc_S.

independent; for sample ZnPc_S, this component should present itself as a missing fraction in the total summed polarisation, but seems to be almost non-existing. The latter finding, however, should not be taken as a reliable proof that the fast component is not present in ZnPc_S, since the experimental conditions in which this particular data set was taken lead to the existence of a systematic error in the measurement of the maximum FB-asymmetry used to calibrate the initial polarisation fractions. The fact that the positive muon beam produced at RAL has a beam-spot (10 mm × 15 mm FWHM, *cf.* Section 3.2.6) comparable to the sample's size (16 mm, Section 4.3) results in a considerable fraction of the muons hitting the sample-holder. Hence, the initial polarisations shown in Figure 6.6 are affected by a significative systematic error which voids any attempt at quoting conclusions based on their absolute values.

6.1.3 LF signal of doped samples

A comparative study between the LF signal of a nominally undoped sample, ZnPc_vac, and the tentatively oxygen-doped sample ZnPc_oxy (see Chapter 4) was also performed regarding spin-dynamics in ZnPc, in order to draw an experimental relation between the observed μSR signal and the free charge-carrier content of phthalocyanines. The measurements consisted in a short temperature dependence of the LF signal for both samples at an externally applied field of

0.1 T; its results are shown in Figure 6.8, where no significant differences between the two signals exist. The rather small number of experimental points composing the two data sets is due to the limited time period available for the experiments with the oxygenated sample; this constraint was imposed by the conclusions drawn from the oxygen charging-decharging procedures described in Section 4.2.2, which indicated that the doping stability of the fixed oxygen fraction in charged thin-films is only kept during a limited period of time of a few hours at temperatures equal or lower than room temperature. Furthermore, to prevent oxygen out-take from the doped sample, the temperature dependence focused solely on the range below room temperature, where ZnPc's signal is dominated by a component (the constant component) which is not clearly assigned, as noted in Section 6.1.1 above. The possible reasons why no differences are observed between the signal of the doped sample produced for μSR experiments and that of undoped samples may have to do with the fact that the surface-beam positive muon is still a bulk probe, and doping may have occurred only at the surface.

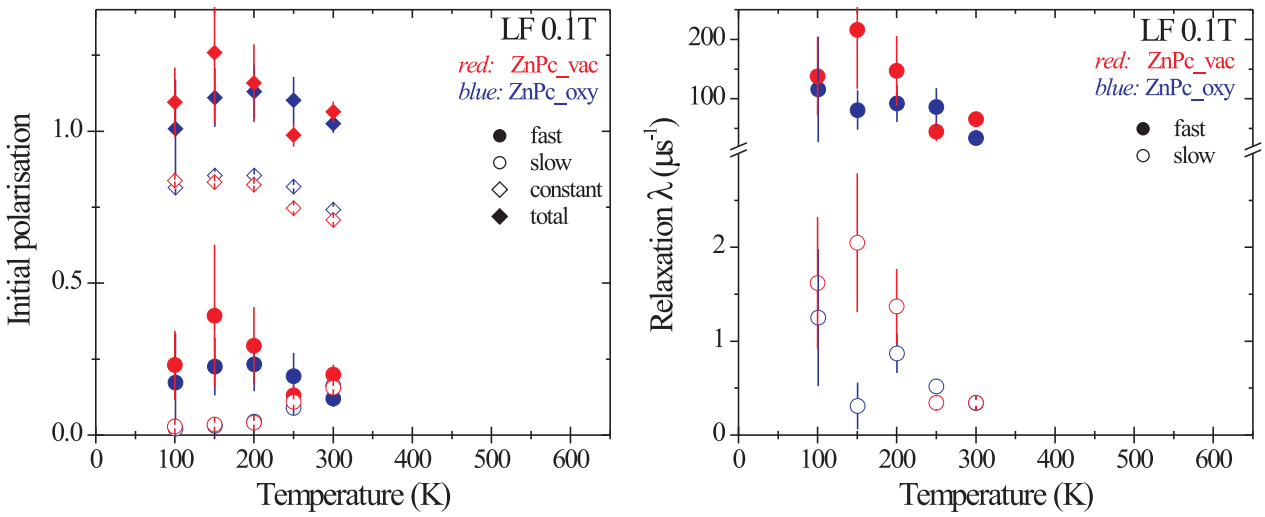

Figure 6.8: Temperature-dependence of the LF signal for the oxygen-doped sample ZnPc_oxy and the undoped sample ZnPc_vac at 0.1 T in the range below room temperature. No significant differences between the two data sets are observed in the investigated temperature range.

6.2 H_2Pc

The study of spin dynamics in H_2Pc was performed with the undoped samples H_2Pc_03 and H_2Pc_06 (Chapter 4) using the EMU instrument, following in close parallel what was done for ZnPc. Given that muon states have the same electronic structure in both compounds, the longitudinal-field signal of H_2Pc is very similar to that of ZnPc, and as such was analysed using the same phenomenological strategy. The time-domain data was thus described by a fit model consisting of one slow relaxing component and one constant component. The fast component has not been explicitly measured in any of the experiments involving the H_2Pc molecule due to the limited time resolution of the EMU instrument, but by analogy with what was found for the signal of sample ZnPc_p3 (measured at the GPS instrument), its fraction should also relate directly to the missing fraction[6].

6.2.1 Field-dependent signal

The field dependence of the LF signal obtained for H_2Pc with sample H_2Pc_03 at 300 K and 600 K is shown in Figures 6.9 and 6.10. For both temperatures, a well defined relaxation peak is observed in the region around 0.03 T; this value matches well the ω_1-ω_2 level-crossing fields expected for state III at 0.030(1) T (300 K) and 0.019(1) T (600 K) if one considers the isotropic hyperfine interaction values obtained from the time-domain fits performed in transverse field at those temperatures (see Section 5.2.2). Once again, but now in H_2Pc, state III is experiencing spin-exchange dynamics, and may be directly related to the slow component.

Also similarly to what was observed with ZnPc, the slow component does not fully describe the LF signal expected from state III, since its polarisation fraction does not follow the repolarisation curve of that state. At 300 K, the slow component exhibits a fraction of less than 25% of the total signal, while at 600 K it exhibits a strong field variation, more akin to a repolarisation behaviour, but which peaks at around 0.1 T with a value over 50%. Nevertheless, the slow component still bears important information about the spin-exchange dynamics of state III, conveyed mostly by its relaxation, from which quantitative results may be extracted with

[6]The remarks discussed for this type of indirect relation in sample ZnPc_S (investigated with the EMU instrument) do not apply to the case of H_2Pc, since the total FB-asymmetry was properly calibrated using a contrasting mask of $ErAl_2$ with the exact shape and size of the two H_2Pc samples on top of a large silver mask covering the full dimensions of the positive muon beam-spot. $ErAl_2$ is a metallic alloy in which all muons form states with a well known relaxed μSR signal, easily distinguishable from the non-relaxed signal of silver.

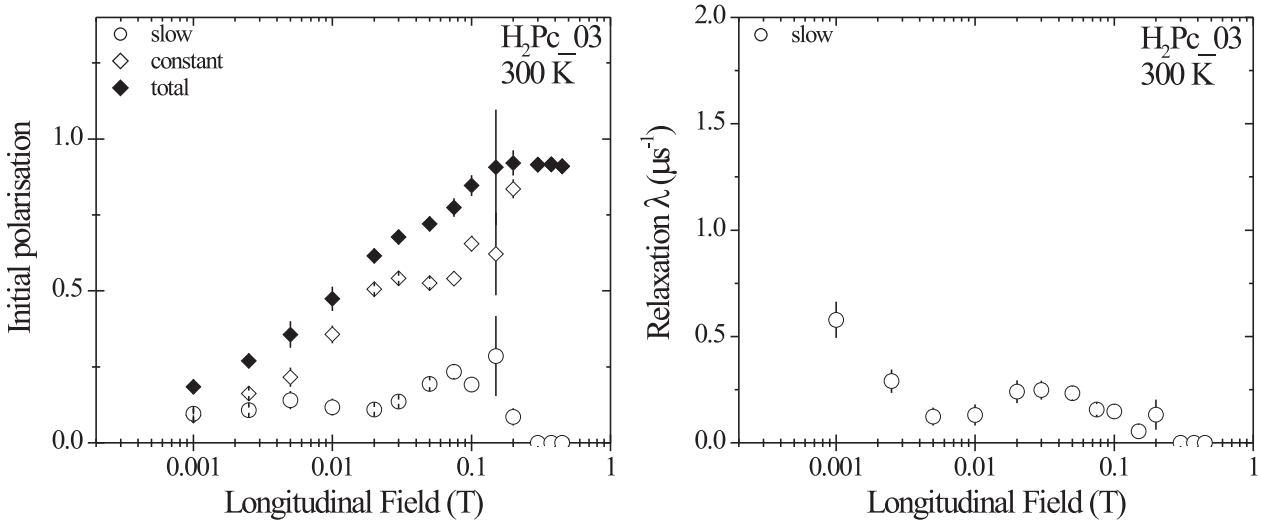

Figure 6.9: Field-dependence of the LF signal for H_2Pc at 300 K. The slow component's relaxation exhibits a peak at around 0.03 T, a value which matches the level-crossing field of state III obtained from the hyperfine parameters at this temperature.

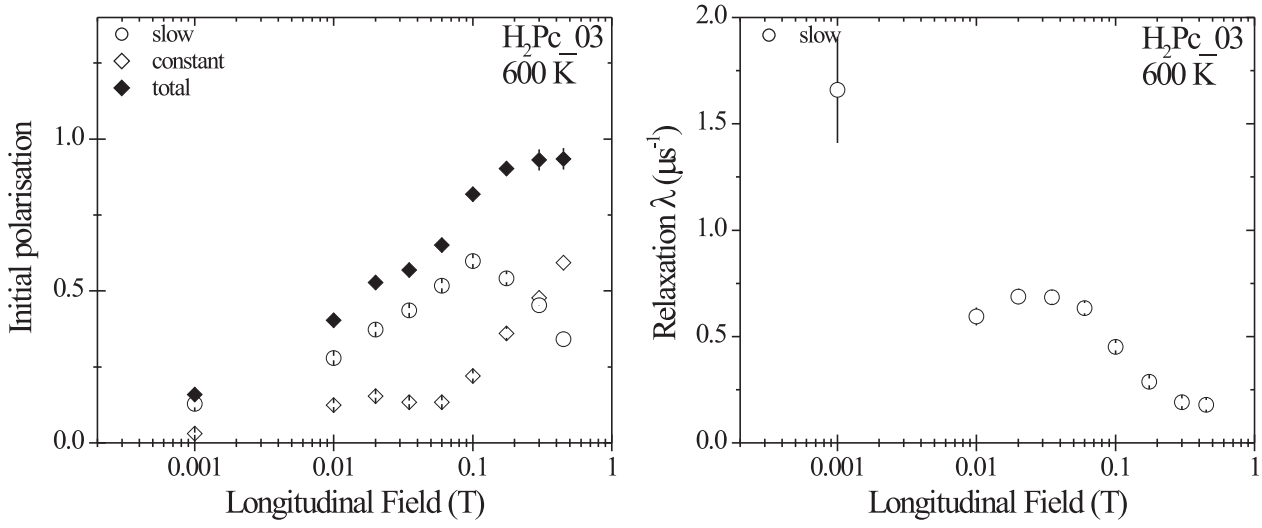

Figure 6.10: Field-dependence of the LF signal for H_2Pc at 600 K. Again, the slow component's relaxation exhibits a peak at around 0.03 T, matching the level-crossing field of state III.

the analysis model described in Section 6.3.

6.2.2 Temperature-dependent signal

The LF signal of H_2Pc was investigated regarding its temperature dependence using samples H_2Pc_03 and H_2Pc_06 under an applied field of 0.1 T. Although this field does not correspond exactly to the relaxation peak field of state III in H_2Pc, it was decided to use the same field chosen for ZnPc in order to allow a more direct comparison between the results of both compounds; the dependence obtained is shown in Figures 6.11 and 6.12.

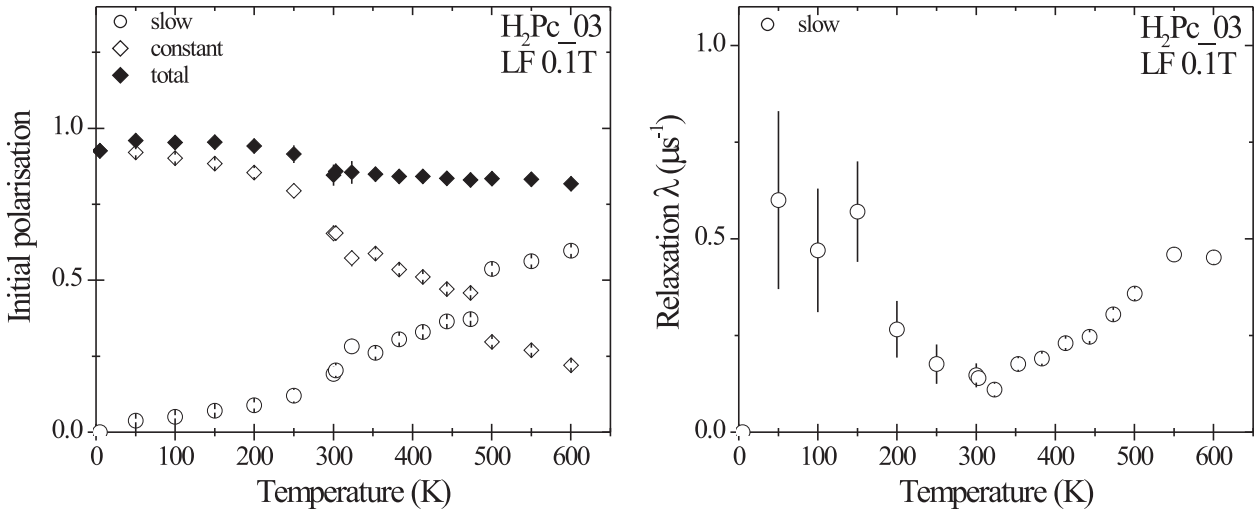

Figure 6.11: Temperature-dependence of the LF signal for sample H_2Pc_03 at 0.1 T. The slow relaxation is seen to increase with temperature above 300 K, exhibiting a behaviour parallel to that of ZnPc_S. Below this temperature, the relaxation rises as temperature decreases; this variation is not related to a real change in the characteristics of the dynamical phenomena responsible by the existence of the slow relaxing component, but to the temperature dependence of the hyperfine parameters of state III in H_2Pc (see text).

Above 300 K, the relaxation rate of the slow component in sample H_2Pc_03 exhibits a behaviour similar to that observed for ZnPc_S, rising monotonously with temperature; below room temperature, the slow component is still visible, but with a relaxation rate that decreases with increasing temperature, which leads to the formation of a relaxation dip at around 320 K. As commented later (Section 6.3.2), the variation at sub-room temperatures may be due to the effect that a shift of hyperfine parameters for state III would have in the relaxation rate, and not

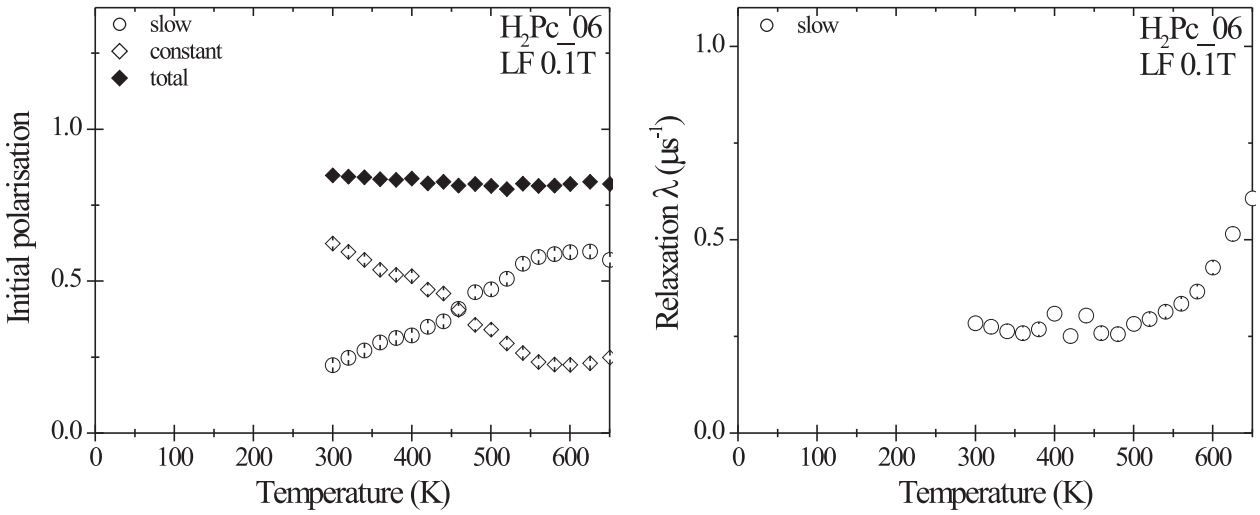

Figure 6.12: Temperature-dependence of the LF signal for sample H_2Pc_06 at 0.1 T. The slow relaxation increases with temperature in a manner similar to the signal observed in ZnPc_p3, *i.e.* exhibiting a plateau to about 500 K and rising steeply beyond this temperature.

properly to a change in the characteristics of the phenomena underlying the dynamics of that state. Sample H_2Pc_06, on its hand, shows a relaxation signal very similar to that of sample ZnPc_p3, bearing higher values than H_2Pc_03 and a relaxation plateau to 500 K which rises from then on to a value of about 0.6 μs^{-1} at 650 K. This difference of behaviours is analogue to that described for the ZnPc_S and ZnPc_p3 samples in Section 6.1.2, and correlates again with the absence of any type of treatment in the case of sample H_2Pc_03 and the vacuum annealing performed with sample H_2Pc_06 before the μSR measurements.

Also in close parallel to what was observed in the case of ZnPc, the temperature dependence of the initial polarisations is the same for the two measured H_2Pc samples. The slow component's fraction increases with temperature as the constant component decreases, with the crossing point between the two fractions occurring at around 450 K and the sum of both fractions remaining approximately constant. Finally, the missing fraction in both samples is the same, indicating that the polarisation fraction of the fast component, and therefore the population of state III, is equal as well.

6.3 Analysis considering a spin-exchange model for ZnPc and H_2Pc

As referred in the preceding sections, both the existence of a relaxation peak for the slow component at the ω_1-ω_2 level-crossing of state III in ZnPc and H_2Pc, and the fact that the fast component (observed directly in sample ZnPc_S only) may be attributed to the LF oscillating polarisation expected from that state, offer strong evidence supporting that the μSR LF signal of these two compounds in the high-temperature range is primarily due to state III. Furthermore, the LF relaxation peak of the slow component is a distinctive label of spin exchange dynamics in the slow spin exchange regime; state III is thus experiencing a spin scattering interaction with paramagnetic entities which, as discussed later on in Chapter 7, are the material's free charge carriers. Hence, the theory of spin exchange for paramagnetic muon states described in Section 3.4.4, Chapter 3, may be used to extract the spin-flip rate underlying the spin scattering of state III with the free charge carriers in ZnPc and H_2Pc from the experimental data presented above, and ultimately draw conclusions about the charge diffusion properties of those materials. The former subject is addressed in the next sections, while the latter is left for the discussion carried out in Section 7.2.2, Chapter 7.

6.3.1 A model for spin-exchange of axially symmetric paramagnetic states in polycrystalline samples

The LF relaxation rate of the non-oscillating polarisation of an axially symmetric paramagnetic muon state undergoing slow spin exchange dynamics relates with the spin-flip rate λ_{SF} according to equation (3.235) (see Section 3.4.4),

$$\lambda_L = \lambda_{SF} \sum_{n,m=1}^{4} \frac{\omega_{nm}^2}{\lambda_{SF}^2 + \omega_{nm}^2} \, a_{nm}^z \ , \tag{6.1}$$

where the transition frequencies ω_{nm} and amplitudes a_{nm}^z depend on the hyperfine parameters of the muon state and the angle θ between the symmetry axis of the hyperfine tensor and the externally applied field. The latter dependence is in fact quite strong, as shown in Figure 6.13; for the same spin-flip rate, the non-oscillating relaxation λ_L expected for a muoniated radical state with the hyperfine parameters of state III in ZnPc covers several orders of magnitude depending on the orientation of the hyperfine symmetry axis.

In a polycrystalline sample, this traduces in an LF non-oscillating signal which is not

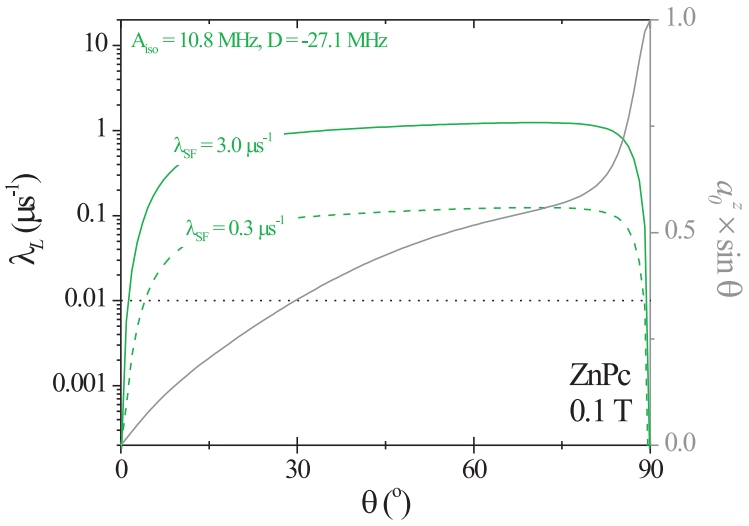

Figure 6.13: Angular dependence of the LF relaxation rate for an axially symmetric muonium state possessing the same hyperfine parameters as those of state III in ZnPc, as it undergoes spin exchange dynamics with spin-flip rates of $3.0\,\mu s^{-1}$ and $0.3\,\mu s^{-1}$. The LF relaxation rate depends sensitively on the orientation of the hyperfine symmetry axis, and may even assume values which are experimentally indistinguishable from a non-relaxing signal, as suggested by the dotted horizontal line, a rough experimental limit for the minimum relaxation rate capable of being measured with the EMU instrument.

characterised by a single relaxation rate, but by an integral of exponential functions over a broad range of relaxation rates weighted by the solid angle factor $\sin\theta$ and the non-oscillating amplitude a_0^z (itself a function of θ), conducing to a muon polarisation given by[7]

$$P_{\mu_z}(t) = \int_0^{\pi/2} a_0^z(\theta)\ e^{-\lambda_L(\theta)\,t}\ \sin\theta\ d\theta\ . \tag{6.2}$$

This integral may be used to extract the spin-flip rate from the LF experimental data of ZnPc and H_2Pc by fitting the time-domain FB-asymmetry histograms with a numerical calculation of (6.2), having as a basis the angular dependence of the LF relaxation rate (6.1). For each angle θ, it is necessary to compute the transition frequencies ω_{nm}, the amplitudes a_{nm}^z and the non-oscillating amplitude a_0^z given the hyperfine parameters A_{iso} and D of state III (already known from the TF measurements presented in Chapter 5), and provide the fitting parameter λ_{SF} in order to build the integrand function, which may then be integrated for all the acquisition instants t_i using *e.g.* Simpson's rule. This direct fit procedure, however, becomes considerably slow if one desires the integration algorithm to produce a muon polarisation trial function precise enough to exhibit numerical errors below the typical experimental errors recorded for the FB-asymmetry in the data under consideration. Besides that drawback, this type of approach turns out to be very sensitive to the presence of other components in the LF-signal, leading to difficult analysis paths which often produce quite unrealistic fit parameters.

A different route of analysis that allows measuring the spin-flip rate from the μSR LF data of ZnPc and H_2Pc without the problems of the direct approach, but based instead on the results obtained from the phenomenological description performed in Sections 6.1 and 6.2, was therefore developed specifically for this task. It starts by noting that the result of (6.2) is a time dependence which, due to the specific angular variations of λ_L and the product $a_0^z \times \sin\theta$, will possess two main contributions: the first, corresponding to the middle range of θ angles (in Figure 6.13, it spans from about 15° to 85°), consists in an approximately exponential function with a relaxation rate with the same order of magnitude as the spin-flip rate λ_{SF}; the second, originated by the upper range of θ angles ($> 85°$), has a very small relaxing character, which in an experimental time-limited μSR histogram will not be distinguished from a purely non-relaxing function. Thus, the LF non-oscillating polarisation expected from an axially symmetric muonium state undergoing spin exchange dynamics at a given spin-flip rate appears naturally as the sum of an exponentially relaxed function with a non-relaxing one. This fact justifies the

[7] We note that all angle-dependent parameters figuring in this expression, namely a_0^z, λ_L and $\sin\theta$, assume the same value for θ and $\pi - \theta$, allowing the integral to be evaluated only in the first quadrant.

phenomenological shape found for the LF signal of ZnPc and H_2Pc, leaving quite clear that the relaxing and non-relaxing contributions may be identified respectively with the slow and constant components of the signal[8].

It becomes therefore possible to obtain the spin-flip rate λ_{SF} of a given dataset from the slow component's relaxation by setting up a fast algorithm that computes the expected relaxation value for the relaxing contribution of a signal of the type of Equation (6.2) given solely the hyperfine parameters A_{iso} and D of state III and a spin-flip rate value λ_{SF}, and reversing it. This may be done comparing the integral $P_{\mu_z}(t)$, Equation (6.2), with a functional dependence $\tilde{P}_{\mu_z}(t)$ consisting of a relaxing component with amplitude $\tilde{a}$ and relaxation $\tilde{\lambda}$ summed with a non-relaxing component with amplitude $\tilde{b}$,

$$\tilde{P}_{\mu_z}(t) = \tilde{a}\, e^{-\tilde{\lambda} t} + \tilde{b} \ , \tag{6.3}$$

and establishing a method to seek the value of $\tilde{\lambda}$ that makes $\tilde{P}_{\mu_z}(t)$ the nearest possible to $P_{\mu_z}(t)$. The inversion of this relation yields promptly the spin-flip rate λ_{SF} which best matches the observed slow component's relaxation $\tilde{\lambda}$. One could also equate the inclusion of information about the relative amplitudes $\tilde{a}$ and $\tilde{b}$ of the slow and constant components to obtain the value of λ_{SF} best agreeing with the overall observed LF signal, but the existence of other contributions due to states I and II, especially in the constant component, end up degrading the ability for the method to find an univocal result for λ_{SF}. Indeed, a method fully based in the slow component's relaxation $\tilde{\lambda}$ presents the advantage of being quite robust, since from the physics point of view, this parameter depends uniquely on the dynamical phenomena, and not on other parameters such as *e.g.* the relative populations between states I, II and III.

Quantitative aspects of the analysis model

In order to determine mathematically the best value of $\tilde{\lambda}$ that makes the trial function $\tilde{P}_{\mu_z}(t)$ the nearest possible to the exact spin exchange polarisation $P_{\mu_z}(t)$, a figure of merit q was defined in the sense of minimum squared deviations between $\tilde{P}_{\mu_z}(t)$ and $P_{\mu_z}(t)$ over the experimental time window $[0, t_{max}]$ of a μSR histogram. This figure, which was chosen to read explicitly

$$q(\tilde{a}, \tilde{\lambda}, \tilde{b}) = \frac{1}{t_{max}} \int_0^{t_{max}} \left[P_{\mu_z}(t) - \tilde{P}_{\mu_z}(t) \right]^2 dt \ , \tag{6.4}$$

[8] In fact, the attribution of the non-relaxing contribution arising from the integral (6.2) to the constant component can only be performed partially, as it will be noted a few paragraphs down.

was found to be easily minimised as a function of $\tilde{a}$, $\tilde{\lambda}$ and $\tilde{b}$ using a simple numerical optimisation program based on the `UMINF` routine provided by the IMSL Fortran 90 MP Library package. Following several algebraic simplifications aiming the reduction of time needed for the computation of each q value for a set of parameters, the explicit expression eventually used with the optimisation procedure was

$$q(\tilde{a},\tilde{\lambda},\tilde{b}) = \frac{1}{t_{max}}(q_1+q_2+q_3)\ , \tag{6.5}$$

with

$$q_1 = \int_0^{\pi/2} a_0^z(\theta)\,\sin\theta \int_0^{\pi/2} a_0^z(\theta')\,\sin\theta'\ \frac{1-e^{-(\lambda_L(\theta)+\lambda_L(\theta'))t_{max}}}{\lambda_L(\theta)+\lambda_L(\theta')}\ d\theta' d\theta \tag{6.6}$$

$$q_2 = -2\int_0^{\pi/2} a_0^z(\theta)\,\sin\theta \left\{ \tilde{a}\ \frac{1-e^{-(\lambda(\theta)+\tilde{\lambda})t_{max}}}{\lambda(\theta)+\tilde{\lambda}} + \tilde{b}\ \frac{1-e^{-\lambda(\theta)\,t_{max}}}{\lambda(\theta)} \right\}\ d\theta \tag{6.7}$$

$$q_3 = \tilde{a}^2\ \frac{1-e^{-2\tilde{\lambda}\,t_{max}}}{2\tilde{\lambda}} + \tilde{b}^2\,t_{max} + 2\tilde{a}\tilde{b}\ \frac{1-e^{-\tilde{\lambda}\,t_{max}}}{\tilde{\lambda}}\ . \tag{6.8}$$

The translation procedure of A_{iso}, D and λ_{SF} values in the secondary parameters $\tilde{a}$, $\tilde{\lambda}$ and $\tilde{b}$ by the minimisation of $q(\tilde{a},\tilde{\lambda},\tilde{b})$ is analogous to the estimation of parameters in a chi-squared fit, and such as the minimum chi-squared obtained in a fit has statistical significance regarding the goodness-of-fit, also the minimum value of q attained for a given minimisation possesses some meaning in what concerns the adequacy of the values found for the secondary parameters $\tilde{a}$, $\tilde{\lambda}$ and $\tilde{b}$. We choose not to dwell amid the statistics of q, since it is out of the scope of this work, but we nevertheless briefly derive a rule-of-thumb which may be used as a guide to the confidence one should ascribe to the values of $\tilde{a}$, $\tilde{\lambda}$ and $\tilde{b}$ obtained from a given minimisation, in view of the experimental data they are modelling. In fact, the squared discrepancy per unit time between the optimised trial function $\tilde{P}_{\mu_z}(t)$ and the exact $P_{\mu_z}(t)$ muon polarisation function, which is precisely the minimum value of q, must lie within the squared experimental error per unit time of the FB-asymmetry. From the definition of the FB-asymmetry, equation (3.27), it is straightforward to show that the variance of the FB-asymmetry value recorded in a time bin t_i in an ideal situation ($\alpha = 1$, $\beta = 1$, no background counts) is given by (*cf.* Section 3.2.4)

$$\sigma^2_{\mathrm{FB}}(t_i) = 4\ \frac{\sigma^2_{\mathrm{B}}(t_i)\,\Delta N^2_{\mathrm{F}}(t_i) + \sigma^2_{\mathrm{F}}(t_i)\,\Delta N^2_{\mathrm{B}}(t_i)}{\left(\Delta N_{\mathrm{B}}(t_i) + \Delta N_{\mathrm{F}}(t_i)\right)^4}\ , \tag{6.9}$$

where $\Delta N_{\mathrm{B}}(t_i)$ and $\Delta N_{\mathrm{F}}(t_i)$ are the positron counts in the backward and forward histograms during the time bin at t_i respectively, and $\sigma^2_{\mathrm{B}}(t_i)$ and $\sigma^2_{\mathrm{F}}(t_i)$ are its variances. Since the quantity $\sigma^2_{\mathrm{FB}}(t_i)$ takes its lowest value at the histogram's first valid time bin, a set of $\tilde{a}$, $\tilde{\lambda}$ and $\tilde{b}$ values

only describes the exact muon polarisation function reliably within errors if its corresponding q value satisfies

$$q(\tilde{a},\tilde{\lambda},\tilde{b}) < \sigma^2_{\mathrm{FB}}(0)/\Delta t \ , \tag{6.10}$$

Δt being the time bin width, and $\sigma^2_{\mathrm{FB}}(0)$ reading

$$\begin{aligned} \sigma^2_{\mathrm{FB}}(0) &= 4\,\frac{\Delta N_{\mathrm{B}}(0)\,\Delta N^2_{\mathrm{F}}(0) + \Delta N_{\mathrm{F}}(0)\,\Delta N^2_{\mathrm{B}}(0)}{\left(\Delta N_{\mathrm{B}}(0) + \Delta N_{\mathrm{F}}(0)\right)^4} \\ &\approx \frac{1}{4}\,\frac{\tau_\mu}{\Delta t}\,\frac{1}{N_0} \ , \end{aligned} \tag{6.11}$$

as positron counts follow Poisson statistics ($\sigma^2 = \Delta N$), and the number of positron counts in the first time bin of the backward and the forward detectors is of the order of

$$\Delta N_{\mathrm{B}}(0) \approx \Delta N_{\mathrm{F}}(0) \approx \frac{1}{2}\ N_0\ \Delta t/\tau_\mu \tag{6.12}$$

if there is a total of N_0 counts in the two detectors. Hence, q should always comply to

$$q < \frac{1}{4}\,\frac{\tau_\mu}{\Delta t^2}\,\frac{1}{N_0} \ , \tag{6.13}$$

which, for a typical μSR data set collected at RAL in LF geometry ($N_0 = 10$ million events, $\Delta t = 16\,\mathrm{ns}$), evaluates to about 0.0018.

Adequacy of the model for the description of the existing experimental data

ZnPc

The adequacy of the analysis model developed for the description of the existing experimental data was briefly ascertained with a series of simulations addressing the field dependence of the expected $\tilde{a}$, $\tilde{\lambda}$ and $\tilde{b}$ parameters for state III in the regime of slow spin exchange. The simulation results, a part of which is compared to the actual data for the case of ZnPc_p3 in Figures 6.14 and 6.15, match well what is experimentally observed for this sample at 600 K when the spin-flip rate is about $3.0\,\mu\mathrm{s}^{-1}$. The q values for these simulations are also displayed in Figure 6.16, where it may be seen that it remains typically one order of magnitude below the critical value of 0.0018 derived above.

The simulated relaxation rate for state III exhibits a behaviour clearly parallel to that of the experimental data, with a relaxation peak at 0.08 T, an approximately flat plateau for fields below the peak field, and a rapid decrease beyond it. Also with λ_{SF}= $3.0\,\mu\mathrm{s}^{-1}$, the $\tilde{a}$ and $\tilde{b}$ parameters, and the complementary of their sum, $1-(\tilde{a}+\tilde{b})$, tally more or less well the slow,

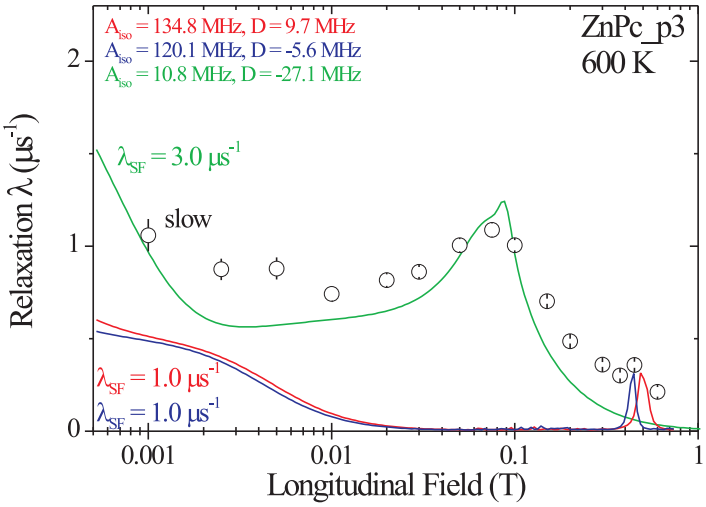

Figure 6.14: Field dependence of the simulated LF relaxation rates expected for states I, II and III in polycrystalline ZnPc as they undergo spin exchange dynamics at spin-flip rates of $1.0\,\mu s^{-1}$, $1.0\,\mu s^{-1}$ and $3.0\,\mu s^{-1}$ respectively. The simulated data regarding state III is the one matching the experimental data, with a relaxation peak at 0.08 T.

constant and fast components' initial polarisations at 600 K when multiplied by a factor of 0.6. The fact that a closer correspondence is obtained only if this factor is included is an indication that the population of the muon state III must be of that order, a value rather higher than the one obtained in TF measurements. Still, and even with the inclusion of this factor, the matching of $\tilde{b}$ with the constant component is rather poor when compared to $\tilde{a}$ and $1-(\tilde{a}+\tilde{b})$ and their experimental counterparts; nevertheless, the same trends are clearly shared between $\tilde{b}$ and the constant component's polarisation — namely a minimum near the relaxation peak field. In fact, the two quantities seem to differ from an approximately field-independent amount; we envisage this difference as a contribution to the LF signal of ZnPc not due to state III, but which might possibly have its origin in states I and II.

Although initially considered as well for simulation studies, no temperature dependent data was simulated in this work. Still, the qualitative behaviour with temperature expected for $\tilde{a}$ and $\tilde{b}$ is easily inferred from Figure 6.13, where it becomes clear that the relative weight between the two contributions, relaxing and non-relaxing, depends sensitively on the spin-flip rate λ_{SF}. This is due to the cross-over from the angular range giving rise to the relaxing contribution to the (apparently) non-relaxing one occurring in a region where the product $a_0 \times \sin\theta$ has a

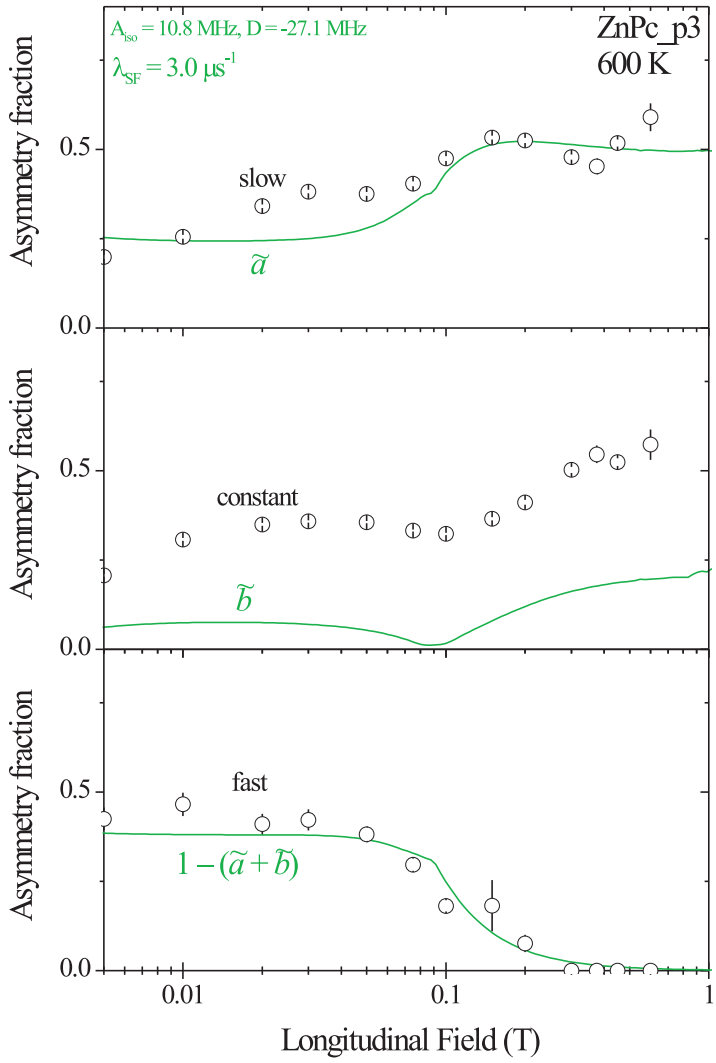

Figure 6.15: Field dependence of the simulated relaxing ($\tilde{a}$), non-relaxing ($\tilde{b}$) and missing ($1-(\tilde{a}+\tilde{b})$) asymmetry fractions generated in the LF signal of state III as it undergoes spin exchange dynamics with λ_{SF}= 3.0 μs^{-1} in a polycrystalline sample of ZnPc. The three curves were multiplied by a factor of 0.6 to better match the experimental data.

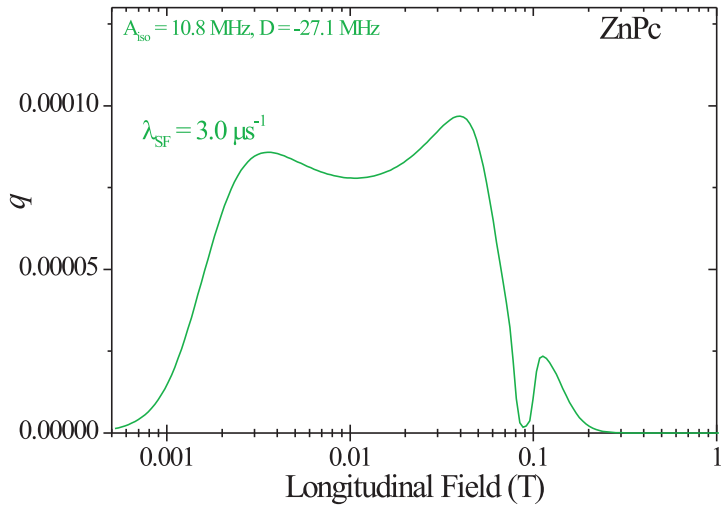

Figure 6.16: Field dependence of the figure-of-merit q, defined in Equation (6.4), used to mathematically determine the values of $\tilde{a}$, $\tilde{\lambda}$ and $\tilde{b}$. The curve shown corresponds to the situation of the two previous figures; it remains typically one order of magnitude below the critical value of 0.0018 referred in the previous section.

high derivative, which leads to a weight transfer from the non-oscillating contribution to the oscillating one with increasing spin-flip rate. Hence, a temperature rise should produce an increase in the slow component's fraction at the expense of the constant component; indeed, this is the qualitative behaviour observed in the temperature dependent data of ZnPc shown in Section 6.1.2, and is taken here as sufficient proof that the temperature dependence of the data is properly described by the analysis model.

H_2Pc

A set of simulations as a function of applied longitudinal field was also performed with H_2Pc, in similarity with what was done for ZnPc. Figures 6.17 and 6.18 show simulations produced with the hyperfine parameters of state III in H_2Pc at 600 K with a spin-flip rate $\lambda_{SF} = 2.0\,\mu s^{-1}$, equated with the data collected for sample H_2Pc_03 at the same temperature.

The simulated relaxation rate has again a dependence which exhibits a clear peak, now at about 0.05 T, in rather satisfactory agreement with the experimental data. Though the close similarity of shapes is somewhat debatable, it is assumed that the analysis model is still valid for the description of the H_2Pc data, especially if one takes into account the good correspondence

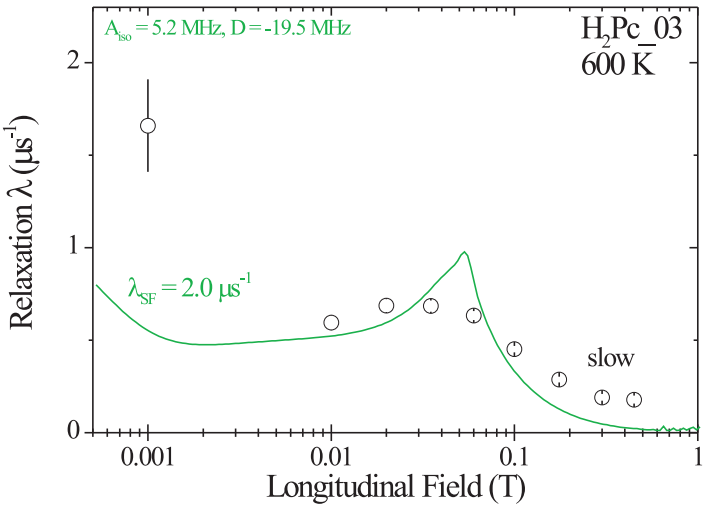

Figure 6.17: Field dependence of the simulated LF relaxation rates expected for state III in polycrystalline H_2Pc at a temperature of 600 K and under spin exchange dynamics with λ_{SF}= 2.0 μs^{-1}.

existing between the initial polarisation of the slow and constant components, and the simulated values of $\tilde{a}$ and $\tilde{b}$. Contrary to what happened with ZnPc, the curves for these two parameters are already a good match to the experimental data when no multiplying factor is used, indicating that the population of state III in H_2Pc must be close to unity. This result is parallel to what was observed in the high transverse-field measurements of Chapter 5, where a larger population of state III in H_2Pc relative to ZnPc had been established.

6.3.2 Analysis results

ZnPc

The analysis model considered in Section 6.3.1 was employed to extract the temperature dependence of the spin-flip rate λ_{SF} from the temperature-dependent LF measurements laid out in Sections 6.1.2 (ZnPc) and 6.2.2 (H_2Pc). In ZnPc, this was done using the functional relation between the values $\tilde{\lambda}$ expected for the slow component's relaxation and λ_{SF} shown in Figure 6.19, established from the minimisation of the figure-of-merit q taking into account the hyperfine parameters $A_{iso} = 10.8$ MHz and $D = -27.1$ MHz determined for state III in this compound (see tables 5.2 and 5.3) and the externally applied field of 0.1 T.

The results regarding the two samples ZnPc_S and ZnPc_p3 are depicted in Figures 6.20

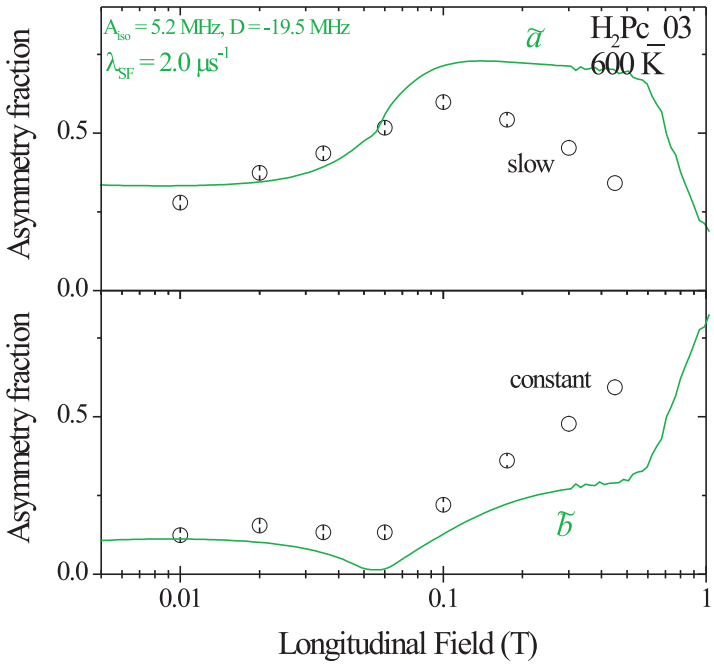

Figure 6.18: Field dependence of the simulated $\tilde{a}$ and $\tilde{b}$ quantities expected for state III in polycrystalline H_2Pc at a temperature of 600 K and under spin exchange dynamics with λ_{SF}= 2.0 μs^{-1}. Contrary to what was necessary regarding the ZnPc simulations, no multiplying factor had to be included in order to have the best match to the experimental data.

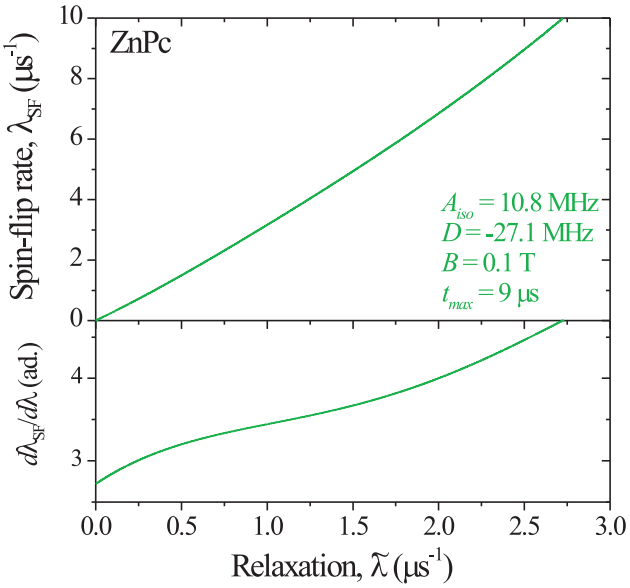

Figure 6.19: Functional relation between the values $\tilde{\lambda}$ expected for the slow component's relaxation and the spin-flip rate λ_{SF} in ZnPc at 0.1 T. Since the experimental time window used for the phenomenological fits of the LF data was only 9 μs, t_{max} was set to this same value for the computation of the figure-of-merit q with which this functional relation was deduced. The lower plot shows the derivative $d\lambda_{SF}/d\tilde{\lambda}$, a quantity necessary to compute the errors of the deduced λ_{SF} values from the experimental errors estimated for $\tilde{\lambda}$.

and 6.21, where the spin-flip rate has also been displayed in an Arrhenius plot. The temperature dependence of λ_{SF} is seen to be consistent with an activated behaviour above room temperatures bearing activation energies of 71(8) meV and 84(9) meV in ZnPc_S and ZnPc_p3 respectively, and pre-exponential factors of 6(1) μs^{-1} and 17(4) μs^{-1}. The energy scale of the dynamical phenomena underlying the temperature dependence of the spin-flip rate in ZnPc is thus the same within errors for the two investigated samples, whereas the absolute spin-flip rate values are higher in the sample which has suffered the vacuum annealing treatment (ZnPc_p3).

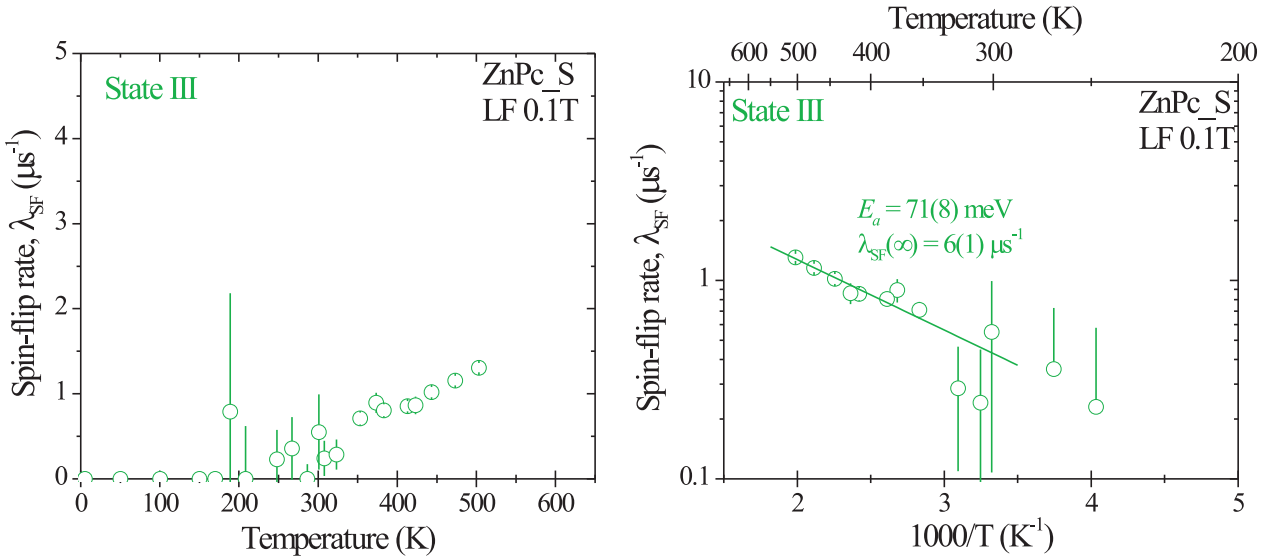

Figure 6.20: Temperature dependence of the spin-flip rate λ_{SF} in sample ZnPc_S at 0.1 T. The spin-flip rate has a temperature activated behaviour above 300 K.

H_2Pc

The extraction of spin-flip rates from the H_2Pc temperature dependent LF data was more complex than in ZnPc, since, as discussed in Chapter 5, the hyperfine parameters of state III vary with temperature. A functional relation between $\tilde{\lambda}$ and λ_{SF} had therefore to be derived for each temperature point, taking into account the hyperfine parameters of state III at that same temperature, linearly interpolated from the fitted A_{iso} and D values obtained from the high transverse field measurements. Figures 6.22 and 6.23 display the resulting temperature dependence of λ_{SF} for the two samples H_2Pc_03 and H_2Pc_06.

Above room temperature, the non-annealed sample H_2Pc_03 exhibits a simple temperature activated behaviour with activation energy 130(9) meV and pre-exponential factor 34(7) μs^{-1},

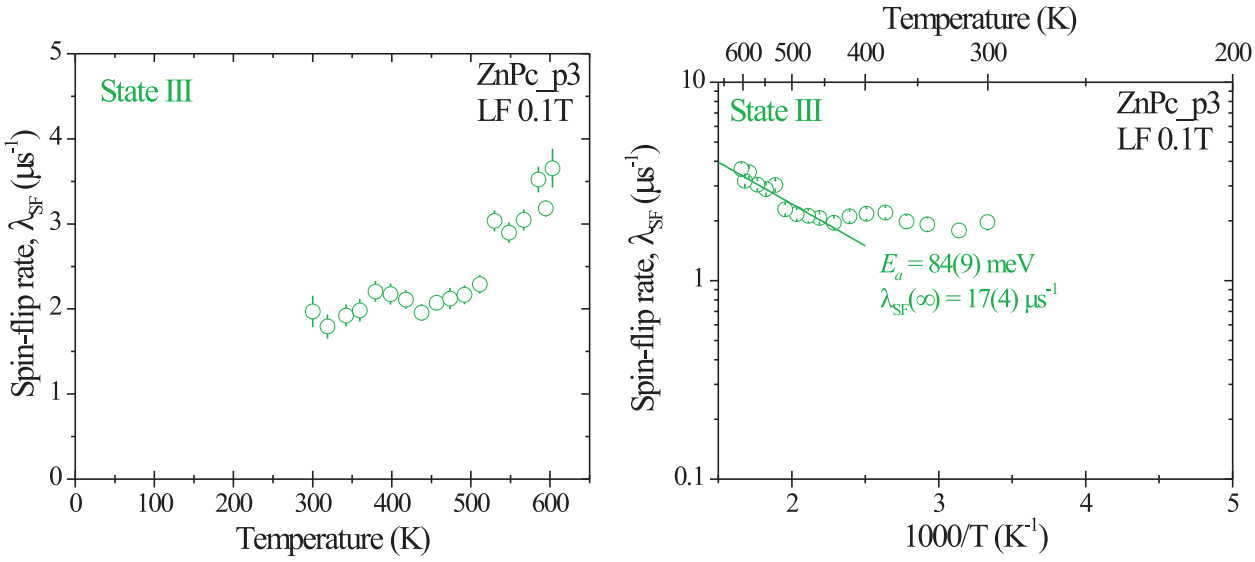

Figure 6.21: Temperature dependence of the spin-flip rate λ_{SF} in sample ZnPc_p3 at 0.1 T. The spin-flip rate also exhibits a temperature activated behaviour, now above 450 K, but with the same activation energy as the one found for sample ZnPc_S.

whereas the vacuum annealed sample H_2Pc_06 apparently shows three distinct regions of activated growth with temperature. These three regions correspond to three distinct activation energies of 26(2) meV, 141(6) meV and 376(12) meV, and pre-exponential factors 2.1(2) μs^{-1}, 33(4) μs^{-1} and 3900(900) μs^{-1} respectively. Again, there is a common energy scale between the two samples (the 130(9) meV and 141(6) meV components in H_2Pc_03 and H_2Pc_06). A finalising remark should be done regarding the odd variation of λ_{SF} at the lower temperatures both for sample H_2Pc_03 as for H_2Pc_06, and how it may be related to the incomplete variation one has for the hyperfine parameters of state III in H_2Pc. In the case of H_2Pc_03, the conversion from $\tilde{\lambda}$ to λ_{SF} below room temperature used the same values of A_{iso} and D measured at 300 K, which lead to a clear over-estimation of λ_{SF}; in fact, the temperature variation of λ_{SF} at temperatures below 300 K should follow that observed above 300 K, *i.e.* it should increase with increasing temperature. For H_2Pc_06, the effect is more troublesome: the over-estimation of λ_{SF} ends up creating a distinct region with a falsely different slope. Hence, the activation energy 26(2) meV should not be considered as a valid component of the temperature variation of λ_{SF} in this sample, and as so will be ignored for the rest of this work.

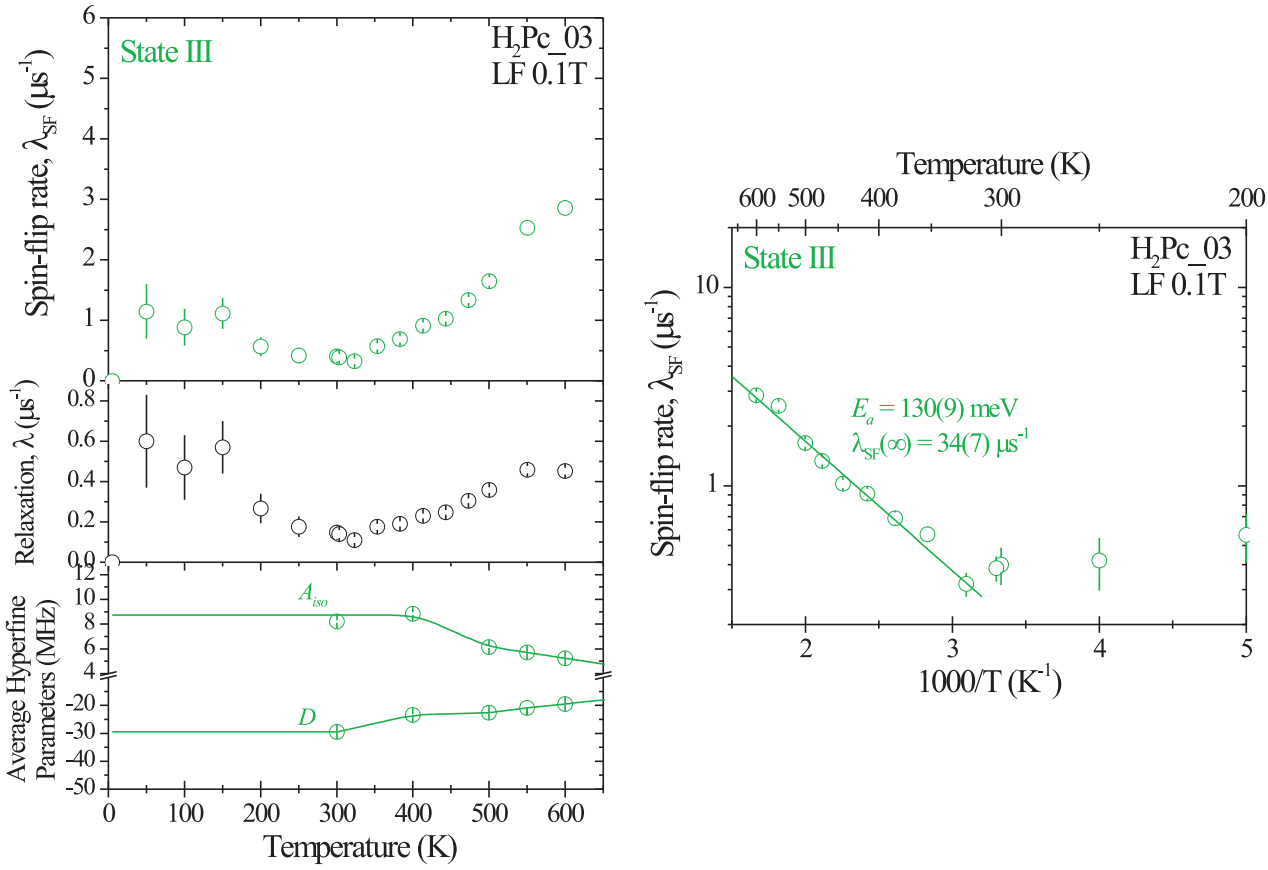

Figure 6.22: Temperature dependence of the spin-flip rate λ_{SF} in sample H_2Pc_03 at 0.1 T. Also shown are the original slow component's relaxation, equated to $\tilde{\lambda}$, and the hyperfine parameters used to deduce the functional relation between λ_{SF} and $\tilde{\lambda}$. The spin-flip rate has a temperature activated behaviour above 350 K.

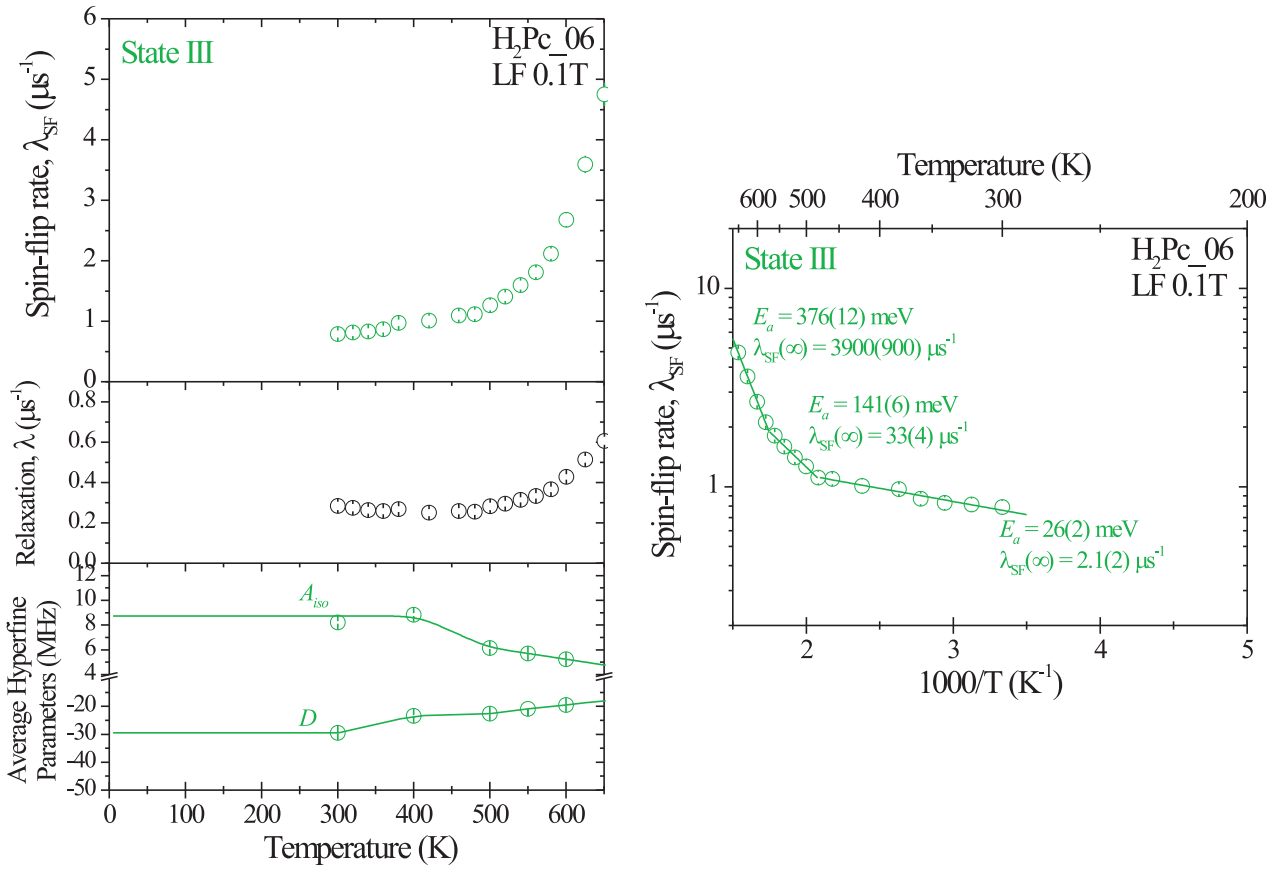

Figure 6.23: Temperature dependence of the spin-flip rate λ_{SF} in sample H_2Pc_06 at 0.1 T. The spin-flip rate has a temperature activated behaviour above 300 K, divided in three distinct regions. The intermediate region exhibits an activation energy identical to that obtained with sample H_2Pc_03.

Chapter 7

Discussion and conclusions

This final chapter is dedicated to the discussion of the experimental results and corresponding analysis presented in the two previous chapters. Those results are interpreted here in the light of what is currently known about organic muoniated radicals and phthalocyanines to construct what will hopefully be a consistent picture for the spectroscopic and spin-dynamical properties of the muon states formed in this type of compounds.

7.1 Spectroscopy of paramagnetic muon states in H_2Pc and ZnPc

7.1.1 States I and II

Hyperfine parameters and relative populations

If one compares the contact hyperfine interaction values determined for states I and II in ZnPc and H_2Pc (tables 5.2, 5.3 and 5.6) with the hyperfine parameter of isolated Mu (Table 3.3), one immediately sees that a strong electron transfer from the muoniated radical to the phthalocyanine molecule occurs upon the reaction of muonium addition. Less than 4% of unpaired spin density is left at both muon sites, relating well with what is typically known for muoniated radicals [99, 69, 95]. Figure 7.1 illustrates the transfer of charge from the paramagnetic state I in H_2Pc to the rest of the molecule; it is an iso-value surface plot of the SOMO orbital generated by the adduct, obtained from the site assignment electronic structure calculations.

Since the two states I and II correspond to muon adducts at the outer benzene rings of the phthalocyanine molecule, a natural comparison with the cyclohexadienyl radical (C_6H_6Mu),

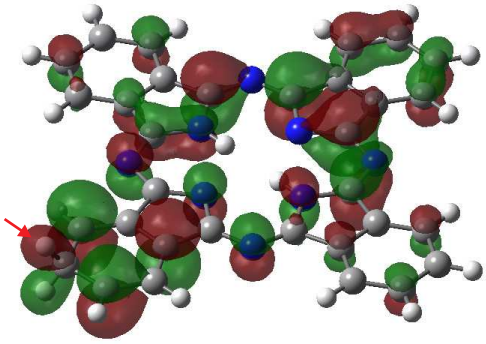

Figure 7.1: Iso-value surface plot of the SOMO orbital generated by the muonium adduct in H_2Pc that gives rise to state I. The electron is highly distributed over the whole molecule *via* conjugated orbitals, residing mainly in the inner ring and the added benzene ring. Only a small fraction of electronic density exists at the adduct (red arrow). The green and red colours indicate the relative signs of the wavefunction in each point of space.

formed by muonium addition to benzene (Figure 7.2), emerges. The isotropic hyperfine interaction of C_6H_6Mu, nevertheless, is of 514.6 MHz, a value considerably higher than those of the order of 100-150 MHz observed in states I and II. The source of the decrease is the well known *substituent effect* [99, 95], often observed in free-radical EPR and μSR-chemistry research. The addition of substituent groups to the cyclohexadienyl radical reduces the spin density at the muon by de-confinement of the unpaired radical electron; the effect is the more pronounced as the number and complexity of the benzene ring substituents increases. This effect has been extensively studied by Roduner [99], who, in addition to devising a phenomenological expression capable of describing its systematics, suggested a pair of phenomenological rules for monosubstituted benzenes: first, the *meta*[1] isomer shows the smallest substituent effect, and second the *para* isomer shows the weakest signal. The benzene ring where muon addition takes place for states I and II in ZnPc and H_2Pc may therefore be considered as a disubstituted cyclohexadienyl radical, with substituents at the *meta* and *para* positions for state I, and *ortho* and *meta* positions for state II (Figure 7.3). If one translates the second empirical rule of Roduner for the phthalocyanine system, one concludes that the population of state I must be lower than that of state II, as indeed is observed both in ZnPc and H_2Pc. Although the same type of reasoning

[1]The designations *ortho*-, *meta*- and *para*- refer to substitution positions in the benzene ring which are respectively next-to, second-next-to and opposite to the muon addition site.

cannot be used with the first rule (both states have *meta* substituents), the general trend in cyclohexadienyl radicals is that the *para* position possesses a smaller substituent effect than the *ortho* position [99]. ZnPc and H_2Pc comply to this trend, since the hyperfine interaction of state I is larger (*i.e.* less affected) than the one of state II.

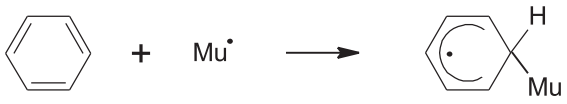

Figure 7.2: Formation of the cyclohexadienyl radical by muonium addition to a benzene ring.

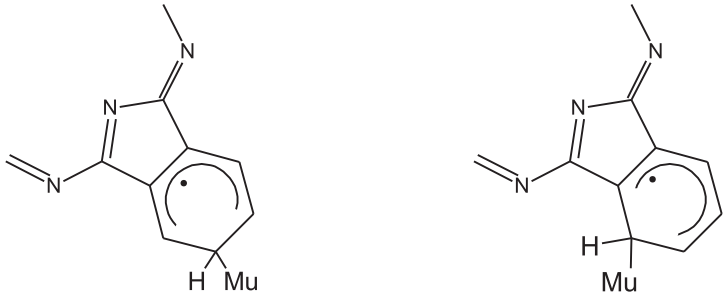

Figure 7.3: Muon states I (left) and II (right) in phthalocyanines as a highly substituted cyclohexadienyl radical. State I may be related with a radical highly substituted at the *meta* and *para* positions, while state II corresponds to the same substituents at the *ortho* and *meta* positions.

Finally, it should be noted that the relative populations between the two states do not obey the Boltzmann ratio expected from the formation energies calculated in Section 5.1.3, pointing to the fact that the initial formation of these states must be guided by the geometric muon capture radius instead of the electrostatic potential well depth. They exhibit a very weak temperature dependence either in ZnPc as in H_2Pc (figures 5.8 and 5.16), maintaining the population of state II above that of state I.

Temperature dependence of the hyperfine interaction

All four hyperfine parameters regarding states I and II in ZnPc were shown in Section 5.1.2 to have a temperature activated behaviour with the same activation energy. The temperature dependence of the hyperfine interaction in muoniated organic radicals is again a well-known effect; it arises due to thermal excitation of molecular vibrations, which in our case must involve

the C_α–Mu and the C_α–C_β bonds of the radical[2]. Relative motion between these two bonds interferes with the hyperconjugation of the C_α–Mu σ and the C_β p_z orbitals, producing a time-averaged overlap smaller than the one for the static situation. As temperature rises and the relevant vibrational modes become more populated, the effective overlap is decreased, accounting for the observed reduction of the isotropic parameter of the radical. The dipolar component of the hyperfine interaction is also gradually shifted to zero by that type of motion, although not due to the lessening of the hyperconjugative effect, but because it continuously reorients the hyperfine symmetry axis, averaging it out as a preferred direction in space.

In a simple approach, the temperature dependence of the hyperfine interaction may be quantitatively parameterised taking a situation in which only one vibrational mode v capable of coupling to it exists[3]. In first order, the shift of the hyperfine parameters at a given temperature T will be proportional to the population $n_v(T)$ of that vibrational state,

$$A(T) - A(0) \propto n_v(T) \ ,$$

which in thermal equilibrium is proportional to a Boltzmann factor,

$$n_v(T) \propto e^{-E_v/k_B T} \ ,$$

E_v being the energy of the mode. Thus, $A(T)$ will be given by

$$A(T) - A(0) = k \ e^{-E_v/k_B T} \ , \tag{7.1}$$

where the constant k is determined by taking the limit $T \to \infty$ of (7.1),

$$A(\infty) - A(0) = k \times 1 \ . \tag{7.2}$$

$A(T)$ therefore explicitly reads

$$A(T) = A(0) + (A(\infty) - A(0))\, e^{-\frac{E_v}{k_B T}} \ , \tag{7.3}$$

an equivalent expression to the fit equation (5.1) of Chapter 5, and where the activation energy E_a is now identified with the vibrational energy of the mode coupling to the hyperfine interaction.

In order to better understand the temperature dependence of the hyperfine parameters in ZnPc and H_2Pc, and confirm its origin as being due to molecular motion, a normal mode

[2] In general, the thermal excitation of rotational modes is also a source of temperature dependence for the hyperfine interaction. We will ignore this effect here, however, since the structure of the adduct and its surrounding C–H groups generates a barrier of large energy against the rotation of the Mu–C_α–H group.

[3] *i.e.* involving any bonds relevant for the hyperconjugative effect.

analysis calculation was performed for the two molecules in their bare forms. No Mu adduct was considered in the analysis, since the loss of symmetry rendered the computation unwieldy for a molecule with the size of phthalocyanine. This limitation implies that the normal modes obtained from the computation will not include the effect of the C_α–Mu bond in the vibrational properties of the molecule. Nevertheless, it is still reasonable to consider that the low energy modes of the bare molecule are a good approximation for the low energy modes of the adducted molecule. Since the mass difference between the carbon atoms and the hydrogen atoms is large, the low frequency modes of the bare molecule are determined mainly by the motion of its carbons; in particular, at the benzene rings the C–H groups behave as a whole, oscillating around the equilibrium position of the carbons. For the adducted molecule, the same is true; in a low energy mode, the Mu–C_α–H group oscillates as a whole, with a frequency which relative to the original C–H group will be shifted by an amount typically given by the square root of the Mu–C_α–H and C–H mass ratio, *i.e.* of a few percent.

The computation was done with GAUSSIAN 98, using an optimised geometry obtained under the same functionals, pseudo-potentials and wavefunction basis as those used for the geometry optimisation employed in the hyperfine parameter calculations. The normal modes obtained were then closely inspected, looking for all modes which implied relative motion between the six carbon atoms at the outer benzene rings. At low energies ($E_v < 600\,\mathrm{cm}^{-1}$), most of those modes were found to be of librational character[4], as opposed to stretching ones, which as expected were seen to dominate in the region of higher energy. Our attention was therefore focused on the librational modes, which we divided in *ortho*-flapping modes and *para*-wiggling modes, according to what is shown in Figure 7.4. The frequencies and corresponding energies of the modes involving carbon libration below $600\,\mathrm{cm}^{-1} = 74.4\,\mathrm{meV}$ are indicated in Table 7.1 for ZnPc and Table 7.2 for H_2Pc. The last column shows the expected population ratio at room temperature between the components indicated.

As it becomes evident, the measured 42(6) meV activation energy of the hyperfine parameters in ZnPc is consistent with a coupling to the first four libration modes of the outer ring carbons, providing evidence that states I and II are located at the outer benzene rings within the approximation of a rigid Mu–C_α–H group. In H_2Pc, and although no real fit to the activation energy exists, the same may be inferred, since the data was seen to be consistent with the activation energy extracted from the ZnPc data, which also relates well to the first modes

[4]The librational modes correspond to atomic oscillations transverse to the plane of the molecule.

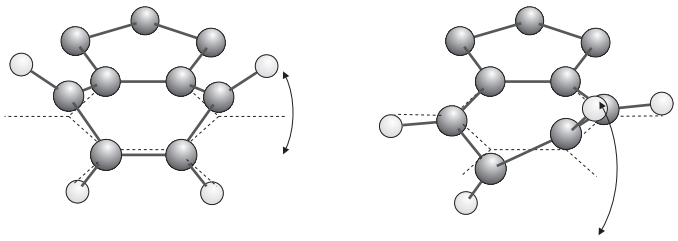

Figure 7.4: Low-energy librational carbon modes able to couple with the hyperfine interaction of states I and II in ZnPc and H_2Pc. These modes may be subdivided in *ortho*-flapping modes, shown on the left, and *para*-wiggling modes, shown on the right, depending on the relative sign of the oscillation amplitudes of each C atom in the outer benzene ring.

Table 7.1: Energies and expected populations at 300 K for the calculated librational modes of the outer ring carbons in ZnPc below 600 cm^{-1}.

frequency (cm^{-1})	*energy* (meV)	*population*	*type*
361.6	44.8	1.00	*o*-flap
362.1	44.9	1.00	*o*-flap
364.9	45.2	0.98	*p*-wiggle
372.1	46.1	0.95	*o*-flap
420.8	52.2	0.75	*p*-wiggle
445.2	55.2	0.67	*p*-wiggle
533.2	66.1	0.44	*p*-wiggle
541.5	67.1	0.42	*p*-wiggle
566.3	70.2	0.37	*p*-wiggle
582.9	72.3	0.35	*p*-wiggle

Table 7.2: Energies and expected populations at 300 K for the calculated librational modes of the outer ring carbons in H_2Pc below 600 cm^{-1}.

frequency (cm^{-1})	*energy* (meV)	*population*	*type*
357.8	44.4	1.00	*o*-flap
359.2	44.5	0.99	*o*-flap
362.2	44.9	0.98	*p*-wiggle
372.6	46.2	0.93	*o*-flap
414.6	51.4	0.76	*p*-wiggle
415.7	51.5	0.76	*p*-wiggle
442.0	54.8	0.67	*p*-wiggle
525.6	65.2	0.45	*p*-wiggle
528.1	65.5	0.44	*p*-wiggle
551.9	68.4	0.39	*p*-wiggle
557.9	69.2	0.38	*p*-wiggle

of Table 7.2.

As a final remark regarding the temperature dependence of the hyperfine interaction, the possible influence of the Mu adduct may still be briefly commented citing known μSR results for the muoniated cyclohexadienyl radical, C_6H_6Mu. In this radical, it has been shown that a coupling to the so called *wagging* modes of the H–C_α–Mu group (see Figure 7.5) needs to be considered in order to correctly describe the temperature dependence of its hyperfine constant [139]. The normal modes introduced by the wagging degree of freedom were seen to have characteristic frequencies around $450\,cm^{-1}$ in C_6H_6Mu [62], a value which is still in range to bear some influence on the temperature dependence of the hyperfine interaction of the I and II Mu adducts in ZnPc and H_2Pc. One may therefore not rule out the possibility that this wagging mode will also be an important mode for the description of that dependence in addition to the libration modes presented above.

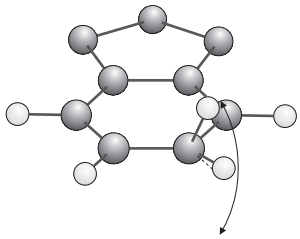

Figure 7.5: Wagging motion of the H–C–Mu group in the outer benzene ring of phthalocyanines. It consists in the asymmetric out-of-plane distortion of the H–C–Mu angle, with the *alpha* carbon remaining at rest on its equilibrium position.

Influence of the central atom

Very few changes were observed between the signals of the paramagnetic states I and II formed in ZnPc and those in H_2Pc, as let seen by the fit results presented in Chapter 5. The most important one is probably the shift to lower values of both hyperfine frequencies in H_2Pc[5], which may be understood in terms of the amount of charge transferred from the two radicals to the rest of the phthalocyanine molecule being smaller in ZnPc. As compared to H_2Pc, the presence of the zinc atom in the central region of ZnPc carries with it a large distribution of negative charge (28 more electrons than the 2 present in H_2Pc) which increases the total Coulomb repulsion in the molecule, and force a higher delocalisation of negative charge to its outer regions. The effect

[5]Here we compare values standing on the same foot, *i.e.* tables 5.1 and 5.6.

of Coulomb repulsion is nevertheless minute, producing structural changes in ZnPc (mostly the dilation of distances in the central region) on the order of just 1-2%.

Although no quantitative estimates were obtained for the dipolar parameters of H_2Pc, the careful comparison of FFT transforms between this compound and ZnPc suggests quite clearly that the states in H_2Pc are also less anisotropic than in ZnPc. This again may have to do with the unpaired spin distribution close to the muon site being larger in ZnPc than H_2Pc; if it is larger, so is its polar gradient (see appendix C), and thus the anisotropic parameter.

Finally, the absolute populations of the two states are quite smaller in H_2Pc when compared to ZnPc. This is probably another by-product of the structural changes induced by the extra negative charge brought to the molecule by the Zn atom. The intermolecular contacts between hydrogen atoms of adjacent molecules in the molecular plane are certainly smaller in H_2Pc [32], which may lead to a lower formation probability of states at those sites due to a confinement effect (*i.e.* by lack of space).

7.1.2 State III

Possible sites and electronic structure

When compared to typical radicals, the hyperfine contact interaction of state III is quite low, suggesting it must reside in a site of naturally low spin density. Furthermore, its hyperfine tensor is dominated by the dipolar term, indicating that the radical's unpaired spin distribution is highly asymmetric relative to the muon position. Thus, not only does the order of magnitude of the hyperfine interaction distinguishes state III from states I and II, but also fundamental differences exist in the spatial configuration of the unpaired spin.

Since no stable addition sites at double bonds were found with the electronic structure calculations referred in Chapter 5 that could be directly related to state III, the formation of state III does not apparently imply the breaking of a double bond. This means that the muon site is either interstitial (*i.e.* in-between molecules), or corresponds to a location where a chemical bond with the molecule may be established without double-bond breaking processes. In phthalocyanines, one site that conforms to the latter hypothesis does exist; it is site *e* of Figure 5.11, located next to a bridging azamethine nitrogen. The nitrogen atom has a pair of lone, non-bonding electrons in the plane of the molecule which are available for bonding to the muon; a radical state formed there necessarily has a low hyperfine interaction by hyperconjugation hinderance, since the overlap between the in-plane N–Mu σ bond and the plane-perpendicular

p_z orbitals of the two β carbons bonding the α nitrogen is poor (Figure 7.6). The occurrence of this type of Mu anchoring to lone electron pairs is often observed in compounds possessing C=O carbonyl groups, as *e.g.* acetone [19].

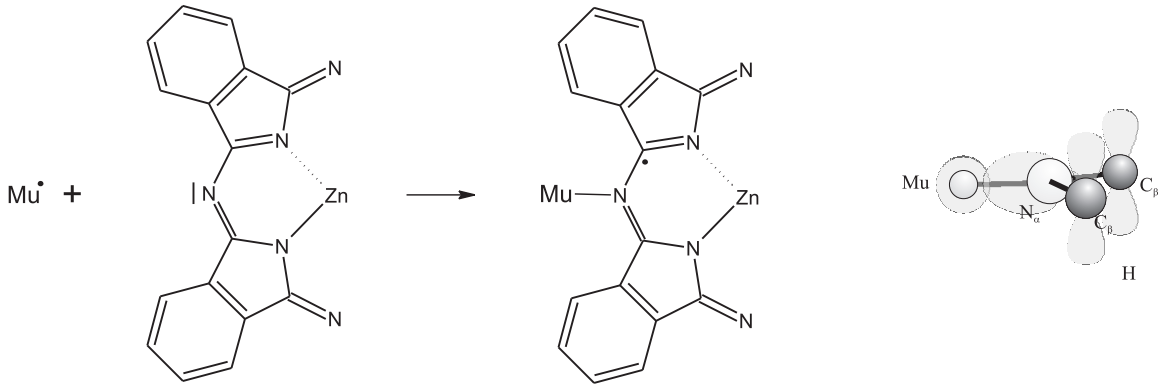

Figure 7.6: Possible location of state III at an azamethine bridge. The muon bonds to the lone electron pair of the nitrogen atom *(left)*; the resulting N–Mu σ orbital is perpendicular to the p_z orbitals of the β carbons, leading to a small hyperconjugative effect *(right)*.

Nevertheless, two arguments may be put against this site assignment. First, the failure in finding an electrostatically stable hydrogen state at site *e*. It clearly shows that the phthalocyanine molecule will have a tendency to segregate hydrogen atoms trying to stick at that position. Although the site is located at a quite open space, implying in principle a very small relaxation of the neighbouring atoms, the fact is that the extra electron brought by Mu to the molecule will be placed at the β carbons, being immediately dispersed in the central C–N skeleton. The bonding effect the molecule gains by having this extra electron is therefore too small to counteract the energy rise accompanying the necessary atom relaxation. This is also in agreement with the well-known high chemical stability of phthalocyanines. Secondly, not much credibility may be given to the existence of a stabilising effect due to the solid-state structure of β phase phthalocyanine. The slipped stacking of this arrangement does not seem to interfere with the in-plane surroundings of that site, which remains open enough for the segregation to act (Figure 7.7).

The only possible sites consistent with our findings seem therefore to be interstitial positions. In view of what was just referred about the segregating effect of phthalocyanine, those positions will be located as far as possible from neighbouring molecules, typically half-way between two of them. There are therefore two possible positions meeting this criteria, one contained in

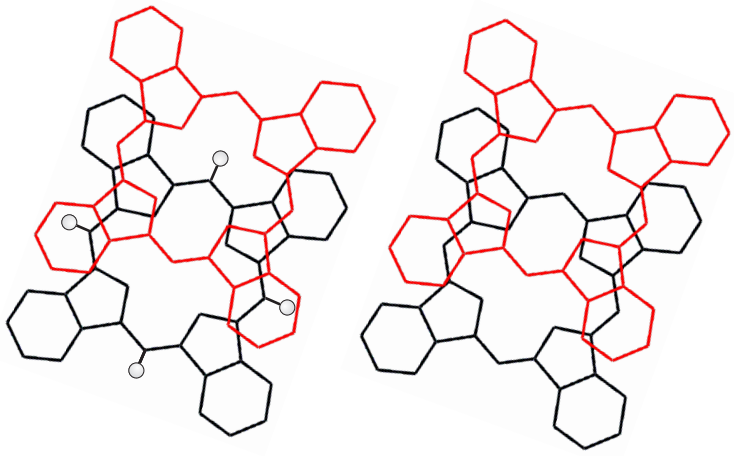

Figure 7.7: Stabilising effect of the solid state structure of phthalocyanine in the muon addition to the azamethine bridge. The molecule staking does not seem to interfere much with the in-plane surroundings of that site.

the molecular plane, and another out of that plane. From these, the out-of-plane site is actually the most plausible, since it is the only one where the radical may have a low contact hyperfine interaction. This is dictated by the overlap that a $1s$ wavefunction centred at the positive muon would have with the electronic distribution of the neighbouring molecules; although this overlap is rather small *a priori* for the out-of-plane case, it is even smaller for the in-plane site as most of the spin density of phthalocyanines resides at their centre. So, for a paramagnetic state formed in an in-plane position there is no real mechanism capable of explaining a high decrease of spin density at the muon. On the contrary, an out-of-plane state may have a low contact interaction if its electron is shared with the LUMO orbitals of the two phthalocyanine molecules bridged by the muon, which have π character [97, 64] and are therefore directed outwards from the molecular plane. Should a Mu atom be placed half-way between those molecules, its higher energy unpaired electron would immediately fall to a wavefunction dominated by the two LUMO orbitals; this wavefunction has of course a minimum at the muon site, giving thus rise to a low contact interaction. It should be noted that the two LUMO orbitals have a mensurable overlap (the origin of electrical conduction in phthalocyanines is actually credited to this fact [51]), so it is quite credible that the actual transfer of the Mu electron to an overlaped LUMO-LUMO wavefunction will take place. Figure 7.8 qualitatively depicts where the muon state would be located in this situation, and how the LUMO-Mu-LUMO overlap would look like. One should note that the configuration of state III we propose here is remarkably similar to the structure

of the Mu^0_{BC} centre found in the elemental and III-V semiconductors. In Mu^0_{BC}, the muon, although being located at the bond centre between two atoms, actually resides in the node of the unpaired spin wavefunction, which has anti-bonding character (see Section 3.3.2 in Chapter 3). That state also has a large dipolar parameter due to the directional structure of the wavefunction.

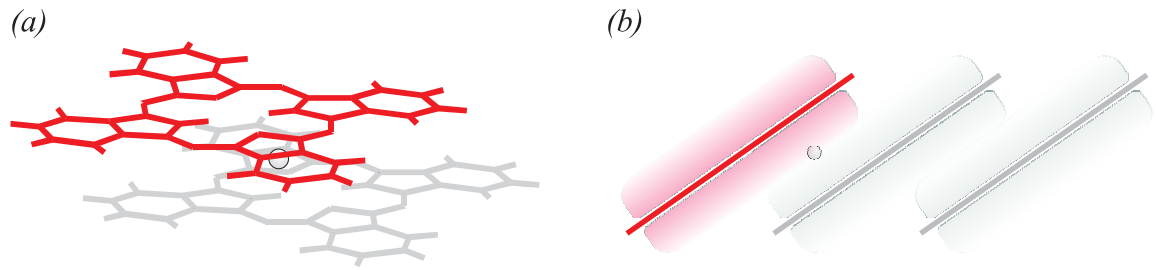

Figure 7.8: Possible location of state III at an out-of-plane interstitial site, seen *(a)* in perspective, and *(b)* in cut-view. In this situation, the the muon sits at the node of the LUMO-LUMO overlap.

Finally, one further fact is consistent with the suggested assignment of state III, which is the existence of evidence leading to believe that the hyperfine tensor of state III exhibits full anisotropy. From the close observation of the Fourier transform spectra taken in high transverse field measurements, it becomes apparent that the frequency distribution regarding state III is not well described by the pattern characteristic of axial symmetry; a distribution relative to a fully anisotropic state, with a quite high full anisotropy parameter η[6] seems more appropriate, as shown in Figure 7.9. A state formed at the location proposed for state III will have a spatial distribution close to the sum of the two LUMO orbitals involved; relative to the muon, that distribution is not at all axially symmetric, but will still have some oblate character, justifying the negative sign of the dipolar parameter. Fits to the time-domain signals of ZnPc and H_2Pc in high transverse field using a fully anisotropic powder function for the description of state III were tried in order to confirm its full anisotropy, but the data was found not to possess enough sensitivity to yield conclusive values for η.

[6]This quantity is defined in appendix C as $\eta = \frac{A'_{yy} - A'_{xx}}{D}$, where A'_{xx} and A'_{yy} are the x and y principal values of the hyperfine tensor.

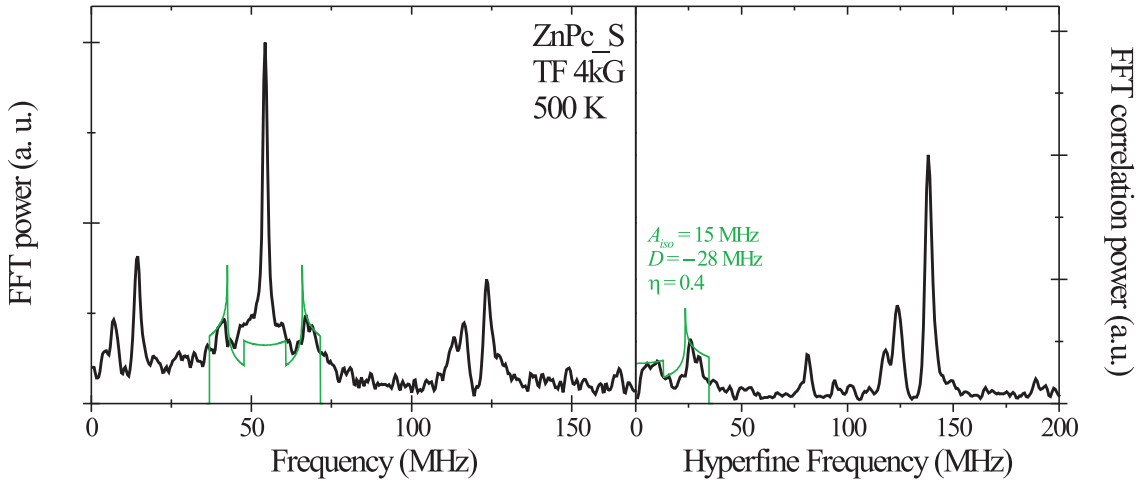

Figure 7.9: Simulated frequency distribution considering a fully anisotropic symmetric hyperfine interaction for state III in ZnPc. The Fourier and frequency pair correlation power transforms are consistent with state III exhibiting full anisotropy.

Influence of the central atom

Contrarily to what was observed for states I and II, the configuration of the central region in the ZnPc and H_2Pc molecules was seen not to exert any significant influence in the population of state III. Indeed, this parameter was found to be fairly identical for both ZnPc and H_2Pc at all temperatures, revealing that the exact structure of the molecule is less important in determining the formation probability of this state. Although not being a proof that state III is located at an interstitial position, this is in better agreement with that type of location than with the anchoring at a bridging nitrogen, since the latter would put the positive muon nearer to the molecule. Smaller structural differences would have a larger influence in the configuration of the local electrostatic potential minimum for that situation, which would in turn reveal as different formation probabilities of the state.

The temperature dependence of the hyperfine interaction of state III, on the other hand, is clearly dependent on the existence or not of the central atom. While in ZnPc no dependence seems to exist, in H_2Pc the hyperfine parameters suffer a strong red-shift with increasing temperature. Assuming the shift is due to molecular vibrations, this means that the modes which couple to state III in H_2Pc do not exist in ZnPc. This clearly reveals that central H modes in H_2Pc have a major influence in the hyperfine interaction of state III; its site needs therefore to

be within the range of the central H atoms for it to be affected, a fact being consistent with the out-of-plane interstitial site assignment of Figure 7.8. Table 7.3 shows the normal modes of H_2Pc where libration of the central H atoms has the largest amplitude, as obtained from the normal mode analysis described in the last section. The energies of those modes are higher than the ones involved in the shift of the hyperfine interaction of states I and II, originating a more steep temperature dependence for state III[7].

Table 7.3: Normal modes of H_2Pc where libration of the central H atoms has the largest amplitude. Stretching modes have considerably higher energies, and are note shown here.

frequency (cm^{-1})	*energy* (meV)	*type*
481.8	59.7	H libration
584.2	72.4	H libration
647.8	80.3	H libration

In ZnPc, the same out-of-plane site would couple to vibrations of the central part of the molecule also; these vibrations, however, have a much lower energy than the central H modes of H_2Pc because the Zn atom makes the central region of ZnPc much heavier. The expected temperature shift in ZnPc is therefore significantly smaller than in H_2Pc for an interstitial site position of state III, again in agreement with what was observed. The relation between the frequencies of the relevant modes concerning motion of the central region in H_2Pc and ZnPc, together with the observed temperature dependence of the hyperfine interaction of state III in H_2Pc but not in ZnPc, substantiate further the site assignment of this state at an out-of-plane location.

7.2 Spin dynamics in H_2Pc and ZnPc

7.2.1 Origin of the observed spin dynamics

The origin of μSR spin dynamics in solid organic compounds may be broadly attributed to either irreversible interactions (*e.g.* a chemical reaction), cycle exchange interactions (*e.g.* molecular

[7]The higher energy of the central H modes produces a change in their populations with a higher derivative, and hence a steeper temperature dependence of the hyperfine interaction.

Table 7.4: Normal modes of ZnPc where the oscillation of the central Zn atom has the largest amplitude.

frequency (cm^{-1})	*energy* (meV)	*type*
143.0	17.7	Zn libration
215.0	26.7	Zn stretching
215.1	26.7	Zn stretching

motion) or spin exchange processes (*e.g.* scattering with charge carriers) [99, 10]. In the case of ZnPc and H_2Pc, all existing evidences point to spin exchange as being the responsible by the spin dynamics observed in longitudinal field geometry, as on the one hand irreversible and cycle exchange interactions are ruled out for these compounds, while on the other distinct signatures typical of spin exchange dynamics are clearly recognised in the LF data collected and presented in Chapter 6. Indeed, no strong field dependence of amplitudes for the paramagnetic precessions in high transverse fields exist, as would be expected for irreversible interactions [85, 106, 71], as much as there is no molecular motion, since the energy scale of the phenomena giving rise to the LF relaxation rate, which is of the order of the activation energies found in Chapter 6 for the spin-flip rate ($\sim 100\,\text{meV}$), is quite different from the activation energy found for the hyperfine interaction shift in the high transverse field measurements described in Chapter 5 ($\sim 40\,\text{meV}$). This means that the vibrational modes responsible for local molecular motion, which couple to the hyperfine frequency and shift it to lower values, are not the same as those that couple to the process responsible for the LF spin dynamics. Long-range motion (muon diffusion), another type of cycle exchange interaction, is also rejected as an acceptable hypothesis, since it would lead to a narrowing of the dipolar hyperfine parameter with increasing temperature as the anisotropy would be progressively averaged out, and that is definitely not observed in the specific case of ZnPc.

Positive support to an assignment of the observed dynamics to spin exchange processes comes from LF relaxation peak exhibited by both materials at the $\omega_1 - \omega_2$ level crossing field of state III. In fact, any axially symmetric paramagnetic muon state undergoing spin exchange dynamics in the slow spin exchange regime will generate an LF μSR signal which shows maximum relaxation rate at the state's level crossing (*cf.* Section 3.4.4). The spin exchange regime is

definitely slow, not only due to the existence of the relaxation peak[8], but also because the high transverse-field precession lines of state III are not collapsed to an apparent diamagnetic precession.

Spin exchange dynamics usually arises from the physical process of spin scattering of the paramagnetic muonium centre with a paramagnetic species; in the case of ZnPc and H_2Pc, the paramagnetic species are charge carriers diffusing through the material. The reasons one may put forward to support this conclusion are threefold. Firstly, phthalocyanines are semiconductors, and as such must have a considerable number of mobile charge carriers at any instant. Secondly, because state III, which is the paramagnetic state directly involved in the observed spin dynamics, is believed to be located at a site in-between molecules, where the valence molecular orbitals of adjacent molecules overlap; since charge carrier diffusion occurs via that overlap, state III resides precisely in a diffusion path, becoming therefore particularly exposed to the effect of passing-by carriers. And thirdly, due to the temperature dependence of the LF relaxation above room temperature in all ZnPc and H_2Pc samples, which increases as temperature rises. The relaxation increase is a clear indication that the spin-flip rate also increases with temperature, which may be connected to the existence of more charge carriers moving at higher velocities. Hence, the spin dynamics observed in ZnPc and H_2Pc is due to spin scattering events of state III with the material's charge carriers.

7.2.2 State III as a microscopic probe of charge carrier diffusion

Since there is strong evidence that state III is undergoing spin scattering processes with charge carriers, this state may be seen as a microscopic probe sensitive to the diffusion characteristics of the charge carriers in the material, and the (slow component's) LF relaxation rate may be taken as an observable capable of being related with the mobility of those carriers. The mobility of the charge carriers in phthalocyanines is therefore accessible *via* a μSR observable, turning the μSR technique in a powerful tool to probe the microscopic mobility of charge carriers in phthalocyanines.

As it was seen in Chapter 6, it is possible to extract the spin-flip rate λ_{SF} from the slow component's relaxation. λ_{SF}, on its hand, relates at a given temperature T with the carriers density $n(T)$ and their relative speed to the muon $v(T)$ by Equation (3.223),

$$\lambda_{SF} = n(T)\, v(T)\, \sigma_{SF} \; ; \tag{7.4}$$

[8] In the fast spin exchange regime, the field dependence of the LF relaxation does not possess a peak.

if one assumes that the spin-flip cross section σ_{SF} does not vary with temperature, the temperature dependence of the spin-flip rate λ_{SF} is therefore only due to the combined effect of $n(T)$ and $v(T)$. Since the density of charge carriers is exponential in a non-degenerate semiconductor[9], $n(T)$ is given by

$$n(T) = n(T=\infty)\ e^{-\frac{E_n}{k_B T}}\ , \tag{7.5}$$

where E_n is related with the energy of the level which produces the charge carriers, while for non-band-like diffusion of charge carriers[10] $v(T)$ is

$$v(T) = \frac{l}{\tau(T)}\ , \tag{7.6}$$

$\tau(T)$ being an average residence time for the charge carrier at localised sites, and l the average distance between those sites (each molecule will typically be a charge localisation site). Since the quantity $1/\tau(T)$ is the probability per unit time that a jump of a charge carrier from one localised site to the next site occurs, it is reasonable to relate it directly to the carrier mobility $\mu(T)$ by

$$\frac{l}{\tau(T)} = k \times \mu(T)\ , \tag{7.7}$$

and since the mobility in organic semiconductors is usually taken as exponentially increasing [86, 50], *i.e.*

$$\mu(T) = \mu(T=\infty)\ e^{-\frac{E_\mu}{k_B T}}\ , \tag{7.8}$$

where E_μ is roughly the polaron binding energy (for tunnelling processes) or the energy barrier height (for hopping processes), the spin-flip rate will read

$$\lambda_{SF} = n(T=\infty)\, l\, k\, \mu(T=\infty)\, \sigma_{SF}\ e^{-\frac{E_n+E_\mu}{k_B T}}\ , \tag{7.9}$$

meaning that the activation energy measured with the μSR spin-flip rate is $E_n + E_\mu$. This is actually the same activation energy measured for conductivity data, since

$$\sigma = e\ n(T)\ \mu(T)\ . \tag{7.10}$$

Hence, the activation energies measured with the temperature dependence of the LF signal, summarised in Table 7.5, can be compared to literature values for the activation energy of conductivity data in phthalocyanines.

[9] Which is our case, as all phthalocyanine samples investigated above room temperature are nominally undoped, and the temperatures used are not high enough for Fermi-Dirac statistics to stand

[10] The low charge carrier mobilities known for phthalocyanines ($\sim 10^{-5}\,\mathrm{cm}^2/\mathrm{Vs}$) rule out the possibility that band-like motion is the mechanism responsible for charge diffusion in Pcs.

Table 7.5: Summary of activation energies and pre-exponential factors extracted from the spin-flip temperature variations obtained in Chapter 6.

sample	E_a (meV)	$\lambda(\infty)$ (μs^{-1})
ZnPc_S	71(8)	6(1)
ZnPc_p3	84(9)	17(4)
H_2Pc_03	130(9)	34(7)
H_2Pc_06	141(6)	33(4)
	376(12)	3900(900)

Most authors use the concept of activation energy to characterise the conductivity of their samples, finding values close to 0.3 eV in thin-film samples of both in ZnPc and H_2Pc [3, 123, 101, 102, 124, 1, 96, 93]. As a general trend, the activation energies are larger in disordered films, reaching 0.35 eV, and smaller in polycrystalline material, where they may be as low as 0.25 eV. In any case, these values are considerably larger than the activation energies one obtains using μSR results, except for the case of H_2Pc_06, where one of the two activation energies falls in the range found in conductivity literature.

However, the fact that the values obtained with μSR are not compatible with those of conductivity studies does not mean that state III is not probing charge carrier diffusion in the material. In reality, one needs to consider the fact that the measurement of a sample's conductivity is not a local technique as μSR always is. At the microscopic level, phthalocyanines are stacked columns of molecular discs in many polycrystals, and conductivity data should be dominated by the slower components of conduction in an experiment where there is an ordered movement of charge carriers, namely jumps between different columns. The 0.3 eV energy should therefore be related with that type of jumps, and that is what is observed in sample H_2Pc_06 at the higher temperatures, giving the 0.376 eV activation energy. At lower temperatures, however, these jumps are less important, particularly if one considers that in a μSR experiment there is nothing forcing the charge carriers to jump, as the electric field does in conductivity data. Carrier

jumps inside columns should then be visible in the low temperature range, with an energy barrier smaller than the column-to-column jump barrier. It is reasonable to assume that the energy barrier for a column-to-column jump is larger than the barrier for a molecule-to-molecule jump inside a column, especially since the activation energies found in the literature for amorphous films are systematically larger than the those for polycrystalline ones. This fact indicates that ordering and orbital overlap decreases the jump barrier in phthalocyanines, and charge carrier jumps inside columns are the ones corresponding to a path of higher ordering and overlap. Furthermore, state III is placed along that same path, and will naturally be more sensitive to carriers diffusing along columns. We therefore interpret the activation energies obtained from the μSR LF experiments as the energy barriers for charge carrier jumps *within* a column.

7.3 Copper phthalocyanine

CuPc has a peculiar electronic structure which may explain why two diamagnetic-like muon signals with such different relaxation rates are observed in this compound. The molecule has a lone electron on a half-occupied level positioned in the middle of the HOMO-LUMO gap, corresponding mainly to a $3d_{x^2-y^2}$ character orbital originated from the Cu atom [64]. When an extra electron is added to the molecule, forming the $CuPc^-$ ion, it is energetically more favourable to deposit it directly into the LUMO than pairing it with the lone Cu electron in the $3d$ orbital. Theoretical calculations predict that the configuration having both electrons in the Cu $3d$ orbital is in fact the first excited state of the $CuPc^-$ ion, the ground state being formed with one electron in the Cu $3d$ orbital and one in the LUMO of the Pc molecule [64].

We attribute the two observed muon signal components in muoniated CuPc molecules to the formation of these two configurations, the $(3d)^1(\mathrm{LUMO})^1$ ground state and the $(3d)^2$ first excited state, by the lone Cu electron and the muonium's electron. In spin terms, the two electrons always pair, forming an $S = 0$ spin state independently of the spatial configuration. The molecular site at which muonium addition occurs is not straightforwardly known, but it is assumed that similar localisations to those found in ZnPc and H_2Pc will be assumed by the positive muon.

For the $(3d)^2$ configuration (excited state), the spatial wavefunctions of the two electrons are identical, centred on the Cu atom and away from the muon sites (which we assume to be similar to those in ZnPc and H_2Pc). No unpaired spin will persist at the muon's site, leaving

it in a purely diamagnetic environment. The slow relaxing component originates thus, in this interpretation, from the full pairing of the two electrons in the $(3d)^2$ configuration, the non-zero relaxation probably arising from dipolar broadening due to nearby protons.

On the other hand, for the $(3d)^1(\mathrm{LUMO})^1$ configuration (ground state), a residual hyperfine field at the muon exists as a result of the up-down spin imbalance caused by the different layout of the two spatial wavefunctions. This produces the strongly relaxing component of the muon precession signal if exchange or spin-flip dynamics between the two electrons operates fast enough to collapse the expected frequency line pair into a diamagnetic-like signal.

Finally, the parallel spin-coupling of the lone Cu electron and the radical's electron, giving rise to a $S = 1$ triplet state, should also be considered. It's unlikely that such a state would live long enough to be identified with one of the two μSR components considered here, in particular since both signals are seen at all temperatures up to 600 K. Nevertheless, it is well possible that the missing fraction observed at low temperature might be the consequence of an unresolved state of that type existing prior to the formation of the two finally observed spin configurations.

Appendix A

μ^+ spin precession

The precession of the muon's spin in the presence of a magnetic field is the main basis of many of μSR's applications. It consists in the clockwise rotation of the spin component perpendicular to the field around that field's axis. If one considers the muon's spin to be initially directed along the polar and azimuthal angles (θ, ϕ), with the spin quantisation axis lying in the z direction, it is easy to check that

$$|\psi(0)\rangle = e^{-\imath\,\phi/2}\cos(\theta/2)|\alpha_\mu\rangle + e^{\imath\,\phi/2}\sin(\theta/2)|\beta_\mu\rangle \tag{A.1}$$

represents the corresponding spin wavefunction at time $t = 0$[1]. It should be noted that if the muon's spin initially has a component perpendicular to z, then $\cos(\theta/2)$ and $\sin(\theta/2)$ are different from zero, and the two terms in the equation above exist. This means that the initial wavefunction is a linear combination of the eigenstates (3.4) and (3.5) in that situation, and as such will exhibit a time dependence. Time evolution is governed by the time-evolution operator

$$\hat{U}(t) = e^{-\frac{\imath}{\hbar}\hat{H}t}\ ; \tag{A.2}$$

at subsequent times t the spin wavefunction therefore becomes

$$\begin{aligned} |\psi(t)\rangle &= \hat{U}(t)\{e^{-\imath\phi/2}\cos(\theta/2)|\alpha_\mu\rangle + e^{\imath\phi/2}\sin(\theta/2)|\beta_\mu\rangle\} \\ &= e^{\imath(\omega_\mu t-\phi)/2}\cos(\theta/2)|\alpha_\mu\rangle + e^{-\imath(\omega_\mu t-\phi)/2}\sin(\theta/2)|\beta_\mu\rangle\ , \end{aligned} \tag{A.3}$$

where the relations (3.4) and (3.5) have been used. As it is noted in Section 3.2.1, the direction of the muon spin as a function of time is given by the expectation value of the Pauli spin operator

[1]This expression actually underlies a choice of gauge to represent the phase of the wavefunction. The spin wavefunction is assumed here to have real positive coefficients whenever ϕ is zero and θ lies in the first quadrant.

$\hat{\vec{\sigma}}_\mu$,

$$\hat{\vec{\sigma}}_\mu = \frac{\hat{\vec{S}}_\mu}{\hbar/2} \; ;$$

its x and y components are usually written as a function of the Pauli ladder operators

$$\hat{\sigma}_{\mu_+} = \hat{\sigma}_{\mu_x} + \imath\, \hat{\sigma}_{\mu_y} \tag{A.4}$$

$$\hat{\sigma}_{\mu_-} = \hat{\sigma}_{\mu_x} - \imath\, \hat{\sigma}_{\mu_y} \; , \tag{A.5}$$

which act on the basis set $\{|\alpha_\mu\rangle, |\beta_\mu\rangle\}$ according to

$$\hat{\sigma}_{\mu_+}|\alpha_\mu\rangle = 0 \qquad ; \quad \hat{\sigma}_{\mu_-}|\alpha_\mu\rangle = 2|\beta_\mu\rangle \tag{A.6}$$

$$\hat{\sigma}_{\mu_+}|\beta_\mu\rangle = 2|\alpha_\mu\rangle \quad ; \quad \hat{\sigma}_{\mu_-}|\beta_\mu\rangle = 0 \; . \tag{A.7}$$

The x, y components of the Pauli operator are therefore

$$\hat{\sigma}_{\mu_x} = \frac{1}{2}(\hat{\sigma}_{\mu_+} + \hat{\sigma}_{\mu_-}) \tag{A.8}$$

$$\hat{\sigma}_{\mu_y} = \frac{1}{2\imath}(\hat{\sigma}_{\mu_+} - \hat{\sigma}_{\mu_-}) \; , \tag{A.9}$$

and one gets

$$\hat{\sigma}_{\mu_x}|\alpha_\mu\rangle = +|\beta_\mu\rangle \qquad \hat{\sigma}_{\mu_y}|\alpha_\mu\rangle = +\imath\,|\beta_\mu\rangle \qquad \hat{\sigma}_{\mu_z}|\alpha_\mu\rangle = +|\alpha_\mu\rangle \tag{A.10}$$

$$\hat{\sigma}_{\mu_x}|\beta_\mu\rangle = +|\alpha_\mu\rangle \qquad \hat{\sigma}_{\mu_y}|\beta_\mu\rangle = -\imath\,|\alpha_\mu\rangle \qquad \hat{\sigma}_{\mu_z}|\beta_\mu\rangle = -|\beta_\mu\rangle \; . \tag{A.11}$$

Finally, the expectation values of the x, y, z components of the Pauli spin operator for the muon may be computed using the time-dependent wavefunction (A.3):

$$\begin{aligned}
\langle\hat{\sigma}_{\mu_x}(t)\rangle &= \langle\psi(t)|\hat{\sigma}_{\mu_x}|\psi(t)\rangle \\
&= \langle\psi(t)|\left(e^{\imath(\omega_\mu t-\phi)/2}\cos(\theta/2)|\beta_\mu\rangle + e^{-\imath(\omega_\mu t-\phi)/2}\sin(\theta/2)|\alpha_\mu\rangle\right) \\
&= \left(e^{\imath(\omega_\mu t-\phi)} + e^{-\imath(\omega_\mu t-\phi)}\right)\cos(\theta/2)\sin(\theta/2) \\
&= \cos(-\omega_\mu t+\phi)\sin\theta \; ,
\end{aligned} \tag{A.12}$$

$$\begin{aligned}
\left\langle\hat{\sigma}_{\mu_y}(t)\right\rangle &= \langle\psi(t)|\hat{\sigma}_{\mu_y}|\psi(t)\rangle \\
&= \langle\psi(t)|\left(\imath\, e^{\imath(\omega_\mu t-\phi)/2}\cos(\theta/2)|\beta_\mu\rangle - \imath\, e^{-\imath(\omega_\mu t-\phi)/2}\sin(\theta/2)|\alpha_\mu\rangle\right) \\
&= \left(\imath\, e^{\imath(\omega_\mu t-\phi)} - \imath\, e^{-\imath(\omega_\mu t-\phi)}\right)\cos(\theta/2)\sin(\theta/2) \\
&= \sin(-\omega_\mu t+\phi)\sin\theta \; ,
\end{aligned} \tag{A.13}$$

$$\begin{aligned}
\langle\hat{\sigma}_{\mu_z}(t)\rangle &= \langle\psi(t)|\hat{\sigma}_{\mu_z}|\psi(t)\rangle \\
&= \langle\psi(t)|\left(e^{\imath(\omega_\mu t-\phi)/2}\cos(\theta/2)|\alpha_\mu\rangle - e^{-\imath(\omega_\mu t-\phi)/2}\sin(\theta/2)|\beta_\mu\rangle\right) \\
&= \cos^2(\theta/2)+\sin^2(\theta/2) \\
&= \cos\theta\ . \qquad \text{(A.14)}
\end{aligned}$$

$\left\langle\hat{\vec{\sigma}}_\mu(t)\right\rangle$ is therefore a unitary vector whose projection on the xy plane rotates clockwise with angular frequency ω_μ, maintaining its z-projection constant.

Appendix B

The μSR time histogram

In μSR experiments, the muon polarisation is followed *via* the counting of positrons emitted along fixed directions in space as a function of time. The counts are recorded in time histograms, one for each positron detector; the shape of those histograms depends not only on the time evolution of the muon polarisation, but also on specific details of the detectors, such as their efficiencies in detecting positrons of different energies, or their geometries. In order to obtain the explicit expression of the time histogram for a positron detector like the one shown in Figure 3.10, we will consider first the decay of a single positive muon in the sample at an instant t after implantation, when its spin $\vec{S}_\mu$ makes an angle φ with the direction along the telescope's centre, as depicted in Figure B.1.

In principle, the probability that a decay positron with a certain energy will be detected should match the probability of it being emitted, as given by dW in equation (3.15). In practice, however, it will be lower, since there is the chance that the positron is not detected, either due to it being absorbed somewhere along the way before reaching the telescope (which is quite probable to happen if the positron is emitted with a low energy), or just to a natural miss of the detection system derived from the quantum nature of the positron-scintillator interaction and the statistics of signal production and processing (*id.*). The detection efficiency depends strongly on the energy of the emitted positron, and to express this fact it is usual to define a *detection efficiency function* $D(\epsilon)$, so that the probability per unit time dW_{D} that a positron with energy ϵ is *detected* along a solid angle $d\Omega$ becomes

$$\begin{aligned} dW_{\mathrm{D}}(\epsilon,\theta) &= dW(\epsilon,\theta)\, D(\epsilon) \\ &= \frac{1}{\tau_\mu}\,\frac{n(\epsilon)}{2\pi}\,(1+a(\epsilon)\cos\theta)\; D(\epsilon)\, d\epsilon\, d\Omega\ , \end{aligned} \tag{B.1}$$

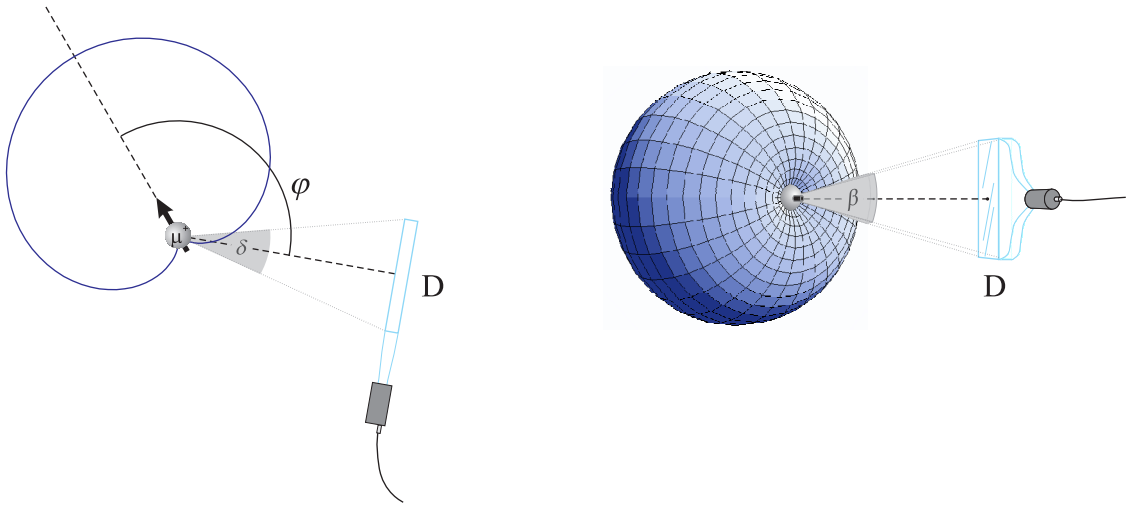

Figure B.1: Geometry of the positron detector D used for the calculations in this appendix. The left presents the top side view, while the right shows it in perspective. The angular positron emission pattern for $\epsilon = 1$ was superimposed to both drawings.

where one obviously has $D(\epsilon) \leq 1$ for all positron energies ϵ. Defining the quantities η_ϵ and α_ϵ as

$$\eta_\epsilon = \frac{\int_0^1 n(\epsilon)\, D(\epsilon)\, d\epsilon}{\int_0^1 n(\epsilon)\, d\epsilon} \tag{B.2}$$

$$\alpha_\epsilon = \frac{\int_0^1 n(\epsilon)\, a(\epsilon)\, D(\epsilon)\, d\epsilon}{\int_0^1 n(\epsilon)\, a(\epsilon)\, d\epsilon}\ , \tag{B.3}$$

the pure angular dependence of $dW_{\rm D}$ may be written as

$$\begin{aligned} dW_{\rm D}(\theta) &= \int_0^1 \frac{1}{2\pi}\, \frac{n(\epsilon)}{\tau_\mu}\, (1 + a(\epsilon)\cos\theta)\ D(\epsilon)\, d\Omega\, d\epsilon \\ &= \frac{1}{2\pi\tau_\mu}\, \frac{1}{2}\, \eta_\epsilon \left(1 + \frac{1}{3}\, \alpha_\epsilon\, \cos\theta\right)\, d\Omega\ . \end{aligned} \tag{B.4}$$

Noting that (B.2) implies η_ϵ being always lower than 1, and comparing (B.4) with the probability that the positron is emitted along $d\Omega$, equation (3.19),

$$dW(\theta) = \frac{1}{2\pi\tau_\mu}\, \frac{1}{2} \left(1 + \frac{1}{3}\, \cos\theta\right)\, d\Omega\ ,$$

it becomes clear that η_ϵ is a net detection efficiency over the full positron energy range. It represents the fraction of detected *vs.* emitted positrons due to $D(\epsilon)$, as better seen by integrating equation (B.4) over the full 4π solid angle,

$$\int_{4\pi} dW_{\rm D}(\theta) = \int_{4\pi} \frac{1}{2\pi\tau_\mu}\, \frac{1}{2}\, \eta_\epsilon \left(1 + \frac{1}{3}\, \alpha_\epsilon\, \cos\theta\right)\, d\Omega\ = \frac{\eta_\epsilon}{\tau_\mu}\ .$$

The quantity α_ϵ is the asymmetry factor change relative to the 1/3 average found in equation (3.19). Depending on the shape of $D(\epsilon)$, it may correspond to an enhancement or a decrease relative to the 1/3 value; it normally produces the former, since $D(\epsilon)$ is usually larger at higher energies, where the product $n(\epsilon)a(\epsilon)$ is positive.

The total probability per unit time that the positron emitted from the decaying muon is detected in the telescope will then be

$$W_{\rm D} = \int_{\Omega_{\rm D}} \frac{1}{2\pi\tau_\mu}\,\frac{1}{2}\,\eta_\epsilon \left(1+\frac{1}{3}\,\alpha_\epsilon\,\cos\theta\right)\,d\Omega\ , \tag{B.5}$$

where $\Omega_{\rm D}$ is the solid angle subtended by D. In the simple case shown in Figure B.1, $\Omega_{\rm D}$ is easily expressed in terms of the telescope's angular apertures (or acceptances) (δ,β) defined in that figure, so that (B.5) becomes

$$\begin{aligned} W_{\rm D} &= \int_{\pi/2-\beta/2}^{\pi/2+\beta/2} \left(\int_{\varphi-\delta/2}^{\varphi+\delta/2} \frac{1}{2\pi\tau_\mu}\,\frac{1}{2}\,\eta_\epsilon \left(1+\frac{1}{3}\,\alpha_\epsilon\,\cos\theta\right)\,d\theta \right) \sin\phi\,d\phi \\ &= \frac{1}{\tau_\mu}\,\frac{\delta}{2\pi}\,\sin(\beta/2)\,\eta_\epsilon \left(1+\frac{1}{3}\,\frac{\sin(\delta/2)}{\delta/2}\,\alpha_\epsilon\,\cos\varphi\right)\ , \end{aligned} \tag{B.6}$$

where we have used ϕ and θ for the integration's polar and azimuthal angles, respectively[1]. Rearranging this expression by further defining

$$\eta_g = \sin(\beta/2)\,\frac{\delta}{2\pi} \tag{B.7}$$

$$\alpha_g = \frac{\sin(\delta/2)}{\delta/2}\ , \tag{B.8}$$

one gets

$$W_{\rm D} = \frac{1}{\tau_\mu}\,\eta_g\,\eta_\epsilon \left(1+\frac{1}{3}\,\alpha_g\,\alpha_\epsilon\,\cos\varphi\right)\ . \tag{B.9}$$

η_g and α_g are respectively the geometric efficiency of the telescope and the geometric asymmetry factor change; their dependence on δ and β is shown in Figure B.2. It should be noted that both quantities are lower than 1, but while the geometric efficiency approaches 1 as the telescope gets nearer to covering the whole 4π solid angle, the asymmetry factor change approaches zero. That is to say that the larger the detector, the more positrons will be detected, but the less pronounced will become the imbalance between the number of detected positrons when the muon spin is pointing to and away from the telescope.

[1]This is an unorthodox choice of notation, chosen to allow the angle φ between the detector's normal and the muon spin to have any value between zero and 2π.

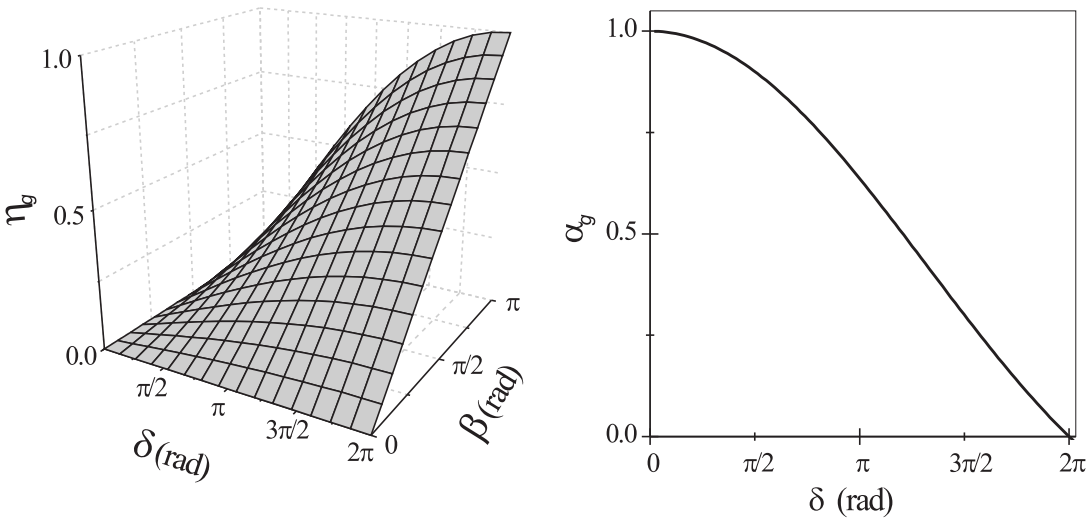

Figure B.2: Geometric efficiency η_g (left) and geometric asymmetry factor change α_g (right) of the positron telescope D

Finally, (B.9) may still be reduced to

$$W_{\mathrm{D}} = \frac{1}{\tau_\mu}\,\eta_{\mathrm{D}}\left(1 + A_{\mathrm{D}}\,\left\langle\hat{\vec{\sigma}}_\mu(t)\right\rangle . \hat{r}_{\mathrm{D}}\right)\ , \tag{B.10}$$

if one notes that $\cos\varphi = \left\langle\hat{\vec{\sigma}}_\mu(t)\right\rangle . \hat{r}_{\mathrm{D}}$, where $\left\langle\hat{\vec{\sigma}}_\mu(t)\right\rangle$ is the muon spin direction at time t and $\hat{r}_{\mathrm{D}}$ is a unitary vector along the direction defined by the sample and the positron telescope, and introduces the telescope detector's efficiency η_{D} and the detector's asymmetry factor A_{D}

$$\eta_{\mathrm{D}} = \eta_\epsilon\,\eta_g \tag{B.11}$$

$$A_{\mathrm{D}} = \frac{1}{3}\,\alpha_g\,\alpha_\epsilon\ , \tag{B.12}$$

both depending on the detection efficiency function and the geometry of the telescope detector. It should be referred that, in spite of having performed the calculation of W_{D} for the specific case of Figure B.1, equations (B.9) and (B.10) still hold for a generic detector placed anywhere around the sample. The explicit forms of η_ϵ, α_ϵ, η_g and α_g will of course be different, but their general trends are the same as the ones referred above.

Knowing the probability W_{D} that a positron is detected in the telescope detector, one may now derive the shape of the time histogram of positron counts registered in D. The number of positrons emitted in a time interval $[t, t+dt]$ after implantation equals the number of muons

decaying in that same interval,

$$dN_{\mu^+}(t) = N_{\mu^+}(t)\, dt \ , \tag{B.13}$$

where $N_{\mu^+}(t)$, given by the radioactive decay law

$$N_{\mu^+}(t) = N_0 \ e^{-t/\tau_\mu} \tag{B.14}$$

with N_0 being the total number of muons implanted in the sample, is the number of muons surviving in the sample until t. According to the meaning of $W_{\rm D}$, the number of positrons detected in D is therefore

$$dN_{\rm D}(t) = \langle W_{\rm D} \rangle^{ensemble} \ N_{\mu^+}(t)\, dt \ , \tag{B.15}$$

noting that the probability $W_{\rm D}$ has to be averaged over the implanted muon ensemble. Taking equation (B.10) and the definition of the ensemble's polarisation (3.11), this average is

$$\begin{aligned} \langle W_{\rm D} \rangle^{ensemble} &= \left\langle \frac{1}{\tau_\mu}\, \eta_{\rm D} \left(1 + A_{\rm D} \ \left\langle \hat{\vec{\sigma}}_\mu(t) \right\rangle \,.\, \hat{r}_{\rm D} \right) \right\rangle^{ensemble} \\ &= \frac{1}{\tau_\mu}\, \eta_{\rm D} \left(1 + A_{\rm D} \ \langle \left\langle \hat{\vec{\sigma}}_\mu(t) \right\rangle \rangle^{ensemble} \,.\, \hat{r}_{\rm D} \right) \\ &= \frac{1}{\tau_\mu}\, \eta_{\rm D} \left(1 + A_{\rm D} \ \vec{P}_\mu(t) \,.\, \hat{r}_{\rm D} \right) \ . \end{aligned} \tag{B.16}$$

Hence, the positron counts $dN_{\rm D}(t)$ in D will be

$$dN_{\rm D}(t) = N_0\, \eta_{\rm D}\, \frac{e^{-t/\tau_\mu}}{\tau_\mu} \left(1 + A_{\rm D} \ \vec{P}_\mu(t) \,.\, \hat{r}_{\rm D} \right) \ dt \ , \tag{B.17}$$

which for a finite time bin of width Δt centred in t_i finally reads

$$\Delta N_{\rm D}(t_i) = N_0\, \eta_{\rm D}\, \frac{e^{-t_i/\tau_\mu}}{\tau_\mu} \left(1 + A_{\rm D} \ \vec{P}_\mu(t_i) \,.\, \hat{r}_{\rm D} \right) \ \Delta t \ . \tag{B.18}$$

It should be noted that this expression is of course valid only if Δt is sufficiently small so that $\vec{P}_\mu(t)$ and e^{-t/τ_μ} may be equaled to their central value in the interval $[t_i - \Delta t/2, t_i + \Delta t/2]$. This may not be true if, for instance, $\vec{P}_\mu(t)$ is rapidly changing because of a fast precessional or exponential behaviour, in which case the function's mean value over that interval would have to be used.

Appendix C

The hyperfine interaction tensor

The hyperfine interaction between the electron's spin $\vec{S}_e$ and the positive muon's spin $\vec{S}_\mu$ appears naturally by the application of the laws of electromagnetism to the interaction between the magnetic moments of both spins. We start by considering that the muon spin magnetic moment $\vec{\mu}_\mu$ generates a dipolar vector potential at a given position $\vec{r}$ relative to the muon given by (see *e.g.* [54])

$$\vec{A}_\mu(\vec{r}) = \frac{\mu_0}{4\pi\, r^3}\ \vec{\mu}_\mu \times \vec{r}\,, \tag{C.1}$$

from which a magnetic field

$$\vec{B}_\mu(\vec{r}) = \vec{\nabla} \times \left(\frac{\mu_0}{4\pi\, r^3}\ \vec{\mu}_\mu \times \vec{r}\right) \tag{C.2}$$

derives. If one places the electron at $\vec{r}$, the electron-muon system will acquire a magnetic interaction energy of

$$E_{\mu,e} = -\vec{\mu}_e.\vec{B}_\mu = -\frac{\mu_0}{4\pi}\ \gamma_e\gamma_\mu\ \vec{S}_e\,.\,\vec{\nabla} \times \left(\vec{S}_\mu \times \frac{\vec{r}}{r^3}\right)\ , \tag{C.3}$$

where the gyromagnetic ratios (see the footnote of table's 3.2 caption) γ_e and γ_μ of the electron and the muon were used in order to express the magnetic moments in terms of the spin angular moments. Using the circular commuting properties of the mix product, and recognising that in general the electron will not be at a fixed position, but distributed according to a probability density given by the square of the electronic wavefunction $\psi(\vec{r})$, equation (C.3) changes to

$$\begin{aligned} E_{\mu,e} &= \frac{\mu_0}{4\pi}\ \gamma_e\gamma_\mu\ \int \vec{\nabla}.\left(\vec{S}_e \times \left(\vec{S}_\mu \times \frac{\vec{r}}{r^3}\right)\right)\ |\psi(\vec{r})|^2\ d^3\vec{r} \\ &= \frac{\mu_0}{4\pi}\ \gamma_e\gamma_\mu\ \left\{\int \vec{\nabla}.\left(|\psi(\vec{r})|^2\ \vec{S}_e \times \left(\vec{S}_\mu \times \frac{\vec{r}}{r^3}\right)\right)\ d^3\vec{r} - \right. \\ &\quad \left. - \int \vec{S}_e \times \left(\vec{S}_\mu \times \frac{\vec{r}}{r^3}\right)\ .\,\vec{\nabla}|\psi(\vec{r})|^2\ d^3\vec{r}\right\}\ , \end{aligned} \tag{C.4}$$

where the relation $\vec{\nabla}.(f\vec{A}) = (\vec{\nabla}(f).\vec{A} + f(\vec{\nabla}.\vec{A})$ from vector algebra was also used. The first integral in (C.4) is zero, since from Gauss's theorem it is ia flux over a closed surface,

$$\int \vec{\nabla}.\left(|\psi(\vec{r})|^2\ \vec{S}_e \times \left(\vec{S}_\mu \times \frac{\vec{r}}{r^3}\right)\right)\ d^3\vec{r}\ = \int_S |\psi(\vec{r})|^2\ \vec{S}_e \times \left(\vec{S}_\mu \times \frac{\vec{r}}{r^3}\right)\ dS, \tag{C.5}$$

which evaluated at $r \to \infty$ vanishes due to the fact that $\psi(\vec{r})$ must be an exponentially decreasing function with distance to represent a valid state in Hilbert space. Hence, the magnetic interaction energy of the muon-electron system is

$$E_{\mu,e} = -\frac{\mu_0}{4\pi}\ \gamma_e\gamma_\mu\ \int \vec{S}_e \times \left(\vec{S}_\mu \times \frac{\vec{r}}{r^3}\right).\vec{\nabla}|\psi(\vec{r})|^2\ d^3\vec{r}\,, \tag{C.6}$$

which, using the relation $\vec{A} \times (\vec{B} \times \vec{C}) = \vec{B}(\vec{A}.\vec{C}) - \vec{C}(\vec{A}.\vec{B})$ and the fact that $\gamma_e$is negative, is finally written as

$$E_{\mu,e} = \frac{\mu_0}{4\pi}\ |\gamma_e|\gamma_\mu\ \int \frac{1}{r^2}\left\{\vec{S}_\mu(\vec{S}_e.\hat{r}) - \hat{r}(\vec{S}_e.\vec{S}_\mu)\right\}.\vec{\nabla}|\psi(\vec{r})|^2\ d^3\vec{r}\,. \tag{C.7}$$

The integral in equation (C.7) can be split in two contributions,

$$I_1 = -\vec{S}_e.\vec{S}_\mu \int \frac{1}{r^2}\ \hat{r}.\vec{\nabla}|\psi(\vec{r})|^2\ d^3\vec{r} \tag{C.8}$$

$$I_2 = \int \frac{1}{r^2}\ (\vec{S}_e.\hat{r})(\vec{S}_\mu.\vec{\nabla}|\psi(\vec{r})|^2)\ d^3\vec{r} \tag{C.9}$$

from which I_1 can be straightly evaluated if one considers the gradient in spherical coordinates, $\vec{\nabla}f = \frac{\partial f}{\partial r}\hat{r} + \frac{1}{r}\frac{\partial f}{\partial \theta}\hat{\theta} + \frac{1}{r\sin\theta}\frac{\partial f}{\partial \phi}\hat{\phi}$:

$$\begin{aligned} I_1 &= -\vec{S}_e.\vec{S}_\mu \int \frac{1}{r^2}\ \hat{r}.\hat{r}\ \frac{\partial(|\psi(\vec{r})|^2)}{\partial r}\ d^3\vec{r} \\ &= -\vec{S}_e.\vec{S}_\mu \int_0^{2\pi}\int_0^{\pi}\int_0^{\infty} \frac{1}{r^2}\ \frac{\partial(|\psi(\vec{r})|^2)}{\partial r}\ r^2\ \sin\theta\, dr\, d\theta\, d\phi \\ &= -\vec{S}_e.\vec{S}_\mu \int_0^{2\pi}\int_0^{\pi} [|\psi(\infty)|^2 - |\psi(0)|^2]\sin\theta\, d\theta\, d\phi \\ &= 4\pi\ |\psi(0)|^2\ \vec{S}_e.\vec{S}_\mu\ ; \end{aligned} \tag{C.10}$$

the integral is proportional to the electronic density at the muon's position, independently of any specific spatial dependence of the wavefunction. To compute the integral I_2, on the other hand, one needs some information about the spatial symmetry of the wavefunction $\psi(\vec{r})$. In the following, we consider the three possible cases: *(i)* when the electronic cloud is isotropic, *i.e.* $\psi(\vec{r}) = \psi(r)$; *(ii)* when the electronic cloud is axially symmetric, meaning that $\psi(\vec{r}) = \psi(r,\theta)$ whenever the symmetry axis coincides with the z-axis of the coordinate system; and finally *(iii)* when $\psi(\vec{r})$ does not exhibit any type of symmetry.

Isotropic wavefunction

If the electron wavefunction is isotropic, it only depends on the radial coordinate, and the gradient of $|\psi(\vec{r})|^2$ is once again

$$\vec{\nabla}|\psi(\vec{r})|^2 = \frac{\partial(|\psi(r)|^2)}{\partial r}\ \hat{r}\ ; \tag{C.11}$$

since the radial unit vector $\hat{r}$ is given in terms of the cartesian unit vectors $\hat{x}$, $\hat{y}$ and $\hat{z}$ and the spherical angles θ and ϕ by

$$\hat{r} = \sin\theta\cos\phi\ \hat{x} + \sin\theta\sin\phi\ \hat{y} + \cos\theta\ \hat{z}\ , \tag{C.12}$$

the dot products inside the integral (C.9) can be evaluated to give (see the integration over the r coordinate done in (C.10))

$$\begin{aligned} I_2^{iso} &= \int \frac{1}{r^2}\ (\vec{S}_e.\hat{r})(\vec{S}_\mu.\hat{r})\frac{\partial(|\psi(r)|^2)}{\partial r}\ d^3\vec{r} \\ &= -\ |\psi(0)|^2 \int_0^{2\pi}\int_0^{\pi} (S_{e_x}\sin\theta\cos\phi + S_{e_y}\sin\theta\sin\phi + S_{e_z}\cos\theta)\times \\ &\quad \times\ (S_{\mu_x}\sin\theta\cos\phi + S_{\mu_y}\sin\theta\sin\phi + S_{\mu_z}\cos\theta)\sin\theta\, d\theta\, d\phi\ ; \end{aligned} \tag{C.13}$$

when the product inside the integral is performed, the crossed factors $S_{e_x}S_{\mu_y}$, $S_{e_x}S_{\mu_z}$, *etc* will multiply odd functions of ϕ and disappear upon the ϕ integration. One is left with

$$\begin{aligned} I_2^{iso} &= -\ |\psi(0)|^2\pi \int_0^{\pi} (S_{e_x}S_{\mu_x}\ \sin^3\theta + S_{e_y}S_{\mu_y}\ \sin^3\theta + 2\,S_{e_z}S_{\mu_z}\ \cos^2\theta\ \sin\theta)\ d\theta \\ &= -\ |\psi(0)|^2 \left(S_{e_x}S_{\mu_x}\ \frac{4}{3} + S_{e_y}S_{\mu_y}\ \frac{4}{3} + 2\,S_{e_z}S_{\mu_z}\ \frac{2}{3}\right) \\ &= -\frac{4\pi}{3}\ |\psi(0)|^2\ \vec{S}_e.\vec{S}_\mu\ ; \end{aligned} \tag{C.14}$$

the interaction energy is therefore

$$\begin{aligned} E_{\mu,e}^{iso} &= \frac{\mu_0}{4\pi}\ |\gamma_e|\gamma_\mu\ (I_1 + I_2^{iso}) \\ &= \frac{\mu_0}{4\pi}\ |\gamma_e|\gamma_\mu\ \left(4\pi - \frac{4\pi}{3}\right)\ |\psi(0)|^2\ \vec{S}_e.\vec{S}_\mu \\ &= \frac{\mu_0}{4\pi}\ |\gamma_e|\gamma_\mu\ \frac{8\pi}{3}\ |\psi(0)|^2\ \vec{S}_e.\vec{S}_\mu \\ &= \frac{2\pi}{\hbar}A_{iso}\ \vec{S}_e.\vec{S}_\mu\ , \end{aligned} \tag{C.15}$$

where A_{iso} is known as the *contact hyperfine coupling constant*,

$$A_{iso} = \frac{\hbar}{2\pi}\ \frac{\mu_0}{4\pi}\ |\gamma_e|\gamma_\mu\ \frac{8\pi}{3}\ |\psi(0)|^2\ , \tag{C.16}$$

due to the fact that a finite unpaired spin density is necessary at the muon's position for the interaction to exist. The interaction is accordingly called *contact hyperfine interaction*, or *Fermi contact interaction* since Fermi was the first to infer its existence and derive the energy associated to it. (C.15) may be cast in tensorial form as

$$E^{iso}_{\mu,e} = \frac{2\pi}{\hbar}\ \vec{S}_e.\begin{bmatrix} A_{iso} & 0 & 0 \\ 0 & A_{iso} & 0 \\ 0 & 0 & A_{iso} \end{bmatrix}.\vec{S}_\mu\ , \tag{C.17}$$

showing that the hyperfine interaction tensor's principal values A'_{xx}, A'_{yy} and A'_{zz} all have the same value, and are equal to A_{iso}.

Axially symmetric wavefunction

When the electronic distribution has an axially symmetric character, the wavefunction will depend both on the radial distance r to the muon and the polar angle θ defined with its symmetry axis. The probability density gradient in (C.9) is therefore

$$\vec{\nabla}|\psi(\vec{r})|^2 = \frac{\partial(|\psi(r,\theta)|^2)}{\partial r}\ \hat{r} + \frac{1}{r}\frac{\partial(|\psi(r,\theta)|^2)}{\partial\theta}\ \hat{\theta}, \tag{C.18}$$

with the polar unitary vector $\hat{\theta}$ being given by

$$\hat{\theta} = \cos\theta\cos\phi\ \hat{x} + \cos\theta\sin\phi\ \hat{y} - \sin\theta\ \hat{z}\ . \tag{C.19}$$

Again, one evaluates the dot products in (C.10) to obtain

$$\begin{aligned} I_2^{ax} &= \int \frac{1}{r^2}\ (\vec{S}_e.\hat{r})(\vec{S}_\mu.\hat{r})\frac{\partial(|\psi(r,\theta)|^2)}{\partial r}\ d^3\vec{r} + \int \frac{1}{r^2}\ (\vec{S}_e.\hat{r})(\vec{S}_\mu.\hat{\theta})\frac{1}{r}\frac{\partial(|\psi(r,\theta)|^2)}{\partial\theta}\ d^3\vec{r} \\ &= I_2^{iso} + \int_0^{2\pi}\int_0^{\pi}\int_0^{\infty}(S_{e_x}\sin\theta\cos\phi + S_{e_y}\sin\theta\sin\phi + S_{e_z}\cos\theta)\times \\ &\quad \times\ (S_{\mu_x}\cos\theta\cos\phi + S_{\mu_y}\cos\theta\sin\phi - S_{\mu_z}\sin\theta)\frac{1}{r}\frac{\partial(|\psi(r,\theta)|^2)}{\partial\theta}\sin\theta\, dr\, d\theta\, d\phi\ , \end{aligned} \tag{C.20}$$

where the second integral, which we denote as I_3^{ax}, represents the dipolar contribution to the hyperfine interaction arising from the non-isotropic shape of the wavefunction. Just as what happened in the calculation of (C.14), the integration over ϕ eliminates all crossed terms in I_3^{ax},

which becomes

$$\begin{aligned} I_3^{ax} &= (S_{e_x}S_{\mu_x} + S_{e_y}S_{\mu_y} - 2\,S_{e_z}S_{\mu_z})\;\pi \int_0^\pi \int_0^\infty \sin^2\theta\cos\theta \frac{1}{r}\frac{\partial(|\psi(r,\theta)|^2)}{\partial\theta} dr\,d\theta \\ &= \left\{-\frac{1}{2}(S_{e_x}S_{\mu_x} + S_{e_y}S_{\mu_y}) + S_{e_z}S_{\mu_z}\right\} \times \\ &\quad \times (-2\pi)\int_0^\pi \int_0^\infty \sin^2\theta\cos\theta \frac{1}{r}\frac{\partial(|\psi(r,\theta)|^2)}{\partial\theta} d\theta\,dr\ . \end{aligned} \tag{C.21}$$

It is customary to define a *dipolar parameter* D as (*cp.* (C.16))

$$D = \frac{\hbar}{2\pi}\;\frac{\mu_0}{4\pi}\;|\gamma_e|\gamma_\mu\;(-2\pi)\int_0^\pi \int_0^\infty \sin^2\theta\cos\theta \frac{1}{r}\frac{\partial(|\psi(r,\theta)|^2)}{\partial\theta} d\theta\,dr\ , \tag{C.22}$$

to write the interaction energy in the form

$$\begin{aligned} E_{\mu,e}^{ax} &= \frac{\mu_0}{4\pi}\;|\gamma_e|\gamma_\mu\;(I_1 + I_2^{ax}) = \frac{\mu_0}{4\pi}\;|\gamma_e|\gamma_\mu\;(I_1 + I_2^{iso} + I_3^{ax}) \\ &= \frac{2\pi}{\hbar}\left(A_{iso}\,\vec{S}_e.\vec{S}_\mu + D\left\{-\frac{1}{2}(S_{e_x}S_{\mu_x} + S_{e_y}S_{\mu_y}) + S_{e_z}S_{\mu_z}\right\}\right)\ ; \end{aligned} \tag{C.23}$$

in a tensorial notation,

$$\begin{aligned} E_{\mu,e}^{ax} &= \frac{2\pi}{\hbar}\left(\vec{S}_e.\begin{bmatrix} A_{iso} & 0 & 0 \\ 0 & A_{iso} & 0 \\ 0 & 0 & A_{iso} \end{bmatrix}.\vec{S}_\mu + \vec{S}_e.\begin{bmatrix} -\frac{D}{2} & 0 & 0 \\ 0 & -\frac{D}{2} & 0 \\ 0 & 0 & +D \end{bmatrix}.\vec{S}_\mu\right) \\ &= \frac{2\pi}{\hbar}\;\vec{S}_e.\begin{bmatrix} A_{iso} - \frac{D}{2} & 0 & 0 \\ 0 & A_{iso} - \frac{D}{2} & 0 \\ 0 & 0 & A_{iso} + D \end{bmatrix}.\vec{S}_\mu \end{aligned} \tag{C.24}$$

in which the quantity

$$\mathbf{D} = \begin{bmatrix} -\frac{D}{2} & 0 & 0 \\ 0 & -\frac{D}{2} & 0 \\ 0 & 0 & +D \end{bmatrix} \tag{C.25}$$

is the traceless dipolar tensor, and the total hyperfine interaction tensor is

$$\mathbf{A} = \begin{bmatrix} A'_{xx} & 0 & 0 \\ 0 & A'_{yy} & 0 \\ 0 & 0 & A'_{zz} \end{bmatrix} = \begin{bmatrix} A_{iso} - \frac{D}{2} & 0 & 0 \\ 0 & A_{iso} - \frac{D}{2} & 0 \\ 0 & 0 & A_{iso} + D \end{bmatrix}\ . \tag{C.26}$$

Often, the perpendicular $A_\perp$ and parallel $A_\parallel$ hyperfine parameters

$$A_\perp = A_{iso} - \frac{D}{2} \tag{C.27}$$

$$A_\parallel = A_{iso} + D \tag{C.28}$$

are used to express the hyperfine interaction tensor; conversely,

$$A_{iso} = \frac{A_{\parallel} + 2A_{\perp}}{3} \tag{C.29}$$

$$D = \frac{2}{3}(A_{\parallel} - A_{\perp}) \ . \tag{C.30}$$

It is not difficult to show that the absolute sign of the dipolar parameter D distinguishes prolate-shaped electronic distributions from oblate-shaped ones. If we consider (C.22), and suppose that $|\psi(r,\theta)|^2$ is prolate, the partial derivative $\frac{\partial(|\psi(r,\theta)|^2)}{\partial\theta}$ will be negative in the first θ quadrant and positive in the second; the opposite happens with the product $\sin^2\theta\cos\theta$, which makes the integrand of (C.22) to be negative over the full θ range of 0 to π. Since the integral is multiplied by -2π, that will result in D having a positive value. For the case of an oblate distribution, the only factor that changes in the integrand of (C.22) is $\frac{\partial(|\psi(r,\theta)|^2)}{\partial\theta}$, which will exhibit a symmetric variation along θ; it starts with positive values in the first quadrant and moves to negative ones in the second. The integrand will therefore be positive throughout all values of θ, resulting in a negative value for D.

Fully anisotropic wavefunction

While isotropy leads to the three principal values of the hyperfine interaction tensor being all equal, and axial symmetry to two of them still sharing the same value, in the case of a fully anisotropic wavefunction the values of A'_{xx}, A'_{yy} and A'_{zz} will all be different. The process used to derive the expressions for $\mathbf{A}$ in the cases of isotropy and axial symmetry may be followed, now using the full expression for the gradient of $|\psi(r,\theta,\phi)|^2$,

$$\vec{\nabla}|\psi(\vec{r})|^2 = \frac{\partial(|\psi(r,\theta,\phi)|^2)}{\partial r}\ \hat{r} + \frac{1}{r}\frac{\partial(|\psi(r,\theta,\phi)|^2)}{\partial\theta}\ \hat{\theta} + \frac{1}{r\ \sin\theta}\frac{\partial(|\psi(r,\theta,\phi)|^2)}{\partial\phi}\ \hat{\phi} \tag{C.31}$$

and the relation between the azimuthal unitary vector $\hat{\phi}$ and $\hat{x}$, $\hat{y}$ and $\hat{z}$,

$$\hat{\phi} = -\sin\phi\ \hat{x} + \cos\phi\ \hat{y} \tag{C.32}$$

in (C.9). The algebra is somewhat irksome, and in the end a result resembling (C.23), but bearing different weights in the products of the spin components, is obtained. Independently of that, the total hyperfine tensor may always be written in a form similar to (C.26) by using the parameters

$$A_{iso} = \frac{A'_{xx} + A'_{yy} + A'_{zz}}{3} \tag{C.33}$$

$$D = \frac{2A'_{zz} - (A'_{xx} + A'_{yy})}{3} \tag{C.34}$$

$$\eta = \frac{A'_{yy} - A'_{xx}}{D}\ , \tag{C.35}$$

which relate to the principal values of the tensor by

$$A'_{xx} = A_{iso} - \frac{D}{2}(1+\eta) \quad \text{(C.36)}$$

$$A'_{yy} = A_{iso} - \frac{D}{2}(1-\eta) \quad \text{(C.37)}$$

$$A'_{zz} = A_{iso} + D \ . \quad \text{(C.38)}$$

Appendix D

Explicit expression of the Q matrix

$$\mathbf{Q} = \begin{bmatrix}
0 & \omega_\mu & & & & & & & -a_{zx} & -a_{zy} & -a_{zz} & a_{xy} & a_{yy} & a_{yz} \\
 & 0 & & & & a_{zx} & a_{zy} & a_{zz} & & & -a_{xx} & & -a_{xy} & -a_{xz} \\
 & & 0 & & & -a_{yx} & -a_{yy} & -a_{yz} & a_{xx} & a_{xy} & a_{xz} & & & \\
 & & & 0 & \omega_e & & -a_{xz} & a_{xy} & & -a_{yz} & a_{yy} & & -a_{zz} & a_{zy} \\
 & & & & 0 & a_{xz} & & -a_{xx} & a_{yz} & & -a_{yx} & a_{zz} & & -a_{zx} \\
 & & & & & 0 & -a_{xy} & -a_{xx} & -a_{yy} & a_{yz} & & -a_{zy} & a_{zx} & \\
 & & & & & & 0 & \omega_e & \omega_\mu & & & & & \\
 & & & & & & & 0 & & \omega_\mu & & & & \\
 & & & & & & & & 0 & & \omega_\mu & & & \\
 & & & & & & & & & 0 & \omega_e & & & \\
 & & & & & & & & & & 0 & & & \\
 & & & & & & & & & & & 0 & \omega_e & \\
 & & & & & & & & & & & & 0 & \\
 & & & & & & & & & & & & & 0
\end{bmatrix}$$

Notes about this expression:

i Only the upper triangle of Q is represented, since it is an antisymmetric matrix;

ii The geometry conventions of Chapter 3 are followed, namely that the external magnetic field is applied along the z-axis;

iii ω_μ and ω_e are the Larmor frequencies of the positive muon and the electron in the applied field B: $\omega_\mu = \gamma_\mu B$, $\omega_e = -\gamma_e B$;

iv The hyperfine tensor is represented in this expression by

$$\mathbf{A} = \frac{1}{\pi} \begin{bmatrix} a_{xx} & a_{xy} & a_{xz} \\ a_{yx} & a_{yy} & a_{yz} \\ a_{zx} & a_{zy} & a_{zz} \end{bmatrix} .$$

Bibliography

[1] A.O. Abu-Hilal, A.M. Saleh and R.D. Gould, Materials Chemistry and Physics **94**, 165-171 (2005)

[2] C.M. Aegerter and S.L. Lee, Appl. Mag. Res. **13**, 75 (1997)

[3] N. Amar, R.D. Gould and A.M. Saleh, Vacuum **50**, 53-56 (1998)

[4] C.D. Anderson and S.H. Neddermeyer, Phys. Rev. **50**, 263 (1936)

[5] V.I. Arkhipov, E.V. Emelianova, P. Heremans and H. Bässler, Phys. Rev. B **72**, 235202 (2005)

[6] N.W. Ashcroft and N.D. Mermin, *Solid State Physics* (Saunders College, Orlando, 1976)

[7] D. Baeriswyl, D.K. Campbell and S. Mazumdar, in *Conjugated Conducting Polymers*, edited by H.G. Kiess, Springer Series in Solid-State Sciences Vol. 102 (Springer-Verlag, New York, 1992)

[8] S.J. Blundell, P.A. Pattenden, F.L. Pratt, R.M. Valladares, T. Sugano, and W. Hayes Europhys. Lett. **31**, 573 (1995)

[9] S.J. Blundell, Contemporary Phys. **40**, 175-192 (1999)

[10] S.J. Blundell, Chem. Rev. **104**, 5717-5735 (2004)

[11] C.J. Brabec, N.S. Sariciftci and J.C. Hummelen, Adv. Funct. Mater. **11**, 15-26 (2001)

[12] J.H. Brewer, K.M. Crowe, F.N. Gygax, R.F. Johnson, B.D. Patterson, D.G. Fleming and A. Schenck, Phys. Rev. Lett. **31**, 143 (1973)

[13] J. Brewer, *Muon Spin Rotation/Relaxation/Resonance* in *Encyclopedia of Applied Physics*, Vol. 11 (VCH Publishers, New York, 1994)

[14] J.H. Burroughes, D.D.C. Bradley, A.R. Brown, R.N. Marks, K. Mackay, R.H. Friend, P.L. Burns and A.B. Holmes, Nature **347**, 539-541 (1990)

[15] M. Calvete, *Binuclear Phthalocyanines: Synthesis, Characterisation and Optical Limiting Properties*, PhD. Thesis (Fakultät für Chemie und Pharmazie, Eberhard-Karls Universität, Tübingen, 2004)

[16] M. Celio and P.F. Meier, Phys. Rev. B **27**, 1908-1910 (1983)

[17] C. Chan, W. Gao and A. Kahn, J. Vac. Sci. Technol. A **22**, 1488-1492 (2004)

[18] K.H. Chow, B. Hitti and R.F. Kiefl, *μSR on Muonium in Semiconductors and Its Relation to Hydrogen* in *Semiconductors and Semimetals 51A: Identification of Defects in Semiconductors*, edited by M. Stavola, Vol. 51, series editors R.K. Willardson and E.R. Weber (Academic Press, Boston, 1998)

[19] S.F.J. Cox, D.A. Geeson, C.J. Rhodes, E. Roduner, C.A. Scott and M.C.R. Symons, Hyperfine Interactions **32**, 763-768 (1986)

[20] S.F.J. Cox, J. Phys. C: Solid State Phys. **20**, 3187-3319 (1987)

[21] S. F. J. Cox, E. A. Davis, S. P. Cottrell, P. J. C. King, J. S. Lord, J. M. Gil, H. V. Alberto, R. C. Vilão, J. Piroto Duarte, N. Ayres de Campos, A. Weidinger, R. L. Lichti, and S. J. C. Irvine Phys. Rev. Lett. **86**, 2601-2604 (2001)

[22] S.F.J. Cox, J. Phys.: Condens. Matter **15**, R1727-R1780 (2003)

[23] S.F.J. Cox, J.S. Lord, S.P. Cottrell, J.M. Gil, H.V. Alberto, A. Keren, D. Prabhakaran, R. Scheuermann and A. Stoykov, J. Phys.: Condens. Matter **18**, 1061-1078 (2006)

[24] S.F.J. Cox, J.L. Gavartin, J.S. Lord, S.P. Cottrell, J.M. Gil, H.V. Alberto, J. Piroto Duarte, R.C. Vilão, N. Ayres de Campos, D.J. Keeble, E.A. Davis, M. Charlton and D.P. van der Werf, J. Phys.: Condens. Matter **18**, 1079-1119 (2006)

[25] M.F. Craciun, S. Rogge and A. F. Morpurgo, J. Am. Chem. Soc. **127**, 12210-12211 (2005)

[26] M.F. Craciun, S. Rogge, M.J.L. den Boer, S. Margadonna, K. Prassides, Y. Iwasa and A. F. Morpurgo, Adv. Mater. **18**, 320-324 (2006)

[27] P. Dalmas de Réotier and A. Yaouanc, J. Phys. Cond. Matt. **9**, 9113 (1997)

[28] C.D. Dimitrakopoulos and P.R.L. Malenfant, Adv. Mater. **14**, 101-103 (2002)

[29] *Dictionary of Organic Compounds*, Vol. 5, 4$^{\text{th}}$ Edition (Eyre & Spottiswoode Publishers, London, 1965)

[30] S. Dick, H. Peisert, D. Dini, M. Hanack, M.J. Cook, I. Chambrier and T. Chassé, J. Appl. Phys. **97**, 073715 (2005)

[31] S. Eidelman et al. (Particle Data Group), Phys. Lett. B **592**, 1 (2004)
partial update for the 2006 edition available on the PDG WWW pages
(URL: http://pdg.lbl.gov/)

[32] M.K. Engel, Kawamura Rikagaku Kenkyusho Hokoku, Volume Date, **8**, 11-54 (1997)

[33] L.A. Eriksson, V.G. Malkin, O.L. Malkina and D.R. Salahub, J. Chem. Phys. **99**, 9756-9763 (1993)

[34] L.A. Eriksson, O.L. Malkina, V.G. Malkin and D.R. Salahub, J. Chem. Phys. **100**, 5066-5074 (1994)

[35] T.L. Estle, S. Estreicher and D.S. Marynick, Phys. Rev. Lett. **58**, 1547-1550 (1987)

[36] J.B. Foresman and A. Frisch, *Exploring Chemistry with Electronic Structure Methods* (2nd Ed., Gaussian Inc., Pittsburgh, 1996)

[37] S.R. Forrest, Chem. Rev. **97**, 1793-1896 (1997)

[38] J.I. Friedman and V.L. Teledgi, Phys. Rev. **105**, 1681 (1957)

[39] R.H. Friend, R.W. Gymer, A.B. Holmes, J.H. Burroughes R.N. Marks, C. Taliani, D.D.C. Bradley, D.A. dos Santos, J.L. Brédas, M. Lögdlund and W.R. Salaneck, Nature **397**, 121-128 (1999)

[40] W. Gao and A. Kahn, Appl. Phys. Lett. **79**, 4040-4042 (2001)

[41] Computer code GAUSSIAN 98, revision A.9, Gaussian Inc, Pittsburgh, PA, 1998.

[42] R.L. Garwin, L.M. Lederman and M. Weinrich, Phys. Rev. **105**, 1415 (1957)

[43] G.H. Gelinck, T.C.T. Geuns and D.M. de Leeuw, Appl. Phys. Lett. **77**, 1487-1489 (2000)

[44] S.E. Gledhill, B. Scott, B.A. Gregg, Journal of Materials Research **20**, 3167-3179 (2005)

[45] J.M. Gil, H.V. Alberto, R.C. Vilão, J. Piroto Duarte, P.J. Mendes, L.P. Ferreira, N. Ayres de Campos, A. Weidinger, J. Krauser, Ch. Niedermayer and S.F.J. Cox, Phys. Rev. Lett. **83**, 5294 (1999)

[46] J.M. Gil, P.J. Mendes, L.P. Ferreira, H.V. Alberto, R.C. Vilão, N. Ayres de Campos, A. Weidinger, Y. Tomm, Ch. Niedermayer, M. Y. Yakushev, R.D. Tomlinson, S.P. Cottrell and S.F.J. Cox, Phys. Rev. B **59**, 1912 (1999)

[47] J.M. Gil, H.V. Alberto, R.C. Vilão, P.J. Mendes, L.P. Ferreira, N. Ayres de Campos, A. Weidinger, J. Krauser, Ch. Niedermayer, and S.F.J. Cox, Phys. Rev. B **64**, 075205 (2001)

[48] M. Goldhaber, L. Grodzins and A.W. Sunyar, Phys. Rev. **106**, 826 (1957)

[49] B.A. Gregg, S.G. Chen and R.A. Cormier, Chem. Mater. **16**, 4586-4599 (2004)

[50] F. Gutmann and L.E. Lyons, *Organic Semiconductors* (John Wiley & Sons, New York, 1967)

[51] T. Inabe and H. Tajima, Chem. Rev. **104**, 5503-5533 (2004)

[52] I.G. Ivanter and V.P. Smilga, Sov. Phys. JETP **27**, 301-306 (1968)

[53] I.G. Ivanter and V.P. Smilga, Sov. Phys. JETP **28**, 796-801 (1969)

[54] J.D. Jackson, *Classical Electrodynamics* 3rd. Edition (Wiley, New York, 1998)

[55] H.T. Jonkman and J. Kommandeur, Chem. Phys. Lett. **15**, 496-499 (1972)

[56] H.E. Katz, A.J. Lovinger, J. Johnson, C. Kloc, T. Siegrist, W. Li, Y.Y. Lin and A. Dodabalapur, Nature **404**, 478-481 (2000)

[57] A. Keren, P. Mendels, I. A. Campbell and J.S. Lord, Phys. Rev. Lett. **77**, 1386-1389 (1996)

[58] H.R. Kerp and E.E. van Faassen, *Proceedings of the 11th Workshop on Quantum Solar Energy Conversion* (1999)

[59] H.R. Kerp and E.E. van Faassen, Chem. Phys. Lett. **332**, 5-12 (2000)

[60] B. Kessler, Appl. Phys. A **67**, 125-133 (1998)

[61] R.F. Kiefl, M. Celio, T.L. Estle, S.R. Kreitzman, G.M. Luke, T.M. Riseman and E.J. Ansaldo, Phys. Rev. Lett. **60**, 224-226 (1988)

[62] M. Kira, H. Sakurai, Journal of the American Chemical Society **99**, 3892 (1977)

[63] S.L. Lee, F.L. Pratt, S.J. Blundell, C.M. Aegerter, P.A. Pattenden, K.H. Chow, E.M. Forgan, T. Sasaki, W. Hayes and H. Keller, Phys. Rev. Lett. **79**, 1563 (1997)

[64] M.S. Liao and S. Scheiner, J. Chem. Phys **114**, 9780-9791 (2001)

[65] R.L. Lichti, *μSR on Muonium in Semiconductors and Its Relation to Hydrogen* in *Semiconductors and Semimetals 51A: Identification of Defects in Semiconductors*, edited by M. Stavola, Vol. 51, series editors R.K. Willardson and E.R. Weber (Academic Press, Boston, 1998)

[66] J.S. Lord, S.P. Cottrell, P.J.C. King, H.V. Alberto, N. Ayres de Campos, J.M. Gil, J. Piroto Duarte, R.C. Vilão, R.L. Lichti, S.K.L. Sue, B.A. Bailey, A. Weidinger, E.A. Davis and S.F.J. Cox, Physica B: Condensed Matter **308-310**, 920 (2001)

[67] J. S. Lord, Journal of Physics: Conference Series **17**, 81-86 (2005)
Fifth International Conference on Fine Particle Magnetism

[68] B.W. Lovett, S.J. Blundell, J.S. Stiessberger, F.L. Pratt, Th. Jestädt, W. Hayes, S.P. Cottrell and I.D. Reid, Phys. Rev. B **63**, 054204 (2001)

[69] R.M. Macrae, Magn. Reson. Chem. **38**, S33-S42 (2000)

[70] B. Maennig, M. Pfeiffer, A. Nollau, X. Zhou, K. Leo and P. Simon, Phys. Rev. B **64**, 195208 (2001)

[71] P.F. Meier Phys. Rev. A **25**, 1287-1294 (1982)

[72] E.J. Meijer, D.M. de Leeuw, S. Setayesh, E. van Veenendal, B.H. Huisman, P.W.M. Blom, J.C. Hummelen, U. Scherf and T.M. Klapwijk, Nature Materials **2**, 678-682 (2003)

[73] Ö. Mermer, G. Veeraraghavan, T.L. Francis, Y. Sheng, D.T. Nguyen, M. Wohlgenannt A. Kessler, M.K. Al-Suti and M.S. Kahn, Phys. Rev. B **72**, 205202 (2005)

[74] J. Mizuguchi and S. Matsumoto, J. Phys. Chem. A **103**, 614-616 (1999)

[75] P.J. Mohr and B.N. Taylor, *CODATA Recommended Values of the Fundamental Physical Constants: 2002* (CODATA — the Committee on Data for Science and Technology, 2006) (http://physics.nist.gov/constants)

[76] M.A. Morrison, T.L. Estle and N.F. Lane, *Understanding More Quantum Physics* (Prentice-Hall, New Jersey, 1991)

[77] F.H. Moser and W.H. Rhodes, *Phthalocyanine Compounds* in *Encyclopedia of Chemical Technology*, Vol.17, 777-787 (John Wiley, New York, 1982)

[78] M. Muccini, Nature Materials **5**, 605-613 (2006)

[79] K.A. Nguyen and R. Pachter, J. Chem. Phys. **114**, 10757-10767 (2001)

[80] http://nobelprize.org/nobel_prizes/chemistry/laureates/2000/index.html

[81] J.E. Northrup and M.L. Chabinyc, Phys. Rev. B **68**, 041202 (2003)

[82] V.G. Nosov and I.V. Yakovleva, Sov. Phys. JETP **16**, 1236-1294 (1963)

[83] V.G. Nosov and I.V. Yakovleva, Nuclear Phys. **68**, 609-631 (1965)

[84] L. F. Pascios and P. A. Christiansen, J. Chem. Phys. **82**, 2664 (1985)

[85] B.D. Patterson, Rev. Mod. Phys. **60**, 69-159 (1988)

[86] M.Pfeiffer, A. Beyer, T. fritz and K. Leo, Appl. Phys. Lett. **73**, 3202-3204 (1998)

[87] F.L. Pratt, S.J. Blundell, W. Hayes, K. Nagamine, K. Ishida and A.P. Monkman, Phys. Rev. Lett. **79**, 2855-2858 (1997)

[88] F.L. Pratt, S.J. Blundell, Th. Jestadt, B.W. Lovett, R.M. Macrae and W. Hayes, Magn. Reson. Chem. **38**, S27-S32 (2000)

[89] F.L. Pratt, S.J. Blundell, I.M. Marshall, T. Lancaster, A. Husmann, C. Steer, W. Hayes, C. Fischmeister, R.E. Martin and A.B. Holmes, Physica B **326**, 34-40 (2003)

[90] F.L. Pratt, T. Lancaster, M. L. Brooks, S. J. Blundell, T. Prokscha, E. Morenzoni, A. Suter, H. Luetkens, R. Khasanov, R. Scheuermann, U. Zimmermann, K. Shinotsuka and H. E. Assender, Phys. Rev. B **72**, 121401R (2005)

[91] T.Prokscha, E.Morenzoni, N.Garifianov, H. Glücklera, R.Khasanov, H.Luetkens and A.Suter, Physica B **326** 51–54 (2003)

[92] W. Rehwald and H.G. Kiess, in *Conjugated Conducting Polymers*, edited by H.G. Kiess, Springer Series in Solid-State Sciences Vol. 102 (Springer-Verlag, New York, 1992)

[93] F.T. Reis, D. Mencaraglia, S. Oould Saad, I. Séguy, M. Oukachmih, P. Jolinat and P. Destruel, Synthetic Metals **138**, 33-37 (2003)

[94] M. Reufer, M.J. Walter, P.G. Lagoudakis, A.B. Hummel, J.S. Kolb, H.G. Roskos, U. Scherf and J.M. Lupton, Nature Materials **4**, 340-346 (2005)

[95] C.J. Rhodes, J. Chem. Soc., Perkin Trans. **2**, 1379-1396 (2002)

[96] A.S. Riad, M.T. Korayem and T.G. Abdel-Malik, Physica B **270**, 140-147 (1999)

[97] G. Ricciardi, A. Rosa and E.J. Baerends, J. Phys. Chem. A **105**, 5242-5254 (2001)

[98] E. Roduner and H. Fischer, Chem. Phys. **54**, 261-276 (1981)

[99] E. Roduner, *The Positive Muon as a Probe in Free Radical Chemistry - Potential and Limitations of the μSR Techniques*, Lecture Notes in Chemistry Vol. 49 (Springer-Verlag, Berlin/Heidelberg, 1988)

[100] G. Ruani, C. Fontanini, M. Murgia and C. Taliani, J. Chem. Phys. **116**, 1713-1719 (2002)

[101] R. Sathyamoorthy, S. Senthilarasu, S. Lalitha, A. Subbarayan, K. Natarajan and X. Mathew, Sol. En. Mat. & Sol. Cel. **82**, 169-177 (2004)

[102] A.M. Saleh, A.O. Abu-Hilal and R.D. Gould, Current Applied Physics **3**, 345-350 (2003)

[103] G. Schatz, A. Weidinger and J.A. Gardner, *Nuclear Condensed Matter Physics - Nuclear Methods and Applications* (John Wiley & Sons, Chichester, 1996)

[104] J.R. Sheats, H. Antoniadis, M. Heuschen, W. Leonard, J. Miller, R. Moon, D. Roitman and A. Stocking, Science **273**, 884 (1996)

[105] W.R. Scheidt and W. Dow, J. Am. Chem. Soc. **99**, 1101-1104 (1977)

[106] A. Schenck, *Muon Spin Rotation Spectroscopy - Principles and Applications in Solid State Physics* (Adam Hilger, Bristol, 1985)

[107] Roland Schmechel, J. Appl. Phys. **93**, 4653-4660 (2003)

[108] M. Senba, J. Phys. B: At. Mol. Opt. Phys. **21**, 3093-3111 (1988)

[109] M.Senba, J. Phys. B: At. Mol. Opt. Phys. **22**, 2027-2040 (1989)

[110] M. Senba, D.G. Fleming, D.J. Arseneau, D.M. Garner and I.D. Reid, Phys. Rev. A **39**, 3871-3883 (1989)

[111] M. Senba, J. Phys. B: At. Mol. Opt. Phys. **23**, 1545-1562 (1990)

[112] M. Senba, J. Phys. B: At. Mol. Opt. Phys. **23**, 4051-4070 (1990)

[113] M. Senba, Hyperfine Interactions **65**, 779-792 (1990)

[114] M. Senba, D.J. Arseneau, A.C. Gonzalez, J.R. Kempton, J.J. Pan, A. Tempelmann and D.G. Fleming, Hyperfine Interactions **65**, 793-800 (1990)

[115] M. Senba, J. Phys. B: At. Mol. Opt. Phys. **24**, 3531-3549 (1991)

[116] M. Senba, J. Phys. B: At. Mol. Opt. Phys. **26**, 3213-3222 (1993)

[117] M. Senba, Phys. Rev. A **50**, 214-227 (1994)

[118] M. Senba, Hyperfine Interactions **87**, 953-958 (1994)

[119] M. Senba, J. Phys. B: At. Mol. Opt. Phys. **31**, 5233-5260 (1998)

[120] M. Senba, Phys. Rev. A **62**, 042505 (2000)

[121] M. Senba, J. Phys. B: At. Mol. Opt. Phys. **34**, 4437-4454 (2001)

[122] M. Senba, J. Phys. B: At. Mol. Opt. Phys. **38**, 1305-1328 (2005)

[123] S. Senthilarasu, R. Sathyamoorthy, S. Lalitha and A. Subbarayan, Solid-State Electronics **49**, 813-817 (2005)

[124] R. Seoudi, G.S. El-Bahy and Z.A. El Sayed, Journal of Molecular Structure **753**, 119-126 (2005)

[125] Y. Scheng, T.D. Nguyen, G. Veeraraghavan, Ö. Mermer, M. Wohlgenannt, S. Qiu and U. Scherf, Phys. Rev. B **74**, 045213 (2006)

[126] V.P. Smilga and Yu.M. Belousov, *The Muon Method in Science*, Proceedings of the Lebedev Physics Institute - Academy of Sciences of Russia Vol. 219 (Nova Science Publishers, New York, 1994)

[127] S. Steudel, K. Myny, V. Arkhipov, C. Deibel, S. de Vusser, J. Genoe and P. Heremans, Nature Materials **4**, 597-600 (2005)

[128] W. J. Stevens, H. Basch and M. Krauss, J. Chem. Phys. **81**, 6026 (1984).

[129] V.G. Storchak and N.V. Prokof'ev, Rev. of Mod. Phys. **70**, 929-978 (1998)

[130] A. Troisi and G. Orlandi, Phys. Rev. Lett. **86**, 086601 (2006)

[131] R.E. Turner, R.F. Snider and D.G. Fleming, Phys. Rev. A **41**, 1505-1516 (1990)

[132] Y. J. Uemura, W. J. Kossler, X. H. Yu, H. E. Schone, J. R. Kempton, C. E. Stronach, S. Barth, F. N. Gygax, B. Hitti, and A. Schenck, C. Baines, W. F. Lankford, Y. Onuki and T. Komatsubara, Phys. Rev. B **39**, 4726-4729 (1989)

[133] R.C. Vilão, *Estudo das interacções do hidrogénio com defeitos estruturais em semicondutores do tipo calcopirite utilizando técnicas de muões*, MSc. Thesis (Faculty of Sciences and Technology, University of Coimbra, Coimbra, 2002)

[134] C.G. Van de Walle Phys. Rev. Lett. **85**, 1012-1015 (2000)

[135] C.G. Van de Walle and J. Neugebauer, Nature **423**, 626-628 (2003)

[136] J.M. Warman, M.P. de Haas, G. Dicker, F.C. Grozema, J. Piris and M.G. Debije, Chem. Mater. **16**, 4600-4609 (2004)

[137] Z.H. Xiong, D. Wu, Z.V. Vardeny and J. Shi, Nature **427**, 821-824 (2004)

[138] T. Yamazaki, K. Nagamine, K. Crowe and J. Brewer, μSR Newsletter **1** (1974)

[139] D. Yu, P. W. Percival, J. C. Brodovitch, S. K. Leung, R. F. Kiefl, K. Venkateswaran and S. F. J. Cox, Chem. Phys. **142**, 229 (1990)

[140] J. F. Ziegler, J. P. Biersack and U. Littmark, *The Stopping and Range of Ions in Solids* 2nd Edition (Pergamon Press, New York, 2003)
http://www.SRIM.org

[141] X. Zhang and S.A. Jenekhe, Macromolecules **33**, 2069 (2000)

Este trabalho foi parcialmente financiado pelos seguintes programas / This work was partially supported by the following programmes:

Ministério da Educação do Estado Português / Fundo Social Europeu (FSE)
Programa PRODEP III
Acção 5.3 - Formação Avançada de Docentes do Ensino Superior
Portuguese Ministry of Education / European Social Fund (ESF)
Programme PRODEP III
Action 5.3 - Advanced Formation for High Education Teaching Staff

European Commission - 6th Framework Programme
Key Action: Strengthening the European Research Area, Research Infrastructures
Contract No. RII3-CT-2004-505925